



UNIVERSIDAD NACIONAL AUTÓNOMA DE MÉXICO
DOCTORADO EN CIENCIAS BIOMÉDICAS
INSTITUTO DE NEUROBIOLOGÍA

**RESPUESTA AL PRECONDICIONAMIENTO HIPÓXICO DE UN CÚMULO
NOVEDOSO DE CÉLULAS GFAP+ Y NESTINA+ DEL TECHO DEL CUARTO
VENTRÍCULO**

TESIS
QUE PARA OPTAR POR EL GRADO DE:
DOCTOR EN CIENCIAS BIOMÉDICAS

PRESENTA:
MARYMAR BECERRA GONZÁLEZ

DIRECTOR DE TESIS
DR. ATAÚLFO MARTÍNEZ TORRES
INSTITUTO DE NEUROBIOLOGÍA

COMITÉ TUTOR
DRA. MARÍA TERESA MORALES GUZMÁN
INSTITUTO DE NEUROBIOLOGÍA

DR. MIGUEL PÉREZ DE LA MORA
INSTITUTO DE FISIOLÓGÍA CELULAR

JURIQUILLA, QUERÉTARO. MAYO 2021



Universidad Nacional
Autónoma de México



UNAM – Dirección General de Bibliotecas
Tesis Digitales
Restricciones de uso

DERECHOS RESERVADOS ©
PROHIBIDA SU REPRODUCCIÓN TOTAL O PARCIAL

Todo el material contenido en esta tesis esta protegido por la Ley Federal del Derecho de Autor (LFDA) de los Estados Unidos Mexicanos (México).

El uso de imágenes, fragmentos de videos, y demás material que sea objeto de protección de los derechos de autor, será exclusivamente para fines educativos e informativos y deberá citar la fuente donde la obtuvo mencionando el autor o autores. Cualquier uso distinto como el lucro, reproducción, edición o modificación, será perseguido y sancionado por el respectivo titular de los Derechos de Autor.

Este trabajo se realizó en el Departamento de Neurobiología Celular y Molecular del Instituto de Neurobiología de la Universidad Nacional Autónoma de México (UNAM), bajo la dirección del Dr. Ataúlfo Martínez Torres. Contó con el apoyo del proyecto Ciencia Básica CONACYT A1-S-7659 y PAPIIT-DGAPA IN204520.

Agradecimientos

Agradezco a la Universidad Nacional Autónoma de México (UNAM) por darme la oportunidad de realizar mis estudios en el Programa de Doctorado en Ciencias Biomédicas (PDCB) en el Instituto de Neurobiología (INB) (No. De cuenta: 515010969). Asimismo, agradezco el apoyo del Consejo Nacional de Ciencia y Tecnología (CONACYT) (no. CVU: 619206, no. de registro becario: 330119, no. apoyo: 385361, convocatoria: 290915), de la convocatoria becas mixtas 2016 - marzo 2017 movilidad en el extranjero (no. convocatoria: 291062) y de la DGAPA-PAPIIT IN200913 por el financiamiento otorgado.

Expreso mi agradecimiento profundo a mi tutor, el Dr. Ataúlfo Martínez Torres quien me ha compartido sus conocimientos y por ofrecerme su apoyo, paciencia y excelente mentoría en la realización de este proyecto. Igualmente, por permitirme formar parte de su prestigioso laboratorio de Neurobiología Molecular y Celular. Extiendo mi gratitud a mi comité tutorial formado por la Dra. María Teresa Morales Guzmán y el Dr. Miguel Pérez de la Mora.

Agradezco el apoyo de integrantes del laboratorio quienes contribuyeron a la realización de este proyecto: al Dr. Ragu Varman Durairaj, a la M. C. Aline Ostos Valverde, a la Dra. Wendy Portillo Martínez y a la M. C. Gabriela Berenice Gómez González. Asimismo, agradezco el apoyo y colaboraciones del Dr. Emilio J. Gualda y el Dr. Pablo Loza-Alvarez del Instituto de Ciencias Fotónicas (Casteldefels, Barcelona) y de la Dra. Annalisa Buffo de la Universidad de Turín (Turín, Italia). Finalmente agradezco la mentoría de la Dra. Adriana Pétriz Reyes y la Dra. Ma. Alejandra González González.

Agradezco el extraordinario apoyo técnico de la Dra. Angeles Edith Espino Saldaña y de la auxiliar de laboratorio Marina Ramírez Romero. Agradezco al MVZ. Martín García Servín y a la Dra. Alejandra Castilla, miembros del bioterio que me proporcionaron los animales experimentales. Finalmente, agradezco a la Ing. Nydia Hernández Ríos por su apoyo en la unidad de microscopía, a la M. en C. Leonor Casanova Rico, Dra. Nuri Aranda López y a Ma. Carmen Mendoza López por su apoyo y coordinación en la unidad de enseñanza del INB y a la Lic. Lourdes Lara Ayala por su colaboración en la unidad de videoconferencia.

Abreviaturas

ABC	Complejo avidina-biotina (por sus siglas en inglés)
Akt	Proteína cinasa B
Aldh1L1	Aldehído deshidrogenasa 1 miembro de la familia L1 (por sus siglas en inglés)
AMPA	Ácido α -amino-3-hidroxi-5-metilo-4-isoxazolpropiónico
AN	Apertura numérica
ATP	Adenosín trifosfato
BAD	Agonista asociado a BCL2 (por sus siglas en inglés)
BCIP	Sal disódica de fosfato de 5-bromo-4-cloro-3-indolilo (por sus siglas en inglés)
BDNF	Factor neurotrófico derivado del cerebro (por sus siglas en inglés)
BER	Reparación por escisión de bases
BHE	Barrera hematoencefálica
BrdU	Bromodesoxiuridina
CCL2	Ligando de quimiocina 2 (por sus siglas en inglés)
CCSV	Clúster celular subventricular
CM	Capa molecular
CO ₂	Dióxido de carbono
CPN	Células progenitoras neurales
CVM	Cordón ventromedial
Cx30	Conexina 30
Cx43	Conexina 43
CXCL10	Ligando 10 de quimiocina con motivo C-X-C (por sus siglas en inglés)
DOI	Densidad óptica integrada
E	Día Embrionario
EEAT	Transportadores de aminoácidos excitadores (por sus siglas en inglés)
EGFP	Proteína verde fluorescente mejorada (por sus siglas en inglés)
EPO	Eritropoyetina
FI	Filamento intermedio
GABA	Ácido gamma-aminobutírico
GB	Glía de Bergmann
GFAP	Proteína ácida fibrilar glial (por sus siglas en inglés)
GLAST	Transportador de glutamato / aspartato (por sus siglas en inglés)
GLT-1	Transportador de glutamato 1 (por sus siglas en inglés)
GVR	Grupo ventral respiratorio
HIF	Factor inducido por hipoxia (por sus siglas en inglés)
IFN	Interferones de tipo I
IGF-1	Factor de crecimiento insulínico tipo 1 (por sus siglas en inglés)
IL10	Interleucina-10

JAK2	Janus cinasa 2 (por sus siglas en inglés)
LCE	Líquido cerebroespinal
LSFM	Microscopía de fluorescencia con hoja de luz (por sus siglas en inglés)
MAPK	Proteínas cinasas activadas por mitógenos (por sus siglas en inglés)
MCP-1	Proteína quimioatrayente de monocitos 1 (por sus siglas en inglés)
NADH	Nicotinamida adenina dinucleótido (forma reducida)
NBT	Cloruro de nitroazul tetrazolio (por sus siglas en inglés)
NER	Reparación por escisión de nucleótidos
NF- κ B	Factor nuclear kappa B
ODD	dominio de degradación dependiente de oxígeno (por sus siglas en inglés)
P	Día Postnatal
PCH	Precondicionamiento hipóxico
PET	Tomografía por emisión de positrones (por sus siglas en inglés)
PFA	Paraformaldehído
PHD	Dominio prolil hidroxilasa (por sus siglas en inglés)
PI3K	Fosfatidilinositol-3-cinasa
pVHL	Proteína supresora de tumores von Hippel-Lindau
REM	Movimientos rápidos de los ojos (por sus siglas en inglés)
ROI	Región de interés
ROS	Especies reactivas de oxígeno (por sus siglas en inglés)
SE	Error estándar (por sus siglas en inglés)
SNC	Sistema nervioso central
STAT3	Transductor de señal y activador de la transcripción 3 (por sus siglas en inglés)
TGF- β	Factor de crecimiento transformante beta (por sus siglas en inglés)
VEGF	Factor de crecimiento endotelial vascular (por sus siglas en inglés)
WB	<i>Western blot</i>
ZSG	Zona subgranular
ZSV	Zona subventricular

Índice

Agradecimientos.....	III
Abreviaturas.....	IV
Abstract.....	VIII
Resumen	X
I. Introducción	1
II. Anatomía del cerebelo	11
II.1. Localización y organización macroscópica.....	11
II.2. Citología.....	11
II.2.1. Organización del componente neuronal	12
II.2.2. Componente glial.....	16
III. Hipoxia	22
III.1. Precondicionamiento hipóxico	24
III.1.1. Precondicionamiento hipóxico y neurogénesis.....	26
IV. El cerebelo y el control respiratorio	28
IV.1. Barreras del SNC	28
IV.1.1. Líquido cerebroespinal.....	29
V. Planteamiento del problema	30
VI. Hipótesis.....	30
VII. Objetivo general.....	30
VIII. Objetivos específicos.....	31
IX. Materiales y métodos.....	32
IX.1. Declaración ética	32
IX.2. Animales.....	32
IX.3. Inducción de PCH.....	32
IX.4. Análisis histológico	33
IX.5. CLARITY	33
IX.6. Microscopía de fluorescencia por hoja de luz	34
IX.7. Pruebas conductuales.....	35
IX.8. Procesamiento de tejidos e imágenes	35
IX.9. Tinción rápida de Golgi.....	36
IX.10. <i>Western blot</i>	36

IX.11. Inmunofluorescencia para microglía	37
IX.12. Ensayo de incorporación de bromodesoxiuridina (BrdU).....	38
IX.13. Análisis estadístico	39
X. Resultados.....	40
X.1. Desarrollo del CVM y del CCSV	40
X.2. La inducción del PCH se refleja en el aumento de tolerancia	42
X.3. La coordinación motora no es afectada significativamente por el PCH.....	43
X.4. Cambios en la expresión de EGFP en el cerebelo en respuesta al PCH.....	45
X.5. El CVM reduce la expresión de la EGFP en respuesta al PCH	47
X.6. La expresión de la EGFP disminuye en respuesta al PCH en el lóbulo I	48
X.7. La GB adquiere un fenotipo diferente en respuesta al PCH	50
X.8. El PCH afecta los niveles de marcadores de identidad gliales y neuronales evaluados por WB.....	51
X.9. El PCH no induce el aumento en el número de neuronas granulares NeuN+ en la CM	54
X.10. El PCH induce el aumento en el tamaño del soma de la microglía del lóbulo I.....	55
X.11. El PCH induce la incorporación limitada de BrdU en el techo del IV ventrículo ..	58
XI. Discusión	60
XII. Consideraciones finales y conclusiones	71
XIII. Referencias	74
XIV. Anexos.....	90

Abstract

The cerebellar cortex consists of neuronal and glial cells contained in 10 anteroposteriorly oriented lobules, which fold around the white matter together with the deep cerebellar nuclei. The cytoarchitecture of the cortex is stratified into three cell layers that are characterized by their homogeneous distribution. On the other hand, electrophysiological studies revealed that at the roof of the fourth ventricle the cerebellum includes cells with diverse ionic current profiles, suggesting the existence of cellular and functional diversity in the lobules I and X.

Lobules I and X are in direct contact with the cerebrospinal fluid (CSF) and form the anterior part of the roof of the IV ventricle. The cellular diversity of the region includes a structure called the subventricular cellular cluster (SVCC), where the end-feet of the Bergmann glia (BG) form the dorsal limit and the ependymal glial cells form the ventral limit. The SVCC holds glial fibrillary acidic protein (GFAP)-positive ependymal cells, GFAP-positive subependymal cells, neurons, oligodendrocytes, and possibly precursor cells. In addition to the SVCC, another structure called the ventromedial cord (VMC) was identified, which is composed of GFAP- and Nestin-positive cells (González-González et al., 2017).

The VMC is in the ventral medial section of the SVCC, next to the monolayer of ependymal cells that form the ventral limit of the SVCC. The VMC is restricted to a few cells (6-12) in a mediolateral direction with respect to the sagittal plane. The cells of the VMC are distributed along the sagittal plane, on the surface of the lobules I and X. The morphology of the glia of the VMC is different from the rest of the glia of the cerebellum. The cell soma is in close contact with the ventricle, where a pair of cilia emerges and contact the CSF, at the opposite end, a single process extends through the cerebellar parenchyma. Some of the VMC GFAP+ cells were also positive for Nestin, cells that express both GFAP and Nestin are considered a population of potential neural progenitor cells (NPCs) in the mature brain (Lemke, 2009).

The glia of the VMC resembles NPCs of the subgranular zone (SGZ) of the hippocampus and those from the subventricular zone (SVZ) from the lateral ventricles since they are GFAP+ and Nestin+. The SGZ progenitors are relatively inactive but proliferate and differentiate in response to hypoxic preconditioning (HPC). HPC consists in a moderate

exposure to hypoxia and results in the development of hypoxia tolerance and to other deleterious factors.

In this work, we investigated the ontogeny of the GFAP⁺ and Nestin⁺ cells of the VMC and its response to the HPC. Using light sheet fluorescence microscopy (LSFM) we observed cerebella from transgenic mice that express the enhanced Green Fluorescent Protein (EGFP) under the GFAP promoter. We found that HPC decreases EGFP levels. Western blot assays indicated that the astrocyte-identity markers GFAP and aldehyde dehydrogenase 1 family member L1 (Aldh1L1) had a temporary reduction (up to 50%) that was statistically significant. In contrast, the expression levels of Nestin (progenitor cells), NeuN (neurons) and Iba1 (microglia) increased in response to HPC. Using the Golgi technique, it was determined that processes of the BG increase the absolute protrusion length, and the soma area was reduced. Furthermore, HPC induced a slight activation of the microglia (adjacent to the VMC) determined by an increase in the soma area. HPC induced a limited incorporation of bromodeoxyuridine (BrdU, is an analog of the nucleoside thymidine used to assess cell proliferation) in cells of the roof of the IV ventricle (ruling out its proliferative effect). Unexpectedly, we observed that the cells of the floor of the IV ventricle incorporated BrdU.

In conclusion, the VMC is present from embryonic day 15, and this, along with other glial types of the area present plasticity in its morphology in response to the HPC, where the communication between the CSF-parenchymal interfaces probably enable that the area of the roof of the IV ventricle immediately adapts to maintain the cellular integrity for a prolonged period.

Resumen

La corteza del cerebelo se compone de células neuronales y gliales contenidas en 10 lóbulos orientados en sentido anteroposterior, los cuales se pliegan alrededor de la materia blanca junto con los núcleos profundos. La citoarquitectura de la corteza se estratifica en tres capas celulares que se caracterizan por su distribución homogénea. Por otra parte, estudios electrofisiológicos revelaron que en el techo del IV ventrículo el cerebelo incluye células con perfiles diversos de corrientes iónicas, sugiriendo la existencia de diversidad celular y funcional en los lóbulos I y X.

Los lóbulos I y X contactan directamente el líquido cerebroespinal y forman la parte anterior del techo del IV ventrículo. La diversidad celular de la región incluye una estructura llamada clúster celular subventricular (CCSV), donde los pies terminales de la glía de Bergmann forman el límite dorsal y las células gliales endodimales forman el límite ventral. El CCSV contiene células endodimales positivas para la proteína ácida fibrilar glial (GFAP), células subendodimales positivas para GFAP, neuronas, oligodendrocitos y posiblemente células precursoras. Además del CCSV, se identificó una estructura llamada cordón ventromedial (CVM), compuesto de células positivas a GFAP y Nestina (González-González et al., 2017).

El CVM está ubicado en la sección ventral medial del CCSV, adyacente a la monocapa de células endodimales que forman el límite ventral del CCSV. El CVM está restringido a unas pocas células (6-12) en una dirección mediolateral con respecto al plano sagital. Las células de esta estructura se distribuyen a lo largo del plano sagital, en la superficie de los lóbulos I y X. La glía del CVM tiene una morfología que se distingue del resto de la glía del cerebelo. El soma celular está en estrecho contacto con el ventrículo, donde emergen un par de cilios que contactan al líquido cerebroespinal. En la dirección opuesta, un solo proceso se extiende a través del parénquima cerebeloso. Algunas de las células GFAP+ del CVM también son positivas para Nestina, células que expresan tanto GFAP como Nestina se consideran como una población potencial de células progenitoras neurales en el cerebro maduro (Lemke, 2009).

La glía del CVM se parece a las células progenitoras neurales de la zona subgranular (ZSG) del hipocampo y de la zona subventricular (ZSV) de los ventrículos laterales en ser GFAP+

y Nestina+. Los progenitores de la ZSG son relativamente inactivos, pero proliferan y se diferencian en respuesta al preconditionamiento hipóxico (PCH). El PCH consiste en una exposición moderada a la hipoxia y da como resultado el desarrollo de tolerancia a la hipoxia y a otros factores nocivos.

En este trabajo, investigamos la ontogenia de las células GFAP+ y Nestina+ del CVM y su respuesta al PCH. Usando microscopía de fluorescencia de hoja de luz (LSFM) observamos cerebelos de ratones transgénicos que expresan la Proteína Verde Fluorescente mejorada bajo el promotor GFAP. Encontramos que el PCH disminuye la fluorescencia de la EGFP. Las pruebas de *Western blot* indicaron que los marcadores de identidad de astrocitos GFAP y aldehído deshidrogenasa 1 miembro de la familia L1 (Aldh1L1) disminuyeron transitoriamente (hasta en un 50%), de forma estadísticamente significativa. En contraste, los niveles de expresión de Nestina (células progenitoras), NeuN (neuronas) e Iba1 (microglía) aumentaron en respuesta al PCH. Utilizando la técnica de Golgi, se determinó que la GB tuvo un aumento considerable en la longitud absoluta de proyecciones y el área de los somas se redujo. Además, el PCH generó una leve activación de la microglía (adyacente al CVM) determinada por un aumento en el área del soma. El PCH indujo la incorporación limitada de bromodesoxiuridina (BrdU, es un análogo del nucleósido timidina utilizado para identificar células en proliferación) en células del techo del IV ventrículo (descartando su efecto proliferativo). Inesperadamente, observamos que las células del piso del IV ventrículo incorporaron BrdU.

En conclusión, el CVM se encuentra presente desde el día embrionario 15, y éste, junto con otros tipos gliales del área presentan plasticidad en su morfología en respuesta al PCH, donde la comunicación entre las interfaces líquido cerebroespinal-parénquima probablemente permiten que el área del techo del IV ventrículo se adapte de forma inmediata para mantener la integridad celular por un periodo prolongado.

I. Introducción

La corteza del cerebelo se distribuye en 10 lóbulos (I-X, de acuerdo con la clasificación de Larsell & Jansen, 1972) que se orientan sobre el plano sagital. Los lóbulos IV-IX se dirigen hacia la piamadre y los lóbulos I, II y X contactan hacia la cavidad del IV ventrículo. Estos últimos tienen un revestimiento de células ependimales cuyos cilios se extienden hacia la cavidad ventricular lo que permite la recolección de señales provenientes del líquido cerebrospinal (LCE) (**Figura 1**). El LCE desempeña funciones importantes en el transporte de hormonas y la transducción de señales a través del cerebro; así, las células que forman la pared del ventrículo están en una posición estratégica para detectar cambios que permiten el control homeostático (Cipolla, 2009; Del, 1995).

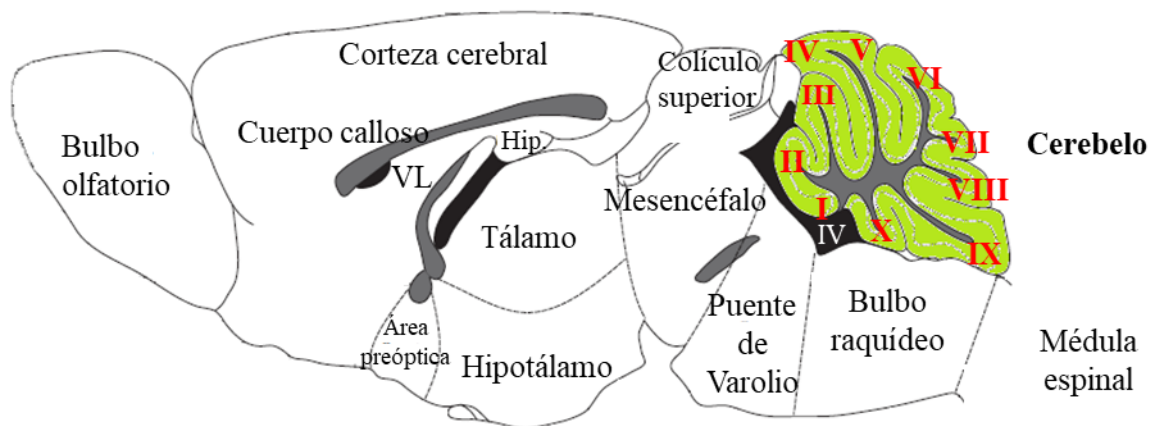


Figura 1. Esquema de corte sagital del encéfalo de ratón. En el cerebelo (verde) se indican los lóbulos del I al X. Los lóbulos I, II y X están en contacto con el IV ventrículo (IV). Modificado de Paxinos & Franklin, 2001.

En el cerebelo, la corteza está formada por tres capas celulares, la capa molecular, la capa de células de Purkinje y la capa granular (materia gris) en donde las células neuronales y gliales están ordenadas de una manera homogénea. La corteza cerebelar forma pliegues y surcos profundos alrededor de la materia blanca, misma que se organiza también en tres pares de núcleos profundos del cerebelo. Sin embargo, se demostró a través de técnicas electrofisiológicas, distintos perfiles de corriente que corresponden a diversos tipos celulares localizados en los lóbulos I, II y X, y junto con el uso de marcadores de identidad muestran que dicha diversidad celular forma una estructura llamada clúster celular subventricular (CCSV) (González-González et al., 2017). Esta población celular está delimitada en la parte dorsal por los pies terminales de la glía de Bergmann (GB) y en la parte ventral por células endpendimales que contactan directamente al LCE. Se muestra la diversidad celular del CCSV (**Figura 2** y **Figura 3**), que incluye:

1. Células endpendimales positivas a la proteína ácida fibrilar glial (GFAP) que revisten la cavidad ventricular.
2. Células subependimales GFAP+.
3. Neuronas.
4. Oligodendrocitos.
5. Y un quinto perfil de corriente que parece corresponder a células progenitoras neurales (CPN) (Reyes-Haro et al., 2013).

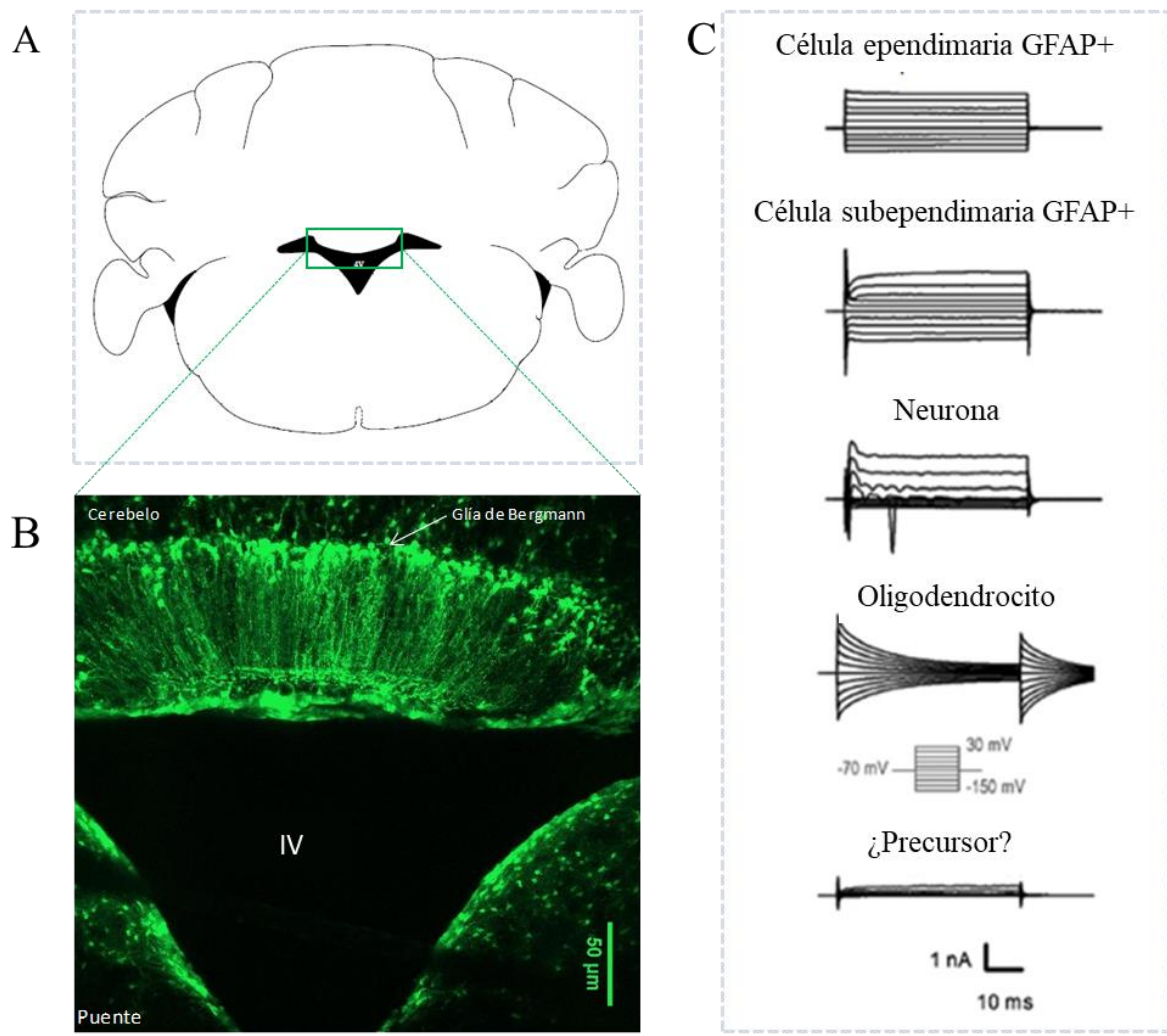


Figura 2. Corte coronal del cerebelo de un ratón transgénico GFAP::EGFP a nivel del lóbulo X. **A:** Esquema del cerebelo sobre el eje coronal. **B:** Corte coronal de cerebelo GFAP::EGFP mostrando el área en la que se realizaron los registros eléctricos de la población del CCSV. **C:** Perfiles de corriente de varios tipos celulares en la zona subventricular del cerebelo, (Modificado de Reyes-Haro et al., 2013).

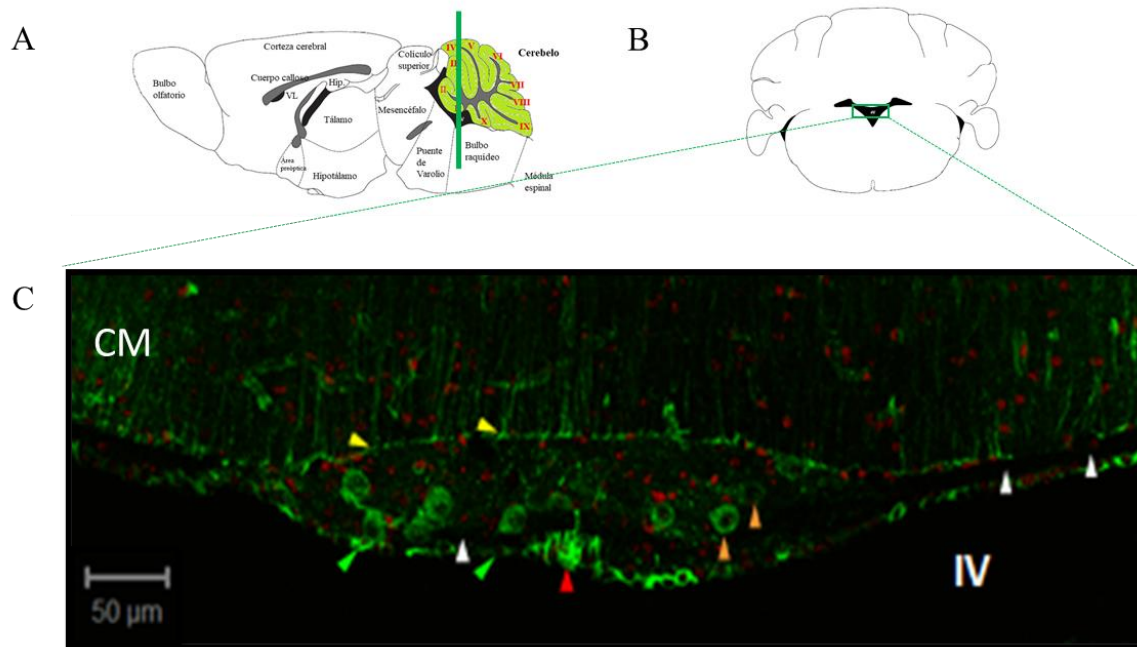


Figura 3. El clúster celular subventricular y sus componentes. **A:** Esquema de corte sagital, la línea verde indica el corte mostrado en el esquema **B**. **C:** Observamos el CCSV que cuenta con células Nestina+ (flechas naranjas), CVM Nestina+ (flecha roja), células endodimales que establecen el límite ventral del CCSV (flechas verdes), los pies terminales de la glía de Bergmann establecen el límite dorsal del CCSV (flechas amarillas) y las flechas blancas indican las regiones que corresponden a tractos neuronales. CM: Capa molecular, CE: Células endodimales, IV: IV ventrículo (Modificado de González-González et al., 2017).

Adicionalmente, a las células endodimales que forman el límite ventral del CCSV les interseca en la zona media, una estructura parecida a una *corriente* rostrocaudal de células con características gliales, denominada cordón ventromedial (CVM) (**Figura 3** cabeza de flecha roja; González-González et al., 2017). La glía de este CVM es GFAP+, Nestina+ y se extiende en sentido anteroposterior en la superficie del lóbulo I (**Figura 4**).

A nivel morfológico, la glía del CVM es de un solo tipo y contrasta con el resto de la glía del cerebelo. Esta glía posee un soma que se localiza adyacente a las células endodimales (**Figura 5A**) del cual emerge un proceso primario que se extiende hacia el parénquima del cerebelo y en el lado contrario, un par de cilios contactan directamente al LCE (**Figura 5B-D**). Esta glía expresa la GFAP y buena parte de esta población expresa Nestina, proteína que se encuentra en CPN (González-González et al., 2017; Lemke, 2009) y en células troncales. El criterio clave que describe a las células troncales es su capacidad de autorrenovación y su

multipotencialidad. Una célula progenitora es multi- o unipotente, con capacidad de autorrenovación limitada (Filippov et al., 2003).

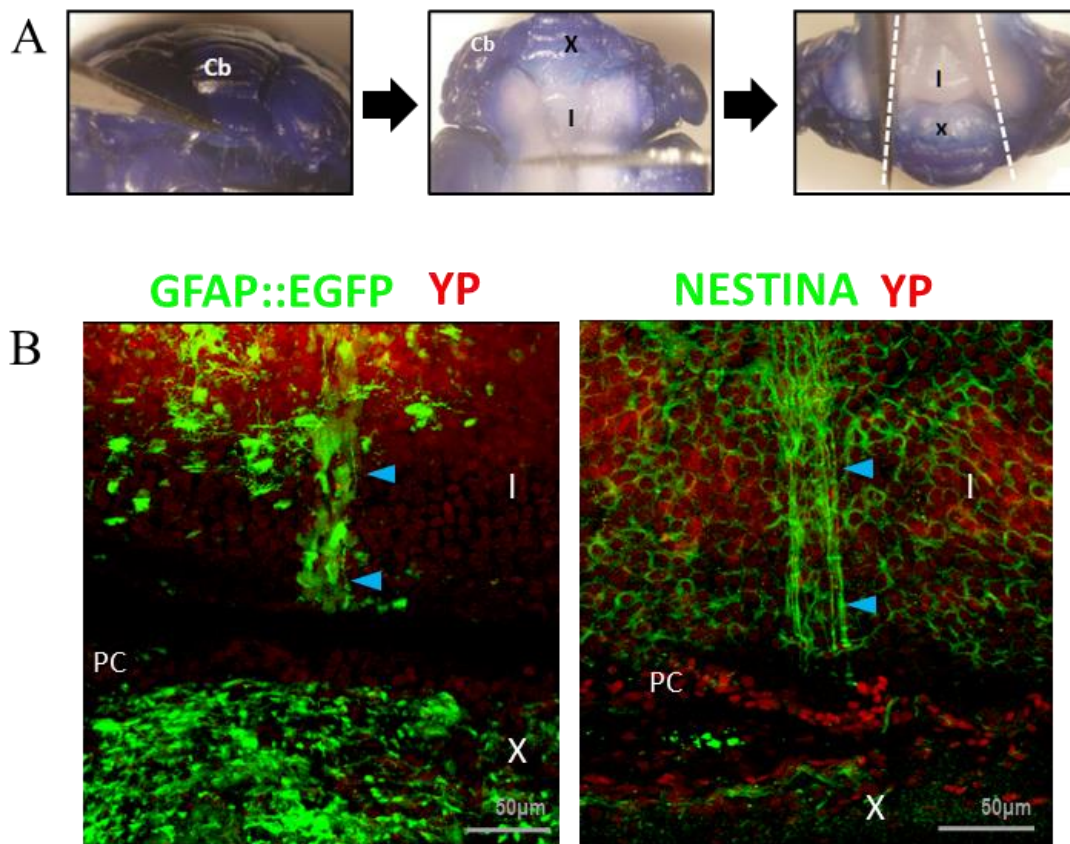


Figura 4. El CVM posee glía GFAP+ y Nestina+. **A:** Preparación del cerebelo en montaje completo. **B:** Células gliales del CVM que expresan GFAP, Nestina o ambas (flechas azules), se extiende sobre el lóbulo I del cerebelo. Cb: Cerebelo, X: lóbulo X, I: lóbulo I, GFAP: Proteína ácida fibrilar glial, YP: Yoduro de propidio, PC: Plexo coroideo (modificado de González-González et al., 2017).

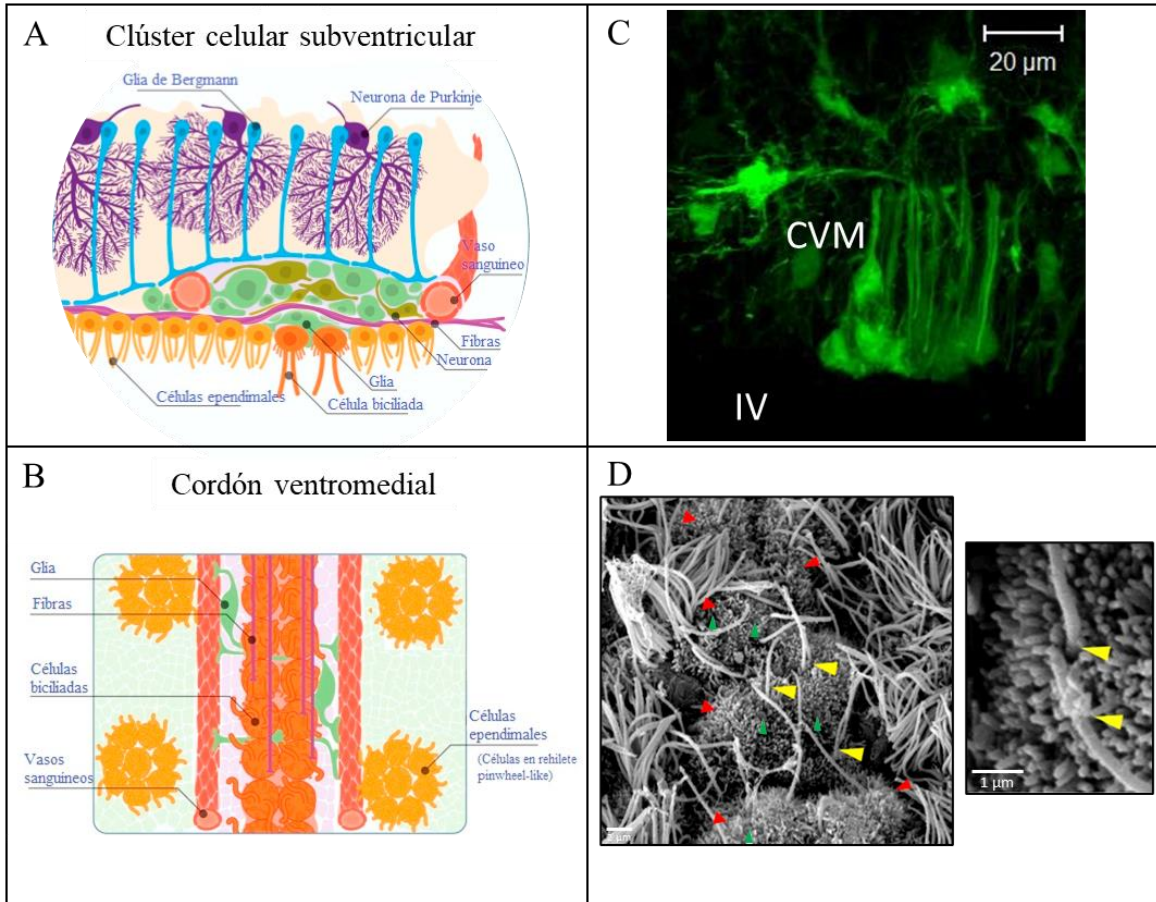


Figura 5. Morfología de la glía del CVM. **A:** Esquema en disposición coronal del CCSV y sus componentes. Se observa que el CVM está representado por las células biciliadas. **B:** Vista por la parte ventral del cerebelo del CVM, este esquema representa a la (Figura 4), también observamos los componentes que rodean al CVM. **C:** Células del CVM que expresan la EGFP bajo el promotor de GFAP. **D:** A través de la microcopia electrónica de barrido, se localiza al CVM por disposición anatómica y se observa que consiste en pares de células biciliadas (imagen aumentada, flechas amarillas) con microvellosidades (flechas verdes) a las cuales están adosadas vesículas (flechas blancas). CVM: Cordón ventromedial, IV: Cuarto ventrículo (modificado de González-González et al., 2017).

Además de la morfología característica de la glía del CVM, resulta interesante evaluar la ontogénesis de dicha estructura. La ontogenia se refiere al desarrollo de un organismo y, para este trabajo, el desarrollo de la glía del CVM dentro de un individuo de una especie determinada. Es importante precisar el momento en que el CVM aparece durante el desarrollo, ya que al igual que sucede con otro tipo de glía; alteraciones en la interacción del CVM con vías de desarrollo existentes pueden resultar en cambios en el fenotipo (Bennett et al., 2018; Matejuk & Ransohoff, 2020).

Por otro lado, en la ZSG del hipocampo maduro, existen CPN que demuestran propiedades electrofisiológicas de astrocitos maduros y además expresan GFAP y Nestina. Son relativamente inactivas pero pueden desencadenar su actividad por estímulos externos e internos (Zaverucha-do-Valle et al., 2013; Zhang & Jiao, 2015). Un ejemplo de esto es su capacidad para proliferar y diferenciarse en respuesta al PCH (Lang et al., 2015; Santilli et al., 2010). Este PCH se genera cuando los niveles de oxígeno (O_2) se reducen sin rebasar el umbral que induce daño celular irreversible, esta condición es ampliamente estudiada por sus efectos neuroprotectores y plásticos (Gossman et al., 2019).

Cabe destacar, que la respuesta inmediata a la hipoxia implica la activación de los quimiorreceptores periféricos y centrales que estimulan la respiración, la actividad cardíaca y la circulación sanguínea, con el objetivo de mantener el intercambio de O_2 con el dióxido de carbono (CO_2) y el pH en condiciones fisiológicas. La sensación de falta de aire, inducida por la inhalación de CO_2 produce el aumento en la presión parcial de CO_2 , la vía para la detección del CO_2 involucra el cambio en el pH, detectado por neuronas en el grupo ventral respiratorio (GVR) y en los complejos de Bötzingen mismos que generan los ritmos respiratorios. Dichas neuronas reciben o mandan proyecciones distribuidas en regiones del cerebelo, tronco encefálico, mesencéfalo, hipotálamo, tálamo, área amígdala-hipocampal e ínsula en una red putativa. Las áreas cerebelosas conectadas al GVR, son los lóbulos VI, III, I, II y Crus II, también se conecta con los núcleos fastigio, interpuesto y dentado. En respuesta a la hipercapnia (aumento de CO_2) el núcleo fastigio puede modular la salida respiratoria mediante influencias en las neuronas del GVR. Por otra parte, se puede asumir que ante la sensación de falta de aire el cerebelo estaría involucrado en aspectos motores para la respuesta respiratoria, sin embargo, la sensación de falta de aire se presenta en cuádrupléjicos, en donde el oscilador respiratorio del tronco encefálico está intacto pero su actividad no puede ser transmitida mediante fibras bulboespinales hacia las células de la asta anterior de la musculatura respiratoria. Imágenes donde se puede visualizar el flujo sanguíneo (mediante tomografía por emisión de positrones - PET) por inhalar una mezcla de CO_2 muestran activaciones cerebelares intensas (correlacionadas positivamente con la intensidad de sensación de falta de aire) cerca de la línea media e inactivaciones intensas (correlacionadas negativamente con la intensidad de sensación de falta de aire) bilateralmente, en el lóbulo posterior, en donde no se detecta activación en las áreas neocorticales motoras o áreas

premotoras. Además, patrones de distribución entre áreas con inactivaciones dentro del cerebelo y su relación de inactivaciones con otras áreas sugieren que el cerebelo responde al aumento de CO₂ involucrándose con diversas regiones en donde interactúa como parte de una red mutuamente inhibitoria de mayor tamaño que no está relacionada con la información motora mediada por procesamiento cortical sino con áreas que sirven a funciones cognitivas más generales (Parsons et al., 2001).

Notablemente, la sensibilidad de la glía ante cambios fisiológicos en la presión parcial de O₂ ha sido estudiada en diversas zonas del sistema nervioso central (SNC), donde la glía se exhibe como un sensor especializado de O₂, adaptada para la detección rápida de cambios en la oxigenación en el SNC (Angelova et al., 2015). Acompañando el desbalance en los niveles de O₂, surge el aumento o la disminución de CO₂, el cual se difunde con facilidad a través de la barrera hematoencefálica y al LCE, generando cambios en el pH cerebral, los cuales son detectados en el SNC en la superficie ventral del bulbo raquídeo y en el núcleo retrotrapezoide. Dichas áreas se involucran en el control cardiorrespiratorio del tronco encefálico y son áreas conectadas con la sustancia gris periacueductal, el hipotálamo, la amígdala, la corteza y el cerebelo.

Por otra parte, se ha demostrado que el núcleo fastigio del cerebelo es inervado por las neuronas de Purkinje que se originan del vermis del cerebelo, daños a este núcleo atenúan las respuestas respiratorias compensatorias ante niveles altos de CO₂ (Calton et al., 2016). Además, el núcleo fastigio participa en los mecanismos intrínsecos de neuroprotección provocados por estímulos de preconditionamiento (Golanov et al., 2017).

En resumen:

1. En la ZSG del hipocampo, CPN con propiedades astrocíticas se encuentran normalmente en estado quiescente; pero son capaces de proliferar y diferenciarse en respuesta al PCH.
2. En diversas partes del SNC la glía posee sensibilidad ante los cambios de O₂ y CO₂.
3. El CO₂ se difunde con facilidad al LCE, en donde es detectado por la superficie ventral de bulbo y núcleo retrotrapezoide. Áreas que, a su vez, están conectadas con el cerebelo (entre otras estructuras).

4. El núcleo fastigio participa en las respuestas respiratorias compensatorias ante niveles altos de CO₂ y recibe estímulos nerviosos provenientes de las neuronas de Purkinje que pertenecen a la parte del vermis del cerebelo.

La expresión de GFAP y Nestina también está asociada a células gliales que responden a condiciones de hipoxia a través de la activación del factor inducido por hipoxia (HIF) (Duan et al., 2015; Hirayama et al., 2015). La respuesta consiste en que cierta glía madura conserva tanto la capacidad de reanudar la proliferación como de regular positivamente características del desarrollo, lo que puede implicar cierto grado de desdiferenciación hacia un estado inmaduro reanudando la multipotencia, el cual tiene implicaciones para el intento de reconstituir neuronas después de una lesión cerebral (Buffo et al., 2008). Además, se genera una cascada de eventos que proveen neuroprotección ante insultos subsecuentes. Dicho mecanismo de neuroprotección prevalece por un periodo aproximado de siete días (Emerson et al., 1999; Zhang et al., 2011). En este sentido, hay evidencia de plasticidad neuronal y reparación en respuesta al PCH en áreas cerebrales distintas de los dos sitios neurogénicos bien conocidos, en el parénquima del SNC maduro de mamíferos (el cual es comúnmente considerado como no neurogénico) algunos procesos de gliogénesis y en menor extensión de neurogénesis ocurren. Esta génesis celular es altamente heterogénea en cuanto a su posición, identidad y destino de los progenitores (Bonfanti, 2013). Sin embargo, hay poca evidencia de proliferación celular en el cerebelo adulto (Ahlfeld et al., 2017; Feliciano et al., 2015; Mandalos et al., 2018; Ponti et al., 2008). La GB extiende sus procesos hacia el IV ventrículo, pero no parecen entrar en contacto con el LCE, ya que sus pies terminales están limitados por una membrana basal que los aísla de las células de la ZSV, que a su vez aísla el CVM (González-González et al., 2017). Dado que la función del CVM no se ha dilucidado, su identidad peculiar plantea una serie de preguntas. Así, el propósito de este estudio fue explorar si las células positivas a la GFAP que forman el CVM responden al PCH.

En este proyecto se investigó si la glía del CVM presenta cambios en la plasticidad estructural relacionados con el estímulo del PCH, dirigiendo patrones distintos en cambios en la morfología glial, en la expresión de proteínas de identidad celular y/o en la inducción de proliferación. En el proceso, también observamos el impacto del PCH en la GB en el

cerebelo de ratones juveniles, prestando especial atención a las células que están cerca del CVM. Para ello, utilizamos una combinación de técnicas que incluyeron inmunofluorescencia, CLARITY, microscopía de hoja de luz (LSFM) y además evaluamos la incorporación de BrdU para determinar eventos de proliferación celular del CVM después del PCH.

II. Anatomía del cerebelo

II.1. Localización y organización macroscópica

El cerebelo se encuentra dorsal al tronco encefálico. Procesa información de diversas fuentes incluyendo la médula espinal, el tallo cerebral y el telencéfalo y proyecta a distintos centros cerebrales involucrados en adaptaciones posturales y en la generación de movimientos. La anatomía gruesa del cerebelo murino es típica de la mayoría de los mamíferos; se distinguen dos hemisferios unidos por un vermis, estos a su vez, se dividen en tres lóbulos por dos fisuras transversales: la primaria, define los lóbulos anterior y posterior, y la posterolateral, separa el lóbulo posterior del lóbulo floclonodular (Kandel et al., 2000).

La parte más externa del cerebelo es la corteza. Al seccionarse sagitalmente por el vermis se aprecia su distribución en una serie de diez lóbulos (I-X) de donde surgen las extensiones laterales llamadas hemisferios. En conjunto, los lóbulos envuelven la materia blanca que contiene a los núcleos cerebelosos profundos (fastigio, interpuesto y dentado), siendo éstos la única salida del cerebelo. El cerebelo forma el techo del IV ventrículo el cual tiene forma romboidal (vista sagital), se eleva hasta un vértice llamado el *fastigium* que divide el techo superior del inferior. En la parte media del techo superior se encuentra el velo medular superior (que es una delgada lámina de sustancia blanca entre los pedúnculos cerebelosos) y detrás de esta superficie externa esta la llingula, es decir, el lóbulo I. La parte rostral del techo inferior está formada por el nódulo, es decir, el lóbulo X el cual se encuentra frente a la úvula (lóbulo IX), que es la parte inferior del vermis que cuelga entre la amígdala cerebelosa (lóbulos HIX). Lateral al lóbulo X está el velo medular inferior, que es una lámina delgada de tejido neuronal que se extiende sobre el IV ventrículo para conectar el lóbulo X con sus flóculos. La parte caudal del techo inferior consiste en la tela coroidea de donde se une el plexo coroideo. La unión entre la tela coroidea y el velo medular inferior está al nivel del receso lateral (Miller et al., 2012)

II.2. Citología

El cerebelo está formado por neuronas y células gliales distribuidas en la corteza y en la materia blanca. El componente neuronal está formado por 6 tipos, que incluyen a las neuronas de Purkinje, las células en cesta, estrelladas, de Golgi, de Lugaro y granulares. Por

otro lado, el componente glial consiste en astrocitos protoplasmáticos, fibrosos y la glía especializada de Bergmann. Estos tipos celulares y sus conexiones se organizan en estratos homogéneos a lo largo de los 10 lóbulos como se describe a continuación:

II.2.1. Organización del componente neuronal

La corteza del cerebelo se divide en tres capas: 1) la molecular, 2) la de células de Purkinje y 3) la de células granulares.

1) La capa molecular, es la capa más externa de la corteza del cerebelo, contiene una densidad baja de células de tres tipos: en cesta, estrelladas y de Lugaro.

Células en cesta, que ocupan una posición más profunda que el de las *células estrelladas*, se distribuyen en las capas superficiales de la capa molecular. También se localizan las dendritas de las neuronas de Purkinje y las fibras paralelas. Las ramificaciones dendríticas de las células en cesta y estrelladas, junto con los axones de estas últimas, están confinados a la capa molecular. Mientras que los axones de las células estrelladas terminan en las dendritas de las neuronas de Purkinje, los axones de las células en cesta se extienden de la capa molecular a la capa de las neuronas de Purkinje y hasta las primeras decenas de micras en la capa granular (Eccles et al., 2013; Voogd & Ruigrok, 2012) (**Figura 6**). Los axones de las células en cesta hacen sinapsis con el soma de las neuronas de Purkinje y terminan envolviendo el cono axonal. *Las células de Lugaro* se restringen a la capa molecular y su orientación es perpendicular al eje largo de la folia, sus axones hacen sinapsis con células estrelladas y en cesta, una ramificación axonal se extiende en la parte profunda de la capa molecular con disposición paralela a las fibras paralelas y contactan a las células de Golgi y de Purkinje. Las células de Lugaro son el objetivo principal del plexo serotoninérgico en la corteza cerebelosa. Las fibras paralelas y los axones de las células de Lugaro terminan en las células en cesta y en las células estrelladas.

2) Capa de células de Purkinje. Contiene únicamente a los somas de las neuronas GABAérgicas e inhibitoras de Purkinje. Sus grandes somas forman una monocapa de donde las dendritas surgen en dirección a las meninges; a su vez, ramificaciones dendríticas se extienden en la capa molecular, donde las ramas primarias y secundarias son lisas y el resto posee espinas dendríticas gruesas y cortas, dichas espinas son las que forman contactos

sinápticos con las fibras paralelas que surgen de las células granulares. Por el polo inferior de la célula surge un único axón que termina en los núcleos vestibulares o en los núcleos del cerebelo. Las colaterales axónicas varias, terminan en otras células de Purkinje, de Golgi, de Lugaro y probablemente en células en cesta (Voogd & Ruigrok, 2012). Se muestra a las neuronas de Purkinje (**Figura 6**, color rojo), cuyas dendritas tienen una ramificación profusa en la vista sagital (Snell, 2016).

3) Capa de células granulares. Contiene cuatro tipos de células: una de alta densidad de células granulares cuyo neurotransmisor excitador es el glutamato, a la vez, en dicha capa se localizan las células unipolares en cepillo, células de Golgi e interneuronas inhibitorias. Las células granulares están provistas de dendritas cortas en forma de garra y sus axones ascienden a la capa molecular en donde se bifurcan en fibras que se orientan paralelas al eje largo de la folia, se observa la disposición de estas fibras (**Figura 6**, color verde) en la vista coronal en comparación con la vista sagital. En la trayectoria de los axones y de las fibras paralelas, ambos hacen contacto sináptico con espinas de ramificaciones dendríticas de las neuronas de Purkinje y otras dendritas y neuronas (Voogd & Ruigrok, 2012). Esta capa posee a las células en cepillo, que son excitadoras y su única dendrita es contactada por una fibra musgosa. Sus axones terminan en rosetas de fibras musgosas en las células granulares. Las células de Golgi e interneuronas inhibitorias son de diferentes tamaños, sus dendritas se extienden a la capa molecular y sus axones se ramifican como un plexo en la capa granular que contacta a las dendritas de los glomérulos cerebelosos y células en cepillo. Las células de Golgi colocalizan con los neurotransmisores inhibitorios ácido gamma-aminobutírico (GABA) y glicina, reciben contactos de las colaterales de las neuronas de Purkinje, y fibras musgosas, paralelas y trepadoras, además de células en cesta y de Lugaro y su plexo axonal se orienta perpendicular al eje largo de la folia (Voogd, 2003).

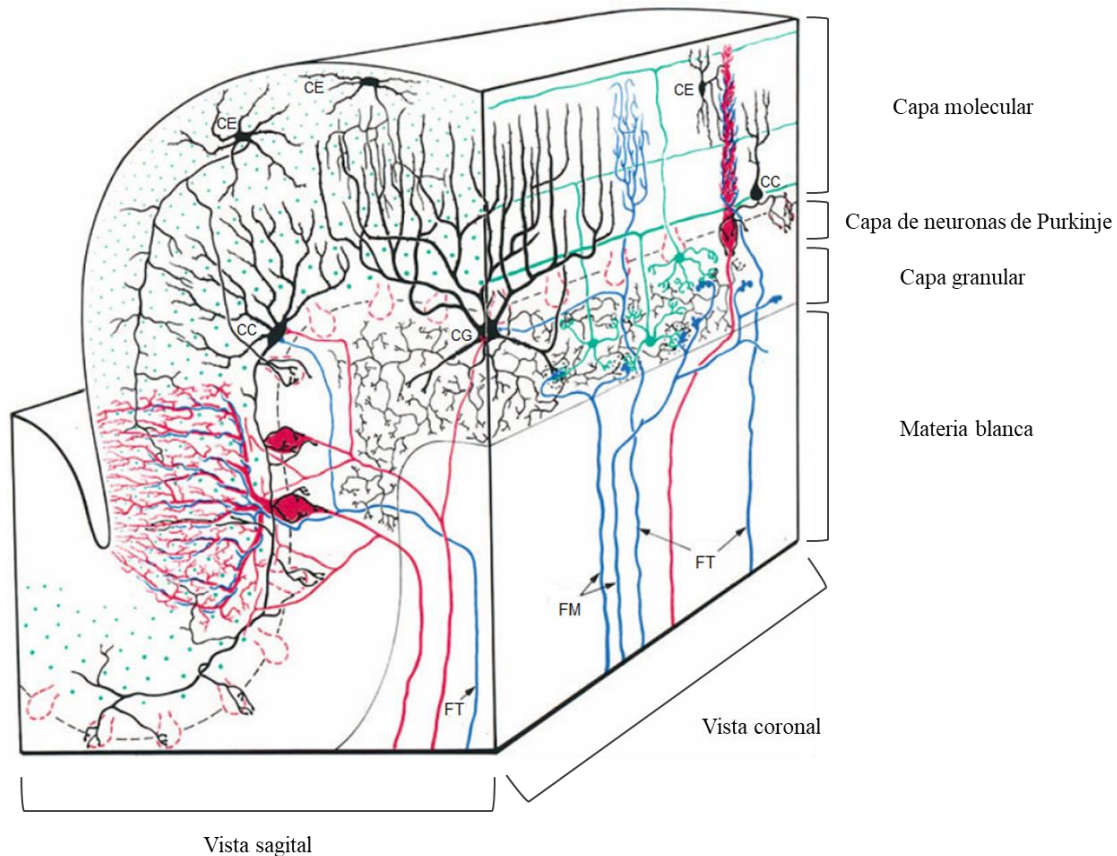


Figura 6. Citoarquitectura del cerebelo. Organización de los componentes celulares de la corteza del cerebelo. CE: células estrelladas, CC: células en cesta, CG: células de Golgi, FM: fibras musgosas, FT: fibras trepadoras. Modificado de Eccles et al., 2013.

Las dos principales aferencias a la corteza cerebelosa son las fibras trepadoras y las fibras musgosas. Las fibras trepadoras están orientadas perpendicularmente respecto al eje largo de la folia, las fibras musgosas están orientadas transversalmente y emiten colaterales que terminan como agregados longitudinales de terminales de fibras musgosas (Voogd, 2014) (**Figura 6**).

Las fibras trepadoras tienen su origen en las olivas inferiores contralaterales. Cada fibra trepadora inerva una sola neurona de Purkinje, estas fibras terminan con múltiples sinapsis en las espinas cortas de las dendritas proximales de las neuronas de Purkinje y sus colaterales terminan en neuronas de los núcleos cerebelosos y en células de Golgi. Las fibras

trepadoras son excitadoras y usan glutamato como su neurotransmisor (Barmack & Yakhnitsa, 2003).

Las fibras musgosas se originan de múltiples fuentes extracerebelosas. Los axones de las células en cepillo y las colaterales de los axones pertenecientes a neuronas de los núcleos cerebelosos son consideradas fibras musgosas. Los múltiples orígenes extracerebelosos de las fibras musgosas corresponden a diversas zonas del tallo cerebral y de la médula espinal, al entrar al cerebelo se distribuyen transversalmente y sus colaterales entran en la materia blanca de las folias; finalizando como agregados longitudinales de terminales de fibras musgosas (rosetas). Las rosetas hacen contacto sináptico con dendritas de células granulares y con células de Golgi, a este conjunto se le denomina glómulo cerebeloso (**Figura 6**). Las fibras musgosas son excitadoras y usan glutamato como neurotransmisor primario con excepción de las fibras secundarias vestibulo-cerebelosas que utilizan acetilcolina (Fore et al., 2020).

Sistemas de fibras aferentes se organizan de manera difusa en el cerebelo y usan noradrenalina, serotonina o acetilcolina como neurotransmisores. Las inervaciones serotoninérgicas al cerebelo tienen origen en las formaciones reticulares medular y pontina. El origen principal de las fibras noradrenérgicas es del *locus coeruleus* dorsal, las fibras se restringen a la corteza del cerebelo, donde se organizan al azar formando un plexo de fibras con varicosidades en donde la mitad de estas contacta a las células de Purkinje y dendritas de células granulares o de interneuronas en la corteza del cerebelo. Fibras colinérgicas se esparcen como un plexo con cuentas en la corteza del cerebelo y en sus núcleos, el origen de sus fibras se desconoce, salvo una porción de estas fibras que inervan parte de los núcleos y de la corteza cerebelosa, que tienen origen en el núcleo tegmental pedúnculo pontino, el cual está implicado en promover y sostener la excitación cortical, es decir, que la señalización colinérgica originada del núcleo tegmental pedúnculo pontino promueven los estados activados corticales de vigilia y movimientos rápidos de los ojos (REM) en el sueño (Vacas et al., 2013; Voogd & Ruigrok, 2012).

II.2.2. Componente glial

La glía del SNC incluye a la glía radial, astrocitos, oligodendrocitos, células NG2 (células progenitoras de oligodendrocitos) y microglía (Allen & Lyons, 2018). Los astrocitos son las células gliales más abundantes en el SNC, en respuesta a un estímulo, pueden sufrir cambios dependientes de contexto en su expresión genética en un proceso llamado reactividad que puede tener efectos protectores o tóxicos en neuronas circundantes (Clarke et al., 2021). Morfológica y funcionalmente se distinguen poblaciones heterogéneas de astrocitos en el cerebelo, incluyendo astrocitos fibrosos (encontrados en la materia blanca), astrocitos protoplásmicos (presentes en su mayoría en la materia gris); además se encuentra la glía radial en el área periventricular durante el desarrollo, células endoteliales, astrocitos perivasculares y la glía de Bergmann (Pestana et al., 2020; Sidoryk-Wegrzynowicz & Strużyńska, 2021).

En la actualidad se reconoce que los astrocitos son altamente heterogéneos a nivel morfológico, molecular y funcional, incluso en la misma región del sistema nervioso. Estos pueden compartir genes transcritos en común, pero existe suficiente variación en la expresión de su transcriptoma para producir subtipos únicos de astrocitos especializados en realizar funciones específicas. La ventaja más importante de la diversidad astrocítica es que permite la creación de unidades especializadas entre neurona y glía, las cuales pueden dirigir comportamientos complejos, dicha especialización es adquirida durante estados embrionarios a través de señales provenientes de circuitos neuronales (Clarke et al., 2021; Pestana et al., 2020). Los astrocitos mantienen la homeostasis de iones y neurotransmisores, la homeostasis del agua y mantienen el pH celular, y su posición en la sinapsis tripartita les permite participar en la remodelación sináptica para mantener la especificidad de señalizaciones. Un ejemplo de lo anterior, fue evaluado en la influencia de la interrupción de la transmisión dopaminérgica sobre los cambios plásticos en la sinapsis glutamatérgica tripartita en la substantia nigra pars reticulata (principal núcleo de salida del circuito de los ganglios basales, particularmente sensible a la depleción patológica de dopamina) y sobre la actividad de calcio astrocítica que se da mediante la unión astrocito-astrocito (mediada por conexinas) la cual es afectada por elementos neuronales sinápticos, en donde la plasticidad de uniones gap responde a la neurotransmisión. Como resultado de la perturbación en la

transmisión dopaminérgica, ratas de 6 semanas de edad lesionadas con 6-hidroxi-dopamina (análogo de dopamina que imita la pérdida neuronal dopaminérgica parkinsoniana) mostraron una regulación al alza de Conexina 43 (Cx43) junto con un aumento en la sincronización de la red astrocítica la cual era dependiente de la actividad neuronal. Además, se observó la relocalización de procesos astrocíticos perisinápticos hacia estructuras neuronales sinápticas, conduciendo a un mayor número de sinapsis tripartitas e ilustrando el papel regulador de las conexinas en la actividad neuronal (Bosson et al., 2015; Hillen et al., 2018). Además, los astrocitos liberan constantemente factores neurotróficos como quimiocinas (proteína quimioatrayente de monocitos 1 – MCP-1, ligando 10 de quimiocina con motivo C-X-C – CXCL10, ligando de quimiocina 2 – CCL2,) o citocinas (interferones de tipo I - IFN, el factor de crecimiento transformante beta – TGF- β , interleucina-10 – IL10 y el factor de crecimiento insulínico tipo 1 – IGF-1), así como metabolitos que apoyan la función, supervivencia y diferenciación neuronal. Estos factores son liberados mediante exocitosis o por liberación de exosomas (Jayaraj et al., 2019; Kawabori & Yenari, 2015; Matias et al., 2019; McDonough & Weinstein, 2016; Venturini et al., 2019; S. Xu et al., 2020).

Pese a que se sabe que un gran número de proteínas son expresadas de forma selectiva por astrocitos, estos no han sido asociados con una marca molecular canónica que defina de manera específica y selectiva su fenotipo. Las características morfológicas y sus relaciones con neuronas y capilares definen su fenotipo más que cualquier marcador molecular. En este sentido, la GFAP es un marcador clásico para la identificación de astrocitos maduros, pese a no ser expresado en todos los astrocitos del SNC, presenta distintas isoformas a través de diferentes patrones de *splicing*, que se expresan de forma variable en subconjuntos específicos de astrocitos, así, GFAP se regula diferencialmente ante daños y/o enfermedades en áreas específicas del cerebro de ratón (Matias et al., 2019).

Cuando se despolariza, la glía responde con una relación lineal de corriente-voltaje y por ende no son eléctricamente excitables y son células que no generan potenciales de acción, es en gran parte eléctricamente silenciosa, con un potencial en reposo de entre -85 a -90 mV debido a la abundante expresión de canales de K⁺. Por ello, los astrocitos son altamente sensibles a cambios en el K⁺ extracelular, los cuales están asociados con la actividad

neuronal, teniendo un papel clave en la regulación del disparo neuronal (Pestana et al., 2020). La mayoría está unida por uniones gap compuestas principalmente de Cx43 y Conexina 30 (Cx30), lo que le confiere una resistencia de entrada baja sobre las células dentro del sincitio astrocítico, minimizando la despolarización debido a niveles elevados de K⁺ local extracelular, manteniendo la recaptura eficiente de K⁺ y el mantenimiento de la homeostasis local (Kiyoshi & Zhou, 2019; Ohno et al., 2018).

Seis tipos de células gliales se encuentran en el cerebelo: astrocitos fibrosos y protoplásmicos, oligodendrocitos, células ependimales, microglía y la glía de Bergmann. Los astrocitos del cerebelo liberan adenosín trifosfato (ATP) y adenosina lo que resulta en la depresión de las corrientes postsinápticas excitadoras espontáneas. La glía de Bergmann libera GABA como mecanismo de inhibición sináptica tónica (Oberheim et al., 2012).

Los astrocitos fibrosos poseen prolongaciones largas y lisas. Se encuentran distribuidos comúnmente en la materia blanca. Los astrocitos protoplasmáticos tienen una mayor complejidad morfológica en comparación a los astrocitos fibrosos. Se encuentran en la capa granular y raras veces en la capa molecular, tienen procesos con ramificaciones muy densas y ordenadas radialmente con un soma central, extienden de 4 a 10 procesos primarios de los cuales surgen miles de procesos de menor tamaño que forman compartimentos para las células granulares y los glomérulos sinápticos. Además, los astrocitos controlan el flujo sanguíneo pudiendo favorecer funciones metabólicas, convierten el glutamato en glutamina para ser liberado en el espacio extracelular y capturado por las neuronas para la síntesis *de novo* de glutamato. Los oligodendrocitos, son una glía formadora de mielina que recubre los axones neuronales. Las células ependimales, son células gliales cúbicas que forman una sola capa que recubren al sistema ventricular y al plexo coroideo, forman un epitelio secretor de LCE, poseen cilios y microvellosidades que pueden variar en cantidad dependiendo de su localización anatómica, sus superficies laterales están unidas entre sí por desmosomas, formando una barrera funcional entre el LCE y el cerebro. En el cerebelo, esta capa de células se encuentra únicamente en el techo del IV ventrículo (lóbulos I, II, y X) que son los que se encuentran en comunicación con el LCE del IV ventrículo (Jiménez et al., 2014; Köhler et al., 2019; Ludwig & Das, 2019).

Por otra parte, la microglía son las células inmunológicas del SNC, inspeccionan la homeostasis del tejido para responder rápidamente ante retos exógenos y endógenos con un resultado protector, estos retos conducen a la expresión de receptores de superficie tales como receptores de fractalquina, receptores a ATP/ADP, receptores a glutamato, receptores a NMDA, receptor al factor de crecimiento transformador $\beta - 1$, receptor 1 de quimiocina CX3C, receptor CD115 y receptores tipo Toll (L. Huang et al., 2019; McDonough et al., 2020). Ante retos particulares pueden presentar un fenotipo reactivo distinto en donde la activación microglial depende de la señalización ATP/ADP (adenosín trifosfato/adenosín difosfato). En su morfología se observan ramificaciones que emergen del soma celular y se comunican con neuronas y otras células gliales a su alrededor (Augusto-Oliveira et al., 2019).

La glía de Bergmann (GB) es un astrocito radial especializado, casi todas las sinapsis sobre las neuronas de Purkinje están contactadas por los finos procesos de la GB que forman aposiciones cercanas a la sinapsis. Su soma es de 15 μm de diámetro, se localiza en la capa de las neuronas de Purkinje, en una proporción aproximada de 8:1. De cromatina compacta, con dos o más procesos con bifurcaciones que envuelven a las dendritas de Purkinje, ascendiendo de forma paralela a la superficie del cerebelo (**Figura 7**), los procesos de la GB cubren hasta 8,000 sinapsis formadas entre las dendritas de las neuronas de Purkinje con las fibras paralelas (Eroglu & Barres, 2010; Reeber et al., 2018). En estados tempranos de desarrollo, son el andamio para la migración de las células granulares de la capa externa a la interna y en el cerebelo maduro, contribuye a la modulación de la transmisión excitadora e inhibitoria de las neuronas de Purkinje y en la amortiguación de los niveles de K^+ extracelular. La GB esta provista de transportadores específicos de astrocitos con los cuales pueden capturar glutamato, GABA y glicina mismos que se unen a receptores al ácido α -amino-3-hidroxi-5-metilo-4-isoxazolpropiónico (AMPA), GABA y glicina localizados en su membrana. La GB también posee receptores para acetilcolina, noradrenalina y dopamina, pero carece de transportadores para monoaminas. La unión de glutamato a receptores AMPA en la GB causa la entrada de calcio (Ca^{2+}) y establece ondas de Ca^{2+} que se extienden a través de múltiples células de GB, acopladas eléctricamente. Se ha observado la unión de interneuronas de la capa molecular con la GB, donde la liberación de ATP por parte de las interneuronas activa receptores purinérgicos en la GB, causando el incremento de Ca^{2+} (Voogd & Ruigrok, 2012). De los 5 transportadores de aminoácidos excitadores 1-5;

(EAAT1-5) el transportador de glutamato / aspartato (GLAST=EAAT1) y el transportador glial (GLT=EAAT2) se encuentran principalmente en astrocitos y son los que capturan la mayoría del glutamato liberado para convertirlo en glutamina por la glutamina-sintetasa y la glutamina se transporta de regreso a las neuronas para sintetizar glutamato o GABA en las neuronas. El transporte de glutamato glial tiene capacidad neuroprotectora, limitando el derrame de glutamato de la sinapsis hacia el espacio extracelular. Breves y pequeños aumentos en la concentración extracelular de glutamato son suficientes para inducir excitotoxicidad (Bordey & Sontheimer, 2003). En el cerebelo, GLAST es el transportador más abundante, siendo 6 veces mayor que GLT-1 y 10 veces mayor que el transportador de glutamato neuronal EAAT4. La mayor densidad de GLAST se encuentra en la glía de Bergmann, lo que los involucra en el transporte de glutamato / glutamina. Además, ratones deficientes de GLAST presentan descoordinación motora moderada (Balderas et al., 2014; Chrobak & Soltys, 2017).

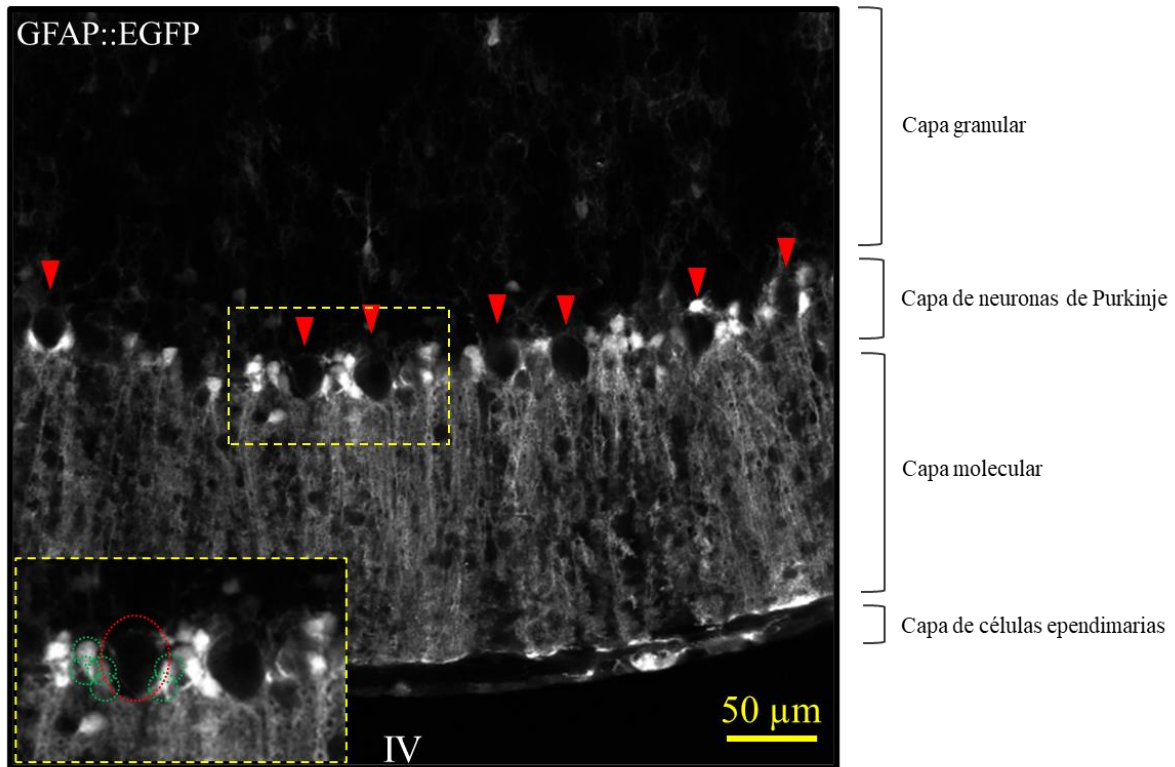


Figura 7. Glía de Bergmann. Corte óptico por microscopía confocal que muestra en el eje coronal la distribución de la glía de Bergmann en la capa de neuronas de Purkinje del lóbulo I del cerebelo. Las puntas de flecha rojas indican la ubicación de los somas de las neuronas de Purkinje, rodeadas por los somas de la glía de Bergmann que expresan la proteína verde fluorescente (EGFP) bajo el promotor de la proteína ácida fibrilar glial (GFAP). El recuadro amarillo permite visualizar la relación entre los somas de glía de Bergmann (círculos verdes) con los de las neuronas de Purkinje (círculo rojo). IV: cuarto ventrículo.

III. Hipoxia

La hipoxia es un concepto heterogéneo, en donde la tensión del O₂ puede variar desde el <0.01% (anoxia) hasta el 5% y puede ser crónica o aguda, con efectos diferenciales en las células. Se refiere a un estado en donde los niveles de O₂ en los tejidos están por debajo de los niveles fisiológicos. La hipoxia ocurre cuando existe un desbalance entre la entrega de O₂ al tejido y su consumo, el desequilibrio de O₂ entre ambos produce dificultad para mantener la función celular (Manninen & Unger, 2016). Episodios agudos de hipoxia deprimen la actividad sináptica, mientras que la exposición prolongada a la hipoxia (≥ 24 h) conduce a la muerte neuronal. Existen efectos positivos de hipoxia breve (≤ 6 h) cuando se administra de forma cíclica, como promover la proliferación de células endoteliales y la angiogénesis (Dai et al., 2011; Saxena & Jolly, 2019). Estos efectos positivos son considerados como un enfoque eficiente para reducir la vulnerabilidad de tejidos y órganos y se le conoce como preconditionamiento hipóxico (PCH). El PCH consiste en episodios cortos repetitivos de hipoxia, seguidos de reoxigenación (Halder et al., 2018; Hertzog et al., 2020; Krock et al., 2011).

La reacción de adaptación a factores ambientales pertenece al proceso neuronal de la percepción y transducción de la señal adaptogénica / advertencia (Rybnikova & Samoilov, 2015). La actividad de ‘advertencia’ es la base para el fenómeno del ‘reflejo anticipatorio de la realidad’, fenómeno homeostático que permite anticipar el curso de eventos futuros para adaptarse mejor al ambiente. En el sistema nervioso, el proceso de adaptación a posibles efectos dañinos se puede manifestar mediante la cascada que se inicia con la señal de ‘advertencia’ la que induce a la reorganización de la plasticidad de los elementos del SNC. En la raíz yace el procesamiento del reflejo anticipatorio de la realidad, que prepara a las células del cerebro a exposiciones nocivas esperadas y se asocia con la inducción de mecanismos protectores determinados genéticamente y adquiridos de manera evolutiva. La homeostasis es la respuesta de las células u organismos a un factor que induce efectos estimulantes o benéficos a dosis bajas y efectos inhibitorios o adversos a dosis altas (Davies, 2016; Rybnikova & Samoilov, 2015).

Las respuestas celulares a la hipoxia son iniciadas a través de la activación del factor inducido por hipoxia 1 (HIF-1), es un heterodímero formado por las proteínas HIF-1 α y HIF-

1 β . En condiciones de normoxia el HIF-1 no está presente en las células, existen niveles altos del HIF-1 β que se expresa constitutivamente en el núcleo y no se ve afectado por cambios en los niveles de O₂, a diferencia del HIF-1 α cuya regulación depende del O₂ y se encuentra en el citoplasma de la célula. En condiciones de normoxia se sintetizan las mismas cantidades del HIF-1 β y del HIF-1 α , pero el HIF-1 α se degrada. El HIF-1 α tiene un dominio conocido como dominio de degradación dependiente de oxígeno (ODD) por ello el HIF-1 α se degrada en presencia de O₂. En condiciones de hipoxia no se puede destruir el HIF-1 α , iniciando la respuesta a la hipoxia.

Básicamente, en presencia de O₂ en el dominio ODD existen 2 residuos de prolina (en la posición 402 y 564) que serán hidroxilados, esto conducirá a la degradación del HIF-1 α . Las enzimas que catalizan esta reacción son las enzimas que contienen el dominio de prolil hidroxilasa (PHD) 1, 2 y 3. Al tener los residuos prolil hidroxilados en HIF-1 α , se adosa la proteína supresora de tumores Von Hippel-Lindau (pVHL) reclutando a las enzimas ubiquitina ligasa para unirse a la proteína HIF-1 α . La ubiquitinación dirige a las células al proteasoma, transformando la proteína en fragmentos de polipéptidos. En condiciones de hipoxia, no se hidroxilan los residuos de prolina, evitando la unión de la pVHL, así, el HIF-1 α se estabiliza en el citoplasma de la célula, se internaliza en el núcleo y dimeriza con HIF-1 β , creando una molécula de HIF-1 que va a actuar como un factor de transcripción. En los genes, la región promotora se encuentra río arriba, que no está involucrada en ser traducida en proteína, sino que controla la expresión del gen que se encuentre río abajo. En esta región promotora se une la enzima ARN polimerasa II, catalizando la transcripción del ADN para producir una pieza de ARN mensajero que ira al citoplasma y será traducido a proteína. La afinidad de la región promotora con la ARN polimerasa II controla el nivel de expresión del gen. El factor de transcripción es cualquier molécula que se une a la región promotora y altera la afinidad de la región promotora para unirse con la ARN polimerasa II. Cada factor de transcripción se une a varias regiones promotoras y en algunos casos mejorara la expresión del gen río abajo mediante el aumento de la afinidad de esa región promotora para la ARN polimerasa II y en otras disminuirá su afinidad, reprimiendo la expresión del gen río abajo. Algunos de los genes claves que elevan su expresión por HIF-1 son el VEGF-A y las enzimas involucradas en la respiración anaeróbica (enzimas involucradas en la glucólisis) (Sendoel & Hengartner, 2014). También se activa la transcripción de numerosos genes involucrados en

la angiogénesis, proliferación y regulación del pH (Mukandala et al., 2016; Span & Bussink, 2015). La hipoxia moderada aumenta la resistencia del cerebro a otras situaciones de estrés donde el óxido nítrico, especies reactivas de oxígeno (ROS) y la misma hipoxia movilizan factores de transcripción para conducir la producción de proteínas citoprotectoras e iniciar señalizaciones de proteínas cinasas que activan defensas celulares contra el estrés oxidativo, inflamación y agotamiento de energía (Sprick et al., 2019).

III.1. Precondicionamiento hipóxico

El precondicionamiento es una estrategia en donde la exposición a un estímulo subletal condiciona a un sistema u órgano a inducir tolerancia o resistencia a un daño subsecuente. Entre los estímulos de precondicionamiento estudiados encontramos la hipoxia, isquemia, estrés oxidativo, anoxia, inhibidores de la fosforilación oxidativa y el ejercicio (Sakakima, 2019). Este fenómeno puede ser inducido en variedad de órganos incluyendo el cerebro, el corazón, el riñón, el hígado, entre otros (Sharp et al., 2004).

La exposición repetitiva a la hipoxia como estímulo de precondicionamiento, inicia la regulación positiva del HIF-1 α , activando genes blancos (tejido-específicos) que conducen a la conservación de energía, plasticidad cerebral y la activación de procesos protectores que incluyen la eritropoyesis, angiogénesis, metabolismo de la glucosa y proliferación celular (Hashimoto & Shibasaki, 2015; Nakayama & Kataoka, 2019). El PCH de cuerpo completo fue uno de los primeros modelos en donde se estudiaron los mecanismos protectores que induce el PCH el cual es conocido como “modelo de autohipoxia”. Los sujetos de estudio son colocados en un frasco sellado para crear un ambiente hipóxico en donde la autohipoxia es inducida mediante el consumo propio de O₂ del animal, que al estar dentro del ambiente hermético reduce la cantidad de O₂ de manera gradual. La aparición de jadeo es utilizada como indicador de la tolerancia del animal, en este punto se permite un periodo de reoxigenación. Es necesario que el procedimiento se repita al menos dos veces más, donde se notará un aumento en la tolerancia del animal, demostrando así el papel protector del PCH (Li et al., 2017; Rybnikova & Samoilov, 2015). A su vez, se desarrolla el aumento de la presión parcial de gases alveolares distintos del O₂, en este caso de CO₂. A la vez, el incremento de CO₂ resulta en la disminución de la presión parcial de O₂, tanto a nivel alveolar como a nivel arterial. El estrés inducido por el PCH dispara respuestas de adaptación,

desarrollando tolerancia en células y tejidos a un periodo de estrés subsecuente. La protección generada por el PCH puede durar hasta 2 semanas (Xu et al., 2011).

El PCH puede ser entendido en relación del tiempo entre el estímulo y la adaptación. La fase de adaptación inmediata (de corta duración) aparece en minutos, durando horas después de la exposición a la hipoxia, esta fase inicia procesos de señalización moleculares que resultaran en estados neuroprotectores, generados por cambios moderados en los niveles de calcio intracelular, modificaciones en la permeabilidad de la membrana a los diferentes iones que surge debido a alteraciones en la expresión funcional de canales iónicos en varios tipos celulares en el cerebro. En particular, la represión de expresión de genes es una de las consecuencias dominantes del preconditionamiento y varios de los genes que se reprimen están relacionados con el metabolismo y con canales iónicos. Ya que estos genes están relacionados con actividades relacionadas con el gasto energético, la represión de sus actividades conduce a la conservación de energía y participan en retrasar la despolarización anóxica (Pignataro et al., 2020; Stenzel-Poore et al., 2007). Otro proceso que contribuye a la neuroprotección es la fosforilación de proteínas, es el principal mecanismo molecular en el cual la función de las proteínas es regulada en respuesta a un estímulo, es un fenómeno reversible y cerca de un tercio de las proteínas en el proteoma humano sirven como substratos para la fosforilación, en el PCH. Por ejemplo, se ha observado que una de las proteínas involucradas en la neuroprotección resulta de la activación de la proteína cinasa activada por mitógenos (MAPK) p38, ésta aumenta en el tejido isquémico y su inhibición empeora el daño cerebral en un modelo de isquemia transitoria. En el preconditionamiento también se ha observado la fosforilación del agonista asociado a BCL2 (BAD) y de la proteína cinasa B (Akt), una cinasa que inhibe la muerte celular mediada por caspasas. También se sabe que activa factores de transcripción ubicuos como CREB y el factor nuclear kappa B (NF- κ B) (Rybnikova & Samoilov, 2015; Uchiyama et al., 2004; Zhao et al., 2013). La fase de adaptación inmediata se caracteriza por una elevación en el factor de transcripción HIF-1 α , regulador de la homeostasis del O₂ celular que desencadena la segunda fase (de larga duración). La segunda fase de adaptación a la hipoxia aparece de 12 a 24 h después del estímulo subletal, esta fase es ‘la inducción de tolerancia’ se requieren cambios en la expresión genética y en la síntesis de proteínas y ocurre a través de genes proadaptativos que son el blanco del HIF-1 α (Li et al., 2017). Se involucra la activación modesta de los sistemas

reguladores glutamatérgicos, de calcio, fosfoinosítido y adenosín monofosfato cíclico (AMPC), en donde calcio, fosfoinositido y el AMPC son los segundos mensajeros.

A continuación, dentro de la segunda fase se desarrolla la fase retrasada de tolerancia cerebral que es la ‘fase de expresión de tolerancia’, inducida por el PCH. Se asocia con la activación de genes proadaptativos y la expresión de sus productos, los cuales afectan la plasticidad intracelular para retener las funciones vitales de las neuronas y la integridad estructural. El control de la actividad del genoma está dirigido por terceros mensajeros inducibles (c-Fos, NGFI-A, HIF-1) o ubicuos (pCREB, NF-κB) que actúan como factores de transcripción y son activados en el citosol, translocados al núcleo en donde se unen a los promotores de genes blanco, regulando su transcripción. Los genes blanco son neurotrofinas (sobre todo el factor neurotrófico derivado del cerebro (BDNF)), enzimas antioxidantes mitocondriales y citosólicas, eritropoyetina (EPO) y el factor de crecimiento del endotelio vascular (VEGF). EPO es reconocido como un agente protector potente contra el daño isquémico que al unirse con receptores a EPO activa vías de señalización protectoras como Janus Cinasa 2 (JAK2) / transductor de señal y activador de la ruta de transcripción 3 (STAT3), la ruta de fosfatidilinositol 3-cinasa (PI3K) / proteína Cinasa B (Akt) y la ruta MAPK, todos conocidos por conferir citoprotección y neuroprotección contra lesiones isquémicas. El VEGF ejerce efectos protectores contra la isquemia cerebral debido a su efecto angiogénico y directa acción neuronal a través de efectos neurotróficos (Baillieul et al., 2017).

III.1.1. Precondicionamiento hipóxico y neurogénesis

En el cerebro maduro, existen poblaciones de astrocitos fuera de los nichos neurogénicos con un potencial neurogénico latente. Por ejemplo, los ataques cerebrovasculares provocan que astrocitos del estriado evoquen un programa neurogénico (Magnusson et al., 2014). La hipoxia tiene un efecto similar en la neurogénesis, en donde el PCH aumenta la proliferación de CPN, supervivencia de neuronas nuevas y su migración, la morfogénesis de espinas en neuronas maduras del giro dentado del hipocampo y neurogénesis en el bulbo olfatorio. Además, la señalización de NOTCH1 es activada después del PCH, la cual es requerida para la neurogénesis inducida por hipoxia (Wu et al., 2018; Zhang et al., 2014). En este sentido, el O₂ es un factor clave que afecta el microambiente de

las CPN, a través del PCH (que no conduce a la apoptosis) se genera un aumento en la densidad celular de las CPN, acompañada de un aumento substancial en la neurogénesis hipocampal. Por otra parte, el PCH inhibe la activación de la caspasa 3, promueve la expresión del HIF y aumenta la expresión del BDNF y el VEGF, promoviendo la angiogénesis y neurogénesis, que en conjunto reducen la muerte neuronal (Huang et al., 2020). Así, la neurogénesis puede ser inducida por lesiones en el tejido, donde se promueve a supervivencia celular y la diferenciación de CPN (Dirnagl et al., 2009).

IV. El cerebelo y el control respiratorio

El cerebelo ha mostrado otras funciones además del control motor, una de esas es el “hambre de aire”, el cual resulta del aumento de CO₂ en sangre arterial, que es percibida por las células del GVR y los complejos de Bötzingen en el bulbo y por el hipotálamo posterior. Varias áreas del cerebelo envían o reciben proyecciones del GVR, que incluyen los lóbulos: cuadrangular (VI), central (III), línula (I, II) y Crus (II). El GVR también se conecta con los núcleos fastigio, interpuesto y el dentado (Parsons et al., 2001). Además, existe actividad eléctrica espontánea en las neuronas del núcleo fastigio relacionada con la respiración. Estas neuronas se localizan en la región rostral; cerca de un tercio de las neuronas moduladas por la respiración son sensibles a retos de hipercapnia y son capaces de recibir, integrar y modular información de aferentes respiratorios, especialmente de los quimiorreceptores. El núcleo fastigio posee sitios quimiosensibles a la relación entre CO₂/H⁺ que facilitan la respuesta respiratoria a la hipercapnia (Xu & Frazier, 2002). La activación eléctrica o química del núcleo fastigio que facilita la salida motora respiratoria es modulada por las entradas inhibitorias de las células de Purkinje (provenientes del vermis medial) durante la respiración eupneica (ciclos respiratorios normales), esta interacción inhibitoria es mediada por el neurotransmisor GABA. Por otro lado, durante situaciones de hipercapnia (aumento de CO₂ en sangre) existe activación cerca de la línea media del cerebelo en varias partes incluyendo la línula (I) (Xu & Frazier, 2002).

IV.1. Barreras del SNC

Existen tres interfaces en el cerebro que protegen a las neuronas de sustancias transportadas por la sangre y que ayudan a mantener el medio apropiado para la función neuronal: 1) La interfaz sangre-LCE, formada por las uniones estrechas de las células epiteliales del plexo coroideo; 2) la interfaz sangre-cerebro (barrera hematoencefálica - BHE), formada por el endotelio cerebral y 3) la interfaz LCE-sangre, formada por el epitelio aracnoideo avascular situado bajo la duramadre que recubre todo el cerebro. La BHE permite el paso de O₂, CO₂ y sustancias lipofílicas pequeñas (<400 Da) por lo que tiene una regulación estricta en el transporte de nutrientes hacia adentro y hacia afuera del cerebro. Es impermeable a moléculas hidrofílicas como la glucosa, aminoácidos y otros nutrientes esenciales para la vida, los cuales cruzan la BHE a través de transportadores específicos en

la membrana endotelial apical o basolateral mediante difusión facilitada. También existen sistemas de transporte mediados por receptores para transportar proteínas y péptidos hacia el cerebro y bombas transporte activo localizados en la parte apical y basolateral de las membranas endoteliales que remueven moléculas desde el cerebro hacia la sangre. La base molecular de la BHE depende de proteínas de unión estrecha interendoteliales, la lámina basal vascular que comprende proteínas de matriz extracelular y la influencia de los pies terminales de los astrocitos y pericitos (Cipolla, 2009). Mientras que la hipoxia severa conduce a una perturbación extensa de la BHE, la inducción moderada de hipoxia genera adaptaciones benéficas en los vasos sanguíneos, iniciando una respuesta de remodelación vascular fuerte y un aumento en la expresión endotelial de proteínas de uniones estrechas, es decir, se mejora la integridad vascular (Cipolla, 2009).

IV.1.1. Líquido cerebroespinal

El LCE es un líquido claro producido en los plexos coroideos que baña al SNC. Ocupa el canal central espinal, el sistema ventricular y el espacio subaracnoideo. El LCE se absorbe directamente a la sangre a través de las granulaciones aracnoideas a los senos venosos duros (Adigun & Al-Dhahir, 2019). En el sistema ventricular, no hay una barrera apreciable entre el LCE y el espacio extracelular del cerebro, por ello la barrera entre la sangre y el LCE sirve para mantener un medio intraventricular estable, necesario para mantener una función neuronal normal (Telano & Baker, 2018).

V. Planteamiento del problema

Si bien se sabe que la respuesta sistémica al PCH es el resultado de diferentes grupos funcionales neuronales, queda por evaluar si el componente glial del cerebelo es blanco del PCH. Se desconoce si el PCH actúa sobre el CVM. Por lo anterior, en este trabajo se diseñó el estudio para dilucidar el momento en el que se puede identificar el CVM durante el desarrollo del cerebelo y por otro lado para determinar los blancos celulares que subyacen al efecto neuroprotector de la glía sobre el cerebelo, inducido por el PCH. Debido a que el PCH produce cambios probablemente benéficos y adaptativos en el SNC es necesario evaluar la participación de los astrocitos en este proceso, ya que se sabe que estas células participan activamente en la remodelación e integridad de la barrera hematoencefálica.

Se sabe también que el cerebelo presenta: 1) nichos de células que expresan GFAP y Nestina que están en contacto con el LCE en el techo del IV ventrículo (CVM y CCSV); 2) células subependimales con perfiles de corrientes iónicas típicos de precursores neurales; 3) células endpendimales que responden al GABA a través de la activación de receptores GABA-A (Reyes-Haro et al., 2013). Por lo anterior, en este trabajo pretendemos esclarecer si la glía GFAP+ y Nestina+ del CVM responden al PCH a través de la proliferación celular.

VI. Hipótesis

El componente glial del CVM del techo del IV ventrículo responde al PCH a través de la proliferación y diferenciación a glía y/o neuronas.

VII. Objetivo general

Describir la organización glial del CVM del techo del IV ventrículo durante la ontogenia y evaluar su respuesta al PCH en el cerebelo de ratones juveniles.

VIII. Objetivos específicos

1. Describir los cambios morfológicos del componente glial del CVM y el CCSV durante la ontogenia hasta el periodo de desarrollo completo del cerebelo, día postnatal (P) 26.
2. Determinar si el PCH afecta el control motor en ratones P26.
3. Explorar el efecto del PCH sobre la GB mediante el análisis de imágenes de alta resolución por LSM de cerebelo clarificado de ratones juveniles.
4. Determinar los efectos del PCH sobre la expresión de la GFAP en la glía ependimaria, GB y el CVM.
5. Explorar los cambios morfológicos que presenta la GB del lóbulo I, inducidos por el PCH.
6. Evaluar la respuesta de marcadores de identidad glial al PCH en el cerebelo de ratón juvenil y los niveles de marcadores neuronales (NeuN) y de CPN (Nestina) en el cerebelo de ratón juvenil (P26).
7. Analizar el efecto del PCH sobre la población de neuronas granulares en el lóbulo I, del cerebelo de ratón juvenil (P26)
8. Determinar si el PCH induce un fenotipo activado en la población microglial del lóbulo I.
9. Dilucidar si las células GFAP+/Nestina+ del CVM proliferan en respuesta al PCH.

IX. Materiales y métodos

IX.1. Declaración ética

Los procedimientos realizados en los animales se llevaron a cabo de acuerdo con los reglamentos de la “Society for Neuroscience”, cumpliendo con lo establecido por las políticas sobre el uso de animales y humanos en la experimentación en neurociencias y sobre las directrices bioéticas locales e internacionales, incluida la NOM-062-ZOO, que está de acuerdo con las recomendaciones de la publicación del “National Institutes of Health” titulada "Guía para el cuidado y uso de animales de laboratorio", y aprobada por nuestro Comité de Bioética institucional (licencia INB-UNAM: INEU / SA / CB089).

IX.2. Animales

Se utilizaron ratones macho en edad P26 de las cepas CD1, GFAP::EGFP y Pax2-GFP criados en las instalaciones para animales del Instituto de Neurobiología UNAM, Juriquilla, Querétaro o en la Universidad de Turín, Italia. Se mantuvieron en un ciclo normal de luz/oscuridad (12 h/12 h) a una temperatura de $20^{\circ}\text{C} \pm 1^{\circ}\text{C}$. Los ratones transgénicos que expresan la EGFP bajo el promotor de GFAP (Nolte et al., 2001) fueron donados amablemente por el Prof. Helmut Kettenmann (Centro Max Delbrück, Berlín). Esta cepa de ratón transgénico se seleccionó para la clarificación cerebral ya que la EGFP se expresa en astrocitos y glía de Bergmann del cerebelo. Los ratones transgénicos que expresan GFP bajo el promotor de Pax2 identifican progenitores de interneuronas GABAérgicas (Cerrato et al., 2018; Leto et al., 2016; Parmigiani et al., 2015). Se proporcionó agua y comida *ad libitum*, y se reemplazó el aserrín para mantener las condiciones de cuidado.

IX.3. Inducción de PCH

Los experimentos fueron conducidos a temperatura ambiente ($22 \pm 2^{\circ}\text{C}$) en ratones macho GFAP::EGFP, CD1 y Pax2-GFP P26, de 20 a 25 g. Se indujo el PCH con la finalidad de evaluar la respuesta de las células positivas a la GFAP que conforman el CVM. Basándonos en estudios previos (Benitez et al., 2014; Liu et al., 2012; López-Aguilera et al., 2012; Zhang et al., 2011), se colocó un ratón adulto dentro de un tubo de 50 mL sellado herméticamente. Una vez que el ratón comenzó a jadear se consideró que ese era el límite de tolerancia y se retiró del tubo. Esto fue considerado como un ciclo de PCH y se realizaron un

total de tres ciclos en cada ratón. Permitimos 15 min de recuperación en condiciones de normoxia entre ciclos. Cabe mencionar que, en el ciclo #1 empezaron a jadear en el segundo 201 ± 22.15 , en el ciclo #2 al segundo 350 ± 39.16 , y en el ciclo #3 al segundo 573 ± 64.83 . Este modelo, también conocido como autohipoxia, es inducido por el propio consumo de O_2 del animal y es uno de los primeros modelos establecidos para PCH (Rybnikova & Samoilov, 2015). Para cada procedimiento experimental, se utilizaron ratones a los que se les indujo el PCH para evaluar los cambios en el CVM y el lóbulo I del cerebelo. 24 ratones fueron divididos en 8 grupos al azar. Se usaron los cerebelos de un grupo como control y se formaron 7 grupos a los cuales se les indujo el PCH. El grupo 1 fue sacrificado al día 1 después de la inducción del PCH, el grupo 2 fue sacrificado al día 2 después del PCH, el grupo 3 fue sacrificado al día 3 después del PCH y así fue con el resto de los grupos, recolectando el tejido sucesivamente durante los días 4, 5 y 6 hasta llegar al día 7 después de la inducción de PCH.

IX.4. Análisis histológico

Para determinar el origen ontogénico del CCSV y del CVM se utilizaron ratones de la cepa GFAP::EGFP en las edades postnatales: P0, P5, P10, P15, P20, P30 ($n = 3$). Previa anestesia para la eutanasia, los ratones fueron perfundidos por vía intracardiaca con paraformaldehído (PFA) al 4%, se aislaron los cerebros, y se dejaron en gradientes de sacarosa al 10%, 20% y 30% para su crioprotección y se congelaron a -80°C . Posteriormente se realizaron cortes de $40\ \mu\text{m}$ en el criostato y se realizó una tinción de núcleos con yoduro de propidio, las muestras se preservaron en un medio de montaje para fluorescencia y se almacenaron a 4°C . Se realizó la toma de fotos en serie por microscopía confocal en cortes coronales de cerebelo.

IX.5. CLARITY

Se llevó a cabo la técnica de CLARITY (Chung & Deisseroth, 2013) para determinar la distribución del componente glial del CVM durante la ontogenia del cerebelo de ratones GFAP::EGFP. Esta técnica se basa en la inmovilización de proteínas por medio de la inmersión del tejido en una malla de hidrogel, así los componentes lipídicos son removidos por difusión pasiva con el detergente iónico SDS. Este protocolo se efectuó en los estados

embrionarios (E) E10, E12, E15, E18 y E19 y en las etapas P0, P5, P10, P15, P20 y P30 (n = 4). Se realizó la captura de imágenes por microscopía confocal.

IX.6. Microscopía de fluorescencia por hoja de luz

Para generar un mapa de alta densidad de la distribución de la GB y el efecto del PCH en la organización de este grupo de células, primero se clarificó el cerebro utilizando la técnica CLARITY como se ha descrito con anterioridad (Chung & Deisseroth, 2013; González-González et al., 2017) en cerebros de ratones GFAP::EGFP. Se utilizó la LSM para obtener imágenes de la mayor parte del cerebelo (Olarte et al., 2018). Las imágenes se obtuvieron con un objetivo 2X con una configuración descrita en (Stefaniuk et al., 2016) utilizando un láser de diodo (Cobolt 06-MLD) en la línea de 488 nm para excitar la EGFP. Para la reconstrucción de la imagen del cerebelo, se unieron *stacks* de 2096 X 1705 μm con el complemento FIJI (Preibisch et al., 2009). Cada *stack* consistió en una exploración horizontal del cerebelo (**Figura 8**); de cada reconstrucción, se seleccionó una región de interés (ROI) tridimensional de $2.73 \times 10^7 \mu\text{m}^3$ de: el vermis cerebeloso y de los hemisferios cerebelosos. Para determinar el número de somas de GB que expresan la EGFP, se realizó el conteo automatizado del centroide de los somas que expresaban la EGFP. Usando MATLAB, se realizó una sustracción del fondo de cada corte óptico que conforman una ROI; cada corte óptico fue binarizado computando un umbral global bajo el algoritmo de Otsu, lo que permitió detectar los somas de la GB, así, los centroides fueron cuantificados automáticamente.

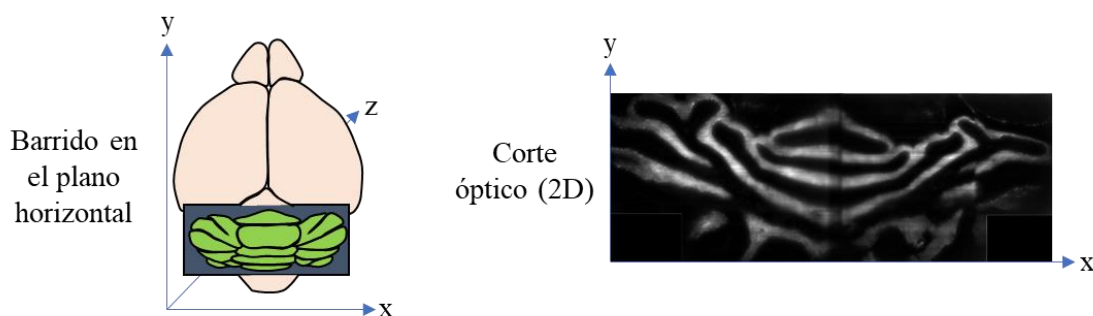


Figura 8. Exploración horizontal por LSM. A la izquierda se muestra un esquema representativo de cómo se realiza el barrido del cerebelo GFAP::EGFP en disposición coronal por LSM. A la derecha se muestra el ejemplo de una reconstrucción de un corte óptico que consiste en 16 cuadrantes.

IX.7. Pruebas conductuales

Para determinar el impacto del PCH se realizó una batería de pruebas para evaluar la coordinación motora. Esta batería incluía una versión de aceleración del Rotarod, la prueba de barras estáticas y la prueba de barras horizontales que se realizaron como en estudios anteriores (Brooks & Dunnett, 2009; Deacon, 2013).

IX.8. Procesamiento de tejidos e imágenes

La fijación del tejido nervioso se llevó a cabo para analizar la expresión de la EGFP en el CVM y el lóbulo I. La anestesia se administró por vía intraperitoneal (pentobarbital, 1 mL / 2.5 kg), y la perfusión intracardiaca se realizó como se describió (Gage et al., 2012; González-González et al., 2017). Después de la inyección de pentobarbital y una vez que los ratones estaban insensibles a un pinchazo en la pata, se administró de forma intracardiaca solución salina tamponada con fosfato PBS (NaCl [137 mM] (JT Baker Cat. No. 3624-05), KCl [2.7 mM] (JT Baker Cat. No. 3040-05), Na₂HPO₄ [10 mM] (SIGMA No. Cat. S9638), KH₂PO₄ [2 mM] (JT Baker, Cat. No. 3252-01) disuelto en agua desionizada (pH = 7.4) para exanguinar seguido de la perfusión con PFA al 4% en PBS, pH = 7.4 logrando la fijación y preservación del tejido.

Para la técnica de montaje completo, el cerebelo se escindió y se transfirió a PFA al 4% a 4° C durante 24 h, y los núcleos se tiñeron con yoduro de propidio (Invitrogen, No. Cat. P3566, 1.5 mM) a una concentración de 500 nM. Para obtener imágenes, expusimos la superficie de los lóbulos I, II y X, como se describió (González-González et al., 2017), lóbulos que están en contacto con el LCE del IV ventrículo. Se utilizó un microscopio confocal LSM 510-Zeiss® con un objetivo Zeiss 10X para obtener una representación tridimensional de la superficie del lóbulo I junto con el CVM. Para determinar el efecto del PCH en la expresión de la EGFP en el lóbulo I, se cuantificó el valor gris medio en proyecciones bidimensionales de series de imágenes sobre el eje Z, calibradas de acuerdo con el objetivo Plan Zeiss 10X EC-NEOFLUAR, A.N. = 0.3, distancia de trabajo = 5.2 mm (Cat. No. 440331-9902). La cuantificación del valor gris medio se realizó utilizando el software de ImageJ, estableciendo un umbral bajo el algoritmo de Otsu. A partir de estos

valores se dedujo la densidad óptica integrada (DOI) del lóbulo I (ROI's = 902.70 X 672.60 μm) y del CVM (ROI's = 38.94 x 265.5 μm).

Asimismo, se utilizó un grupo de ratones GFAP::EGFP P26 para analizar el patrón de expresión de la EGFP en la GB del lóbulo I. Se procesaron secciones coronales del cerebelo de ratones GFAP::EGFP como se describe en estudios anteriores (González-González et al., 2015; González-González et al., 2017). Se colectaron cinco cortes coronales consecutivos de 40 μm y se tomaron imágenes con un microscopio confocal Zeiss LSM-510 para obtener proyecciones bidimensionales de 40 μm con un objetivo 20X Zeiss Plan-APOCHROMAT, A.N. = 0.8, distancia de trabajo = 0.55 mm (Cat. No. 440641- 9911). Las somas de GB que expresan EGFP se cuantificaron manualmente en ImageJ con el complemento de contador de células, estableciendo un umbral bajo el algoritmo de Otsu.

IX.9. Tinción rápida de Golgi

El análisis morfológico de la GB se realizó después de una tinción rápida de Golgi. Se utilizaron tres grupos de ratones CD1 machos P26: dos grupos (n = 6) se sometieron al PCH y se usó un grupo como control. Los cerebelos fueron procesados como se describió previamente 4 y 7 días después del PCH. El procedimiento de Golgi se realizó siguiendo el método publicado por González-González et al., 2015; Rosas-Arellano et al., 2007; Shiga et al., 1983. Después de que el tejido se deshidrató y se incluyó en nitrocelulosa, se obtuvieron secciones sagitales de 120 μm con un vibratomo Leica, VT1000S. Para analizar la GB del lóbulo I, se capturaron imágenes con un microscopio Olympus Ckx41 utilizando un objetivo 40X. Cuarenta y cinco células de cada animal fueron capturadas y procesadas en el software ImageJ. El área del soma, así como la longitud absoluta de protrusiones, se evaluaron siguiendo el método publicado por Hanke & Reichenbach, (1987). Las imágenes se procesaron en el software de ImageJ (versión 1.51r, Wayne Rasband, National Institutes of Health, Bethesda). El algoritmo de Huang se aplicó para el umbral de la GB en muestras de Golgi.

IX.10. Western blot

Se cuantificó con la técnica de *Western blot* el nivel de expresión de GFAP, Aldh1L1, Iba1, NeuN y Nestina en grupos de ratones GFAP::EGFP y CD1. Se obtuvieron extractos de

proteínas totales de cerebelo (n = 4). El tejido se procesó y se homogeneizó en tampón enfriado con hielo [glicina 200 mM (Biorad, No. de cat. 161-0718), NaCl 150 mM, EGTA 50 mM, EDTA 50 mM] y sacarosa 300 mM junto con inhibidores de proteasas (Sigma-Aldrich, USA Cat. No. P8340). El homogeneizado se centrifugó dos veces a 10 000 g durante 15 minutos a 4°C, y los sobrenadantes se recogieron y almacenaron a -80°C. La concentración de proteínas se evaluó mediante el método de Bradford (Bradford, 1976). En cada gel de SDS-poliacrilamida al 10% se cargó un total de 30 µg de proteína y se transfirió a una membrana de difluoruro de polivinilideno (Millipore, EE. UU.). Luego, las membranas se bloquearon con un 5% de leche en polvo sin grasa con TBS-T durante 3 h. Las membranas se incubaron a 4°C durante la noche con uno de los anticuerpos primarios mostrados en la **Tabla 1** (sección de apéndices), y la Actina se usó como control interno para cada muestra. Luego, las membranas se lavaron con TBS-T tres veces y se incubaron durante 4 h con un anticuerpo secundario (**Tabla 1**, sección de apéndices). La actividad de la fosfatasa alcalina acoplada al anticuerpo secundario se detectó con sal disódica de fosfato de 5-bromo-4-cloro-3-indolilo (BCIP) / cloruro de nitro azul tetrazolio (NBT) de acuerdo con las instrucciones del fabricante. Las imágenes se adquirieron con un sistema ChemiDoc XRS Molecular Imager (Bio-Rad Laboratories, Inc., EE. UU.). La densidad óptica de la cantidad de trazas para cada banda se determinó utilizando el software Image Lab 2 (Bio-Rad Laboratories Inc.).

IX.11. Inmunofluorescencia para microglía

La distribución y la morfología de la microglía del lóbulo I se evaluaron 4 días después del PCH, mediante inmunofluorescencia utilizando un anticuerpo policlonal Iba1 (**Tabla 1**, sección de apéndices) en rebanadas coronales de cerebelo de ratones CD1, GFAP::EGFP y Pax2-GFP (Parmigiani et al., 2015) seguido por el anticuerpo secundario (**Tabla 1**, sección de apéndices). Se usó un microscopio confocal Zeiss LSM780 para obtener imágenes de 15 µm en intervalos de 1 µm con un objetivo de 20X. Analizamos el área ventromedial a lo largo de la ZSV del lóbulo I.

Para el análisis del número de células Iba1+, dividimos estas células en dos grupos: células con un área de soma igual o inferior a 50 µm correspondiente a microglía en reposo, y células con soma mayor de 50 µm correspondiente a microglía activada (Davis et al., 2017).

Cada *stack* de imágenes se analizó utilizando el software de Fiji de la siguiente manera: 1) El *stack* se proyectó en el eje Z en una sola imagen utilizando el tipo de proyección de intensidad máxima. 2) El contraste se mejoró utilizando un valor de 0.1 en todos los casos. 3) La imagen resultante se convirtió en un formato binario de 8 bits. 4) Se aplicó un umbral utilizando el algoritmo de “triángulo”. 5) La imagen se recortó en un área limitada (450 μm x 300 μm) que incluía la ZSV y una parte de la capa granular. 6) Se colocó una rejilla de líneas de 1 000 μm^2 en la proyección. 7) Cada cuerpo celular marcado por el anticuerpo Iba1 se delineó a mano con la herramienta de lazo a mano alzada y se convirtió en una ROI. 8) El área de cada soma se obtuvo después de aplicar la función "Medir". Para evaluar la distribución de células Iba1+, cada imagen confocal se dividió en dos zonas según una cuadrícula de líneas de 1 000 μm^2 : 1) La ZSV, delimitada ventralmente por las primeras 2 filas. 2) La supra ZSV que correspondía a las capas molecular, Purkinje y granular que cubrían 8 filas sobre la ZSV. El complemento de contador de células se utilizó para contar el número de células Iba1+ por zona (ZSV y supra ZSV).

IX.12. Ensayo de incorporación de bromodesoxiuridina (BrdU)

Para determinar la proliferación celular después del PCH, usamos el análogo de timidina (BrdU, Sigma-Aldrich Cat. No. B5002). Se utilizaron dos grupos de ratones CD1: uno se usó como control (n = 3) y otro grupo fue analizado cuatro días después de PCH (n = 3). Para cada grupo, se administraron dos inyecciones intraperitoneales de 50 μg / g de BrdU (10 mg / ml), con un intervalo de 6 h. La primera inyección se realizó 30 minutos después del PCH, y se administraron dosis diarias de BrdU durante 5 días. Los ratones se sacrificaron 2 h después de la última inyección y los cerebros se procesaron como se describe anteriormente, el cerebelo crioprotegido se cortó en secciones coronales de 40 μm y las observaciones se centraron en el lóbulo I. El BrdU se detectó utilizando los anticuerpos indicados en la **Tabla 1** (sección de apéndices). Seguido del anticuerpo secundario, las muestras se incubaron en el complejo avidina-biotina (ABC) y se revelaron usando un kit de amplificación de señal de tiramida (TSA) más cumarina (1: 100, Perkin Elmer. Cat. No. NEL703001KT) siguiendo las instrucciones del fabricante.

IX.13. Análisis estadístico

Todos los resultados se repitieron tres veces como mínimo en experimentos independientes. Los datos se presentan como el promedio \pm error estándar (SE) de la media. El análisis de los datos para determinar diferencias estadísticamente significativas de cada procedimiento experimental está indicado en la **Tabla 2** de la sección de apéndices, así como las pruebas *post-hoc* correspondientes. Cuando el análisis arrojó valores de $P \leq 0.05$ se consideró que existía una diferencia significativa. Los análisis estadísticos se realizaron utilizando el siguiente software: GraphPad Prism versión 5.0 para Windows (GraphPad Software, La Jolla California USA). Los análisis de WB se realizaron con el software Image Lab™ de Bio-Rad y los datos se trazaron en SigmaPlot (Systat Software, San Jose, CA).

X. Resultados

X.1. Desarrollo del CVM y del CCSV

Observaciones previas realizadas en nuestro laboratorio mostraron una diversidad celular glial en el techo del IV ventrículo; se identificaron dos componentes que se denominaron CVM y CCSV (González-González et al., 2017; González-González et al., 2016 Tesis Doctoral; Reyes-Haro et al., 2013). Por tanto, la primera parte de este trabajo tuvo como objetivo mostrar el origen y desarrollo de estas estructuras.

La presencia del CVM fue claramente discernible a partir del día E15 (**Figura 9 A**, flechas verdes) en el eje dorso ventral observamos una mayor densidad de células GFAP+ agrupadas en la zona media del lóbulo I, en donde asemejan una ‘corriente’ distribuida en sentido anteroposterior, y está presente a través del desarrollo postnatal desde el día P0 a P30 (**Figura 9 B**, flechas azules). Observamos que el CVM permanece restringido a la zona media del techo del IV ventrículo, sobre el lóbulo I, en donde está distribuido a lo largo del eje dorsoventral hasta el día P5 (**Figura 9 B**, flecha azul, día P5). El CVM queda limitado a la zona media, en un corte coronal, por aproximadamente una decena de células (**Figura 5**). Adyacente al CVM se encuentra la capa de células endodiales (**Figura 9 B**), flechas azules en P20 y P30 y (**Figura 5 A**).

Por otro lado, determinamos el surgimiento del CCSV a partir del día P5 (**Figura 9**, flechas amarillas). Durante su desarrollo, el CCSV muestra un ensanchamiento dorsoventral gradual.

X.2. La inducción del PCH se refleja en el aumento de tolerancia

La segunda parte de este trabajo consistió en determinar la respuesta de los componentes celulares del techo del IV ventrículo al PCH. En primera instancia se evaluó el funcionamiento adecuado del protocolo de PCH que se implementó basado en Gidday et al., 2013 y Ren et al., 2018. Se considera que el PCH induce tolerancia, la cual se denota por un incremento en el lapso de tiempo entre los jadeos que el animal ejecuta a lo largo del tiempo que dura el protocolo (Gidday et al., 2013; Ren et al., 2018). Después de cada ciclo de inducción de PCH, el organismo aumenta su tolerancia acompañado de una disminución continua en el consumo de O₂ y en la producción de CO₂ (Ren et al., 2018) indicativo de una respuesta condicionante o adaptativa. En nuestro estudio, indujimos tres ciclos de PCH (denominados ciclos 1, 2 y 3). En estos protocolos el lapso entre cada jadeo aumentó después de cada exposición a la hipoxia (en segundos: 1: 201 ± 22.15 ; 2: 350 ± 39.16 ; 3: 573 ± 64.83 ($X \pm SE$)). Podemos observar la tolerancia desarrollada por los ratones durante la inducción del PCH (**Figura 10**).

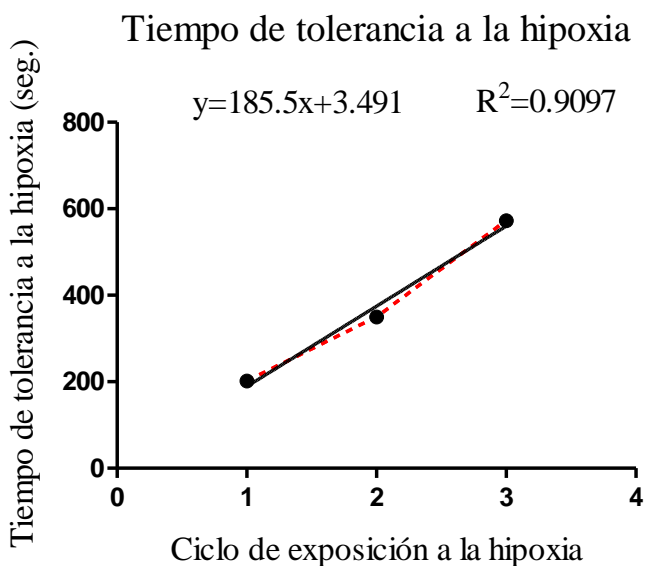


Figura 10. Desarrollo de tolerancia ante la exposición hipóxica. La regresión lineal muestra el aumento consistente de tolerancia ante cada ciclo de inducción de PCH. $n = 9$. El SEM se muestra con una línea punteada roja.

X.3. La coordinación motora no es afectada significativamente por el PCH

Para determinar si el PCH induce algún efecto en el desempeño motor, utilizamos una combinación de pruebas conductuales: la prueba de barras estáticas, la de barras horizontales y Rotarod (Mann & Chesselet, 2014). En términos generales no encontramos diferencias estadísticamente significativas que sugirieran alteraciones motoras severas, con excepción de las alteraciones observadas al día 6 en la prueba de Rotarod, en el que los ratones mostraron una disminución en la distancia recorrida sobre el rodillo. Cabe señalar que, en las pruebas realizadas, los ratones mostraban algunas dificultades para llevarlas a cabo, estas dificultades fueron temporales, no fueron estadísticamente significativas y dejaron de presentarse al día 7 (**Figura 11**).

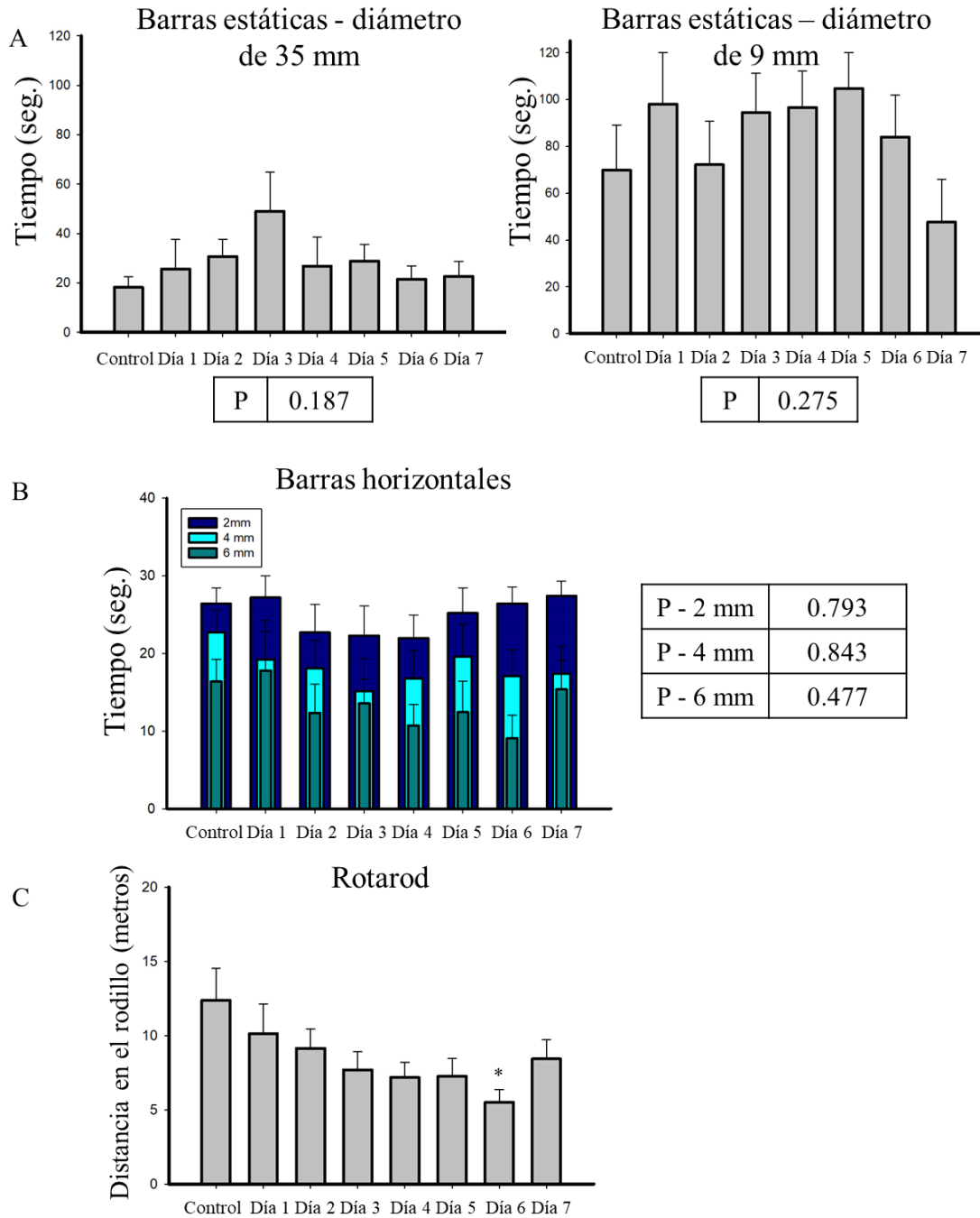


Figura 11. El PCH no afecta significativamente la coordinación motora. **A:** barras estáticas. Se muestra el desempeño en el rodillo más ancho (35 mm) y el más estrecho (9 mm), los tiempos de ejecución más breves indican una mejor coordinación motora. **B:** barras horizontales, los ratones duraron menos tiempo colgando de las barras de 2-6 mm, sugiriendo una reducción en la fuerza de sus extremidades. **C:** prueba de Rotarod, las distancias más largas se relacionan con una mejor coordinación motora y encontramos una disminución estadísticamente significativa únicamente en el día 6 después de la inducción del PCH ($F_{(7,191)} = 2.347$, $P = 0.024$, *Post-hoc*: Tukey's). Los ratones se recuperaron a niveles comparables al control al día 7 en todas las pruebas.

X.4. Cambios en la expresión de EGFP en el cerebelo en respuesta al PCH

Realizamos un análisis global de la expresión de la EGFP en el cerebelo a los 4 días de la inducción del PCH, esto se logró con el uso de ratones transgénicos GFAP::EGFP, CLARITY y obtención de imágenes mediante LSM. Dado que esta cepa transgénica expresa con gran fidelidad la GFAP característica de los astrocitos y GB (Nolte et al., 2001), los cambios en la intensidad de fluorescencia indican cambios en los niveles de expresión de la GFAP. Encontramos que los lóbulos responden al PCH a través de cambios en la expresión de EGFP. Se observó de manera consistente un incremento en la cantidad de somas y la intensidad de fluorescencia en la GB en los hemisferios del cerebelo. Al contrario de los lóbulos evaluados que pertenecen al vermis en donde se observó la disminución en la fluorescencia emitida y en el número de GB que expresan la EGFP (**Figura 12**). La reducción en el número de GB EGFP+ en la zona del vermis ante el PCH se debe interpretar como una reducción en la expresión del gen reportero más que la pérdida de células GFAP+.

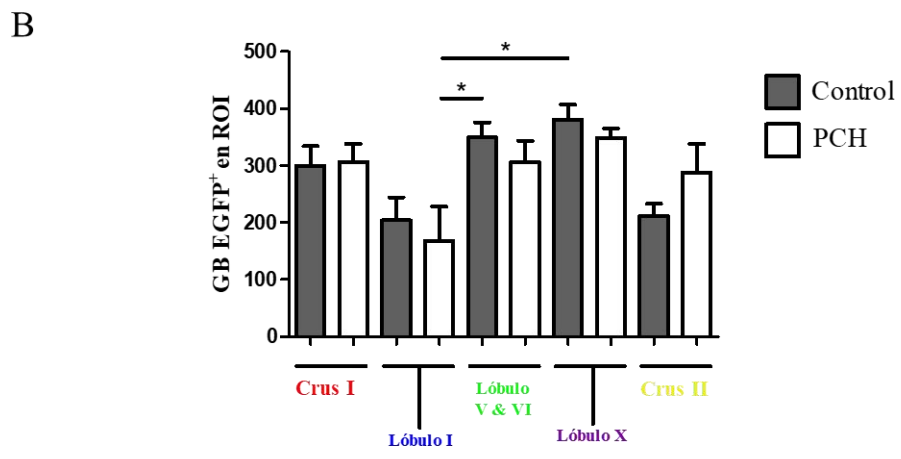
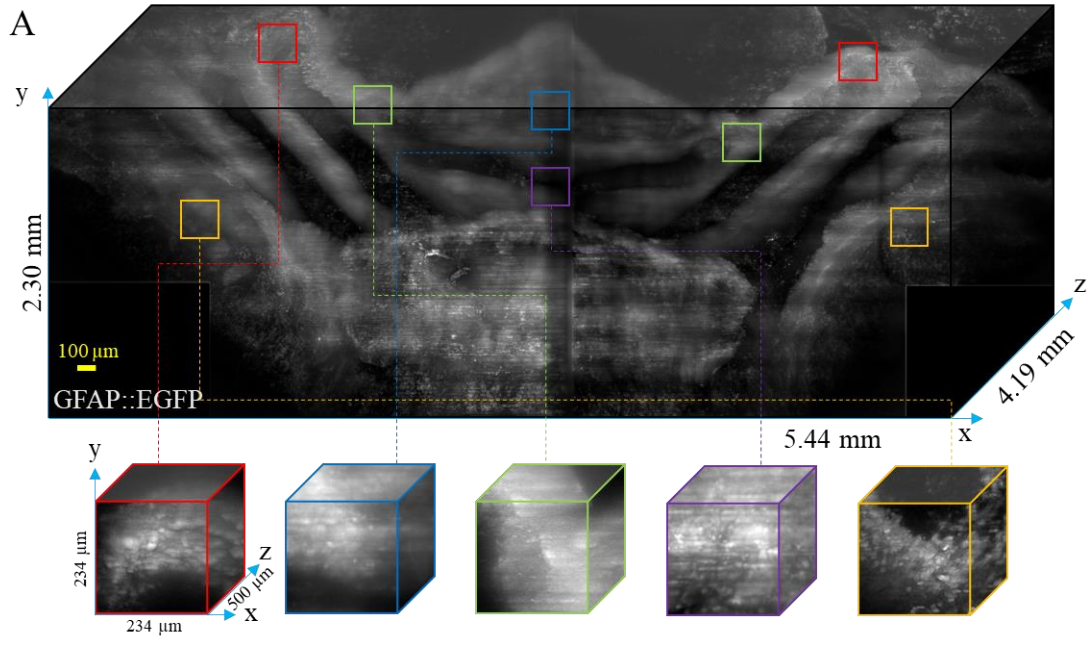


Figura 12. La EGFP se reduce de forma no significativa en diversas áreas del cerebelo clarificado. **A:** reconstrucción de 5.44 x 2.30 x 4.19 mm de cerebelo; los cuadros de color son ROI extraídas del vermis y hemisferios representativos de los lóbulos seleccionados. **B:** la EGFP se reduce en el vermis e incrementa en los hemisferios. Estos no fueron cambios significativos entre cada lóbulo (determinado por la prueba T no pareada) (Crus I: $P = 0.8940$, 299.9 ± 34.08 (N = 9) vs 306.2 ± 32.03 (N = 9). Lóbulo I: $P = 0.6277$, 204.0 ± 40.42 (N = 6) vs 167.7 ± 60.33 (N = 6). Lóbulo V y VII: $P = 0.3427$, 349.5 ± 26.68 (N = 11) vs 305.5 ± 38.10 (N = 8). Lóbulo X: $P = 0.3236$, 380.8 ± 26.07 (N = 5) vs 348.0 ± 17.11 (N = 5). Crus II: $P = 0.1670$, 210.9 ± 22.40 (N = 7) vs 288.0 ± 50.18 (N = 6)). Por otro lado, existe una diferencia significativa global ($F_{(9,62)} = 3.263$, $P = 0.0026$) determinado por la prueba de ANOVA de una vía, (*Post-hoc*: Tukey's) (N = 6, Control), (N = 5, PCH). GFAP: proteína ácida fibrilar glial, EGFP: proteína fluorescente verde mejorada, GB: glía de Bergmann, PCH: preconditionamiento hipóxico.

X.5. El CVM reduce la expresión de la EGFP en respuesta al PCH

La técnica de montaje completo o libro abierto ofrece la posibilidad de visualizar la capa de células endocelulares y las células del CVM que contactan el LCE del IV ventrículo. Como ya se mencionó, el CO₂ se difunde fácilmente a través de la BHE y hacia el LCE, por ello esperamos una respuesta de estas células. Encontramos que, no solo el CVM sufre una disminución en la expresión de la EGFP, sino que la glía endocelular del lóbulo I presenta también una disminución en los niveles de EGFP. Dicha disminución es temporal, puesto que regresa a valores muy cercanos a los normales a partir del día 6 en el lóbulo I y a partir del día 7 en el CVM (**Figura 13**).

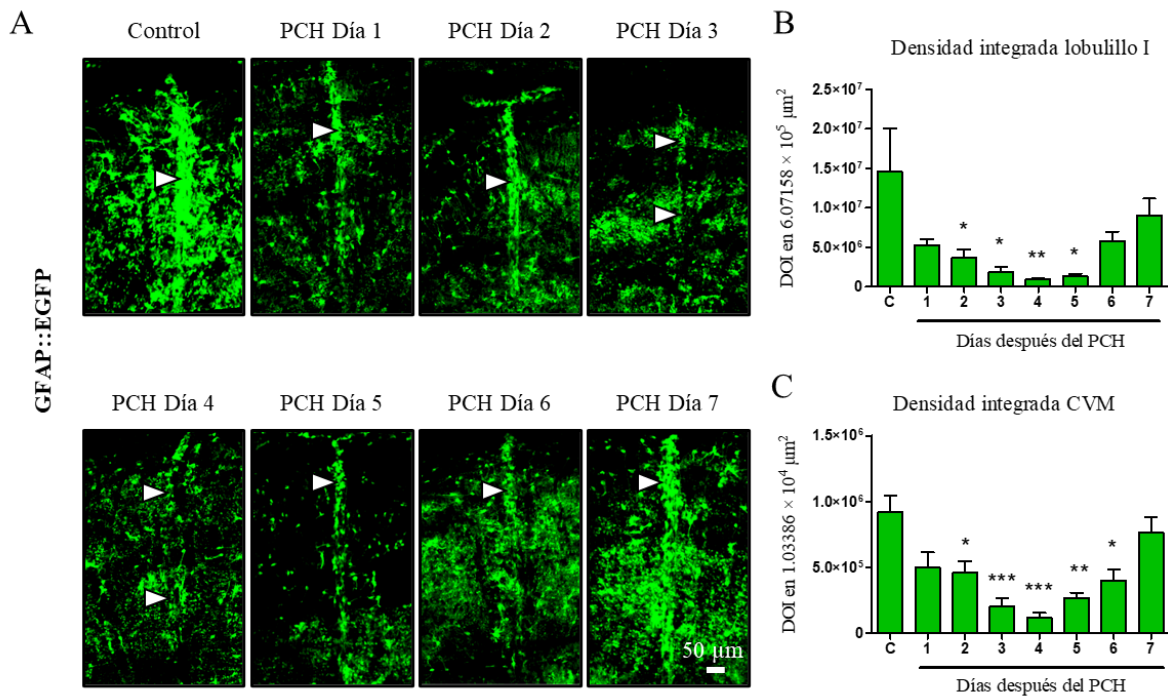


Figura 13. La expresión de la EGFP disminuye temporalmente en respuesta al PCH. **A:** Se muestra el lóbulo I con el CVM (flechas blancas), en respuesta al PCH, la EGFP expresada en la glía del CVM disminuye paulatinamente y muestra los niveles de expresión más bajos al día 4, después, la expresión de la EGFP regresa a su estado basal al día 7. De igual manera sucede con la glía endocelular que expresa la EGFP. **B:** se representa de forma gráfica la cuantificación de la DOI del comportamiento de la EGFP en respuesta al PCH en la glía endocelular del lóbulo I ($F_{(7,16)} = 4.419$, $P = 0.0066$, ANOVA de una vía, *post-hoc*: Tukey's, $N=24$, $n=3$) **C:** Se representa de forma gráfica la cuantificación de la DOI de la EGFP en respuesta al PCH en el CVM ($F_{(7,16)} = 9.275$, $P = 0.0001$, ANOVA de una vía, *post-hoc*: Tukey's. DOI: densidad óptica integrada, PCH: preconditionamiento hipóxico, GFAP: proteína ácida fibrilar glial, EGFP: proteína verde fluorescente mejorada, CVM: cordón ventromedial.

X.6. La expresión de la EGFP disminuye en respuesta al PCH en el lóbulo I

Identificamos la disminución temporal de los somas de GB que expresan EGFP en cortes coronales de ratones transgénicos juveniles GFAP::EGFP en respuesta al PCH. Observamos que 24 horas después del PCH es evidente la desorganización de los somas de la GB, y que en días subsecuentes regresan paulatinamente a su posición original (**Figura 14 A**). También observamos cambios en la disposición de sus procesos primarios desde el día 1 al 5 después del PCH, además la EGFP en los pies terminales cambió su localización a un patrón en puntos, hacia el día 4 (**Figura 14 C**). Posteriormente algunos de los cambios de la GB se revirtieron a sus condiciones basales. Los somas parecen regresar a su posición original y la cantidad de somas de GB que expresan EGFP regresa a valores muy parecidos a los originales (**Figura 14 B**), sin embargo, los procesos de la GB permanecen parcialmente retraídos (cambios morfológicos confirmados por la técnica de Golgi) y los pies terminales aún presentan zonas que conservan el patrón en puntos de la EGFP ambos cambios se aprecian con facilidad (**Figura 14 C**).

Por otro lado, notamos somas ectópicas de GB que parecen no sufrir cambios aparentes en respuesta al PCH a nivel morfológico, incluso al realizar un conteo manual de la cantidad de dicha GB ectópica no encontramos cambios significativamente diferentes (**Figura 15**).

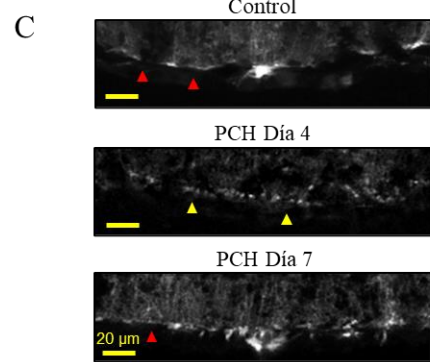
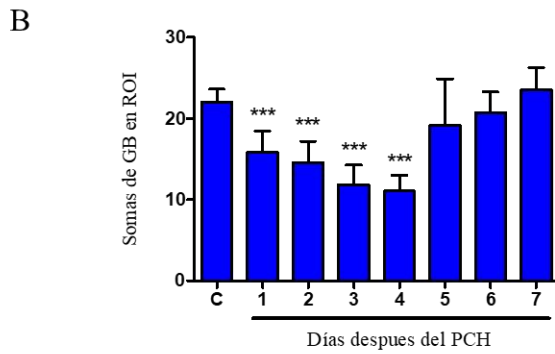
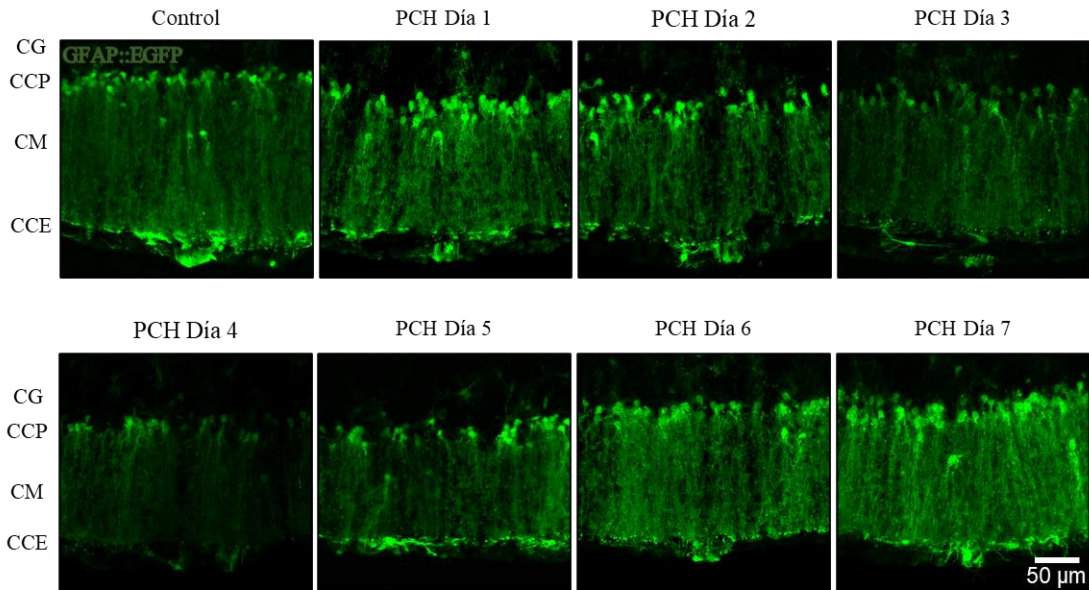


Figura 14. Efecto del PCH en la GFAP de la GB. Captura de imágenes por microscopía confocal de cortes coronales del cerebelo de ratón transgénico GFAP::EGFP, **A:** Se observa la desorganización de somas de GB, así como una disminución en la fluorescencia emitida por estos (cuantificado en **B**, $F_{(7,112)} = 36.04$, $P < 0.0001$, ANOVA de una vía, post-hoc: Tukey's). A su vez, la GB presentó cambios en la disposición de los procesos primarios, dichos cambios regresaron a condiciones muy similares a las originales. **C:** La expresión de EGFP en los pies terminales de la GB cambiaron de un patrón difuso (Control, cabezas de flecha roja) a uno en puntos (Día 4, cabezas de flecha amarillas) regresando parcialmente a su condición normal para el día 7. Barra: 50 μm . PCH: Precondicionamiento hipóxico, CG: capa granular, CCP: capa de células de Purkinje, CM: capa molecular, CCE: capa de células endoteliales, GB: glía de Bergmann, ROI: región de interés (por sus siglas en inglés).

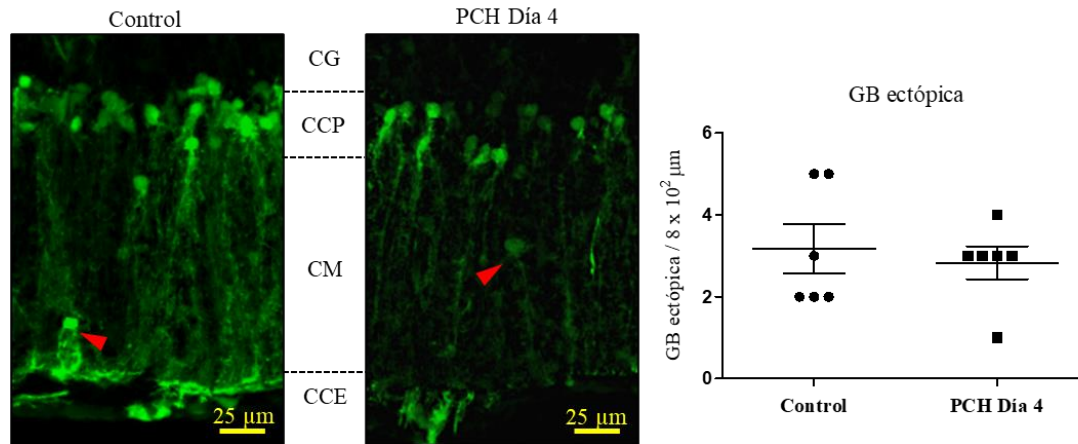


Figura 15. GB GFAP⁺ con somas en una posición ectópica. La GB ectópica fue contada manualmente en proyecciones de imágenes 2D coronales del lóbulo I al día 4 después de la inducción del PCH. Las cabezas de flecha roja indican las GB ectópicas. PCH: preconditionamiento hipóxico, CG: capa granular, CCP: capa de células de Purkinje, CM: capa molecular, CCE: capa de células endodiales, GB: glía de Bergmann. Prueba de T no pareada, P = 0.6545.

X.7. La GB adquiere un fenotipo diferente en respuesta al PCH

Los resultados de la sección previa indicaron la reorganización de la GB en los ratones que expresan EGFP bajo el promotor de GFAP, en los que se observaron cambios temporales en GFAP. Subsecuentemente analizamos estos cambios por la técnica de Golgi rápido, la que nos mostró que la morfología de la GB cambia en respuesta al PCH y no regresa a condiciones normales después de 7 días (**Figura 16**). En condiciones control se distinguen hasta 5 procesos principales de los cuales se despliegan protrusiones que actúan como microdominios. Sin embargo, a los 4 días después del PCH los procesos de la GB se muestran alineados, el área del soma disminuye significativamente y la longitud absoluta de las protrusiones tiene un aumento estadísticamente significativo (**Figura 16**). Podemos entonces distinguir un fenotipo en condiciones fisiológicas en contraste con un fenotipo activo al día 4, mientras que para el día 7 obtenemos un ‘fenotipo preparado’, que estaría (morfológicamente hablando) más cercano al fenotipo activo.

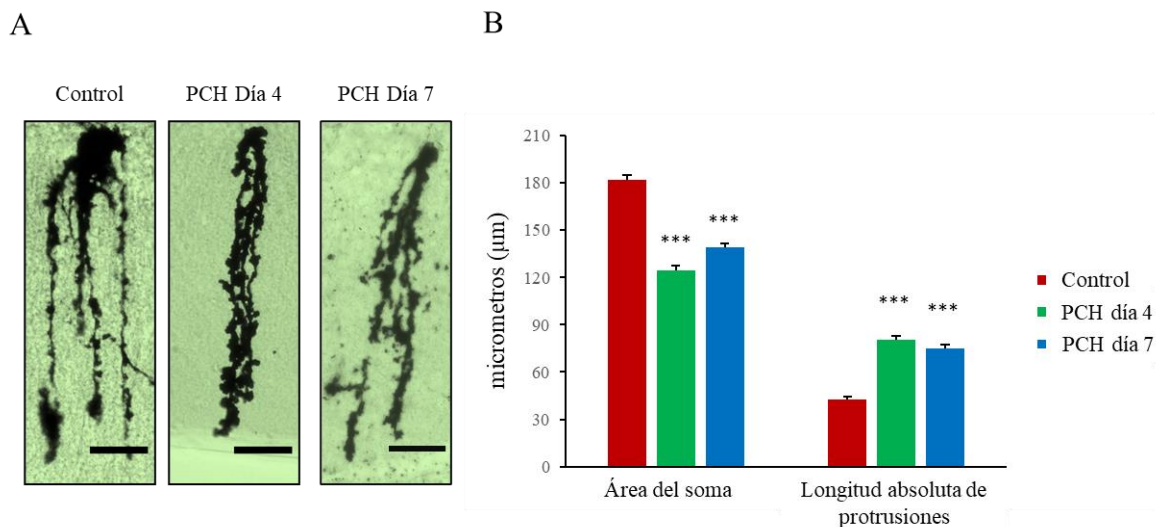


Figura 16. Efecto del PCH en la morfología de la GB. **A:** Imágenes representativas de la GB a los 4 y 7 días después de inducir el PCH. **B:** en respuesta al PCH el área del soma disminuye y permanece significativamente pequeño en comparación al control incluso después de 7 días. A su vez, la longitud absoluta de protrusiones incrementa casi el doble y no recupera sus valores originales al día 7 ($P < 0.0001$, $N=3$, $n=45$ por cada grupo). PCH: preconditionamiento hipóxico. Barra: 100 µm

X.8. El PCH afecta los niveles de marcadores de identidad gliales y neuronales evaluados por WB

Aislamos la proteína total del cerebelo para cuantificar mediante la técnica de WB los niveles de las siguientes proteínas en respuesta al PCH: GFAP-astrocitos, Aldh1L1-astrocitos, Iba1-microglía, NeuN- neuronas y Nestina-CPN. Encontramos que, los niveles de las proteínas GFAP y Aldh1L1 disminuyeron temporalmente, los niveles más bajos se presentaron al día 4 y 5, regresando a valores comparables al control al día 6 y 7 (**Figura 17 B-C**). Para descartar que las respuestas observadas fueran inducidas por la restricción de movimiento del animal dentro del tubo, incluimos un control en donde el ratón fue inmovilizado dentro de un tubo cónico de 50 ml, pero con una apertura donde pudiera respirar con normalidad (D.T.: Dentro del tubo) observamos que no existen diferencias estadísticamente significativas entre el control D.T. y el control donde el ratón estuvo caminando libremente (fuera del tubo, F.T.), que también respiraba con normalidad (**Figura 17 B-F**). A su vez, comprobamos que la respuesta inducida por el PCH no tuviera un efecto diferencial debido a la cepa transgénica GFAP::EGFP, por ello evaluamos que el PCH

indujera también la disminución temporal de la proteína GFAP en los ratones CD1 (**Figura 18**). De manera interesante, al analizar los marcadores Iba1, NeuN y Nestina indicaron el aumento continuo de estas proteínas (basándonos en el aumento de la intensidad de la banda en membrana), de hecho, para el día 7 no regresaron a sus valores originales (**Figura 17 D-F**).

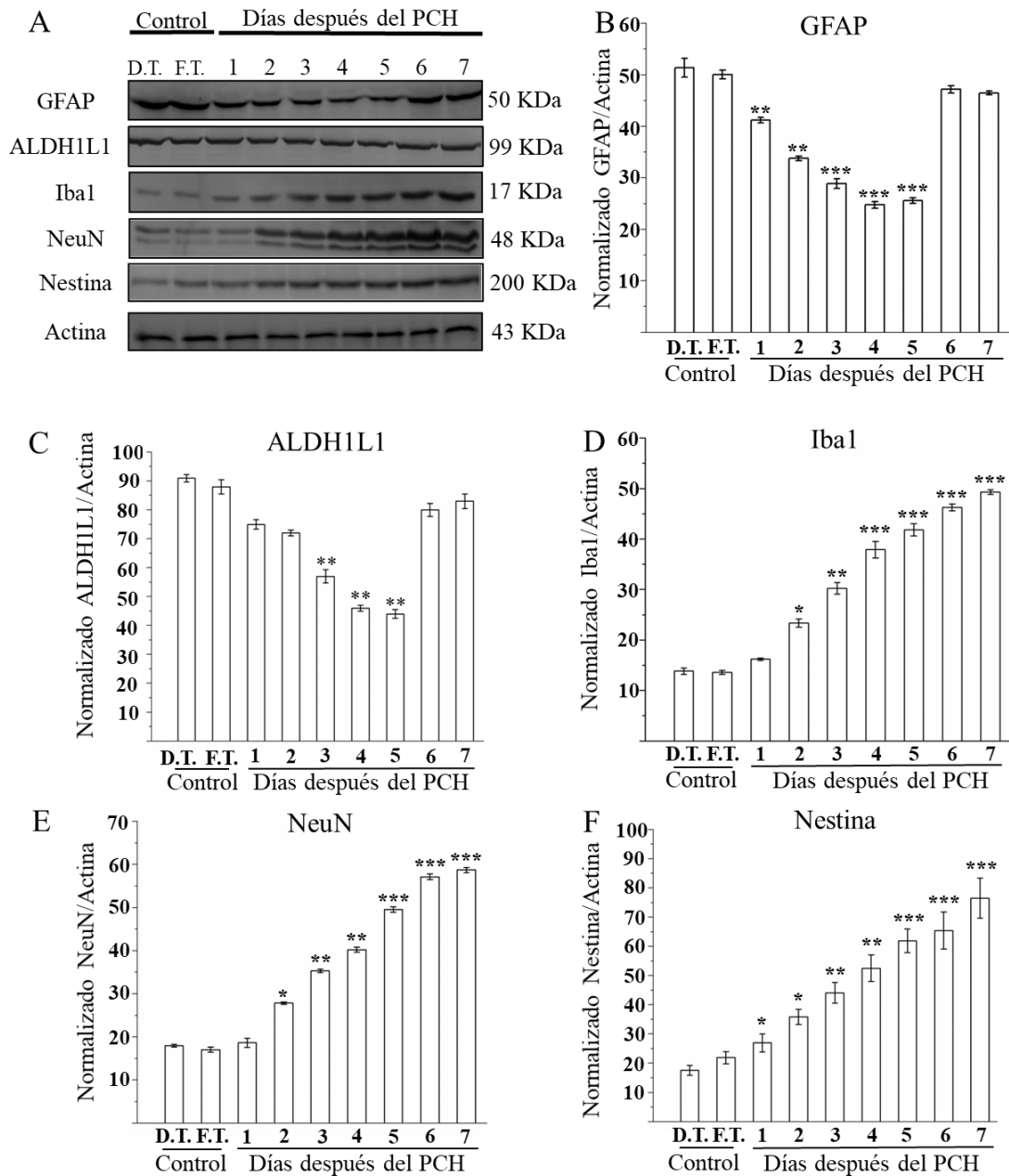


Figura 17. El PCH induce la reducción temporal de las proteínas GFAP y Aldh1L1 y el aumento de Iba1, NeuN y Nestina. **A:** WB's representativos para ratones GFAP::EGFP, **B-C:** Disminución temporal en la expresión de proteínas de identidad glial y astrocítica (GFAP y Aldh1L1), **D-F:** Aumento de las proteínas de identidad microglial, núcleos neuronales y de CPN (Iba1, NeuN y Nestina, respectivamente). La Actina se utilizó como control interno. PCH: preconditionamiento hipóxico, D.T.: dentro del tubo, F.T.: fuera del tubo (referente al hocico del animal).

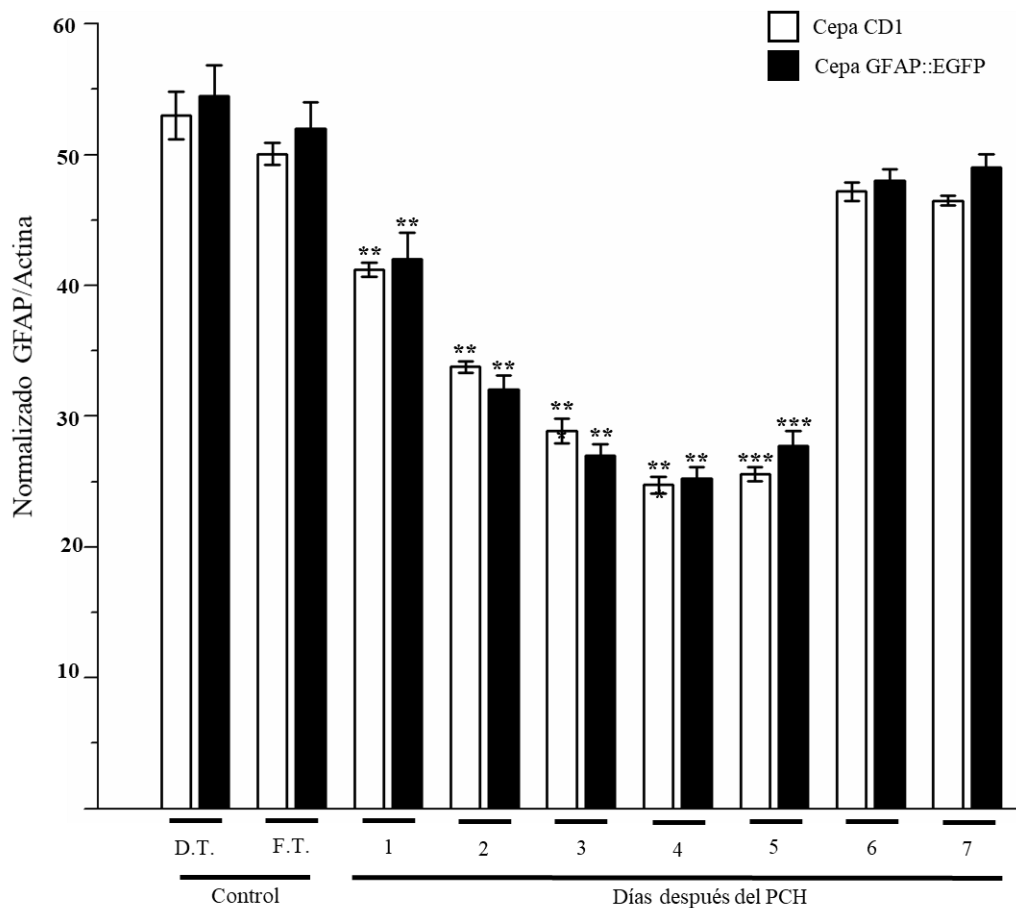


Figura 18. El PCH induce la misma respuesta en los niveles de GFAP entre ratones transgénicos GFAP::EGFP y CD1, descartando un efecto dependiente del transgén. GFAP: proteína ácida fibrilar glial, EGFP: proteína verde fluorescente mejorada, D.T.: dentro del tubo, F.T.: fuera del tubo.

X.9. El PCH no induce el aumento en el número de neuronas granulares NeuN+ en la CM

Dado el aumento de la proteína NeuN en respuesta al PCH, estudiamos mediante inmunofluorescencia si este incremento se debía a una mayor cantidad de neuronas granulares en la capa molecular del lóbulo I. Sin embargo, no encontramos aumento del número de células granulares. Tampoco observamos incremento en la DOI (**Figura 19**). Sugerimos que el incremento de la proteína NeuN observado en los resultados de WB pudiera

estar relacionado con el hecho de que los niveles de su expresión pueden ser indicativos del estado fisiológico de neuronas postmitóticas (Weyer & Schilling, 2003).

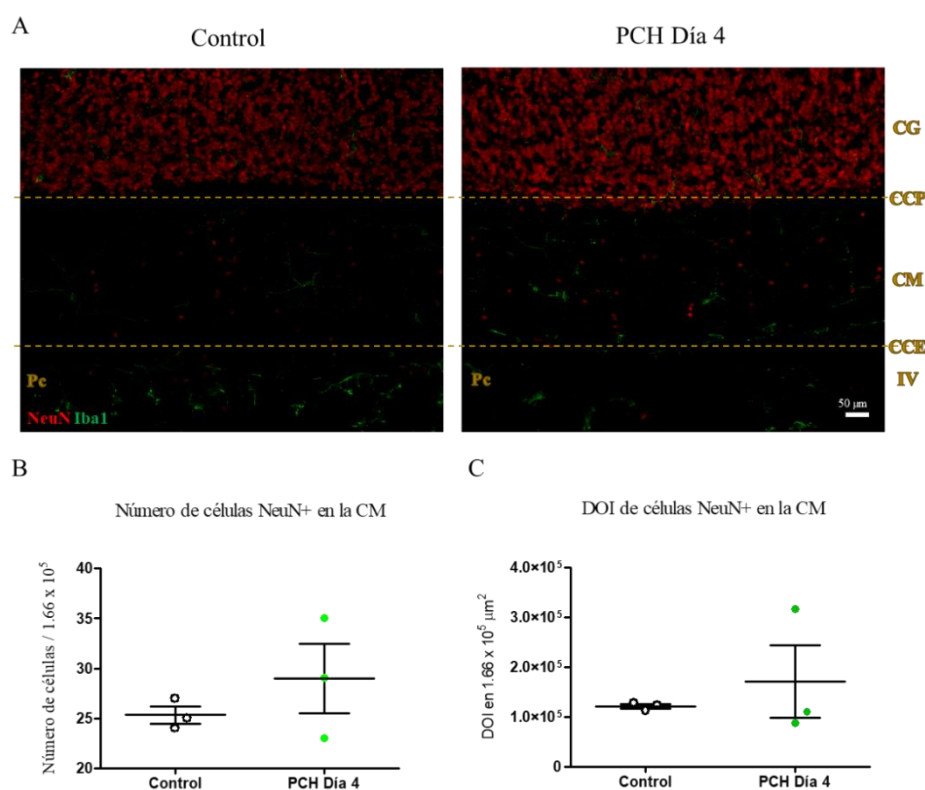


Figura 19. El PCH no aumenta el número de células NeuN+ en la CM. **A:** Cortes coronales representativas del lóbulo I de ratón CD1 del grupo control y al día 4 después de la inducción de PCH. **B:** Representación gráfica de la cuantificación del número de células NeuN+ en la CM muestra que no existen diferencias estadísticamente significativas. **C:** Representación gráfica de la cuantificación de la DOI de células NeuN+ en la CM indica que no existen diferencias estadísticamente significativas. PCH: preconditionamiento hipóxico, CG: capa granular, CCP: capa de células de Purkinje, CM: capa molecular, CCE: capa de células endocelulares, IV: IV ventrículo, Pc: plexo coroideo.

X.10. El PCH induce el aumento en el tamaño del soma de la microglía del lóbulo I

Los niveles de la proteína Iba1 aumentan en respuesta al PCH (**Figura 19**), por lo que quisimos determinar si este incremento está relacionado con el número de células Iba+. Además, describimos la morfología de la microglía mediante inmunofluorescencia con un

anticuerpo anti-Iba1 en secciones coronales de cerebelos de ratones de las cepas CD1 y Pax2/GFP.

En ambas cepas obtuvimos los mismos resultados, en donde el número de células Iba1+ no se alteró de manera significativa en la ZSV 4 días después del PCH, pero observamos una reducción en el número de células cuyos somas eran menores o iguales a $50 \mu\text{m}^2$, estos somas pertenecen a la microglía en reposo cuya morfología está bien definida por tener las siguientes características: 1) cuerpo celular pequeño, 2) ramificaciones delgadas extendidas en todas direcciones, 3) ocupan un territorio de 15-30 μm (Kettenmann & Verkhratsky, 2011). No encontramos diferencias significativas en la microglía cuyo soma fuera mayor a $50 \mu\text{m}^2$ (**Figura 20**).

Determinamos que ante la inducción del PCH únicamente la microglía de la supra ZSV responde al PCH, mientras las otras áreas de la corteza del cerebelo no mostraron alteraciones evidentes.

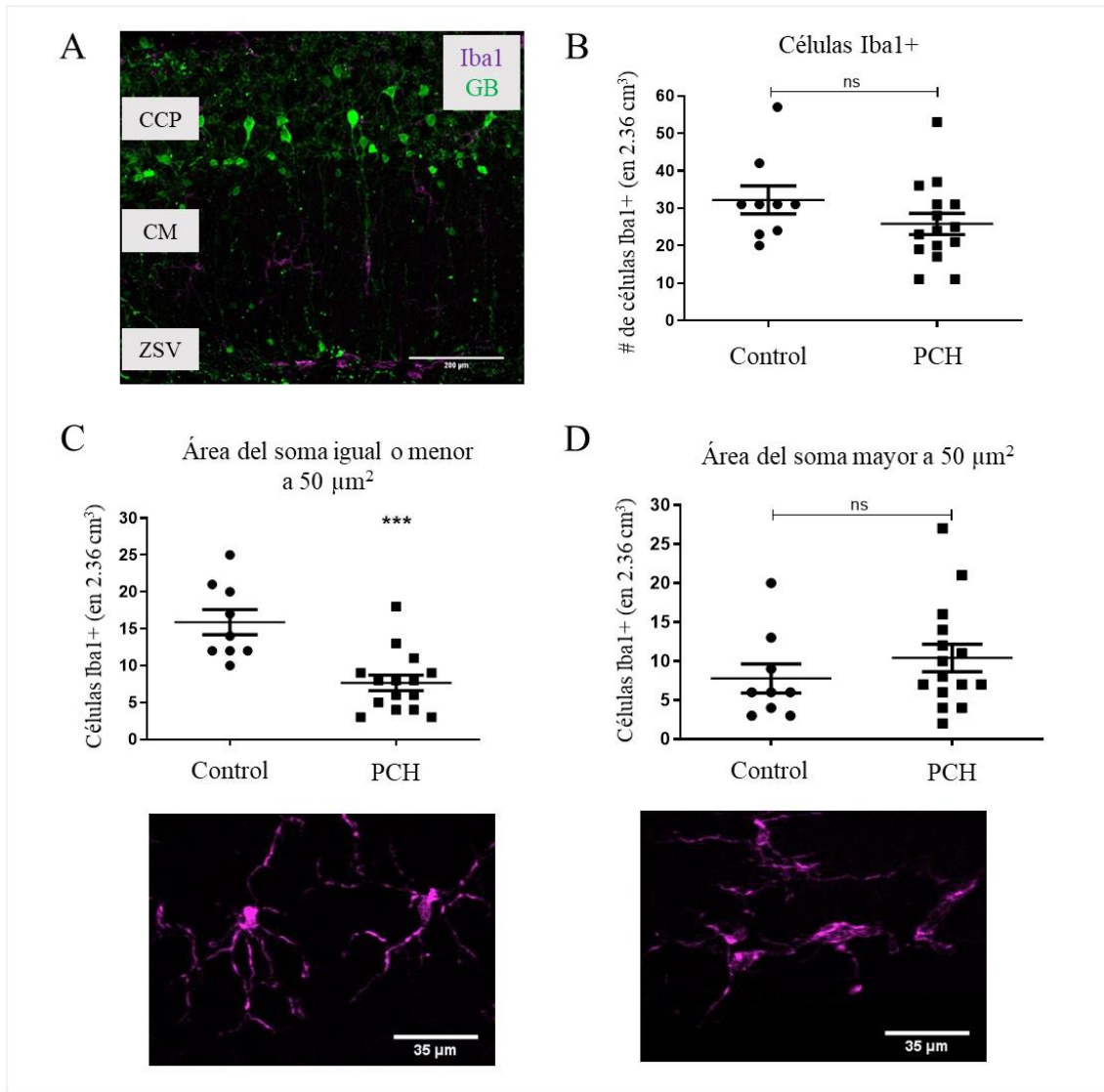


Figura 20. El PCH induce cambios en la morfología microglial. **A:** Imagen representativa de un corte coronal del lóbulo I capturado por microscopía confocal. Se observa la presencia de células Iba1+ en la SZV. **B:** $P = 0.0003$, $N=9$, determinado por prueba de T no pareada. **C:** el número de células Iba1+ con área igual o menor a $50 \mu\text{m}^2$ disminuye en respuesta al PCH al día 4. **D:** no hay diferencias estadísticamente significativas en el número de células con soma mayor a $50 \mu\text{m}^2$ en respuesta al PCH. En C y D se muestran imágenes representativas de células Iba1+ entre el grupo control y después de 4 días de la inducción del PCH para comparar los cambios en el tamaño del soma y la complejidad de las ramificaciones. GB: glía de Bergmann, CCP: capa de células de Purkinje, CM: capa molecular, ZSV: zona subventricular, PCH: preconditionamiento hipoxico.

X.11. El PCH induce la incorporación limitada de BrdU en el techo del IV ventrículo

La expresión de Nestina y GFAP existe no solo en regiones como la zona subventricular, sino también en regiones donde se presenten insultos cerebrales en el SNC de ratones juveniles y adultos. Las células Nestina+ y GFAP+ son consideradas CPN, que no están comprometidas activamente en la actividad mitótica en el cerebro sin lesionar, pero los astrocitos que expresan Nestina son mitóticamente activos en respuesta a un daño (Goldman, 2003; Lang et al., 2015; Pekny & Pekna, 2014; Sergent-Tanguy et al., 2006; Wei et al., 2002). Para evaluar si esto sucede en las células GFAP+ y Nestina+ del CVM se determinó si existe la incorporación de BrdU en respuesta al PCH. Cuantificamos la DOI para determinar cambios entre el control y la respuesta al PCH al día 4. Encontramos diferencias significativas en la integración de BrdU en la capa de células endocelulares, la cual es el recubrimiento que delimita el parénquima cerebeloso del LCE y transmite señales provenientes del LCE a través de sus cilios. No se detectó incorporación considerable de BrdU en la ZSV del techo del IV ventrículo. Sin embargo, de manera interesante se encontró la incorporación de BrdU en el piso del IV ventrículo, que corresponde al bulbo (**Figura 21**).

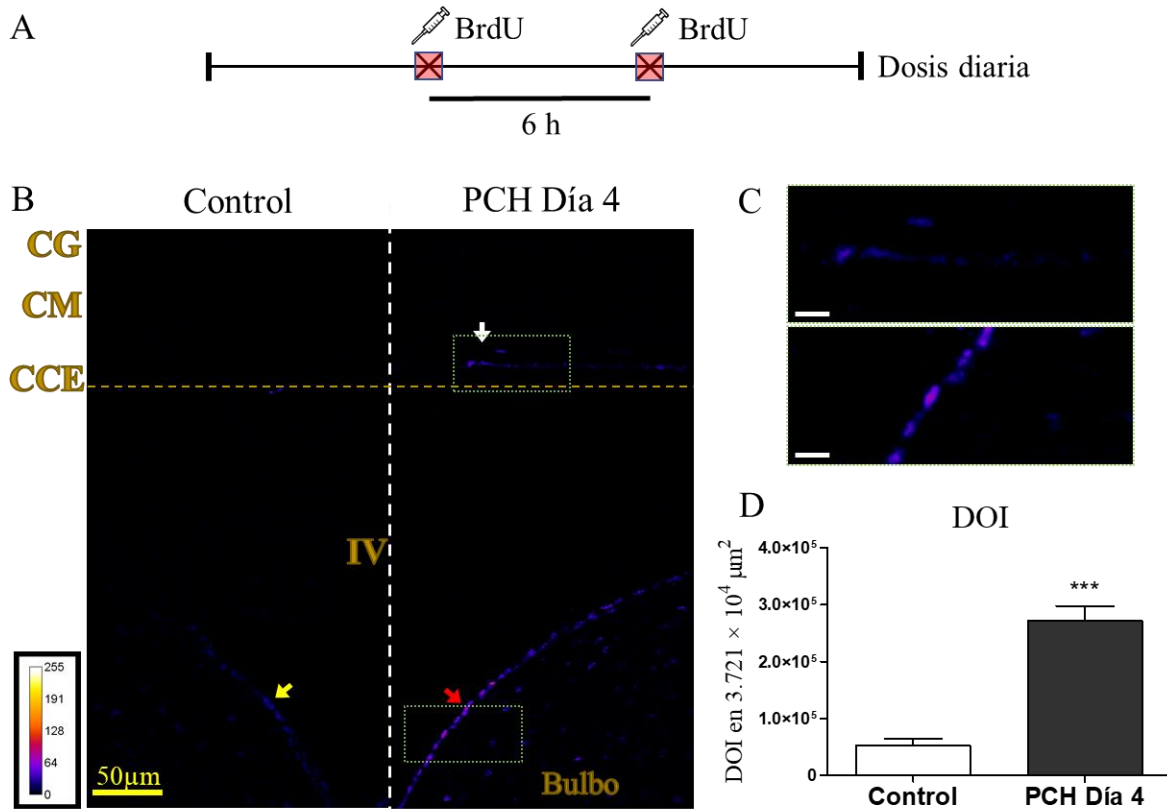


Figura 21. Incorporación de BrdU en el techo del IV ventrículo en respuesta al PCH. **A:** Administración diaria por 5 días después del PCH de dos inyecciones i.p. de BrdU (50 mg/kg, 6 h entre cada dosis). **B:** El grupo control mostró incorporación limitada de BrdU en las células del piso del IV ventrículo que pertenecen al bulbo (flecha amarilla), dicha integración se volvió más evidente 4 días después de la inducción de PCH (flecha roja). En contraste, en el techo del IV ventrículo la incorporación de BrdU fue escasa (flecha blanca). **C:** Magnificación digital de los recuadros señalados en 'B'. **D:** Representación gráfica de la DOI que indica una diferencia estadísticamente significativa de BrdU respecto al control. PCH: preconditionamiento hipóxico, CG: capa granular, CM: capa molecular, CCE: capa de células endoteliales, IV: IV ventrículo, DOI: densidad óptica integrada, barra:50 µm.

XI. Discusión

En este trabajo se evaluaron las respuestas de la glía y del CVM ante el PCH, dado que la glía adapta su función a los requerimientos del ambiente local, por lo que difieren en su metabolismo, expresión genética y morfología (Köhler et al., 2019). Las células del CVM residen en la interfaz del parénquima del cerebelo con el LCE en el cual se difunde con facilidad el CO₂, en consecuencia, la respuesta de la glía del CVM dependerá de su capacidad para adaptarse. El punto clave para sobrevivir a la hipoxia/isquemia es evitar el rápido decaimiento en los niveles de ATP en el tejido, las células nerviosas alteran su metabolismo para promover la supervivencia celular a través de cambios en la expresión genética. La función de los astrocitos es importante para la viabilidad celular durante la hipoxia cerebral. Los niveles de los HIFs aumentan en condiciones de hipoxia, influyendo en las propiedades neuroprotectoras de los astrocitos. Los astrocitos son la fuente principal de eritropoyetina (EPO) en el cerebro y la EPO es inducida a través de HIF-2 dentro de los astrocitos y es mediada por el preconditionamiento hipóxico para funcionar como neuroprotector para los tipos celulares circundantes (Guo et al., 2019; Weidemann et al., 2009).

El PCH no indujo cambios significativos en la coordinación motora. El cerebelo juega un papel clave en la coordinación precisa de las extremidades durante los movimientos voluntarios. En donde la actividad de las células granulares tienen un papel importante en la regulación de la locomoción, incluyendo la coordinación de extremidades individuales (Powell et al., 2015), dichas células exhiben tasas bajas de disparo en ratones despiertos en reposo, en cambio, durante la locomoción las tasas de disparo aumentan de forma dramática donde se involucra el glutamato extracelular (Powell et al., 2015). En este sentido, los astrocitos, incluyendo a la GB, liberan GABA de forma tónica el cual puede controlar la coordinación motora inhibiendo tónicamente la excitabilidad neuronal del cerebelo. La disminución de dicha inhibición tónica en las células granulares resulta en el aumento de la excitabilidad de las células granulares, que se ha demostrado que genera la disfunción del desempeño motor en un modelo del síndrome de Angelman en ratón (Woo et al., 2018). Se sabe que el PCH reduce la degradación de la Cx43, resultando en el aumento de hemicanales Cx43 en membrana, facilitando la liberación de ATP desde la GB que conduce a la acumulación de adenosina extracelular, un potente agente neuroprotector (Lin et al., 2008).

Al unirse a receptores de adenosina A1, en las células granulares se disminuye la entrada GABAérgica, en consecuencia, las células granulares aumentan su excitabilidad (Courjaret et al., 2009).

Observamos que en respuesta al PCH, los niveles de la proteína NeuN aumentaron continuamente en el cerebelo completo. Sin embargo, al enfocarnos en el lóbulo I, encontramos que no hay un aumento significativo en la cantidad de células granulares de la capa molecular ni en su DOI. Es complicado cuantificar de forma precisa la población de células NeuN+ de la capa granular, debido a la alta densidad de células, pero al observar la IF notamos una mayor intensidad en la expresión de NeuN después del PCH (**Figura 19**). Es sabido que los niveles de expresión de NeuN pueden variar con el estado fisiológico de las células granulares del cerebelo (Weyer & Schilling, 2003). Por lo que sugerimos que el incremento continuo en la proteína NeuN, pudiera expresarse de forma diferencial en el cerebelo, como observamos con la EGFP y además es posible que represente un aumento en la actividad de neuronas granulares.

Ante el PCH, no se determinó ninguna diferencia significativa en el déficit motor, pero sí observamos consistentemente dificultades para llevar a cabo la tarea, esto sugiere no solo que el insulto leve que es el PCH no es suficiente para afectar de manera permanente el sistema motor, ya que se recupera de forma efectiva, sino que además es consistente con la idea de que el cerebelo está involucrado en la corrección de errores para los movimientos, teniendo la habilidad de usar la información de errores en la ejecución para adaptar modelos internos y mejorar el desempeño en pruebas subsecuentes (Foerde & Poldrack, 2010).

Cambios en la expresión de GFAP inducidos por el PCH. El aclaramiento del SNC de ratones GFAP::EGFP nos permitió observar respuestas gliales diferenciales del cerebelo que expresa niveles altos de la EGFP bajo el promotor de GFAP. Encontramos que en cerebelo murino existen diferencias en la cantidad de GB en diversas áreas del cerebelo. Sin embargo, en cada lóbulo analizado no encontramos diferencias estadísticamente significativas en la cantidad de somas EGFP+ de la GB en respuesta al PCH. Es importante mencionar que, pese a no ser cambios estadísticos significativos, encontramos mayor o menor cantidad de somas de GB en respuesta al PCH. Los lóbulos I y II (donde se localiza el CVM) presentaron una disminución en la cantidad de somas de GB, contrario al de Crus I

y Crus II, en donde aumentaron (**Figura 12 B**). Consistentemente, al analizar el lóbulo I, la disminución temporal de la DOI en las células endocitiales EGFP+ y el CVM, además de la disminución de somas de GB EGFP+, sugieren que cambios específicos en cada lóbulo pudieran estar relacionados a la organización modular del cerebelo.

Se sabe que las neuronas glutamatérgicas del cerebelo son protegidas por el PCH, el fenotipo tolerante a la hipoxia involucra la amortiguación de la excitotoxicidad regulando a la baja los receptores a AMPA. Además se ha sugerido que se puede evitar la liberación de glutamato a través de mejorar la retroalimentación inhibitoria mediante receptores glutamatérgicos metabotrópicos presinápticos, que disminuyen la probabilidad de liberación (Rybnikova & Samoilo, 2015).

Por otro lado, es razonable especular que la retracción de procesos principales de la GB (evaluado a través de la técnica de Golgi rápida) es debida a que posee receptores a AMPA GluR1 y GluR4 que están involucrados en mantener sus procesos alrededor de las espinas dendríticas de las neuronas de Purkinje, cuando estos receptores son eliminados condicionalmente en la GB, sus procesos se retraen impidiendo el aprendizaje motor asociativo (Zeeuw & Hoogland, 2015). Esto explicaría la leve deficiencia en el desempeño motor y sugiere que probablemente exista la regulación a la baja de receptores a AMPA en la GB.

A su vez, se considera que el aumento en la longitud absoluta de protrusiones en la GB, podría estar involucrado en la restricción de la difusión de neurotransmisores de la hendidura sináptica, ayudando a mejorar la fidelidad de la transmisión sináptica y específicamente en astrocitos, se estimulan las vías MAPK y PI3K vía el receptor mGlu3 incrementando la producción de factores neurotróficos, además que los receptores mGlu del grupo III pueden mejorar la recaptura de glutamato modulando la expresión del transportador de glutamato 1 (GLT-1) y GLAST, contribuyendo a la neuroprotección (Spampinato et al., 2018).

Nosotros sugerimos que en el lóbulo I, se llevan a cabo estos procesos de plasticidad glial (retracción de procesos de la GB por regulación a la baja de receptores a AMPA), que conducen a un fenotipo único en respuesta al PCH, mismo que ejerce una actividad

neuroprotectora, probablemente a través de la recaptura por glutamato, acompañando la retracción de los procesos de las sinapsis de las neuronas de Purkinje, dado que la GB está implicada en la transmisión sináptica mediada por las fibras paralelas (Zeeuw & Hoogland, 2015), la retracción de sus procesos aumenta el número de sinapsis entre las fibras paralelas y las neuronas de Purkinje, induce múltiples inervaciones de las fibras trepadoras sobre las neuronas de Purkinje y perjudica la coordinación motora, esto apoya la idea de los cambios observados en la leve discapacidad temporal en el funcionamiento motor.

Cambios morfológicos y en los niveles de proteínas de identidad gliales en respuesta al PCH en el cerebelo hipóxico. Evaluamos por WB los cambios en los niveles de proteínas de identidad de astrocitos (GFAP y Aldh1L1) ante el PCH. Los niveles de ambas proteínas disminuyeron temporalmente (en un periodo de 7 días). La GFAP es un filamento intermedio (FI) y este junto con el resto de los FI se encarga de facilitar la reorganización celular, pudiendo desensamblarse durante eventos fisiológicos o fisiopatológicos que cambian las propiedades físicas y fisiológicas de las células. Estos cambios se regulan mediante modificaciones postraduccionales, que son reversibles y se evocan a través de la fosforilación de proteínas.

La GFAP tiene múltiples sitios de fosforilación en el extremo N-terminal, dichos sitios tienen un impacto distinto en su dinámica. La fosforilación de sus residuos en el dominio N-terminal inhibe la polimerización y despolimerizan a los filamentos de GFAP. La proteína cinasa asociada a Rho (ROCK), es un regulador clave de la morfología celular, es activada en respuesta al preconditionamiento y está involucrada en el papel protector que se obtiene del preconditionamiento (Sakamoto et al., 2011). Se sabe que ROCK fosforila varios FI, incluyendo a la GFAP en su extremo N-terminal, lo que genera una inhibición casi por completo de la formación de este filamento (Kosako et al., 1997; Yasui et al., 1998). Los anticuerpos de GFAP reconocen un epítipo en el extremo N-terminal, que es donde ocurren las fosforilaciones. Sugerimos que la decaída temporal de GFAP que observamos se deba a que en respuesta al PCH, la parte N-terminal haya sido fosforilada (Li et al., 2017), evitando su detección por el anticuerpo. Otra posibilidad es el favorecimiento en la expresión de otra isoforma. El hecho de que el PCH pudiera generar un aumento en la expresión de la isoforma GFAP δ (en lugar de otras) parece la posibilidad más probable.

Dado que, la regulación de genes es una respuesta esperada de PCH y dependiendo del nivel de expresión, GFAP δ altera las propiedades de la red de FI, en donde puede formar heterodímeros con otro FI tipo III e integrarse en una red de FI o puede colapsar la red de FI (Moeton et al., 2016). Al observar el continuo incremento de la proteína Nestina, sugerimos que la red de FI se estabiliza probablemente a través de la polimerización de isoformas de GFAP con Vimentina y Nestina. La posterior estabilización de GFAP (al día 7 post-hipoxia) junto con el mantenimiento de un continuo aumento en la expresión de Nestina abre la posibilidad de que la co-polimerización principal encargada del mantenimiento de la red de FI en respuesta al PCH esté formada por Nestina y Vimentina. Más aun, mecanismos tales como la metilación y acetilación de histonas y/o ADN ocurren en el PCH (Rybnikova & Samoilov, 2015); diversos estudios demuestran que la acetilación reprime a la GFAP y estimula el *splicing* alternativo del gen GFAP (Kanski et al., 2014).

En conjunto, sugerimos que la disminución de GFAP podría estar relacionada con su desensamble a través de eventos de fosforilación y/o aumente la expresión de una isoforma alternativa de GFAP, permitiendo la modificación de su membrana y generando un fenotipo específico para adaptarse en respuesta al PCH. Lo anterior se ve reflejado en la adquisición morfológica específica en el componente glial en respuesta al PCH. El análisis detallado de la electrofisiología de los astrocitos y la dinámica genética en el contexto del PCH será crucial para el entendimiento de cómo la plasticidad en el cerebelo está controlada.

Es posible que el decaimiento temporal en el control motor no está influenciado directamente por la dinámica de FI, ya que es sabido que en la prueba de rotarod, ratones nulos de GFAP no muestran diferencias significativas en el control motor (Triolo et al., 2006). Con lo anterior, sugerimos que la glía del CVM junto con la glía de la interfaz parénquima del cerebelo –LCE responden a corto y largo plazo para mantener la homeostasis del entorno, es decir, que cambios en la GFAP pueden resultar esenciales para la respuesta plástica glial ante un posible daño neuronal, dado que neuronas y astrocitos pueden actuar como unidades funcionales involucradas en la homeostasis, neurotransmisión y plasticidad.

En el estudio de González-González et al., (2017) observamos por inmunofluorescencia que en la zona del CVM existe la expresión diferencial de Vimentina, es decir, esta se expresa de manera preferencial en la monocapa de células ependimales y en

el CVM, a esto le atribuimos en parte el incremento de la proteína Nestina, que como ya se mencionó, podría co-polimerizar con Vimentina para mantener la integridad de los FI, y también podría estar involucrada en el remodelar la vasculatura el cual es secundario a insultos hipóxicos (Calderone, 2018). El factor de crecimiento vascular endotelial (VEGF) es un blanco de HIF-1, el cual presenta una regulación positiva intensa después del preconditionamiento hipóxico y que promueve remodelación vascular extensa (Rybnikova & Samoilov, 2015).

La Nestina es un FI que se expresa en células en división. Al diferenciarse, los niveles de Nestina disminuyen y esta es reemplazada por filamentos intermedios específicos del tejido. En células maduras participa en la organización estructural de la célula, la cual está regulada rigurosamente por la fosforilación, formando heterodímeros con otros filamentos intermedios como la Vimentina siendo más estables que los homodímeros de Nestina (Hendrickson et al., 2011; Michalczyk & Ziman, 2005). La expresión de Nestina se relaciona con la neuroprotección dado que esta proteína está involucrada en la estabilización de microtúbulos, los cuales podrían desestabilizarse ante daño neuronal.

La diferencia en los niveles de expresión de EGFP en los distintos lóbulos, pudiera ser el resultado de la estabilización temporal de la red de FI dada por la polimerización entre Nestina y Vimentina, el cual podría ayudar a la subsecuente formación de redes de FI que involucren la polimerización de la Vimentina, que es capaz de formar filamentos gliales junto con GFAP, manteniendo su estabilidad (Takemura et al., 2002). Sugerimos que esta cooperación, junto con la fosforilación de GFAP regula la plasticidad de los filamentos gliales y eventualmente la función de los astrocitos. La Nestina, por si misma es incapaz de polimerizar (Schiweck et al., 2018).

La proteína de astrocitos aldehído deshidrogenasa 1 miembro de la familia L1 Aldh1L1 respondió de forma similar a la GFAP. En este sentido, la Aldh1L1 es un regulador principal del metabolismo celular que contribuye a la producción de ATP usando nicotinamida adenina dinucleótido (NADH) a través de la fosforilación oxidativa y la pérdida de función o expresión de este gen se asocia con una disminución de la apoptosis, aumento de la motilidad celular y progresión del cáncer (Kang et al., 2016; Krupenko & Krupenko, 2019). Sugerimos que la regulación negativa de Aldh1L1 es una respuesta al PCH que actúa

en sinergia con otras respuestas para inducir una reducción en la actividad neuronal a través del agotamiento de ATP. Concluyendo que la disminución temporal en los niveles de proteínas de identidad de astrocitos (GFAP y Aldh1L1) forma parte de un evento reversible que parece necesario para la regulación a corto plazo de la plasticidad celular y que además refuerza el papel glial en la neuroprotección.

El factor de crecimiento transformante alfa (TGF- α) es un factor de crecimiento que se expresa en tejido neuronal, tejido vascular y en macrófagos durante la recuperación de una lesión con efectos proliferativos y anti-apoptóticos. Además, el TGF- α se regula al alza significativamente en respuesta al preconditionamiento isquémico (Herrmann et al., 2010; Yang et al., 2017). El TGF- α favorece la producción de VEGF a través de un mecanismo dependiente de la proteína cinasa activada por mitógenos p38 (MAPK) (Herrmann et al., 2010). Curiosamente, la expresión de proteínas de FIs en tumores de astrocitos se ve afectada por el aumento de TGF- α , en donde la transcripción del gen GFAP, sus niveles de ARNm y su síntesis proteica disminuye cerca de un 50%. En contraste, el TGF- α no afecta la transcripción del gen de Vimentina, pero si aumenta la transcripción de Nestina en un 50%. Por otro lado, el incremento del TGF- α está relacionado con el aumento del grado tumoral; al igual que la disminución de GFAP va acompañada por la progresión maligna de astrocitos neoplásicos.

Estos cambios en la expresión genética de proteínas de FI se relacionan con una mayor motilidad y una morfología de menor complejidad (Zhou & Skalli, 2000). Sugerimos que la modulación de la expresión de GFAP y Nestina pudiera indicar un estado en donde los astrocitos progresan hacia un estado menos diferenciado con la finalidad de adaptarse, esto es congruente con el hecho de que la re-expresión de Nestina junto con la disminución de GFAP está fuertemente relacionada con un estatus de dediferenciación y un aumento en la malignidad de glioblastomas que les confiere a las células motilidad y crecimiento celular, asociado con una mayor invasividad y metástasis (Sultana et al., 1998; Veselska et al., 2006). Esto apoya nuestra hipótesis que ante el PCH el aumento de Nestina genere copolímeros con otros FI que sirven como andamios para proteínas citoplásmicas (Mutagene et al., 2013).

Las respuestas observadas de los FI reflejan que son elementos estructurales de múltiples talentos que especifican la citoarquitectura y la citodinámica. Las propiedades

físicas únicas y las capacidades de interacción de estos distintos bloques de construcción moleculares de FI, en combinación con proteínas accesorias, podrían promover la generación de una citoarquitectura altamente dinámica e interconectada, específica del tipo de célula. La Nestina co-polimeriza con otros filamentos intermedios mediante su N-terminal (dominio esencial para el ensamble de proteínas de FI) mientras que el anticuerpo utilizado tiene afinidad por la parte C-terminal en los amino ácidos 402-604, por ello en este caso podemos observar el continuo aumento de Nestina pese a que esté polimerizando.

La expresión de la proteína Iba1 se regula al alta durante varias enfermedades cerebrales y la isquemia, implicando fenotipos microgliales de estado activo, que no necesariamente son perjudiciales. Se ha demostrado que Iba1 coopera con F- Actina y moléculas de señalización para modular el citoesqueleto de Actina durante el plegamiento de la membrana, lo que permite la formación de protrusiones. La remodelación del citoesqueleto de Actina funciona como una plataforma para atraer moléculas de señalización, enzimas y sustratos durante la transducción de señales de varios receptores de superficie, en donde Iba1 aumenta el plegamiento de la membrana plasmática y la migración celular y participa directamente en la regulación de Actina regulada por señalización de Rac (una GTPasa de la familia Rho) (Ohsawa et al., 2004). Dividimos a la población microglial bajo la premisa de que a nivel morfológico el soma mayor a 50 μm es un indicador de estado activo (Davis et al., 2017).

El PCH no indujo cambios en el número de microglía, sin embargo, observamos que existen en condiciones normales dos tipos de microglía: 1) “microglía en reposo”, de soma igual o menor a 50 μm y 2) “microglía activa”, de soma mayor a 50 μm . Espacialmente existe menor cantidad de “microglía activa” en comparación con la “microglía en reposo”, esta última se modifica a un fenotipo activado en respuesta al PCH (**Figura 20 C**). Por otra parte, observamos que la “microglía activa” no presenta cambios estadísticamente significativos en el aumento del tamaño del soma; pero, se observó consistentemente que la media del grupo “microglía grande” que ha sido sometido al PCH es siempre mayor al control (**Figura 20 D**). A nivel morfológico observamos que después del PCH la microglía no adquiere forma ameboidea (característica de la microglía activa clásica descrita), sino que se induce el aumento en el tamaño del soma microglial con la disminución y ensanchamiento de sus

procesos. En este sentido, existen reportes que mencionan el desarrollo de un fenotipo microglial con estas características morfológicas y son conocidas como células microgliales de “fenotipo preparado”, que mantienen la integridad vascular durante la hipoxia crónica leve, sugiriendo un papel protector que depende de la severidad del insulto (Halder & Milner, 2019).

Cuando la microglía no se encuentra presente se reduce la integridad vascular, se desacoplan los astrocitos de la vasculatura y se produce la pérdida de las uniones estrechas endoteliales, promoviendo fragilidad vascular (Halder & Milner, 2019). La microglía adquiere un fenotipo preparado, que se define por el aumento de marcaje de la proteína Iba1 y soma con hipertrofia. La microglía preparada responde a un reto secundario con una activación rápida, que conduce a un comportamiento depresivo (Fumagalli et al., 2015). Para mantener la homeostasis del SNC, la microglía necesita sintonizar finamente su actividad fisiológica, y está controlado por la actividad inhibitoria mediada por las neuronas que, en condiciones normales, previene la activación microglial.

La CX3CL1 (fractalquina) se expresa de forma selectiva en el cerebro por la microglía, siendo un importante regulador de su actividad. El principal efecto de la unión de CX3CR1 a su único ligando CX3CL1 liberado por neuronas es controlar la activación microglial. En condiciones fisiológicas la CX3CL1 anclada a la membrana neuronal es escindida por las metaloproteinasas de tipo desintegrina ADAM10 y ADAM17 y se libera en su forma soluble. La continua liberación de CX3CL1 mantiene a la microglía en un estado no reactivo. Después de un insulto agudo, como lo es la isquemia cerebral, las neuronas afectadas reducen de manera significativa la liberación de CX3CL1, permitiendo la activación microglial. A corto plazo la delección de CX3CR1 induce efectos neuroprotectores en distintos modelos de daño cerebral agudo. La distinción entre el rol protector o patogénico de la respuesta microglial sugieren que depende de la sincronización y/o severidad del insulto (Fumagalli et al., 2015; Halder & Milner, 2019). Sugerimos, que la microglía del lóbulo I coincide con la adquisición de un “fenotipo preparado” que es más cercano a un fenotipo protector M2.

Incorporación limitada de BrdU ante el PCH. La inducción de tolerancia está acompañada por el cambio en la expresión de genes, que está regulada por factores de

transcripción y mecanismos epigenéticos como la metilación del ADN y la modificación de histonas que modifican la estructura de la cromatina para controlar el acceso de los factores de transcripción a los loci de regulación (Dirnagl et al., 2009). El grado de hipoxia usado en este estudio no genera muerte celular, sin embargo, es posible que genere daños a una sola cadena del ADN que requerirá reparación (Xu et al., 2011). Solo después que el ADN se vuelve de una sola hebra debido a resecciones, estas pueden integrar BrdU (Mukherjee et al., 2015).

Por otra parte, se ha demostrado que el PCH puede llegar a dañar tanto el ADN nuclear como el ADN mitocondrial en células cerebrales, estimulando así la reparación del ADN (Huang et al., 2016; Sharp et al., 2004). La respuesta del daño al ADN es un aspecto fundamental de la reprogramación hipóxica que comprende un conjunto de procesos complejos que guían a la célula hacia la reparación del ADN o hacia la muerte celular (Begg & Tavassoli, 2020). El preconditionamiento regula al alza la capacidad de reparación de daños celulares. De hecho, la reparación por escisión de bases (BER) junto con la reparación por escisión de nucleótidos (NER) son las principales vías de reparación del ADN (Mandal et al., 2010), durante el preconditionamiento se ha observado que la actividad de BER aumenta y se sugiere que está asociado con la neuroprotección (Simon et al., 2019). Además, BER es una de las vías principales por la cual se remueven las bases metiladas (Chatterjee & Walker, 2017).

Aunado a lo anterior, se sabe que la incorporación de análogos de timidina como BrdU puede ocurrir durante la reparación o síntesis del ADN (Ara & De montpellier, 2013; Kuhn et al., 2016). En base a nuestras observaciones, sugerimos que la incorporación limitada de BrdU en la monocapa de células endodiales que constituyen en el techo del IV ventrículo, pudiera representar una red de señalización en respuesta a daño al ADN inducido por el PCH. Así, la capa endodial que recubre al IV ventrículo posee un grado de sensibilidad al PCH que podría relacionarse con la regulación al alza de factores que permitan mantener la homeostasis e integridad de esta interfaz (parénquima cerebeloso – LCE). Por el contrario, el revestimiento de células endodiales en el piso del IV ventrículo incorporó una mayor cantidad de BrdU, sugiriendo que esta zona es más sensible al PCH respecto al resto del revestimiento celular ventricular. En este caso, creemos que la incorporación de

BrdU refleja bajos niveles de síntesis de ADN o reparación, que no están relacionados con división celular, sino que son necesarios para mantener la estabilidad del genoma. Esta capa de células que revisten los ventrículos podría mediar la plasticidad funcional de los circuitos neuronales subyacentes, que pueden someterse a modificaciones en su complejidad dendrítica y en el número de sinapsis. O bien, vemos parte de una red que es el resultado final de un ensamble complejo de diversas subredes, que se integran de acuerdo con el tipo de estímulo, en este caso el PCH.

XII. Consideraciones finales y conclusiones

Nuestros estudios confirman que el PCH modifica la estructura y función de las neuronas y la glía del cerebelo, que producen cambios temporales en el comportamiento y fisiología glial en la interfaz del LCE-parénquima y la ZSV del lóbulo I. Sabemos que la serie de estímulos repetitivos de PCH induce neuroprotección que se asocia a plasticidad neuronal (Dirnagl et al., 2009). Nuestras observaciones morfológicas son compatibles con las de la literatura en lo que al preconditionamiento respecta, apoyando la idea de que las células gliales modulan la actividad neuronal a través de cambios plásticos en la glía, resultado de cambios locales en la sinapsis o de respuestas a cambios en posibles redes gliales. En este sentido, está claro que en el cerebelo de ratones juveniles la GB es dinámica y resalta su asociación con el control motor (Saab et al., 2012). Por lo tanto, sugerimos que los contactos entre la glía y las sinapsis son propensos a cambiar el flujo de información dentro de los circuitos neuronales, sugiriendo que las señales gliales en la neurotransmisión pueden estar sujetas a modificaciones dinámicas que anteriormente se creía aplicaban solo a neuronas (Auld & Robitaille, 2003).

Por otra parte, nuestras observaciones sugieren la existencia de mecanismos neuroprotectores endógenos a nivel sistémico, activados en respuesta a condiciones adversas. Mostramos evidencia de una respuesta fisiológica glial diversa en el cerebelo, es decir, es evidencia de especialización fisiológica en microcircuitos locales, sugiriendo que los cambios en el fenotipo disminuyen el daño de un subsecuente insulto perjudicial, con cambios “máximos” de expresión correlacionados temporalmente con la ventana de tiempo ideal terapéutica para la tolerancia inducida por el PCH.

Es conocida la especialización funcional de los microdominios del cerebelo, donde subyacen patrones morfológicos y la codificación molecular. La función del cerebelo se basa en una subdivisión modular. Dichos módulos se organizan combinando conectividad, anatomía y límites químicos. Así, la identificación del CVM y el CCSV han generado preguntas más complejas sobre la dinámica del microcircuito. La neurofisiología de la corteza del cerebelo no es uniforme. Mucha de la diversidad de la glía del SNC muestra una serie de características morfológicas y funcionales que reflejan los circuitos cerebrales en los que se encuentran, mostrando morfologías distintas en diversas regiones del SNC que se

relacionan con la función de las neuronas circundantes. Un ejemplo de diferencia morfológica es la del astrocito clásico estrellado contra la glía de Bergmann, cuyos somas se asocian con los de las neuronas de Purkinje.

Como perspectiva futura, queda por determinar la relación de la vasculatura con el CVM. Mostramos un resultado preliminar que denota cambios en la vasculatura del lóbulo I ante el reto de PCH (**Figura 22**). Estas observaciones indican que la vasculatura del lóbulo I aumenta su diámetro ante el PCH. Además, observamos la presencia de vasos adyacentes al CVM (corriendo en la misma dirección que el CVM sobre el lóbulo I) y que sugieren una relación estrecha con el mismo.

Nuestras observaciones morfométricas sugieren que la línula del cerebelo podría verse implicada en procesos somatosensoriales, que ayuden a regular los cambios en las variaciones de gases en el SNC. Recordemos las similitudes cito-arquitectónicas que se comparten en la distribución celular de la línea media en el mesencéfalo, que se ve acompañado de células serotoninérgicas, las cuales han sido propuestas como sensores de pH a variaciones de O_2 (Richerson, 2004). Al estar acompañadas por un par de estructuras vasculares de distribución superficial anteroposterior (**Figura 22**), ubicadas medio lateralmente con respecto al CVM, necesitamos elucidar si la naturaleza de estos vasos les subyace una mecánica pulsátil, lo cual nos permitiría comprender el papel que desempeña con el CVM. Conociendo si el componente vascular es arterial o venoso permitiría conocer la relación molecular con el CVM que conduce a la homeostasis en respuesta al PCH.

Además de evaluar los cambios morfológicos de los vasos sanguíneos en respuesta al PCH, es importante evaluar los niveles de HIF1- α y sus isoformas, así como las cascadas de señalización dependientes de O_2 que regulan las respuestas gliales al PCH y que activan sistemas neuroprotectores como por ejemplo las enzimas involucradas en la glicolisis y los genes que aumentan su transcripción por la activación de VEGF.

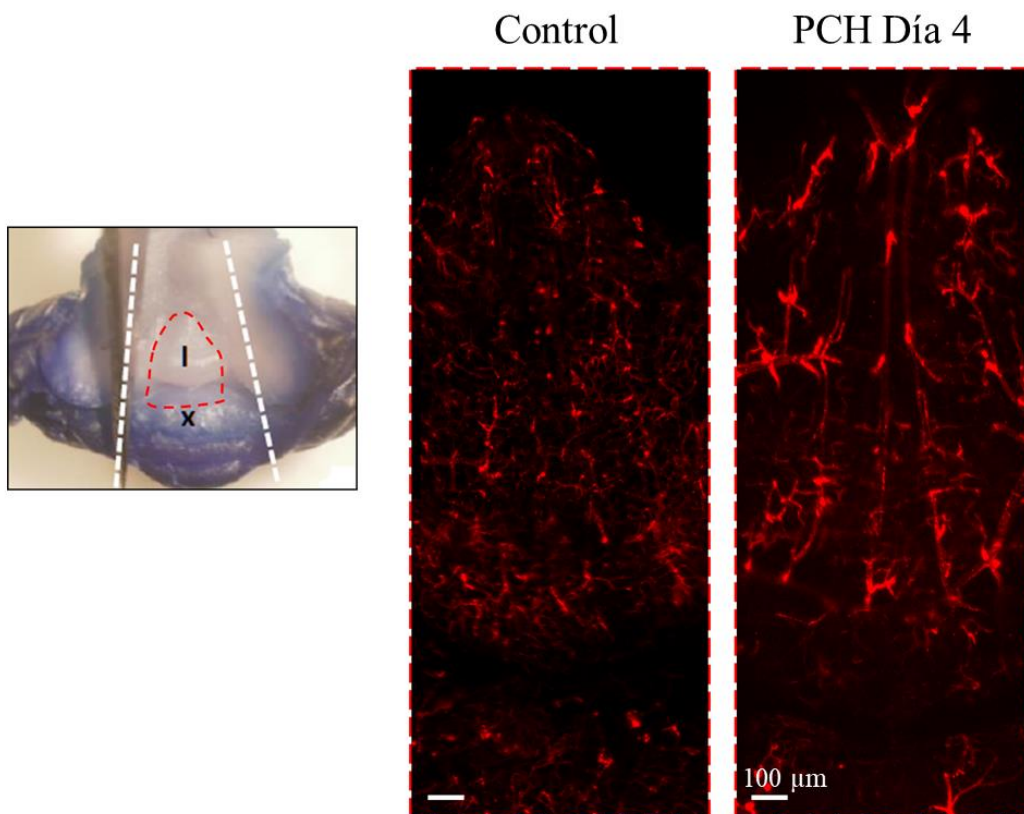


Figura 22. Vista del lóbulo I del cerebelo en preparación de montaje completo. Comparación anatómica de la vasculatura entre ratones CD1 con DiI en control versus ratón con inducción de PCH al día 4, n=2.

XIII. Referencias

- Adigun, O. O., & Al-Dhahir, M. A. (2019). *Anatomy, Head and Neck, Cerebrospinal Fluid*. In StatPearls. StatPearls Publishing. <http://www.ncbi.nlm.nih.gov/pubmed/29083815>
- Ahlfeld, J., Filser, S., Schmidt, F., Wefers, A. K., Merk, D. J., Glaß, R., Herms, J., & Schüller, U. (2017). Neurogenesis from Sox2 expressing cells in the adult cerebellar cortex. *Scientific Reports*, 7(1), 6137. <https://doi.org/10.1038/s41598-017-06150-x>
- Allen, N. J., & Lyons, D. A. (2018). Glia as architects of central nervous system formation and function. *Science*, 362(6411), 181–185. <https://doi.org/10.1126/science.aat0473>
- Angelova, P. R., Kasymov, V., Christie, I., Sheikhabaei, S., Turovsky, E., Marina, N., Korsak, A., Zwicker, J., Teschemacher, A. G., Ackland, G. L., Funk, G. D., Kasparov, S., Abramov, A. Y., & Gourine, A. V. (2015). Functional oxygen sensitivity of astrocytes. *Journal of Neuroscience*, 35(29), 10460–10473. <https://doi.org/10.1523/JNEUROSCI.0045-15.2015>
- Ara, J., & De montpellier, S. (2013). Hypoxic-preconditioning enhances the regenerative capacity of neural stem/progenitors in subventricular zone of newborn piglet brain. *Stem Cell Research*, 11(2), 669–686. <https://doi.org/10.1016/J.SCR.2013.04.007>
- Augusto-Oliveira, M., Arrifano, G. P., Lopes-Araújo, A., Santos-Sacramento, L., Takeda, P. Y., Anthony, D. C., Malva, J. O., & Crespo-Lopez, M. E. (2019). What Do Microglia Really Do in Healthy Adult Brain?. *Cells* 8(10), 1293. <https://doi.org/10.3390/cells8101293>
- Auld, D. S., & Robitaille, R. (2003). Glial cells and neurotransmission: An inclusive view of synaptic function. *Neuron* 40(2), 389–400. [https://doi.org/10.1016/S0896-6273\(03\)00607-X](https://doi.org/10.1016/S0896-6273(03)00607-X)
- Baillieul, S., Chacaroun, S., Doutreleau, S., Detante, O., Pé Pin, J. L., & Verges, S. (2017). Hypoxic conditioning and the central nervous system: A new therapeutic opportunity for brain and spinal cord injuries?. *Experimental Biology and Medicine*, 242, 1198–1206. <https://doi.org/10.1177/1535370217712691>
- Balderas, A., Guillem, A. M., Martínez-Lozada, Z., Hernández-Kelly, L. C., Aguilera, J., & Ortega, A. (2014). GLAST/EAAT1 regulation in cultured Bergmann glia cells: Role of the NO/cGMP signaling pathway. *Neurochemistry International*, 73(1), 139–145. <https://doi.org/10.1016/j.neuint.2013.10.011>
- Barmack, N. H., & Yakhnitsa, V. (2003). Cerebellar climbing fibers modulate simple spikes in Purkinje cells. *Journal of Neuroscience*, 23(21), 7904–7916. <https://doi.org/10.1523/jneurosci.23-21-07904.2003>
- Begg, K., & Tavassoli, M. (2020). Inside the hypoxic tumour: reprogramming of the DDR and radioresistance. *Cell Death Discovery*, 6, 77. <https://doi.org/10.1038/s41420-020-00311-0>

- Benitez, S. G., Castro, A. E., Patterson, S. I., Muñoz, E. M., & Seltzer, A. M. (2014). Hypoxic preconditioning differentially affects GABAergic and glutamatergic neuronal cells in the injured cerebellum of the neonatal rat. *PLoS ONE*, *9*(7). <https://doi.org/10.1371/journal.pone.0102056>
- Bennett, F. C., Bennett, M. L., Yaqoob, F., Mulinyawe, S. B., Grant, G. A., Hayden Gephart, M., Plowey, E. D., & Barres, B. A. (2018). A Combination of Ontogeny and CNS Environment Establishes Microglial Identity. *Neuron*, *98*(6), 1170-1183. <https://doi.org/10.1016/j.neuron.2018.05.014>
- Bonfanti, L. (2013). The (real) neurogenic/gliogenic potential of the postnatal and adult brain parenchyma. *International Scholarly Research Notices*, *2013*,14. <https://doi.org/10.1155/2013/354136>
- Bordey, A., & Sontheimer, H. (2003). Modulation of glutamatergic transmission by Bergmann glial cells in rat cerebellum in situ. *Journal of Neurophysiology*, *89*(2), 979–988. <https://doi.org/10.1152/jn.00904.2002>
- Bosson, A., Boisseau, S., Buisson, A., Savasta, M., & Albrieux, M. (2015). Disruption of dopaminergic transmission remodels tripartite synapse morphology and astrocytic calcium activity within substantia nigra pars reticulata. *Glia*, *63*(4), 673–683. <https://doi.org/10.1002/glia.22777>
- Bradford, M. M. (1976). A rapid and sensitive method for the quantitation of microgram quantities of protein utilizing the principle of protein-dye binding. *Analytical Biochemistry*, *72*(1–2), 248–254. [https://doi.org/10.1016/0003-2697\(76\)90527-3](https://doi.org/10.1016/0003-2697(76)90527-3)
- Brooks, S. P., & Dunnett, S. B. (2009). Tests to assess motor phenotype in mice: A user's guide. *Nature Reviews Neuroscience*, *10*(7), 519–529. <https://doi.org/10.1038/nrn2652>
- Buffo, A., Rite, I., Tripathi, P., Lepier, A., Colak, D., Horn, A.-P., Mori, T., & Gotz, M. (2008). Origin and progeny of reactive gliosis: A source of multipotent cells in the injured brain. *Proceedings of the National Academy of Sciences*. *105*(9), 3581-3586. <https://doi.org/10.1073/pnas.0709002105>
- Calderone, A. (2018). The Biological Role of Nestin(+)-Cells in Physiological and Pathological Cardiovascular Remodeling. *Frontiers in Cell and Developmental Biology*, *6*, 15. <https://doi.org/10.3389/fcell.2018.00015>
- Calton, M. A., Howard, J. R., Harper, R. M., Goldowitz, D., & Mittleman, G. (2016). The cerebellum and SIDS: Disordered breathing in a mouse model of developmental cerebellar purkinje cell loss during recovery from hypercarbia. *Frontiers in Neurology*, *7*, 78. <https://doi.org/10.3389/fneur.2016.00078>
- Cerrato, V., Parmigiani, E., Figueres-Oñate, M., Betizeau, M., Aprato, J., Nanavaty, I., Berchiolla, P., Luzzati, F., de'Sperati, C., López-Mascaraque, L., & Buffo, A. (2018). Multiple origins and modularity in the spatiotemporal emergence of cerebellar astrocyte heterogeneity. *PLoS Biology*, *16*(9).

<https://doi.org/10.1371/journal.pbio.2005513>

- Chatterjee, N., & Walker, G. C. (2017). Mechanisms of DNA damage, repair, and mutagenesis. *Environmental and Molecular Mutagenesis* 58(5), 235–263. <https://doi.org/10.1002/em.22087>
- Chrobak, A. A., & Soltys, Z. (2017). Bergmann Glia, Long-Term Depression, and Autism Spectrum Disorder. *Molecular Neurobiology* 54(2), 1156–1166. <https://doi.org/10.1007/s12035-016-9719-3>
- Chung, K., & Deisseroth, K. (2013). CLARITY for mapping the nervous system. *Nature Methods*. 10, 508–513. <https://doi.org/10.1038/nmeth.2481>
- Cipolla, M. J. (2009). Barriers of the CNS. Michael B. Morgan, M. B. & Claypool, J. (Eds.), *The Cerebral Circulation*. Morgan & Claypool.
- Clarke, B. E., Taha, D. M., Tyzack, G. E., & Patani, R. (2021). Regionally encoded functional heterogeneity of astrocytes in health and disease: A perspective. *Glia*, 69(1), 20–27. <https://doi.org/10.1002/glia.23877>
- Courjaret, R., Tröger, M., & Deitmer, J. W. (2009). Suppression of GABA input by A1 adenosine receptor activation in rat cerebellar granule cells. *Neuroscience*, 162(4), 946–958. <https://doi.org/10.1016/j.neuroscience.2009.05.045>
- Davies, K. J. A. (2016). Adaptive homeostasis. *Molecular Aspects of Medicine*, 49, 1–7. <https://doi.org/10.1016/j.mam.2016.04.007>
- Dai, Y., Bae, K., & Siemann, D. W. (2011). Impact of hypoxia on the metastatic potential of human prostate cancer Cells. *International Journal of Radiation Oncology Biology Physics*, 81(2), 521–528. <https://doi.org/10.1016/j.ijrobp.2011.04.027>
- Davies, K. J. A. (2016). Adaptive homeostasis. *Molecular Aspects of Medicine*, 49, 1–7. <https://doi.org/10.1016/j.mam.2016.04.007>
- Davis, B. M., Salinas-Navarro, M., Cordeiro, M. F., Moons, L., & De Groef, L. (2017). Characterizing microglia activation: a spatial statistics approach to maximize information extraction. *Scientific Reports*, 7(1), 1576. <https://doi.org/10.1038/s41598-017-01747-8>
- De Zeeuw, C. I., & Hoogland, T. M. (2015). Reappraisal of Bergmann glial cells as modulators of cerebellar circuit function. *Frontiers in Cellular Neuroscience*, 9, 246. <https://doi.org/10.3389/fncel.2015.00246>
- Deacon, R. M. J. (2013). Measuring Motor Coordination in Mice. *Journal of Visualized Experiments*, 75. <https://doi.org/10.3791/2609>
- Del, M. R. (1995). The Ependyma: A Protective Barrier Between Brain and Cerebrospinal Fluid. *GLIA*, 14(1), 1-13.

<https://onlinelibrary.wiley.com/doi/pdf/10.1002/glia.440140102>

- Dirnagl, U., Becker, K., & Meisel, A. (2009). Preconditioning and tolerance against cerebral ischaemia: from experimental strategies to clinical use. *The Lancet Neurology* 8(4), 398–412. [https://doi.org/10.1016/S1474-4422\(09\)70054-7](https://doi.org/10.1016/S1474-4422(09)70054-7)
- Duan, S., Shao, G., Yu, L., & Ren, C. (2015). Angiogenesis contributes to the neuroprotection induced by hyperbaric oxygen preconditioning against focal cerebral ischemia in rats. *International Journal of Neuroscience*, 125(8), 625–634. <https://doi.org/10.3109/00207454.2014.956101>
- Eccles, J. C., Ito, M., & Szentágothai, J. (2013). General Survey of the Structure. *The Cerebellum as a Neuronal Machine*. https://doi.org/10.1007/978-3-662-13147-3_2
- Emerson, M. R., Nelson, S. R., Samson, F. E., & Pazdernik, T. L. (1999). Hypoxia preconditioning attenuates brain edema associated with kainic acid-induced status epilepticus in rats. *Brain Research*, 825(1–2), 189–193. [https://doi.org/10.1016/S0006-8993\(99\)01195-6](https://doi.org/10.1016/S0006-8993(99)01195-6)
- Eroglu, C., & Barres, B. A. (2010). Regulation of synaptic connectivity by glia. *Nature*, 468(7321), 223–231. <https://doi.org/10.1038/nature09612>
- Feliciano, D. M., Bordey, A., & Bonfanti, L. (2015). Noncanonical Sites of Adult Neurogenesis in the Mammalian Brain. *Cold Spring Harbor Perspectives in Biology*, 7(10), a018846. <https://doi.org/10.1101/cshperspect.a018846>
- Filippov, V., Kronenberg, G., Pivneva, T., Reuter, K., Steiner, B., Wang, L.-P., Yamaguchi, M., Kettenmann, H., & Kempermann, G. (2003). Subpopulation of nestin-expressing progenitor cells in the adult murine hippocampus shows electrophysiological and morphological characteristics of astrocytes. *Molecular and Cellular Neuroscience*, 23(3), 373–382. [https://doi.org/10.1016/S1044-7431\(03\)00060-5](https://doi.org/10.1016/S1044-7431(03)00060-5)
- Foerde, K., & Poldrack, R. A. (2010). Procedural Learning in Humans. Squire, L. R. (Ed.), *Encyclopedia of Neuroscience* (190-211). Academic Press.
- Fore, T. R., Taylor, B. N., Brunel, N., & Court Hull, X. (2020). Acetylcholine modulates cerebellar granule cell spiking by regulating the balance of synaptic excitation and inhibition. *Journal of Neuroscience*, 40(14), 2882–2894. <https://doi.org/10.1523/JNEUROSCI.2148-19.2020>
- Fumagalli, S., Perego, C., Pischiutta, F., Zanier, E. R., & De Simoni, M. G. (2015). The ischemic environment drives microglia and macrophage function. *Frontiers in Neurology*, 6,81. <https://doi.org/10.3389/fneur.2015.00081>
- Gage, G. J., Kipke, D. R., & Shain, W. (2012). Whole Animal Perfusion Fixation for Rodents. *Journal of Visualized Experiments*, 65. <https://doi.org/10.3791/3564>

- Georg Kuhn, H. G., Eisch, A. J., Spalding, K., & Peterson, D. A. (2016). Detection and phenotypic characterization of adult neurogenesis. *Cold Spring Harbor Perspectives in Biology*, 8(3). <https://doi.org/10.1101/cshperspect.a025981>
- Gidday, J. M., Perez-Pinzon, M. A., & Zhang, J. H. (2013). *Innate tolerance in the CNS: Translational neuroprotection by pre- and post-conditioning*. (ed. 1). Springer, New York, NY.
- Golanov, E. V., Regnier-Golanov, A. S., & Britz, G. W. (2017). Integrity of cerebellar fastigial nucleus intrinsic neurons is critical for the global ischemic preconditioning. *Brain Sciences*, 7(10), 121. <https://doi.org/10.3390/brainsci7100121>
- Goldman, S. (2003). Glia as neural progenitor cells. *Trends in Neurosciences*, 26(11), 590–596. <https://doi.org/10.1016/j.tins.2003.09.011>
- González-González, M.A., Gómez-González, G. B., Becerra-González, M., & Martínez-Torres, A. (2017). Identification of novel cellular clusters define a specialized area in the cerebellar periventricular zone. *Scientific Reports*, 7. <https://doi.org/10.1038/srep40768>
- González-González, M. A., Ostos-Valverde, A., Becerra-Hernández, A., Sánchez-Castillo, H., & Martínez-Torres, A. (2015). The effect of carmustine on Bergmann cells of the cerebellum. *Neuroscience Letters*, 595, 18–24. <https://doi.org/10.1016/J.NEULET.2015.03.068>
- Gossman, W., Alghoula, F., & Berim, I. (2020, nov). *Anoxia (Hypoxic Hypoxia)*. StatPearls Publishing. <http://www.ncbi.nlm.nih.gov/pubmed/29493941>
- Guo, M., Ma, X., Feng, Y., Han, S., Dong, Q., Cui, M., & Zhao, Y. (2019). In chronic hypoxia, glucose availability and hypoxic severity dictate the balance between HIF-1 and HIF-2 in astrocytes. *FASEB Journal*, 33(10), 11123–11136. <https://doi.org/10.1096/fj.201900402RR>
- Halder, S. K., Kant, R., & Milner, R. (2018). Hypoxic pre-conditioning suppresses experimental autoimmune encephalomyelitis by modifying multiple properties of blood vessels. *Acta Neuropathologica Communications*, 6(1), 86. <https://doi.org/10.1186/s40478-018-0590-5>
- Halder, S. K., & Milner, R. (2019). A critical role for microglia in maintaining vascular integrity in the hypoxic spinal cord. *Proceedings of the National Academy of Sciences of the United States of America*, 116(51), 26029–26037. [10.1073/pnas.1912178116](https://doi.org/10.1073/pnas.1912178116)
- Hanke, S., & Reichenbach, A. (1987). Quantitative-morphometric aspects of bergmann glial (Golgi epithelial) cell development in rats - A golgi study. *Anatomy and Embryology*, 177(2), 183–188. <https://doi.org/10.1007/BF00572543>
- Hashimoto, T., & Shibasaki, F. (2015). Hypoxia-Inducible Factor as an Angiogenic Master Switch. *Frontiers in Pediatrics*, 3, 3. <https://doi.org/10.3389/fped.2015.00033>

- Hendrickson, M. L., Rao, A. J., Demerdash, O. N. A., & Kalil, R. E. (2011). Expression of Nestin by Neural Cells in the Adult Rat and Human Brain. *PLoS ONE*, 6(4), 18535. <https://doi.org/10.1371/journal.pone.0018535>
- Herrmann, J. L., Wang, Y., Abarbanell, A. M., Weil, B. R., Tan, J., & Meldrum, D. R. (2010). PRECONDITIONING MESENCHYMAL STEM CELLS WITH TRANSFORMING GROWTH FACTOR-ALPHA IMPROVES MESENCHYMAL STEM CELL-MEDIATED CARDIOPROTECTION. *Shock*, 33(1), 24–30. <https://doi.org/10.1097/SHK.0b013e3181b7d137>
- Hertzog, R. G., Bicheru, N. S., Popescu, D. M., Călborean, O., & Catrina, A.-M. (2020). Hypoxic preconditioning – a non-pharmacological approach in COVID-19 prevention. *International Journal of Infectious Diseases*, 103, 415–419. <https://doi.org/10.1016/j.ijid.2020.11.181>
- Hillen, A. E. J., Burbach, J. P. H., & Hol, E. M. (2018). Cell adhesion and matricellular support by astrocytes of the tripartite synapse. *Progress in Neurobiology*, 165(167), 66–86. <https://doi.org/10.1016/j.pneurobio.2018.02.002>
- Hirayama, Y., Ikeda-Matsuo, Y., Notomi, S., Enaida, H., Kinouchi, H., & Koizumi, S. (2015). Astrocyte-mediated ischemic tolerance. *The Journal of Neuroscience : The Official Journal of the Society for Neuroscience*, 35(9), 3794–3805. <https://doi.org/10.1523/JNEUROSCI.4218-14.2015>
- Huang, L., Wan, Y., Dang, Z., Yang, P., Yang, Q., & Wu, S. (2020). Hypoxic preconditioning ameliorated neuronal injury after middle cerebral artery occlusion by promoting neurogenesis. *Brain and Behavior*, 10(10). <https://doi.org/10.1002/brb3.1804>
- Huang, L., Wu, S., Li, H., Dang, Z., & Wu, Y. (2019). Hypoxic preconditioning relieved ischemic cerebral injury by promoting immunomodulation and microglia polarization after middle cerebral artery occlusion in rats. *Brain Research*, 1723(146388). <https://doi.org/10.1016/j.brainres.2019.146388>
- Huang, Y.-C., Parolini, O., Deng, L., & Yu, B.-S. (2016). Should hypoxia preconditioning become the standardized procedure for bone marrow MSCs preparation for clinical use? *STEM CELLS*, 34(7), 1992–1993. <https://doi.org/10.1002/stem.2389>
- Jayaraj, R. L., Azimullah, S., Beiram, R., Jalal, F. Y., & Rosenberg, G. A. (2019). Neuroinflammation: Friend and foe for ischemic stroke. *Journal of Neuroinflammation*, 16(1). <https://doi.org/10.1186/s12974-019-1516-2>
- Jiménez, A. J., Domínguez-Pinos, M. D., Guerra, M. M., Fernández-Llebrez, P., & Pérez-Fígares, J. M. (2014). Structure and function of the ependymal barrier and diseases associated with ependyma disruption. *Tissue Barriers* 2(3), 1–14. <https://doi.org/10.4161/tisb.28426>
- Kandel, E. R., Schwartz, J. H., & Jessell, T. M. (2000). *Principles of Neural Science* (4th

ed.)fourth addition. *McGraw-Hill Companies*.

- Kang, J. H., Lee, S. H., Lee, J. S., Nam, B., Seong, T. W., Son, J., Jang, H., Hong, K. M., Lee, C., & Kim, S. Y. (2016). Aldehyde dehydrogenase inhibition combined with phenformin treatment reversed NSCLC through ATP depletion. *Oncotarget*, 7(31), 49397–49410. <https://doi.org/10.18632/oncotarget.10354>
- Kanski, R., Sneeboer, M. A. M., van Bodegraven, E. J., Sluijs, J. A., Kropff, W., Vermunt, M. W., Creighton, M. P., de Filippis, L., Vescovi, A., Aronica, E., van Tijn, P., van Strien, M. E., & Hol, E. M. (2014). Histone acetylation in astrocytes suppresses GFAP and stimulates a reorganization of the intermediate filament network. *Journal of Cell Science*, 127(20), 4368–4380. <https://doi.org/10.1242/jcs.145912>
- Kawabori, M., & Yenari, M. (2015). Inflammatory Responses in Brain Ischemia. *Current Medicinal Chemistry*, 22(10), 1258–1277. <https://doi.org/10.2174/0929867322666150209154036>
- Kettenmann, H., & Verkhratsky, A. (2011). Neuroglia, der lebende Nerven Kitt. *Fortschritte Der Neurologie · Psychiatrie*, 79(10), 588–597. <https://doi.org/10.1055/s-0031-1281704>
- Kiyoshi, C., & Zhou, M. (2019). Astrocyte syncytium: a functional reticular system in the brain. *Neural Regeneration Research*, 14(4), 595. <https://doi.org/10.4103/1673-5374.247462>
- Köhler, S., Winkler, U., & Hirrlinger, J. (2019). Heterogeneity of Astrocytes in Grey and White Matter. *Neurochemical Research*, 46, 3–14. <https://doi.org/10.1007/s11064-019-02926-x>
- Kosako, H., Amano, M., Yanagida, M., Tanabe, K., Nishi, Y., Kaibuchi, K., & Inagaki, M. (1997). Phosphorylation of glial fibrillary, acidic protein at the same sites by cleavage furrow kinase and Rho-associated kinase. *Journal of Biological Chemistry*, 272(16), 10333–10336. <https://doi.org/10.1074/jbc.272.16.10333>
- Krock, B. L., Skuli, N., & Simon, M. C. (2011). Hypoxia-Induced Angiogenesis: Good and Evil. *Genes and Cancer*, 2(12), 1117–1133. <https://doi.org/10.1177/1947601911423654>
- Krupenko, S. A., & Krupenko, N. I. (2019). Loss of ALDH1L1 folate enzyme confers a selective metabolic advantage for tumor progression. *Chemico-Biological Interactions* 302, 149–155. <https://doi.org/10.1016/j.cbi.2019.02.013>
- Lang, H., Xing, Y., Brown, L. N., Samuvel, D. J., Panganiban, C. H., Havens, L. T., Balasubramanian, S., Wegner, M., Krug, E. L., & Barth, J. L. (2015). Neural stem/progenitor cell properties of glial cells in the adult mouse auditory nerve. *Scientific Reports*, 5. <https://doi.org/10.1038/srep13383>
- Larsell, O. & Jansen, J. (1972). The comparative anatomy and histology of the cerebellum.

The human cerebellum, cerebellar connections, and cerebellar cortex (1st ed.).
University of Minnesota Press, Minneapolis.

- Lemke, G. (2009). *Developmental neurobiology* (1st ed.). Academic Press/Elsevier.
- Leto, K., Arancillo, M., Becker, E. B. E., Buffo, A., Chiang, C., Ding, B., Dobyns, W. B., Dusart, I., Haldipur, P., Hatten, M. E., Hoshino, M., Joyner, A. L., Kano, M., Kilpatrick, D. L., Koibuchi, N., Marino, S., Martinez, S., Millen, K. J., Millner, T. O., ... Hawkes, R. (2016). Consensus Paper: Cerebellar Development. *Cerebellum*, *15*(6), 789–828. <https://doi.org/10.1007/s12311-015-0724-2>
- Li, S., Hafeez, A., Noorulla, F., Geng, X., Shao, G., Ren, C., Lu, G., Zhao, H., Ding, Y., & Ji, X. (2017). Preconditioning in neuroprotection: From hypoxia to ischemia. *Progress in Neurobiology*, *157*, 79-91. <https://doi.org/10.1016/j.pneurobio.2017.01.001>
- Lin, J. H. C., Lou, N., Kang, N., Takano, T., Hu, F., Han, X., Xu, Q., Lovatt, D., Torres, A., Willecke, K., Yang, J., Kang, J., & Nedergaard, M. (2008). A central role of connexin 43 in hypoxic preconditioning. *Journal of Neuroscience*, *28*(3), 681–695. <https://doi.org/10.1523/JNEUROSCI.3827-07.2008>
- Liu, C., Peng, Z., Zhang, N., Yu, L., Han, S., Li, D., & Li, J. (2012). Identification of differentially expressed microRNAs and their PKC-isoform specific gene network prediction during hypoxic pre-conditioning and focal cerebral ischemia of mice. *Journal of Neurochemistry*, *120*(5), 830–841. <https://doi.org/10.1111/j.1471-4159.2011.07624.x>
- López-Aguilera, F., Plateo-Pignatari, M. G., Biaggio, V., Ayala, C., & Seltzer, A. M. (2012). Hypoxic preconditioning induces an AT2-R/VEGFR-2(Flk-1) interaction in the neonatal brain microvasculature for neuroprotection. *Neuroscience*, *216*, 1–9. <https://doi.org/10.1016/j.neuroscience.2012.04.070>
- Ludwig, P. E., & M Das, J. (2019). *Histology, Glial Cells*. StatPearls. <http://www.ncbi.nlm.nih.gov/pubmed/28722974>
- Magnusson, J. P., Göritz, C., Tatarishvili, J., Dias, D. O., Smith, E. M. K., Lindvall, O., Kokaia, Z., & Frisén, J. (2014). A latent neurogenic program in astrocytes regulated by Notch signaling in the mouse. *Science*, *346*(6206), 237–241. <https://doi.org/10.1126/science.346.6206.237>
- Mandal, R. K., Mittal, T., Kapoor, R., & Mittal, R. D. (2010). NER and BER repair gene polymorphisms in a healthy north Indian cohort and comparison with different ethnic groups worldwide. *Asian Pacific Journal of Cancer Prevention : APJCP*, *11*(6), 1601–1604. <http://www.ncbi.nlm.nih.gov/pubmed/21338203>
- Mandalos, N. P., Karamelas, L., Saridaki, M., McKay, R. D. G., Cohen, M. L., & Remboutsika, E. (2018). A Role for Sox2 in the Adult Cerebellum. *Journal of Stem Cell Research & Therapy*, *8*(7). <https://doi.org/10.4172/2157-7633.1000433>

- Mann, A., & Chesselet, M. F. (2014). Techniques for Motor Assessment in Rodents. Mark S. LeDoux, M. S. (ed.), *Movement Disorders: Genetics and Models: Second Edition* (pp.139-157). Academic Press.
- Manninen, P. H., & Unger, Z. M. (2016). Hypoxia. Prabhakar, H. (ed.), *Complications in Neuroanesthesia* (pp. 169–180). Elsevier Inc.
- Matejuk, A., & Ransohoff, R. M. (2020). Crosstalk Between Astrocytes and Microglia: An Overview. *Frontiers in Immunology*, *11*, 1416.
<https://doi.org/10.3389/fimmu.2020.01416>
- Matias, I., Morgado, J., & Gomes, F. C. A. (2019). Astrocyte Heterogeneity: Impact to Brain Aging and Disease. *Frontiers in Aging Neuroscience*, *11*, 59.
<https://doi.org/10.3389/fnagi.2019.00059>
- McDonough, A., Noor, S., Lee, R. V., Dodge, R., Strosnider, J. S., Shen, J., Davidson, S., Möller, T., Garden, G. A., & Weinstein, J. R. (2020). Ischemic preconditioning induces cortical microglial proliferation and a transcriptomic program of robust cell cycle activation. *Glia*, *68*(1), 76–94. <https://doi.org/10.1002/glia.23701>
- McDonough, A., & Weinstein, J. R. (2016). Neuroimmune Response in Ischemic Preconditioning. *Neurotherapeutics*, *13*(4), 748–761. <https://doi.org/10.1007/s13311-016-0465-z>
- Michalczyk, K., & Ziman, M. (2005). Nestin structure and predicted function in cellular cytoskeletal organisation. *Histology and Histopathology*, *20*(2), 665–671.
<https://doi.org/10.14670/HH-20.665>
- Miller, J., Hdeib, A., & Cohen, A. (2012). Management of Tumors of the Fourth Ventricle. Quiñones-Hinojosa, A. (ed.), *Schmidek and Sweet Operative Neurosurgical Techniques: Indications, Methods, and Results: Sixth Edition* (pp. 367–397). Elsevier Inc.
- Moeton, M., Stassen, O. M. J. A., Sluijs, J. A., van der Meer, V. W. N., Kluivers, L. J., van Hoorn, H., Schmidt, T., Reits, E. A. J., van Strien, M. E., & Hol, E. M. (2016). GFAP isoforms control intermediate filament network dynamics, cell morphology, and focal adhesions. *Cellular and Molecular Life Sciences*, *73*(21), 4101–4120.
<https://doi.org/10.1007/s00018-016-2239-5>
- Mukandala, G., Tynan, R., Lanigan, S., & O'Connor, J. J. (2016). The Effects of Hypoxia and Inflammation on Synaptic Signaling in the CNS. *Brain Sciences*, *6*(1).
<https://doi.org/10.3390/brainsci6010006>
- Mukherjee, B., Tomimatsu, N., & Burma, S. (2015). Immunofluorescence-based methods to monitor DNA end resection. *Methods in Molecular Biology*, *1292*, 67–75.
https://doi.org/10.1007/978-1-4939-2522-3_5
- Mutagene, J. C., Matsuda, Y., Yoshimura, H., Naito, Z., & Ishiwata, T. (2013). The Roles

and Molecular Mechanisms of Nestin Expression in Cancer with a Focus on Pancreatic Cancer. *J Carcinogene Mutagene*, 9. <https://doi.org/10.4172/2157-2518.S9-002>

- Nakayama, K., & Kataoka, N. (2019). Regulation of gene expression under hypoxic conditions. *International Journal of Molecular Sciences*, 20(13). <https://doi.org/10.3390/ijms20133278>
- Nolte, C., Matyash, M., Pivneva, T., Schipke, C. G., Ohlemeyer, C., Hanisch, U. K., Kirchhoff, F., & Kettenmann, H. (2001). GFAP promoter-controlled EGFP-expressing transgenic mice: A tool to visualize astrocytes and astrogliosis in living brain tissue. *GLIA*, 33(1), 72–86. [https://doi.org/10.1002/1098-1136\(20010101\)33:1<72::AID-GLIA1007>3.0.CO;2-A](https://doi.org/10.1002/1098-1136(20010101)33:1<72::AID-GLIA1007>3.0.CO;2-A)
- Oberheim, N. A., Goldman, S. A., & Nedergaard, M. (2012). Heterogeneity of astrocytic form and function. *Methods in Molecular Biology*, 814, 23–45. https://doi.org/10.1007/978-1-61779-452-0_3
- Ohno, Y., Kinboshi, M., & Shimizu, S. (2018). Inwardly rectifying potassium channel kir4.1 as a novel modulator of BDNF expression in astrocytes. *International Journal of Molecular Sciences*, 9(11), 3313. <https://doi.org/10.3390/ijms19113313>
- Ohsawa, K., Imai, Y., Sasaki, Y., & Kohsaka, S. (2004). Microglia/macrophage-specific protein Iba1 binds to fimbrin and enhances its actin-bundling activity. *Journal of Neurochemistry*, 88(4), 844–856. <https://doi.org/10.1046/j.1471-4159.2003.02213.x>
- Olarte, O. E., Andilla, J., Gualda, E. J., & Loza-Alvarez, P. (2018). Light-sheet microscopy: a tutorial. *Advances in Optics and Photonics*, 10(1), 111. <https://doi.org/10.1364/AOP.10.000111>
- Parmigiani, E., Leto, K., Rolando, C., Figueres-Oñate, M., López-Mascaraque, L., Buffo, A., & Rossi, F. (2015). Heterogeneity and Bipotency of Astroglial-Like Cerebellar Progenitors along the Interneuron and Glial Lineages. *The Journal of Neuroscience : The Official Journal of the Society for Neuroscience*, 35(19), 7388–7402. <https://doi.org/10.1523/JNEUROSCI.5255-14.2015>
- Parsons, L. M., Egan, G., Liotti, M., Brannan, S., Denton, D., Shade, R., Robillard, R., Madden, L., Abplanalp, B., & Fox, P. T. (2001). Neuroimaging evidence implicating cerebellum in the experience of hypercapnia and hunger for air. *Proceedings of the National Academy of Sciences*, 98(4), 2041-2046. <https://doi.org/10.1073/pnas.98.4.2041>
- Paxinos, G., & Franklin, K. B. J. (2001) *The Mouse Brain in Stereotaxic Coordinates* (2nd ed.). Academic Press.
- Pekny, M., & Pekna, M. (2014). Astrocyte reactivity and reactive astrogliosis: Costs and benefits. *Physiological Reviews*, 94(4), 1077–1098. <https://doi.org/10.1152/physrev.00041.2013>

- Pestana, F., Edwards-Faret, G., Belgard, T. G., Martirosyan, A., & Holt, M. G. (2020). No longer underappreciated: The emerging concept of astrocyte heterogeneity in neuroscience. *Brain Sciences*, *10*(3). <https://doi.org/10.3390/brainsci10030168>
- Pignataro, G., Brancaccio, P., Laudati, G., Valsecchi, V., Anzilotti, S., Casamassa, A., Cuomo, O., & Vinciguerra, A. (2020). Sodium/calcium exchanger as main effector of endogenous neuroprotection elicited by ischemic tolerance. *Cell Calcium*, *87*, 102183. <https://doi.org/10.1016/j.ceca.2020.102183>
- Ponti, G., Peretto, P., & Bonfanti, L. (2008). Genesis of neuronal and glial progenitors in the cerebellar cortex of peripuberal and adult rabbits. *PLoS One*, *3*(6), e2366. <https://doi.org/10.1371/journal.pone.0002366>
- Powell, K., Mathy, A., Duguid, I., & Häusser, M. (2015). Synaptic representation of locomotion in single cerebellar granule cells. *eLife*, *4*, e07290. <https://doi.org/10.7554/eLife.07290>
- Preibisch, S., Saalfeld, S., & Tomancak, P. (2009). Globally optimal stitching of tiled 3D microscopic image acquisitions. *Bioinformatics*, *25*(11), 1463–1465. <https://doi.org/10.1093/bioinformatics/btp184>
- Preibisch, S., Saalfeld, S., & Tomancak, P. (2009). Globally optimal stitching of tiled 3D microscopic image acquisitions. *Bioinformatics*, *25*(11), 1463–1465. <https://doi.org/10.1093/bioinformatics/btp184>
- Reeber, S. L., Arancillo, M., & Sillitoe, R. V. (2018). Bergmann Glia are Patterned into Topographic Molecular Zones in the Developing and Adult Mouse Cerebellum. *Cerebellum*, *17*(4), 392–403. <https://doi.org/10.1007/s12311-014-0571-6>
- Ren, C., Li, S., Rajah, G., Shao, G., Lu, G., Han, R., Huang, Q., Li, H., Ding, Y., Jin, K., & Ji, X. (2018). Hypoxia, hibernation and Neuroprotection: An Experimental Study in Mice. *Aging and Disease*, *9*(4), 761–768. <https://doi.org/10.14336/AD.2018.0702>
- Reyes-Haro, D., González-González, M. A., Pétriz, A., Rosas-Arellano, A., Kettenmann, H., Miledi, R., & Martínez-Torres, A. (2013). γ -Aminobutyric acid- ρ expression in ependymal glial cells of the mouse cerebellum. *Journal of Neuroscience Research*, *91*(4), 527–534. <https://doi.org/10.1002/jnr.23183>
- Richerson, G. B. (2004). Serotonergic neurons as carbon dioxide sensors that maintain pH homeostasis. *Nature Reviews Neuroscience* *5*(6), 449–461. <https://doi.org/10.1038/nrn1409>
- Rosas-Arellano, A., Ochoa-de la Paz, L. D., Miledi, R., & Martínez-Torres, A. (2007). Brain distribution and molecular cloning of the bovine GABA ρ 1 receptor. *Neuroscience Research*, *57*(3), 347–353. <https://doi.org/10.1016/j.neures.2006.11.003>
- Rybnikova, E., & Samoilov, M. (2015). Current insights into the molecular mechanisms of hypoxic pre- and postconditioning using hypobaric hypoxia. *Frontiers in*

Neuroscience, 9, 388. <https://doi.org/10.3389/fnins.2015.00388>

- Rybnikova, E., & Samoilov, M. (2015). Epigenetic mechanisms of hypoxic preconditioning. *SpringerPlus*, 4(1), 1–32. <https://doi.org/10.1186/2193-1801-4-S1-L39>
- Saab, A. S., Neumeyer, A., Jahn, H. M., Cupido, A., Šimek, A. A. M., Boele, H. J., Scheller, A., Le Meur, K., Götz, M., Monyer, H., Sprengel, R., Rubio, M. E., Deitmer, J. W., De Zeeuw, C. I., & Kirchhoff, F. (2012). Bergmann glial AMPA receptors are required for fine motor coordination. *Science*, 337(6095), 749–753. <https://doi.org/10.1126/science.1221140>
- Sakakima, H. (2019). Endogenous neuroprotective potential due to preconditioning exercise in stroke. *Physical Therapy Research*, 22(2), 45–52. <https://doi.org/10.1298/ptr.r0006>
- Sakamoto, K., Nakahara, T., & Ishii, K. (2011). Rho-Rho kinase pathway is involved in the protective effect of early ischemic preconditioning in the rat heart. *Biological and Pharmaceutical Bulletin*, 34(1), 156–159. <https://doi.org/10.1248/bpb.34.156>
- Santilli, G., Lamorte, G., Carlessi, L., Ferrari, D., Rota Nodari, L., Binda, E., Delia, D., Vescovi, A. L., & De Filippis, L. (2010). Mild Hypoxia Enhances Proliferation and Multipotency of Human Neural Stem Cells. *PLoS ONE*, 5(1), e8575. <https://doi.org/10.1371/journal.pone.0008575>
- Saxena, K., & Jolly, M. K. (2019). Acute vs. Chronic vs. cyclic hypoxia: Their differential dynamics, molecular mechanisms, and effects on tumor progression. *Biomolecules* 9(8). <https://doi.org/10.3390/biom9080339>
- Schiweck, J., Eickholt, B. J., & Murk, K. (2018). Important shapeshifter: Mechanisms allowing astrocytes to respond to the changing nervous system during development, injury and disease. *Frontiers in Cellular Neuroscience*, 12, 261. <https://doi.org/10.3389/fncel.2018.00261>
- Sendoel, A., & Hengartner, M. O. (2014). Apoptotic Cell Death Under Hypoxia. *Physiology*, 29(3), 168–176. <https://doi.org/10.1152/physiol.00016.2013>
- Sergent-Tanguy, S., Michel, D. C., Neveu, I., & Naveilhan, P. (2006). Long-lasting coexpression of nestin and glial fibrillary acidic protein in primary cultures of astroglial cells with a major participation of nestin+/GFAP– cells in cell proliferation. *Journal of Neuroscience Research*, 83(8), 1515–1524. <https://doi.org/10.1002/jnr.20846>
- Sharp, F. R., Ran, R., Lu, A., Tang, Y., Strauss, K. I., Glass, T., Ardizzone, T., & Bernaudin, M. (2004). Hypoxic Preconditioning Protects against Ischemic Brain Injury. *NeuroRx*, 1(1), 26–35. <https://doi.org/10.1602/neurorx.1.1.26>
- Shiga, T., Ichikawa, M., & Hirata, Y. (1983). A Golgi study of Bergmann glial cells in

- developing rat cerebellum. *Anatomy and Embryology*, 167(2), 191–201. <https://doi.org/10.1007/BF00298510>
- Sidoryk-Wegrzynowicz, M., & Strużyńska, L. (2021). Dysfunctional glia: contributors to neurodegenerative disorders. *Neural Regeneration Research*, 16(2), 218. <https://doi.org/10.4103/1673-5374.290877>
- Simon, R., Meller, R., Yang, T., Pearson, A., & Wilson, G. (2019). Enhancing Base Excision Repair of Mitochondrial DNA to Reduce Ischemic Injury Following Reperfusion. *Translational Stroke Research*, 10(6), 664–671. <https://doi.org/10.1007/s12975-018-0680-5>
- Snell, R. S. (2016). Clinical neuroanatomy. Eli M. Mizrahi, E. M, (Eds.), *Neurology Secrets: Sixth Edition* (pp. 11-41). Elsevier.
- Spampinato, S. F., Copani, A., Nicoletti, F., Sortino, M. A., & Caraci, F. (2018). Metabotropic glutamate receptors in glial cells: A new potential target for neuroprotection?. *Frontiers in Molecular Neuroscience*, 11, 414. <https://doi.org/10.3389/fnmol.2018.00414>
- Span, P. N., & Bussink, J. (2015). Biology of hypoxia. *Seminars in Nuclear Medicine*, 45(2), 101–109. <https://doi.org/10.1053/j.semnuclmed.2014.10.002>
- Sprick, J. D., Mallet, R. T., Przyklenk, K., & Rickards, C. A. (2019). Ischaemic and hypoxic conditioning: potential for protection of vital organs. *Experimental Physiology*, 104(3), 278–294. <https://doi.org/10.1113/EP087122>
- Stefaniuk, M., Gualda, E. J., Pawlowska, M., Legutko, D., Matryba, P., Koza, P., Konopka, W., Owczarek, D., Wawrzyniak, M., Loza-Alvarez, P., & Kaczmarek, L. (2016). Light-sheet microscopy imaging of a whole cleared rat brain with Thy1-GFP transgene. *Nature Publishing Group*, 6, 28209. <https://doi.org/10.1038/srep28209>
- Stenzel-Poore, M. P., Stevens, S. L., King, J. S., & Simon, R. P. (2007). Preconditioning reprograms the response to ischemic injury and primes the emergence of unique endogenous neuroprotective phenotypes: A speculative synthesis. *Stroke*, 38(2), 680–685. <https://doi.org/10.1161/01.STR.0000251444.56487.4c>
- Sultana, S., Zhou, R., Sadagopan, M. S., & Skalli, O. (1998). Effects of growth factors and basement membrane proteins on the phenotype of U-373 MG glioblastoma cells as determined by the expression of intermediate filament proteins. *American Journal of Pathology*, 153(4), 1157–1168. [https://doi.org/10.1016/S0002-9440\(10\)65660-X](https://doi.org/10.1016/S0002-9440(10)65660-X)
- Takemura, M., Gomi, H., Colucci-Guyon, E., & Itohara, S. (2002). Protective role of phosphorylation in turnover of glial fibrillary acidic protein in mice. *Journal of Neuroscience*, 22(16), 6972–6979. <https://doi.org/10.1523/jneurosci.22-16-06972.2002>
- Telano, L. N., & Baker, S. (2018, jul). Physiology, Cerebral Spinal Fluid (CSF).

<http://www.ncbi.nlm.nih.gov/pubmed/30085549>

- Triolo, D., Dina, G., Lorenzetti, I., Malaguti, M. C., Morana, P., Del Carro, U., Comi, G., Messing, A., Quattrini, A., & Previtali, S. C. (2006). Loss of glial fibrillary acidic protein (GFAP) impairs Schwann cell proliferation and delays nerve regeneration after damage. *Journal of Cell Science*, *119*(19), 3981–3993. <https://doi.org/10.1242/jcs.03168>
- Uchiyama, T., Engelman, R. M., Maulik, N., & Das, D. K. (2004). Role of Akt signaling in mitochondrial survival pathway triggered by hypoxic preconditioning. *Circulation*, *109*(24), 3042–3049. <https://doi.org/10.1161/01.CIR.0000130647.29030.90>
- Vacas, S., Kurien, P., & Maze, M. (2013). Sleep and Anesthesia - Common mechanisms of action. *Sleep Medicine Clinics*, *8*(1), 1–9. <https://doi.org/10.1016/j.jsmc.2012.11.009>
- Venturini, A., Passalacqua, M., Pelassa, S., Pastorino, F., Tedesco, M., Cortese, K., Gagliani, M. C., Leo, G., Maura, G., Guidolin, D., Agnati, L. F., Marcoli, M., & Cervetto, C. (2019). Exosomes From Astrocyte Processes: Signaling to Neurons. *Frontiers in Pharmacology*, *10*, 1. <https://doi.org/10.3389/fphar.2019.01452>
- Veselska, R., Kuglik, P., Cejpek, P., Svachova, H., Neradil, J., Loja, T., & Relichova, J. (2006). Nestin expression in the cell lines derived from glioblastoma multiforme. *BMC Cancer*, *6*, 32. <https://doi.org/10.1186/1471-2407-6-32>
- Voogd, J. (2003). Cerebellum and Precerebellar Nuclei. Paxinos, G., Jürgen, K. (Eds.), *The Human Nervous System: Second Edition* (pp. 321–392). Elsevier Inc.
- Voogd, J. (2014). What we do not know about cerebellar systems neuroscience. *Frontiers in Systems Neuroscience*, *8*, 227. <https://doi.org/10.3389/fnsys.2014.00227>
- Voogd, J., & Ruigrok, T. J. H. (2012). Cerebellum and Precerebellar Nuclei. Paxinos, G., Jürgen, K. (Eds.), *The Human Nervous System* (pp. 471–545). Academic Press.
- Wei, L. C., Shi, M., Chen, L. W., Cao, R., Zhang, P., & Chan, Y. S. (2002). Nestin-containing cells express glial fibrillary acidic protein in the proliferative regions of central nervous system of postnatal developing and adult mice. *Developmental Brain Research*, *139*(1), 9–17. [https://doi.org/10.1016/S0165-3806\(02\)00509-6](https://doi.org/10.1016/S0165-3806(02)00509-6)
- Weidemann, A., Kerdiles, Y. M., Knaup, K. X., Rafie, C. A., Boutin, A. T., Stockmann, C., Takeda, N., Scadeng, M., Shih, A. Y., Haase, V. H., Simon, M. C., Kleinfeld, D., & Johnson, R. S. (2009). The glial cell response is an essential component of hypoxia-induced erythropoiesis in mice. *Journal of Clinical Investigation*, *119*(11), 3373–3383. <https://doi.org/10.1172/JCI39378>
- Weyer, A., & Schilling, K. (2003). Developmental and cell type-specific expression of the neuronal marker NeuN in the murine cerebellum. *Journal of Neuroscience Research*, *73*(3), 400–409. <https://doi.org/10.1002/jnr.10655>

- Woo, J., Min, J. O., Kang, D. S., Kim, Y. S., Jung, G. H., Park, H. J., Kim, S., An, H., Known, J., Kim, J., Shim, I., Kim, H. G., Justin Lee, C., & Yoon, B. E. (2018). Control of motor coordination by astrocytic tonic GABA release through modulation of excitation/inhibition balance in cerebellum. *Proceedings of the National Academy of Sciences of the United States of America*, *115*(19), 5004–5009. <https://doi.org/10.1073/pnas.1721187115>
- Wu, L.-Y., He, Y.-L., & Zhu, L.-L. (2018). Possible Role of PHD Inhibitors as Hypoxia-Mimicking Agents in the Maintenance of Neural Stem Cells' Self-Renewal Properties. *Frontiers in Cell and Developmental Biology*, *6*, 11. <https://doi.org/10.3389/fcell.2018.00169>
- Xu, F., & Frazier, D. T. (2002). Role of the cerebellar deep nuclei in respiratory modulation. *The Cerebellum*, *1*(35). <https://doi.org/10.1080/147342202753203078>
- Xu, H., Lu, A., & Sharp, F. R. (2011). Regional genome transcriptional response of adult mouse brain to hypoxia. *BMC Genomics*, *12*, 499. <https://doi.org/10.1186/1471-2164-12-499>
- Xu, S., Lu, J., Shao, A., Zhang, J. H., & Zhang, J. (2020). Glial Cells: Role of the Immune Response in Ischemic Stroke. *Frontiers in Immunology*, *11*, 294. <https://doi.org/10.3389/fimmu.2020.00294>
- Yang, T., Li, Q., & Zhang, F. (2017). Regulation of gene expression in ischemic preconditioning in the brain. *Conditioning Medicine*, *1*(1), 47–56. <http://www.ncbi.nlm.nih.gov/pubmed/30035270>
- Yasui, Y., Amano, M., Nagata, K. I., Inagaki, N., Nakamura, H., Saya, H., Kaibuchi, K., & Inagaki, M. (1998). Roles of Rho-associated kinase in cytokinesis; mutations in Rho-associated kinase phosphorylation sites impair cytokinetic segregation of glial filaments. *Journal of Cell Biology*, *143*(5), 1249–1258. <https://doi.org/10.1083/jcb.143.5.1249>
- Zaverucha-do-Valle, C., Gubert, F., Mesentier-Louro, L., Scemes, E., Pitossi, F., Santiago, M. F., & Mendez-Otero, R. (2013). Resident Neural Stem Cells. dos Santos Goldenberg, R. C., Campos de Carvalho, A. C., (Eds.), *Resident Stem Cells and Regenerative Therapy* (pp. 69–87). Elsevier Inc.
- Zhang, J., & Jiao, J. (2015). Molecular Biomarkers for Embryonic and Adult Neural Stem Cell and Neurogenesis. *BioMed Research International*, *2015*, 14. <https://doi.org/10.1155/2015/727542>
- Zhang, K., Zhao, T., Huang, X., Wu, L. ying, Wu, K., Zhu, L. L., & Fan, M. (2014). Notch1 mediates postnatal neurogenesis in hippocampus enhanced by intermittent hypoxia. *Neurobiology of Disease*, *64*, 66–78. <https://doi.org/10.1016/j.nbd.2013.12.010>
- Zhang, N., Yin, Y., Han, S., Jiang, J., Yang, W., Bu, X., & Li, J. (2011). Hypoxic

preconditioning induced neuroprotection against cerebral ischemic injuries and its cPKC γ -mediated molecular mechanism. *Neurochemistry International*, 58(6), 684–692. <https://doi.org/10.1016/j.neuint.2011.02.007>

Zhao, L., Liu, X., Liang, J., Han, S., Wang, Y., Yin, Y., Luo, Y., & Li, J. (2013). Phosphorylation of p38 MAPK mediates hypoxic preconditioning-induced neuroprotection against cerebral ischemic injury via mitochondria translocation of Bcl-xL in mice. *Brain Research*, 1503, 78–88. <https://doi.org/10.1016/j.brainres.2013.01.051>

Zhou, R., & Skalli, O. (2000). TGF- α differentially regulates GFAP, vimentin, and nestin gene expression in U-373 MG glioblastoma cells: Correlation with cell shape and motility. *Experimental Cell Research*, 254(2), 269–278. <https://doi.org/10.1006/excr.1999.4762>

XIV. Anexos

Tabla 1. Lista de anticuerpos utilizados en este estudio. WB: *Western blot*, IF: *Inmunofluorescencia*.

Ac 1	[Ac 1]	Reacciona con	Ac 2	[Ac 2]
Conejo policlonal anti-GFAP – Santa Cruz Biotechnology Inc. – Cat. No. sc-6171	1:2 000	Proteína ácida fibrilar glial	Cabra anti-conejo IgG-AP – Santa Cruz Biotechnology, Inc. – Cat. No. sc-2034	WB: 1:2 500
Ratón monoclonal anti-NeuN – Merck – Cat. No. MAB377	1:2 000	Proteína específica de neuronas de unión al ADN	Cabra anti-ratón IgG (H+L) – Thermo Fisher – Cat. No. R37121 Cabra anti-ratón IgG-AP – Santa Cruz Biotechnology, Inc. – Cat. No. sc-2058	IF: 1:1 000 WB: 1:2 500
Conejo policlonal anti-Iba1 – Wako – Cat. No. 019-19741	1:1 000	Proteína de unión al calcio Iba1 encontrada en microglía	Cabra anti-conejo IgG (H+L) Superclonal Alexa Fluor 647 - Invitrogen Cat No. A27040 Cabra anti-conejo IgG-AP – Santa Cruz Biotechnology, Inc. – Cat. No. sc-2034	IF: 1:1 000 WB: 1:2 500
Ratón monoclonal anti-Nestina – BD Transduction Laboratories – Cat. No. 611659	1:5 000	Filamento intermedio tipo VI Nestina	Cabra anti-ratón IgG-AP – Santa Cruz Biotechnology, Inc. – Cat. No. sc-2058	WB: 1:2 500

Conejo policlonal anti-Aldh1L1 – Abcam – Cat. No. ab87117	1:1 000	Astroцитos	Cabra anti-conejo IgG-AP – Santa Cruz Biotechnology, Inc. – Cat. No. sc-2034	WB: 1:2 500
Cabra policlonal anti-Actina – Santa Cruz Biotechnology Inc. – Cat. No. sc1616	1:2 500	Proteína Actina	Conejo anti-cabra IgG-AP – Santa Cruz Biotechnology, Inc. – Cat. No. sc-2949	WB: 1:2 500
Anti-BrdU – Bio-Rad Cat. No. OBT0030	1:1 000	Tasa de proliferación celular	Cabra anti-rata IgG biotinilado – Vector Laboratories Cat. No. BA-9400	IF: 1:2 000

Tabla 2. Diseños experimentales. N: tamaño de la población, n: tamaño de muestra, Cb: cerebelo, CVM; cordón ventromedial, GB: glía de Bergmann.

Experimento	Cepa	Unidad experimental	Unidad de observación	N	n	Análisis estadístico
Pruebas conductuales: Rotarod Barras estáticas Barras horizontales	CD1	Ratón	Ejecución del ratón en prueba motora	67	6-10	- ANOVA de una vía – <i>Post-hoc</i> : Tukey's - ANOVA de una vía en rangos
LSFM	GFAP::EGFP	Ratón	lóbulos del Cb	11	55	- Prueba de T no pareada (para cada

						lóbulo con PCH vs lóbulo control correspondiente) - ANOVA de una vía – <i>Post-hoc</i> : Tukey's
Montaje completo	GFAP::EGFP	Ratón	Células GFAP+ de la superficie del IV ventrículo del lóbulo I y el CVM	24	3	- ANOVA de una vía – <i>Post-hoc</i> : Tukey's
Cortes en criostato GB ectópica	GFAP::EGFP	Ratón	Células GFAP+ del CVM y de la capa molecular GB ectópica GFAP+ del lóbulo I	24	3	- ANOVA de una vía – <i>Post-hoc</i> : Tukey's - Prueba de T no pareada
Golgi rápido	CD1	Ratón	GB del lóbulo I	9	45	- Prueba de T no pareada
<i>Western Blot</i> (1)	GFAP::EGFP	Ratón	Proteína total del Cb	36	4	- ANOVA de una vía – <i>Post-hoc</i> : Tukey's
<i>Western Blot</i> (2)	GFAP::EGFP vs CD1	Ratón	Proteína total del Cb	54	3	- ANOVA de una vía – <i>Post-hoc</i> : Tukey's
IF-células granulares (NeuN)	CD1	Ratón	Células granulares (NeuN+) de	6	3	- Prueba de T no pareada

			la capa molecular			
IF-microglía (Iba1)	Pax2/GFP y CD1	Ratón	Microglía (Iba1+) de la capa molecular	12	9- 15	- Prueba de T no pareada
BrdU	GFAP::EGFP y CD1	Ratón	CVM	6	3	- Prueba de T no pareada

Response to Hypoxic Preconditioning of Glial Cells from the Roof of the Fourth Ventricle

Marymar Becerra-González,^a Ragu Varman Durairaj,^a Aline Ostos Valverde,^a Emilio J. Gualda,^b Pablo Loza-Alvarez,^b Wendy Portillo Martínez,^c Gabriela Berenice Gómez-González,^a Annalisa Buffo^d and Atáulfo Martínez-Torres^{a*}

^a Instituto de Neurobiología, Departamento de Neurobiología Celular y Molecular, Laboratorio de Neurobiología Molecular y Celular, Universidad Nacional Autónoma de México, Juriquilla, Querétaro 76230, Mexico

^b ICFO-Institut de Ciències Fòniques, The Barcelona Institute of Science and Technology, Av. Carl Friedrich Gauss, 3, 08860 Castelldefels (Barcelona), Spain

^c Instituto de Neurobiología, Departamento de Neurobiología Conductual y Cognitiva, Laboratorio de Plasticidad y Conducta Sexual, Universidad Nacional Autónoma de México, Juriquilla, Querétaro 76230, Mexico

^d Department of Neuroscience Rita Levi-Montalcini, University of Turin, Neuroscience Institute Cavalieri Ottolenghi (NICO), 10043 Orbassano, Torino, Italy

Abstract—The cerebellum harbors a specialized area on the roof of the fourth ventricle that is composed of glial cells and neurons that interface with the cerebrospinal fluid. This region includes the so-called ventromedial cord (VMC), which is composed of cells that are glial fibrillary acidic protein (GFAP)-positive and nestin-positive and distributes along the midline in association with blood vessels. We hypothesized that these cells should compare to GFAP and nestin-positive cells that are known to exist in other areas of the brain, which undergo proliferation and differentiation under hypoxic conditions. Thus, we tested whether cells of the VMC would display a similar reaction to hypoxic preconditioning (HPC). Indeed, we found that the VMC does respond to HPC by reorganizing its cellular components before it gradually returns to its basal state after about a week. This response we documented by monitoring global changes in the expression of GFAP-EGFP in transgenic mice, using light-sheet fluorescence microscopy (LSFM) revealed a dramatic loss of EGFP upon HPC, and was paralleled by retraction of Bergmann glial cell processes. This EGFP loss was supported by western blot analysis, which also showed a loss in the astrocyte-markers GFAP and ALDH1L1. On the other hand, other cell-markers appeared to be upregulated in the blots (including nestin, NeuN, and Iba1). Finally, we found that HPC does not remarkably affect the incorporation of BrdU into cells on the cerebellum, but strongly augments BrdU incorporation into periventricular cells on the floor of the fourth ventricle over the adjacent medulla. *This article is part of a Special Issue entitled: Honoring Ricardo Miledi - outstanding neuroscientist of XX-XXI centuries.* © 2019 IBRO. Published by Elsevier Ltd. All rights reserved.

Key words: Bergmann glia, cerebellum, clarity, light sheet fluorescence microscopy, microglia, hypoxia.

INTRODUCTION

The mammalian cerebellar cortex is composed of three layers of cells that are regularly distributed, in the same pattern throughout all ten of its lobules. In all, the somata of Purkinje neurons and Bergmann glial (BG) cells occupy the so-called Purkinje cell layer, located between the outermost molecular layer (formed by basket and stellate neurons) and the innermost granular

layer (formed by granule and Golgi neurons) (Hoogland et al., 2015; Hibi et al., 2017). The functional organization of the cerebellum is modular, i.e., determined by connections with other brain areas in a zone-specific manner, which has been clearly elucidated (Voogd and Glickstein, 1998; Witter and De Zeeuw, 2015). However, the relationships of cerebellar lobules with the central ventricular system of the brain are variable, because lobules III-VII face the subarachnoid space, while lobules I, II and X face the fourth ventricle. This gives rise to a situation in which ciliated ependymal cells cover the surfaces of the latter lobules and bathe in cerebrospinal fluid (CSF).

Our recent observations on lobules I, II and X on the roof of the fourth ventricle have shown cellular diversity amongst the ependymal cells that contact the CSF as well as the cells that are located just under them, in

*Corresponding author.

E-mail address: ataulfo@unam.mx (A. Martínez-Torres).

Abbreviations: BG, Bergmann glia; CSF, cerebrospinal fluid; EGFP, enhanced green fluorescent protein; GFAP, glial fibrillary acidic protein; HPC, hypoxic preconditioning; LSFM, light sheet fluorescence microscopy; ROI, region of interest; SVZ, subventricular zone; VMC, ventromedial cord.

what is known as the subventricular zone (SVZ). Using patch-clamp electrophysiology and immunofluorescence microscopy, we have shown that within the SVZ reside astroglial cells, oligodendrocytes, neurons, and possibly even glial or neuronal progenitor cells (González-González et al., 2017; Reyes-Haro et al., 2013). Therefore, the organization of this area contrasts dramatically with the homogeneous cytoarchitecture found in the rest of the lobules of the cerebellum, and represents a unique environment in which CSF, blood vessels, and brain parenchyma all converge. Here, in the SVZ, the cells that form the wall of the ventricle are in a strategic position to sense changes in the CSF, which is known to play important roles in signal transduction and to transport hormones and other chemical signals throughout the brain, all parts of maintaining homeostatic control (Del, 1995; Cipolla, 2009; Zhang et al., 2015).

Additionally, on the very roof of the fourth ventricle exists a unique population of ependymal cells that differ from all the rest by being only biciliate, and by extending in a streak-like fashion along the midline (González-González et al., 2017). These we call the ventromedial cord (VMC), which we find also includes certain GFAP+ and nestin+ cells (usually taken as identifying neural stem cells), which have a single process that projects towards the interior of the cerebellum.

Similarly, neuronal progenitor cells in the adult hippocampus display prominent extensions throughout the granular cell layer and, unlike other glial cells within the area, express nestin as well as GFAP in their intermediate filaments (Kriegstein and Alvarez-Buylla, 2009). Such neuronal progenitor cells are found under normal conditions and may be activated after injury in several regions of the adult nervous system, including the spinal cord, the SVZ of the lateral ventricles, and the subgranular zone of the hippocampus (Lang et al., 2015). In the latter region, these neuronal progenitor cells resemble classical glial cells, in that they express nestin and GFAP, and they proliferate and differentiate under HPC a stereotyped method of temporary, mild oxygen deprivation that does not induce any irreversible cellular damage, but is widely employed and studied, due to its neuroprotective and plastic effects (Santilli et al., 2010; Lang et al., 2015).

Many types of mild noxious stimuli are effective in conferring this sort of protection to a range of tissue types (including the brain) as part of the innate tolerance in various organisms. These non-lethal stimuli include temporary ischemia, hyperthermia, physical exercise, lipopolysaccharide, glutamate, and most especially, the use of mild hypoxia (HPC), which has been used repeatedly and successfully to reduce injury from a subsequent serious ischemic insult to the brain (Gidday et al., 2013). Abundant evidence has been presented for neuronal plasticity and repair in response to HPC, in areas of the brain as diverse as the spinal cord and the cerebral cortex, with clear cut indications that parenchymal cellular neogenesis is involved in this repair (Bonfanti, 2013). Less well documented, however, is whether or not the same sort of cell proliferation occurs in the cerebellum in response to HPC – anything like which occurs in the cortex in response to HPC – and if

so, whether this response is significant, compared to the original cellular proliferation that occurs during cerebellar development (Ponti et al., 2008; Feliciano et al., 2015; Ahlfeld et al., 2017; Mandalos et al., 2018).

Thus, we sought in this study to determine whether the GFAP+ cells that form the VMC respond to HPC, and how they respond. Additionally, we sought to determine the impact of HPC on the nearby BG cells in the cerebellum. Here, we focused on BG cells because it is well known that during cerebellar development, these cells provide essential scaffolds for the migration and layering of granular neurons (De Zeeuw and Hoogland, 2015). Additionally, such BG cells surround Purkinje neurons and remain critically important throughout adult life (as has been shown by genetically ablating their AMPA receptors and achieving a severe impairment in motor coordination) (Saab et al., 2012). However, even though BG cells in the region extend their processes towards the fourth ventricle, they do not contact the cells in the VMC directly. Instead, their end-feet are covered with a limiting basal membrane (González-González et al., 2017). Consequently, we felt it was important to determine whether BG cells would respond to HPC, and if so, if their response was anything like that of GFAP+ cells in the VMC.

To evaluate this, we applied a combination of techniques, including immunofluorescence, CLARITY, LSFM and BrdU incorporation – all to assess whether or not cell proliferation occurred in the VMC (and in Bergman glial cells) in response to HPC.

EXPERIMENTAL PROCEDURES

Ethical statement

All procedures on mice were carried out in accordance with the regulations of the Society for Neuroscience: Policies on the Use of Animals and Humans in Neuroscience Research and on local and international bioethical guidelines including the NOM-062-ZOO, which is in accordance with the recommendations of the National Institutes of Health publication titled “Guide for the Care and Use of Laboratory Animals” (National Research Council (U.S.). Committee for the Update of the Guide for the Care and Use of Laboratory Animals. And Institute for Laboratory Animal Research (U.S.), 2011).

Animals

Postnatal 26 (P26) male mice (CD1, GFAP-EGFP and Pax2-GFP mice) bred at the animal facility of the Instituto de Neurobiología UNAM, Juriquilla, Querétaro or at the University of Turin were selected and kept under a controlled 12 h light/12 h dark cycle at 20 ± 1 °C. Mice expressing EGFP under the human GFAP promoter (Nolte et al., 2001) were kindly donated by Prof. Helmut Kettenmann (Max Delbrück Center, Berlin). This transgenic mouse strain was selected for brain clarification since EGFP is strongly expressed in the cerebellum. Water and food *ad libitum* were provided, and cages were replaced *ad lib* to maintain cleanliness and dryness.

Hypoxic preconditioning

Following the protocols used in earlier reports, HPC was produced by placing mice inside 50 ml conical tubes and sealing the caps tightly (Zhang et al., 2011; Liu et al., 2012; López-Aguilera et al., 2012; Benitez et al., 2014). As soon as the mice started gasping, they were removed from the tubes. This we considered to be one cycle of HPC, and this we repeated three times on every mouse, with 15 min of recovery in normal oxygen in-between each cycle. This form of 'auto-hypoxia' is thus produced by the animal's own oxygen consumption and is one of the earliest methods of HPC (Rybnikova and Samoilo, 2015).

Not surprisingly, the mice's ability to tolerate anoxia became longer and longer with each successive trial, the average time of runs 1, 2 and 3 being 201 ± 22.15 , 350 ± 39.16 , and 573 ± 64.83 (seconds \pm SE, respectively). Fig. 1 shows the hypoxia tolerance-time of all the mice exposed to HPC. In other words, the protocol for HPC used here induces immediate tolerance and protection to anoxia, as was documented in Li et al. (2017).

To make sure that this approach to HPC was not inducing some other form of stress-response – some sort of response unrelated to anoxia – we applied the following control. Mice were again placed inside of 50 ml conical tubes, but with the caps of the tubes left open, thus allowing the animals to breath normally, even though they were constrained "inside a tube" ("I.T."). To parallel the HPC treatments above, mice were restrained in these open-tubes for roughly the same mean-times as during the sequence of HPC: 200 s, then 350 s, then 600 s.

All mice were utilized at P26 and were randomly assigned to the various treatment-conditions that we intended to study. Since we knew from the literature that the responses elicited by HPC usually last up to 7 days (Emerson et al., 1999; Rybnikova and Samoilo, 2015), we chose to study the response of the VMC in each mouse, every day for seven days after the HPC. To do so, their cerebellae were processed as described below. (The number of animals we used in each experimental procedure is shown in Table 2).

To determine the impact of HPC on the animals' subsequent motor behavior, we performed a battery that screened motor coordination. This included an accelerated version of the rotarod test, the static rod test, and the horizontal bar test (Brooks and Dunnett, 2009; Deacon, 2013). All equipment was cleaned with 10% alcohol after each trail to prevent any olfactory cues. CD1 male mice underwent HPC at P26. Eight groups were tested and compared: Control group ($n = 10$), 24 h after HPC day 1 ($n = 6$), 48 h after HPC day 2 ($n = 8$), 72 h after HPC day 3 ($n = 8$), 96 h after HPC day 4 ($n = 9$), 120 h after HPC day 5 ($n = 8$), 144 h after HPC day 6 ($n = 9$), 168 h after HPC day 7 ($n = 9$). Each mouse was tested on every apparatus in a single session.

Behavioral tests

To determine motor coordination, we used the static-rod test (Deacon, 2013). Mice were placed on the last 5 cm of various rods, placed high over an overhang. Faced with this, mice spontaneously turn around and back up the rod to the fixed end. Mice were tested on various rods, starting with quite wide rods, but ending up with a tippy, 9 mm wide rod. The maximum time that each mouse took to turn around and walk back to the fixed end of the rod was scored. When a mouse fell off the rod or could not stay upright, it was assigned the maximum test time.

After a brief rest, coordination and forelimb-strength were evaluated with the Horizontal Bar test. This involved placing mice on the central part of a metal bar, hanging by their forepaws. Normally, mice can hang like this for roughly 30 s. So, we recorded if they fell off before 30 s. (Mice were also considered to have reached 30 s, if they reached the end columns of the bar or touched a column with one forepaw). The metal bar was 38 cm long and was 49 cm above the floor; 3 diameters were tested (2 mm, 4 mm, 6 mm).

Finally, the animals were tested in a Rotarod (Series 8, IITC Life Science) to assess motor coordination. In the training phase, the animals underwent 3 sessions of 1 min with a fixed rotation of 5 rpm. In the test phase, the rod started at 5 rpm but gradually increased to 40 rpm, (at an acceleration rate of 20 rpm/min). Each mouse was subjected to three trials, with 2 min maximum for each trial. The distance, time and maximum acceleration of animals on the rod was recorded for each trail. One-Way ANOVA On Ranks was performed for the static rod and parallel bars data. Rotarod data was analyzed using a One-Way ANOVA. (Table 2).

Light sheet fluorescence microscopy

To generate a high-density map of BG cells distribution, and to determine the effects of HPC on the organization of this group of cells, brain clarification was performed

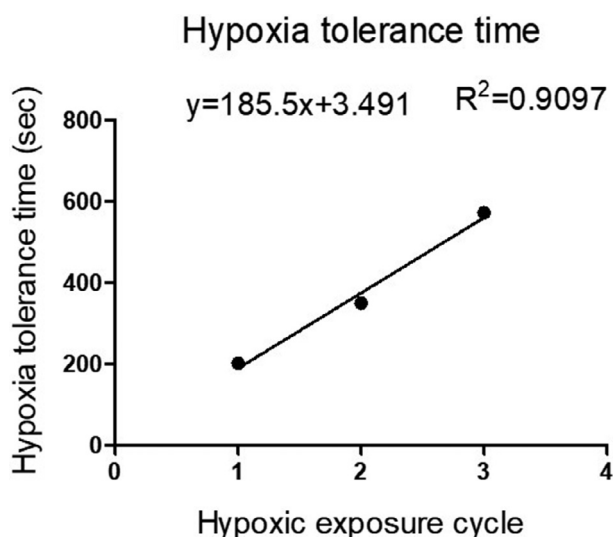


Fig. 1. Tolerance is developed after hypoxic exposure. Linear regression showing that after each run of hypoxic preconditioning (1–3) the tolerance is consistently increased, $n = 9$.

on brains of transgenic GFAP-EGFP mice that had undergone HPC, using the CLARITY technique we described elsewhere (González-González et al., 2017). Mice were euthanized 4 days after HPC ($N = 5$) and compared to control ($N = 6$). LSFM (Olarte et al., 2018) was used to image the whole brain. Imaging was performed with a $2\times$ objective as described in Stefaniuk et al., 2016, using the 488 nm line of a diode laser (Cobolt 06-MLD) for exciting EGFP.

For image reconstruction of the cerebellum, stacks of $2096 \times 1705 \mu\text{m}$ were stitched together with Fiji plugin (Preibisch et al., 2009). Each stack consisted of a horizontal scan of the cerebellum as shown in Fig. 3A. From each reconstruction, a three-dimensional region of interest (ROI) of $2.73 \times 10^7 \mu\text{m}^3$ was selected from (1) the cerebellar vermis and, (2) the cerebellar hemispheres (Fig. 3B). To determine the number of BG somata, the EGFP signal expressed under the GFAP promoter was localized by automated cell counting, using the centroid-localization function in each ROI with MATLAB software, as follows: background subtraction of every ROI was done; each image was binarized by computing a global threshold; centroid calculation was performed, and the number of centroids was displayed. Unpaired t -test was used to compare each lobule (Crus I, I, X, Crus II and V & VII from day 4 post-HPC cerebella) against its corresponding lobule in controls. To compare data obtained from all lobules, One-Way ANOVA tests were run (Table 2).

Tissue processing

Brain fixation was performed to analyze the EGFP-signal from the VMC and from cerebellar lobule I in transgenic GFAP-EGFP mice, HPC was induced at P26 in 7 mice groups, and each group was euthanized one day after the next, for a whole week (Table 2). After intraperitoneal anesthesia with pentobarbital, mice were fixed transcardiac perfusion as previously described (Gage et al., 2012; González-González et al., 2017). This involved perfusion with 4% formaldehyde in phosphate-buffered saline (137 mM NaCl, 2.7 mM KCl, 10 mM Na_2HPO_4 , and 2 mM KH_2PO_4 in deionized water, pH = 7.4). After perfusion, whole cerebellae were excised and transferred to the same 4% PFA fixative at 4 °C for 24 h. For imaging, the surfaces of lobules I, II and X were exposed, those that were in contact with the CSF of the fourth ventricle (González-González et al., 2017).

Imaging

Whole brains were imaged with a Zeiss LSM 510 confocal microscope, utilizing a Zeiss 10X EC Plan-NEOFLUAR, NA = 0.3, WD = 5.2 mm objective lens. Stacks of images of lobule I along the VMC were rendered in ImageJ. To determine the integrated fluorescent signal from GFAP-EGFP mice, renderings were analyzed after calibration from the original $10\times$ image, then, renderings were binarized with Otsu's algorithm and subtracted from the original image to measure the integrated density from lobule I (ROI = $902.70 \times 672.60 \mu\text{m}$) and the VMC (ROI = $38.94 \times 265.5 \mu\text{m}$). One-way ANOVA was used in both, the lobule I and the VMC to

determine statistically significant differences between the means of the 7 post-HPC groups plus control group.

For analyzing the EGFP-signal specifically from BG in lobule I, coronal cerebellar cryo-sections were obtained after intracardiac perfusion and cryoprotection with increasing concentrations of sucrose (10%, 20%, and 30% in PBS) (González-González et al., 2015, 2017). Five consecutive $40 \mu\text{m}$ coronal slices were collected from all 7 groups that underwent HPC at P26. Here, the Zeiss LSM-510 confocal microscope was equipped with a $20\times$ Zeiss Plan-APOCHROMAT, NA = 0.8, WD = 0.55 mm objective. This was used to generate $40 \mu\text{m}$ stacks wherein the EGFP-signal expressed in the BG somata could be quantified in ImageJ, with the cell counter plugin and a One-way ANOVA test was run to compare groups (Table 2).

Rapid Golgi staining

Morphological analysis of Bergmann glial cells was also performed after rapid Golgi staining. This was performed on cerebellae that were perfusion-fixed as indicated above, then subjected to the Golgi procedure as modified by Rosas-Arellano et al. (Diaz-Cintra et al., 1981; Shiga et al., 1983; Rosas-Arellano et al., 2007). This involved post-fixing cerebellar sagittal sections in 4% potassium dichromate in buffered formalin, then transfer to the classical rapid Golgi fixative for 6–11 days, then impregnation in a 0.75% silver nitrate solution for 18–48 h, and finally dehydration and embedding in nitrocellulose. From these samples, $120 \mu\text{m}$ sagittal sections were obtained with a Leica, VT1000S vibratome. Bergmann glial cells of lobule I were imaged with an Olympus Ckx41 light microscope using a $40\times$ objective. Forty-five cells from each animal were imaged and processed with ImageJ software. The diameter and area of the soma, as well as the absolute protrusion-length, were evaluated, as previously reported (Hanke and Reichenbach, 1987). Images were processed with the open source ImageJ software (version 1.51r, Wayne Rasband, National Institutes of Health, Bethesda). Huang's algorithm was applied for thresholding on Bergmann glia in Golgi samples, and the unpaired t -test was used to compare the four- and seven-day post-HPC groups.

Western blot

Western blotting was performed to determine the expression level of GFAP, ALDH1L1, Iba1, NeuN, and Nestin in GFAP-EGFP and CD1 strains, with actin used as loading-control. Total protein extracts from cerebellae ($n = 4$) were obtained. Tissue was processed and homogenated in ice-cold 200 mM glycine buffer (with 150 mM NaCl, 50 mM EGTA, 50 mM EDTA, and 300 mM sucrose, and containing a protease inhibitor (Sigma-Aldrich, USA Cat. No. P8340)). The homogenate was centrifuged twice at $10,000\times g$ for 15 min at 4 °C, and the supernatants were collected and stored at $-80 \text{ }^\circ\text{C}$. Protein concentration was assessed by Bradford's method (Bradford, 1976). Equal concentrations (30 μg) of total proteins were resolved on 10% SDS-polyacrylamide gel and transferred to a polyvinylidene

difluoride membrane (Millipore, USA). Then, the membranes were blocked with 5% non-fat milk powder with 1X TBS-T for 3 h. Membranes were incubated at 4 °C overnight with one of the primary antibodies shown in Table 1, and actin was used as an internal control for each sample. Then the membranes were washed with 1X TBS-T three times and incubated for 4 h with the secondary antibody (see Table 1). Alkaline phosphatase activity was detected with 5-Bromo-4-chloro-3-indolyl phosphate disodium salt (BCIP)/nitro blue tetrazolium chloride (NBT) according to the manufacturer's instructions. The Images were acquired with a Molecular Imager ChemiDoc XRS System (Bio-Rad Laboratories, Inc., USA), and optical density of trace quantity for each band was determined using Image Lab 2 software (Bio-Rad Laboratories Inc.).

Immunofluorescence

NeuN. We tried to understand whether the changes of expression of NeuN detected by Western blot (see below) were related to the response of neurons in the area, thus we examined the area by immunofluorescence 4 days after HPC using a NeuN monoclonal antibody (Table 1) in cryoprotected cerebellar coronal slices of CD1 mice. An unpaired *t*-test was used to analyze collected data for both analyses: cell number and integrated density.

Iba1. The distribution and morphology of microglial cells from lobule I were assessed 4 days after HPC by immunofluorescence using an Iba1 polyclonal antibody (Table 1) in cerebellar coronal slices of CD1 and Pax2-GFP mice (Parmigiani et al., 2015) followed by the secondary antibody (Table 1), coronal slices comprising caudate putamen, lateral ventricles and corpus callosum were used as positive control (as microglia is equally widespread along the entire CNS) and sections incubated with the antibody diluent alone and no primary antibody, followed by secondary antibody and detection reagent

was used as negative control. A Zeiss LSM 780 confocal microscope was used to image 15 μm stacks at 1 μm interval with a 20 \times objective. We analyzed the microglial population within the lobule I and the ventromedial cord in both strains since there were no differences between them the results were pooled together.

For the analysis of the number of Iba1+ cells, we divided these cells into two groups: (1) cells with soma area equal to or less than 50 μm^2 corresponding to “resting” microglia, and (2) cells with soma larger than 50 μm^2 corresponding to “activated” microglia (Davis et al., 2017). Each image stack was analyzed using Fiji software as follows: (1) The stack was projected in the Z-axis into a single image using the maximum intensity projection type. (2) The contrast was enhanced using a 0.1 value in all cases. (3) The resulting image was converted into a binary, 8-bit format. (4) A threshold was applied using the triangle algorithm. (5) The image was cropped into a limited area (450 $\mu\text{m} \times 300 \mu\text{m}$) that included the SVZ and a portion of the granular layer. (6) A line grid of 1000 μm^2 was placed on the projection. (7) Each cell body labeled by the Iba1 antibody was drafted by hand with the freehand lasso tool and converted into a ROI. (8) The area and perimeter of each soma were obtained after applying the “Measure” function.

For assessing Iba1+ cell distribution, each confocal image was divided into two zones based on a line grid of 1000 μm^2 : (1) The SVZ, ventrally delimited by the first 2 rows. (2) The supra SVZ that corresponded to the molecular, Purkinje and granular layers that covered 8 rows above the SVZ. The cell counter plugin was used to assess the number of Iba1+ cells per zone (SVZ and supra SVZ).

Bromodeoxyuridine (BrdU) incorporation assay

To test cell proliferation after HPC, we used the thymidine analog (BrdU, Sigma-Aldrich Cat. No. B5002). Two CD1 mice groups were used: Control ($n = 3$) and four days after HPC ($n = 3$). Lateral ventricles served as a control

Table 1. List of antibodies used in this study. WB = Western blot, IF = Immunofluorescence

1AB	[1AB]	Reacts with	2AB	[2AB]
Polyclonal rabbit anti-GFAP – Santa Cruz Biotechnology Inc. – Cat. No. sc-6171	1:2000	Glial Fibrillary Acidic Protein	Goat anti-rabbit IgG-AP – Santa Cruz Biotechnology, Inc. – Cat. No. sc-2034	WB: 1:2500
Monoclonal mouse anti-NeuN – Merck – Cat. No. MAB377	1:2000	DNA-binding neuron-specific protein NeuN	Goat anti-Mouse IgG (H + L) – Thermo Fisher – Cat. No. R37121	IF: 1:1000
			Goat anti-mouse IgG-AP – Santa Cruz Biotechnology, Inc. – Cat. No. sc-2058	WB: 1:2500
Polyclonal rabbit anti-Iba1 – Wako – Cat. No. 019-19741	1:1000	Calcium-binding protein Iba1 specifically found in microglia	Goat anti-Rabbit IgG (H + L) Superclonal Alexa Fluor 647 – Invitrogen Cat No. A27040	IF: 1:1000
			Goat anti-rabbit IgG-AP – Santa Cruz Biotechnology, Inc. – Cat. No. sc-2034	WB: 1:2500
Monoclonal mouse anti-neslin – BD Transduction Laboratories – Cat. No. 611659	1:5000	Intermediate filament type VI nestin	Goat anti-mouse IgG-AP – Santa Cruz Biotechnology, Inc. – Cat. No. sc-2058	WB: 1:2500
Polyclonal rabbit anti-ALDH1L1 – Abcam – Cat. No. ab87117	1:1000	Astrocytes	Goat anti-rabbit IgG-AP – Santa Cruz Biotechnology, Inc. – Cat. No. sc-2034	WB: 1:2500
Polyclonal goat anti-actin – Santa Cruz Biotechnology Inc. – Cat. No. sc1616	1:2500	Actin protein	Rabbit anti-goat IgG-AP – Santa Cruz Biotechnology, Inc. – Cat. No. sc-2949	WB: 1:2500
Anti-BrdU – Bio-Rad Cat. No. OBT0030	1:1000	Cell proliferation rate	Biotinylated Goat Anti-Rat IgG – Vector Laboratories Cat. No. BA-9400	IF: 1:2000

Table 2. Experimental designs. *N* = Population size, *n* = Sample size, Cb = Cerebellum, VMC = Ventromedial cord, BG = Bergmann glia

Experiment	Mouse strain	Experimental unit	Observational unit	<i>N</i>	<i>n</i>	Statistical analysis
Behavioral tests: Rotarod	CD1	Mice	Motor task	67	6–10	– One-way ANOVA (rotarod) – Post hoc: Tukey's – One-way ANOVA on Ranks
Static rods Parallel bars						
Light sheet	GFAP-EGFP	Mice	Cb lobules	11	55	– Unpaired T-test (Each HPC lobule vs corresponding control lobule) – One Way ANOVA – Post hoc: Tukey's
Whole-mount	GFAP-EGFP	Mice	GFAP- positive cells from the fourth ventricle surface of Lobule I and VMC	24	3	– One Way ANOVA – Post hoc: Tukey's
Cryostat sectioning	GFAP-EGFP	Mice	GFAP- positive cells from VMC and molecular layer	24	3	– One Way ANOVA – Post hoc: Tukey's
Ectopic BG			GFAP- positive ectopic BG from the molecular layer			– Unpaired <i>t</i> -test
Rapid Golgi	CD1	Mice	BG from Lobule I	9	45	– Unpaired <i>t</i> -test
Western Blot (1)	GFAP-EGFP	Mice	Cb total protein	36	4	– One Way ANOVA – Post hoc: Tukey's
Western Blot (2)	GFAP-EGFP vs CD1	Mice	Cb total protein	54	3	– One Way ANOVA – Post hoc: Tukey's
IF- (NeuN)	CD1	Mice	(NeuN ⁺) from molecular layer	6	3	– Unpaired <i>t</i> -test
IF-microglia (Iba1)	Pax2-GFP and CD1	Mice	Microglia (Iba1 ⁺) from molecular layer	12	9–15	– Unpaired <i>t</i> -test
BrdU	GFAP-EGFP and CD1	Mice	VMC	6	3	– Unpaired <i>t</i> -test

since active BrdU incorporation has been widely reported in the area. Cerebellar slices incubated with the antibody diluent alone and no primary antibody, followed by secondary antibody and detection reagent were used as a negative control.

For each group, two I.P. injections of 50 µg/g BrdU (10 mg/mL) were administered every 6 h. The first injection was performed 30 min after HPC, and daily doses of BrdU were given for 5 days. Mice were euthanized 2 h after the last injection and brains were processed as described above. Cryoprotected cerebella were sliced into 40 µm coronal sections and observations focused on lobule I.

BrdU was detected using anti-BrdU 1:1000 (Bio-Rad. Cat. No. OBT0030), followed by the secondary antibody: Biotinylated Goat Anti-Rat IgG Antibody 1:2000 (Vector Laboratories. Cat. No. BA-9400) (Table 1). Later, samples were incubated in Avidin-Biotin Complex (ABC) and revealed using tyramide signal amplification (TSA) plus coumarin (1:100, Perkin Elmer. Cat. No. NEL703001KT) according to the manufacturer's instructions.

Statistical analyses

Statistical analyses were performed using the following software: GraphPad Prism version 5.0 for Windows (GraphPad Software, La Jolla, California, USA). All data were plotted on SigmaPlot (Systat Software, San Jose, CA). Statistical analysis of each experimental procedure is detailed in Table 2.

RESULTS

HPC does not significantly alter motor coordination

It is known that extreme hypoxic conditions can impair motor coordination, likely due to cerebellar damage (Benitez et al., 2014). To determine whether HPC itself might also impair motor coordination, we conducted the following tests: (1) an accelerating version of the rotarod test, (2) the static rods test, and (3) the horizontal bar test. None of these tests revealed any significant disturbances to motor coordination after HPC. Only a very slight deterioration in performance on the rotarod test, 6 days after HPC, could be gleaned, and only after analyzing the results with Tukey's post hoc test (Kim, 2015).

The static rods and parallel bars tests showed no significant differences, although we noticed that HPC-treated mice took a bit more time to cross over the rods and hung onto the bars a bit less tenaciously. In general, though, it was clear that HPC did not induce any gross motor-deficits (Fig. 2).

Changes in Bergmann glia (BG) organization and morphology

A global analysis of EGFP expression in the cerebellum after HPC was achieved by LSFM in clarified samples of transgenic GFAP-EGFP mice. No further immunofluorescence was required, because endogenous fluorescence from formaldehyde fixations was well preserved after clarification. This allowed us to observe the tight palisade that BG processes form,

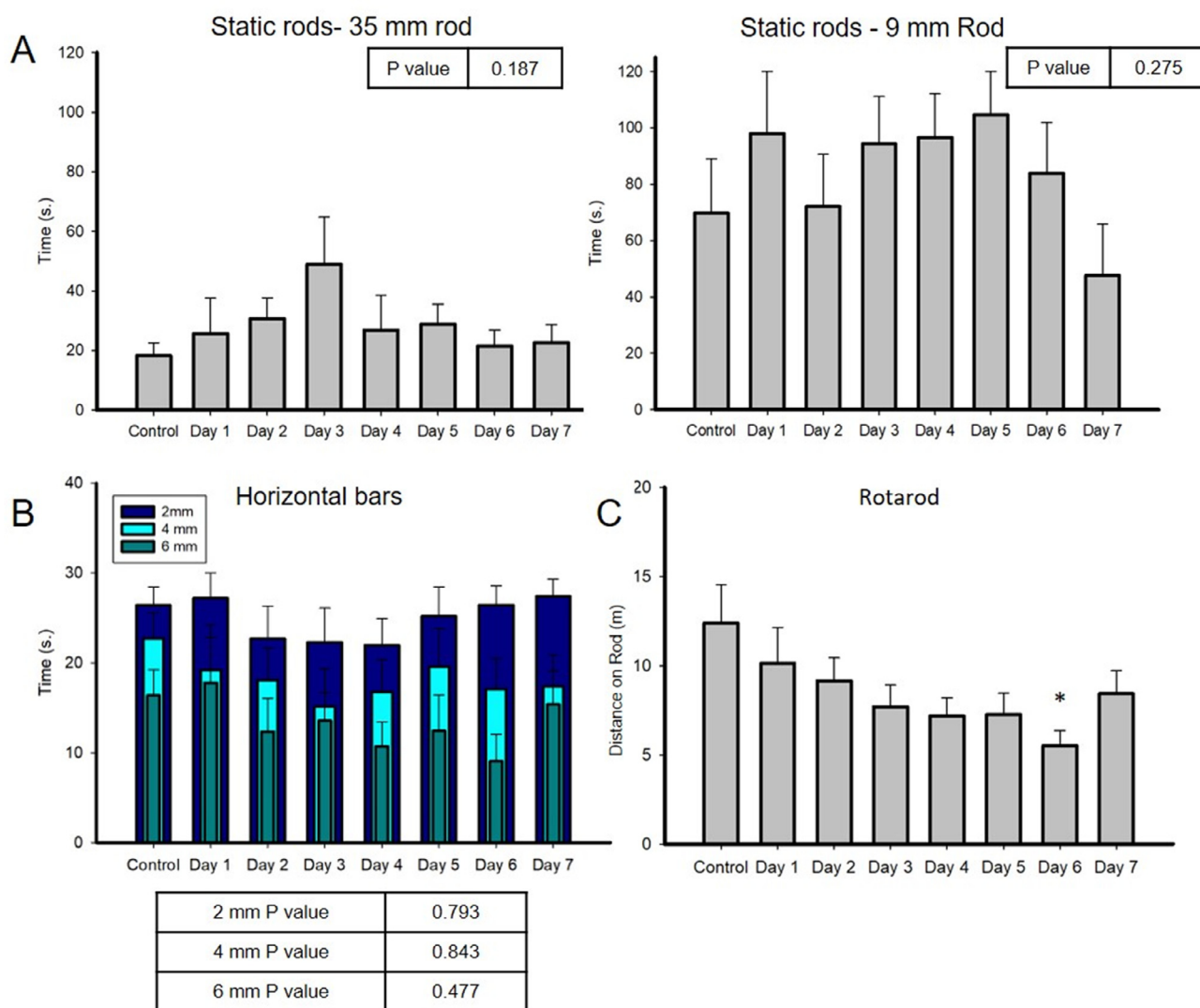


Fig. 2. HPC does not affect gross motor activity. **(A):** Static Rods. Performance on the widest (35 mm) and the narrowest rod (9 mm) are displayed; 28 mm, 22 mm, and 15 mm were also tested. Shorter execution times on the rod indicated better motor coordination, the control group maintained a better execution for both graphs. **(B):** Horizontal bars. Mice tested 2–5 days after HPC lasted less time hanging on the bars (2–6 mm), suggesting slight problems in motor coordination and reduced strength in limbs; however, data were not statistically different. **(C):** Rotarod test. A longer distance correlates with better motor coordination. Shorter distances were recorded from 1 day after HPC, and the only statistically significant difference was found at day 6 ($F_{(7,191)} = 2.347$, P value = 0.024; Tukey's post-hoc test). Mice recovered at day 7.

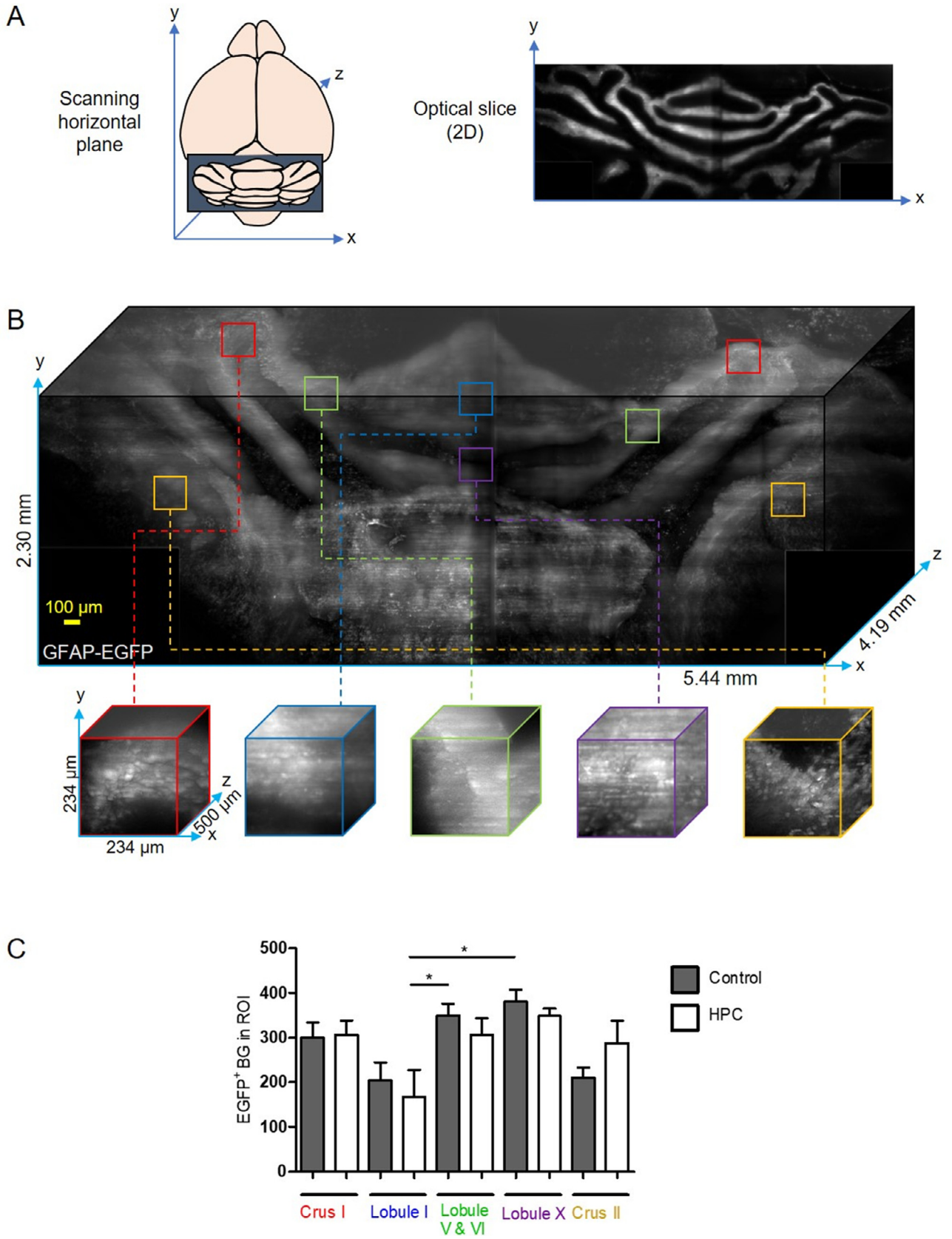
viewed right through the molecular layer of the cerebellum (Fig. 3A). Vermis and hemispheres showed statistical differences in the number of EGFP+ BG somata as determined by One-Way ANOVA and Tukey as post-hoc ($F_{(9,62)} = 3.263$, P value = 0.0026) (Fig. 3C). No significant differences were found when comparing each lobule, as determined by the unpaired t -test.

The only difference we could find after HPC was a reduction in the number of BG somata in the lobules of the vermis, and a larger number of somata in the hemispheres, which may be worthy of further analysis. Fig. 3A, B shows sample images from cerebella of GFAP-EGFP mouse and Fig. 3C contrasts the number of EGFP+ cells from diverse areas of the cerebellum from control and HPC mice. The overall reduction in the number of EGFP+ cells seen here after HPC should not be interpreted as an actual loss of GFAP+ cells.

Rather, we will show below that it simply represents a reduction in the expression of the reporter gene.

EGFP expression in the VMC is decreased after HPC

Since the CSF responds quickly to metabolic changes like those expected after HPC, we analyzed whether the VMC, which we showed earlier is an array of GFAP+ and nestin+ ependymal cells that contact the CSF (González-González et al., 2017), also displayed a reduction in EGFP-expression. Our *en face* preparations exposed the VMC along lobule I, which is the area we analyzed. Indeed, we could clearly observe a gradual decrease in EGFP expression for some days after HPC in the VMC but also in the GFAP+ ependymal cells lining the lobule I. In the latter, the lowest expression was reached by day 4, after which EGFP expression rebounded and held



steady thereafter (Fig. 4A). Integrated density analysis of the images supported this observation, since the lowest pixel density was determined on day 4 (Fig. 4B), which differed from the control (One-Way ANOVA ($F_{(7,16)} = 4.419$, P value = 0.0066)). EGFP expression also decreased in the VMC (Fig. 4C). Also, by day 4, the VMC appeared disorganized and the GFAP+ cells that normally reside along the midline of lobule I were gone, as we showed previously (González-González et al., 2017). Integrated density analysis showed the lowest pixel density in the VMC by day 4 and gradual recovery starting on day 5. Data reflected statistically significant differences as determined by One-Way ANOVA ($F_{(7,16)} = 9.275$, P value = 0.0001), ($N = 24$, $n = 3$).

EGFP expression is decreased in the BG cells after HPC

As mentioned above, BG cells of lobule I showed reduced EGFP expression in coronal slices viewed by confocal microscopy (Fig. 5A). Image analysis revealed a significant difference in the number of BG somata that expressed EGFP, as determined by a one-way ANOVA, ($F_{(7,112)} = 36.04$, $p < 0.0001$ Tukey as post-hoc) Fig. 5B ($n = 3$). Other morphological changes in BG that were notable after HPC included: (1) by day 1, BG somata were slightly displaced from the Purkinje cell layer, and did not return to their original positions until days 5–7; (2) BG processes expressed lower levels of EGFP until day 4–5, after which they returned to their normal levels. Coincident with these changes, BG cellular processes retracted on day 1 and remained withdrawn until day 4–5 (an observation we could confirm by rapid Golgi analyses, below). Additionally, we noted that after HPC, the distribution of EGFP in BG terminal end-feet, which normally looks diffuse, temporarily became punctate from day 2 to 6 (Fig. 5C).

During our analyses of coronal sections from lobule I, we observed some totally ectopic BG cells, both in normal conditions and after HPC (Fig. 5A, B). These cells were recently described by Cerrato et al. (2018). To determine if these ectopic BG cells might respond differently to HPC than the others described above, we first counted them manually in slices from GFAP-EGFP mice; but as shown in Fig. 5D, their numbers and distributions did not change. We can conclude that majority of BG cells in lobule I of the cerebellum respond to HPC by changing their morphology and reducing their expression of EGFP. To further analyze these changes, we processed cerebella by the rapid

Golgi technique 4 days after HPC, when these cells showed the most pronounced changes.

BG processes retracts after HPC

The aforementioned differences found among BG cells by fluorescence microscopy prompted us to observe them more closely *via* silver impregnation at 4 and 7 days after HPC (Fig. 6A). This revealed that as they retracted their soma into the cerebellar parenchyma, their processes became commensurately longer. These morphological changes reached statistical significance, as determined by an unpaired *t*-test (P value < 0.0001) (Fig. 6B). At day 4 the area of the soma was reduced by 31% (SE = 3.25, $n = 3$, P value < 0.0001), and by day 7 there was a slight recovery in the soma (23% SE = 2.69, $n = 3$, P value < 0.0001). Absolute protrusion length of the processes increased 88% by day 4 (SE = 2.54, $n = 3$, P value < 0.0001) and persisted to 75% by day 7 (SE = 2.47, $n = 3$, P value < 0.0001).

Expression of glial and neuronal identity markers after HPC

To assess changes in expression of selective glial and neuronal markers after induction of HPC, we isolated proteins from cerebella before and after HPC and analyzed the expression of GFAP, ALDH1L1, Iba1, NeuN, and nestin. Representative blots are shown in Fig. 7A, $n = 4$ (for GFAP-EGFP mice) and Fig. 8 for CD1 mice. To discard the possibility of stress-induced changes in expression, we considered two control groups: (1) Control “inside a tube” (I.T.), in which the mice’s movements were restrained but they were not made anoxic, because their snouts were outside the tube, so they could breathe normally; and (2) control “outside a tube” (O.T.): true controls of mice never constrained in any tubes. Astrocyte markers GFAP and ALDH1L1 expression started to decline one day after HPC, but by day 4 their expression began to rebound, and by day 6 it returned to control levels (Fig. 7B, C). Microglial marker Iba1 and neuronal marker NeuN increased their expression from day two after HPC and did not return to control levels even after one week (Fig. 7D, E). Nestin also showed an increased expression from day one after HPC and continued to display increasing expression until day 7 (Fig. 7F). Statistical analyses included One-Way ANOVA and Tukey as post-hoc, ($N = 36$, $n = 4$).

Fig. 3. Distribution of Bergmann glial cells in the cerebellum from GFAP-EGFP mice. Clarified brains of GFAP-EGFP mice were observed under the light sheet fluorescence microscope. (A): Scanning plane of the light sheet and an example of one 2D optical slice. (B): Reconstruction of a $5.44 \times 2.30 \times 4.19$ mm volume of cerebellum. Color squares indicate the ROIs extracted for tridimensional stacks shown below. (C): A consistency in the reduction of the EGFP signal was observed in several areas of the cerebellum. No significant differences were found when comparing each lobule as determined by the unpaired *t*-test (Crus I: P value = 0.8940, 299.9 ± 34.08 ($N = 9$) vs 306.2 ± 32.03 ($N = 9$)). Lobule I: P value = 0.6277, 204.0 ± 40.42 ($N = 6$) vs 167.7 ± 60.33 ($N = 6$)). Lobule V & VII: P value = 0.3427, 349.5 ± 26.68 ($N = 11$) vs 305.5 ± 38.10 ($N = 8$)). Lobule X: P value = 0.3236, 380.8 ± 26.07 ($N = 5$) vs 348.0 ± 17.11 ($N = 5$)). Crus II: P value = 0.1670, 210.9 ± 22.40 ($N = 7$) vs 288.0 ± 50.18 ($N = 6$) ($N = 6$, Control), ($N = 5$, HPC). Values are expressed as mean \pm SEM. GFAP: Glial fibrillary acidic protein, EGFP: Enhanced green fluorescent protein, BG: Bergmann glia, HPC: Hypoxic preconditioning.

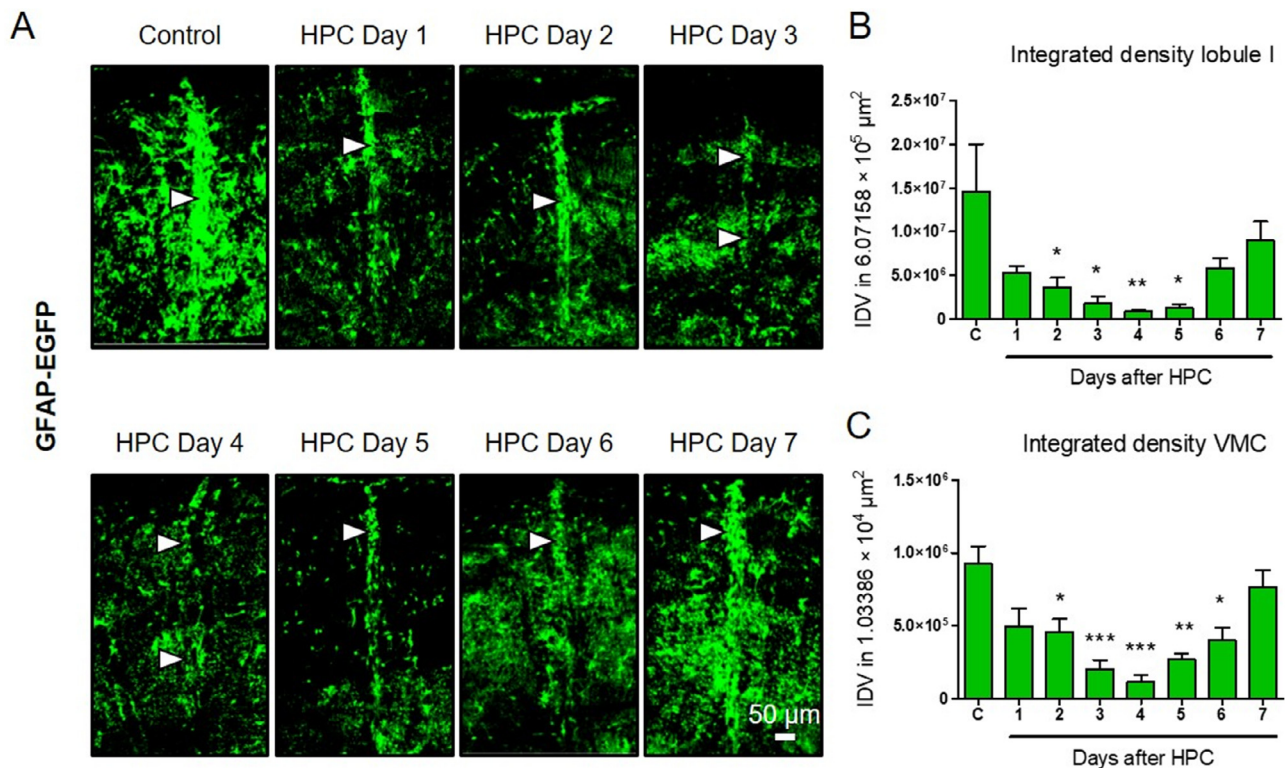


Fig. 4. EGFP expression after hypoxic preconditioning in the VMC of lobule I. The *en face* preparation exposed the VMC on the surface of the roof of the ventricle. **(A):** Confocal images of GFAP-EGFP mice cerebella. White arrowheads point to the VMC, which showed a gradual reduction of EGFP expression day after HPC and recovered after day 4. **(B):** Image analysis showed that the EGFP signal decreased on the roof of the ventricle starting one day after HPC, and from days 2 to 5 the reduction was statistically different ($F_{(7,16)} = 4.419$, P value = 0.0066) as determined by a one-way ANOVA test (post hoc: Tukey), ($N = 24$, $n = 3$). **(C):** Decreased EGFP signal was also observed in the VMC after HPC with a statistically significant reduction from days 2 to 6 and recovered by day 7 ($F_{(7,16)} = 9.275$, P value = 0.0001) as determined by a one-way ANOVA test (post hoc: Tukey). Values are expressed as mean \pm SEM. IDV: Integrated density values, HPC: Hypoxic preconditioning, GFAP: Glial fibrillary acidic protein, EGFP: Enhanced green fluorescent protein, VMC: Ventromedial cord.

Given the observed increase in NeuN expression, we checked to see if there was a change in the number of NeuN+ cells in the molecular layer of the cerebellum after HPC, using two completely straightforward image-analysis techniques: (1) manual cell counting, and (2) optical density. However, no differences in cell number were observed after four days of HPC (Fig. 9), so we can conclude that the increased NeuN in the blots must have been due to increased expression, not to production of new neurons.

Enlargement of microglial somata after HPC

The observed increase in Iba1 expression suggested that microglial cells might be affected by HPC. To evaluate this, we measured the sizes of microglia, using immunofluorescence of coronal slices from CD1 and Pax2-GFP mice cerebella. The data from both strains were similar and thus were pooled together to show that Iba1+ cells were mostly distributed in the SVZ and supra SVZ (Fig. 10A). Although the overall number of Iba1+ cells did not change in those areas after HPC (P value = 0.1896, 32.22 ± 3.759 ($N = 9$) vs 25.80 ± 2.810 ($N = 15$)) (Fig. 10B), we could show by a closer analysis of the morphology of Iba1+ cells in the supra SVZ that their somas became slightly bigger

around 4 days after HPC. At least, we observed a reduction in the number of cells whose soma-areas were below $50 \mu\text{m}^2$ (i.e., “resting state”) (P value = 0.0003, 15.89 ± 1.711 ($N = 9$), vs 7.667 ± 1.054 . ($N = 15$)) (Fig. 10C, D). No statistically significant differences were found in the number of cells whose soma was larger than $50 \mu\text{m}^2$ (i.e., “activated state”) (P value = 0.3402, 7.778 ± 1.854 ($N = 9$) vs 10.40 ± 1.756 ($N = 15$)). In all cases, we used an unpaired *t*-test ($p < 0.05$). Values are expressed as mean \pm SEM. Sample images of the Iba1+ cells are shown in panels of Fig. 10C, D in which the differences in soma areas are observed and the complexity of the processes is contrasted. Thus, it appeared that HPC induced a subtle response in microglial cells exclusively in the supra SVZ.

Limited incorporation of BrdU after HPC

Cells positive for nestin and GFAP in other areas of the brain than those studied here have already been shown to divide and differentiate after hypoxic conditions (Zhu et al., 2005; Horie et al., 2008). Thus, we were interested to see whether cells from the VMC would also incorporate BrdU after HPC. Coronal slices along lobule I were again used to image the VMC, but unfortunately, we could not

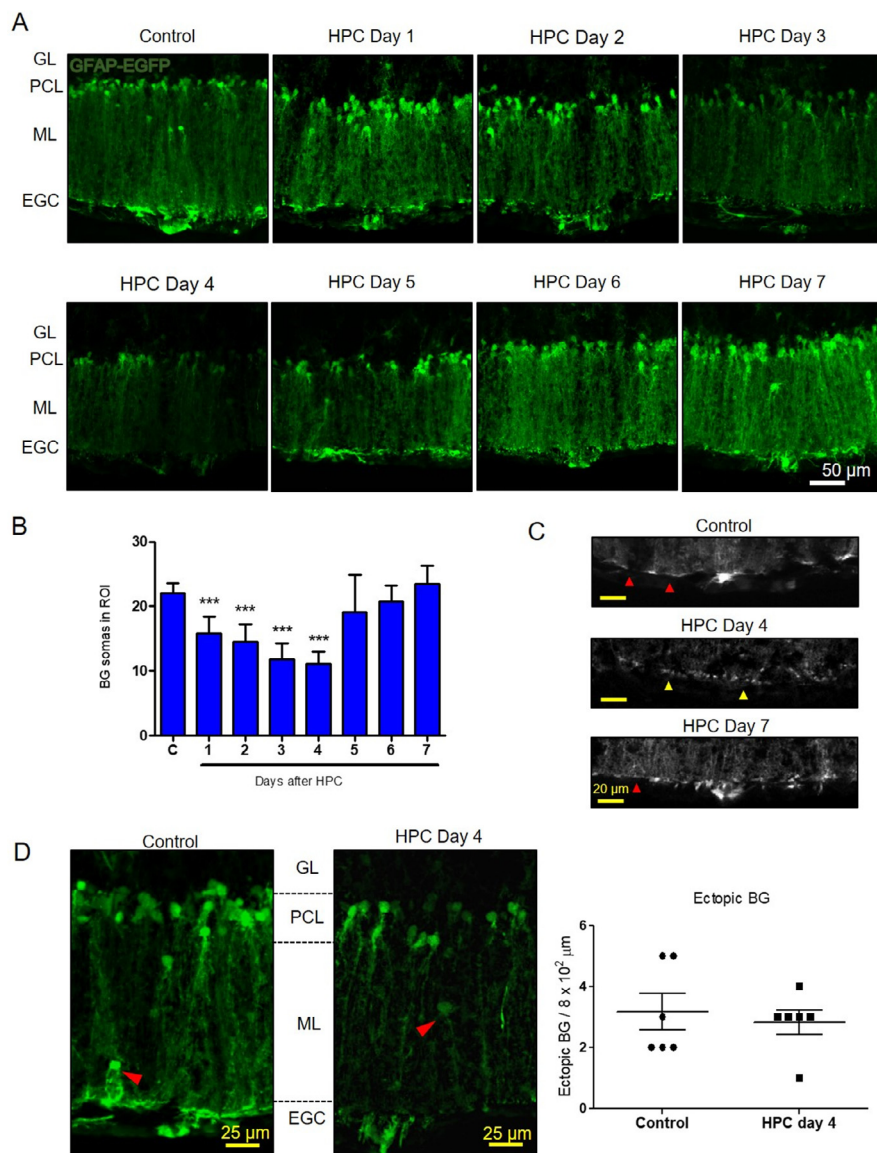


Fig. 5. Effect of HPC on Bergmann glial cells. Coronal slices of lobule I of GFAP-EGFP mice under the confocal microscope showed **(A)**: a reduction in the number of BG somata that express EGFP 1 day after HPC and until day 4; the expression recovered by day 7. **(B)**: Image analysis of the number of EGFP⁺ BG somata revealed a significant difference from day 1 to 4, with a subsequent recovery from day five ($F_{(7,112)} = 36.04$, P value < 0.0001) as determined by a one-way ANOVA test (post hoc: Tukey) ($N = 32$, $n = 4$). Values are expressed as mean \pm SEM. **(C)**: Terminal end-feet of BG as detected by EGFP appeared disorganized after HPC. Yellow arrowheads in panel day 4 point toward EGFP punctate pattern, which contrasts with the continuous fluorescence observed in control and after partial recovery at day 7 (red arrowheads). **(D)**: Ectopic EGFP⁺ BG were manually counted in coronal renderings of lobule I at day 4 after HPC. No differences were detected in cell number; red arrowheads point to displaced BG cells. HPC: Hypoxic preconditioning, GFAP: Glial fibrillary acidic protein, EGFP: Enhanced green fluorescent protein, GL: Granular layer, PCL: Purkinje cell layer, ML: Molecular layer, EGC: Ependymal glial cells. BG: Bergmann glia.

readily demonstrate any BrdU incorporation into this structure. All we could find was a bit of BrdU incorporation into the ependymal glial cells (EGC) on the roof of the ventricle, as well as a few cells in the molecular layer (Fig. 11B), consistent with our previous work (González-González et al., 2017). Furthermore, incorporation of BrdU in the floor of the fourth ventricle, that is in the

medulla, occurred at basal levels in the EGC and also in deep layers. Interestingly, BrdU incorporation was substantially increased four days after HPC in the medulla.

DISCUSSION

In the cerebellum, the roof of the ventricle includes two novel structures that we have named the subventricular cellular cluster (SVCC) and the ventromedial cord (VMC). The VMC is formed by GFAP⁺ and nestin⁺ ependymal cells whose morphology partially resembles radial glia (González-González et al., 2017). The close contact of these VMC cells with the CSF, the choroid plexus, and the underlying blood vessels, would seem to put them in an ideal position to sense variations in this important microenvironment. However, even though the VMC has been described in several mammalian species, such a functional role has never been disclosed (González-González et al., 2017).

To pursue this possibility, we sought here to show that cells in the VMC would respond to relatively mild biochemical changes in their environment, like those induced by HPC, wherein the application of repeated mild hypoxic episodes protects animals from later severe anoxia. We indeed found by image-analyses of EGFP expression with LSFM that lobule-specific changes occurred upon HPC, with clear cut reductions in EGFP expression in lobules I and X, which form the roof of the ventricle and include the VMC. Additionally, we could show that HPC induces morphological changes in the VMC and in the BG cells of lobule I, and that HPC also leads to a transient reduction in the expression of certain astrocyte markers (GFAP and ALDH1L1), plus a prolonged, greater than one week, increase in expression of NeuN, Iba1, and nestin.

Additionally, we documented here that microglia become activated for four days after HPC, specifically in the supra SVZ of lobule I of the cerebellum. On the other hand, we could not demonstrate any incorporation of BrdU into cells on the roof of the fourth ventricle after HPC, although we were surprised to find a robust incorporation of BrdU into cells on the floor of the fourth ventricle under all

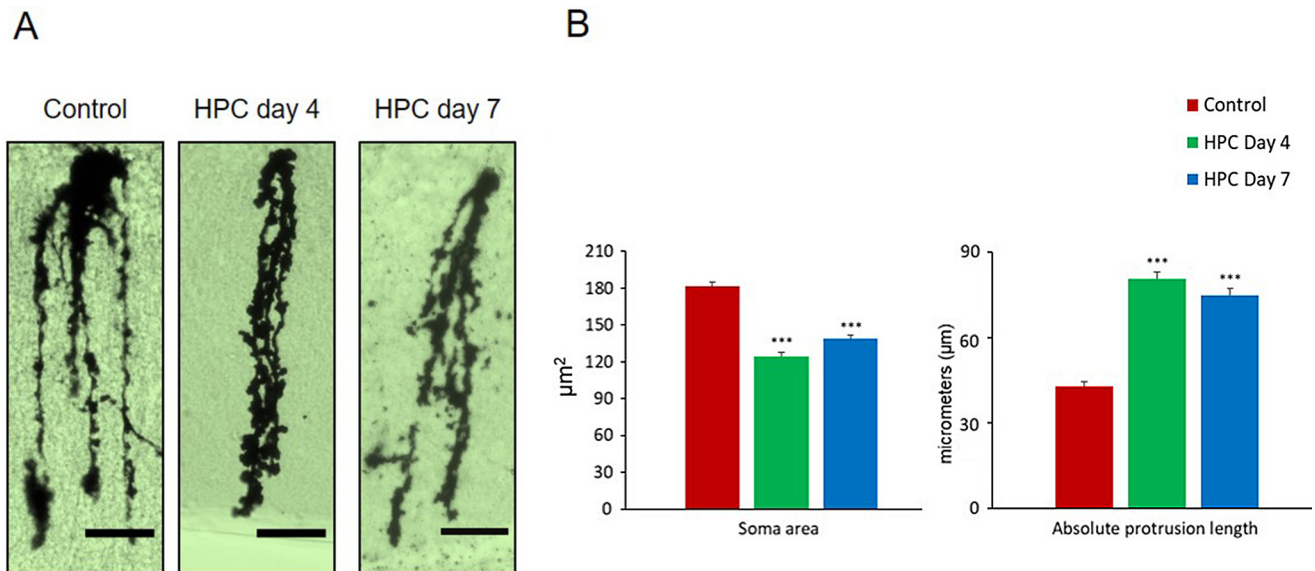


Fig. 6. Effect of HPC on the morphology of Bergmann glial cells. Golgi staining revealed fine differences: **(A)**: sample images of BG cells 4 and 7 days after HPC. **(B)**: The area of the somata were reduced and did not fully recover after 7 days. Additionally, processes retracted while absolute protrusion length was substantially increased and did not fully return to normal conditions at day 7 (P value < 0.0001 , $N = 3$, $n = 45$ for each group: Control, HPC day 4, HPC day 7). Values are expressed as mean \pm SEM. HPC: Hypoxic preconditioning. Bar: 100 μm .

conditions, which became even more robust 4 days after HPC, a unique observation that we intend to pursue in future experiments.

The application of only one behavioral test would not be adequate to assess global motor dysfunction, so in order to determine whether HPC induces any motor disability, we here used a combination of motor tests after HPC. The rotarod is a commonly used tool for testing coordination, and deficits with it are particularly obvious in mice with altered cerebellar function. The static rods test (also a coordination test) has increased sensitivity compared to the rotarod, enabling the detection of more subtle motor deficits. Finally, the horizontal bars test is ideal for rapid screening of coordination and strength in the limbs (Mann and Chesselet, 2014). We employed all three of these tests, but still could not clearly document any distinct motor deficits in our mice after HPC, nothing that was statistically significant. Nevertheless, we were left with the distinct impression that our mice did have some subtle difficulties in performing all of these behavioral tests, for the first few days after HPC. Clearly though, this mild insult was not sufficient to permanently and dramatically affect the motor system and is one more reflection of the cerebellum's exquisite and powerful control over bodily movements (Foerde and Poldrack, 2010).

Regarding the reduced expression of EGFP we observed in several areas of the cerebellum of GFAP-EGFP transgenic mice after HPC, we can be confident that this transgenic mouse line reports with a good level of fidelity the location of astrocytes and BG cells in the cerebellum (Nolte et al., 2001); and since EGFP is under the control of GFAP promoter, we can be certain that the intensity of fluorescence can properly be taken as evidence of changes in the levels of expression of GFAP, which forms the unique type of intermediate filaments that

characterize such glial cells (Eng, 1985; Kobayashi et al., 1986; Sun and Jakobs, 2012). Furthermore, our approach of using LSM for high-resolution imaging of clarified mice cerebella was clearly successful at showing that lobules of the cerebella respond with different intensity, which is likely related to the modular organization of the cerebellum.

The overall reduction in expression of EGFP we observed in transgenic GFAP-EGFP mice after HPC, paralleled by the reduced expression of GFAP and ALDH1L1 on Western blots, is hard to fit with previous work on other regions of the brain. Generally, it is held that ischemia activates astroglia, at least in striatum and cortex, and this activation induces tolerance to further ischemia, via activation of the purinergic P2X7 receptor (Hirayama et al., 2015). Also, the increased expression of Iba1 and the morphological changes that we observed in microglial cells upon HPC contrasts with earlier observations made in striatum and cortex (Hirayama et al., 2015). Further investigations will be needed, to sort out the meaning of these differences.

Regarding the increased lengths of BG processes we observed after HPC (Fig. 6), it would be interesting to determine if this reflects an increase the number of glutamate receptors in contact with Purkinje neurons. If so, it might be one more indication that in the cerebellum, BG cells are dynamic and are deeply implicated in motor control (Saab et al., 2012). Additionally, it could parallel certain changes seen in other systems in response to HPC. For example, in the olfactory bulb, synaptic efficacy appears to be altered for a short period of time after HPC, possibly due to changes in synaptic ultrastructure (Liu et al., 2015). Also, HPC has been described as increasing glutamate receptors and nitric oxide in ways that may relate to its neuroprotective effects (Li et al., 2017).

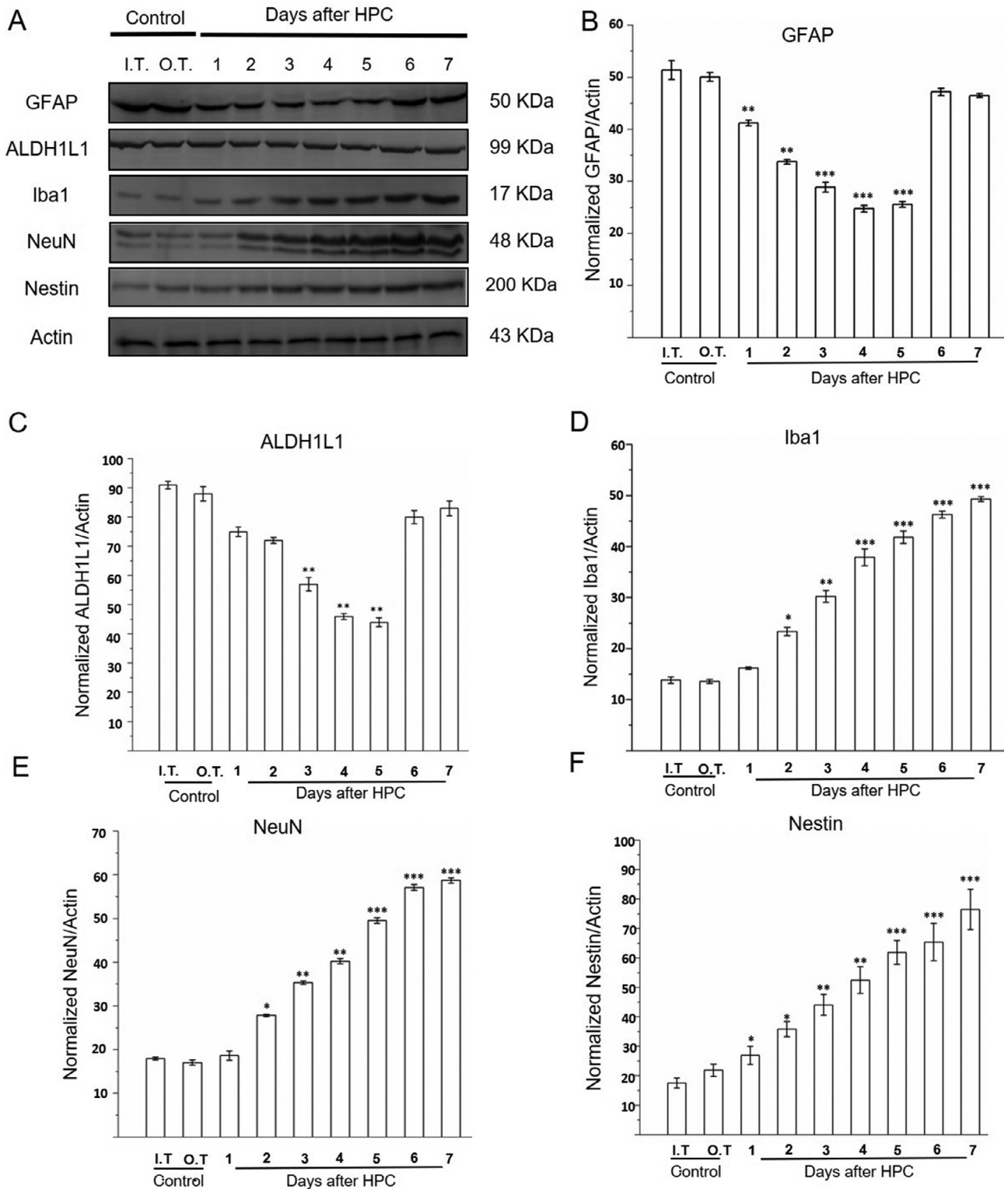


Fig. 7. Reduced expression of glial markers and increased expression in microglial, neuronal and stem cell markers after HPC. **(A)**: Representative blots of proteins isolated from cerebella before and after HPC. **B-F**: Density revealed decreased relative expression of **(B)**: GFAP and **(C)**: ALDH1L1, and increased expression of **(D)**: Iba1, **(E)**: NeuN, and **(F)**: nestin after HPC. Actin was used as internal control. HPC: Hypoxic preconditioning, I.T.: Inside a tube, O.T.: Outside a tube. Values are expressed as mean ± SEM.

Regarding our observations of NeuN levels after HPC, we have the problem that we could not demonstrate any increase by immunofluorescence, yet we did observe

some increase in NeuN expression by Western blotting. Regardless, the salient point is that we most certainly did not observe any increase in the number of NeuN +

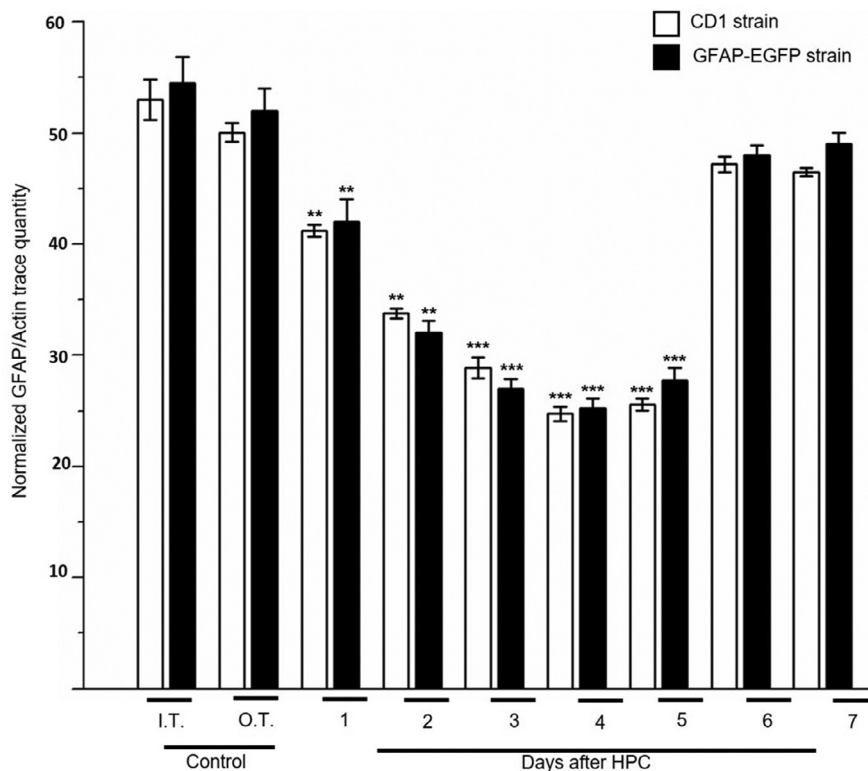


Fig. 8. Expression of GFAP after HPC in CD1 and GFAP-EGFP mice. A comparison between the level of GFAP expression was assessed by Western blot. After HPC there is no difference in the protein expression from day one until recovery at day seven between the strains (GFAP-EGFP vs CD1). Values are expressed as mean \pm SEM. Comparison of HPC with control groups showed significant differences. This supports the EGFP loss assessed by image analysis in coronal slices and *en face* preparation of transgenic GFAP-EGFP mice cerebella (Figs. 4 and 5).

cells in the cerebellum after HPC. NeuN label is normally found in granule neurons and a small population of other neurons in the lower molecular layer of the adult cerebellum (Weyer and Schilling, 2003). Finding no change here was a disappointment, since previous studies have shown that other sorts of preconditioning paradigms (like exercise for example, which also confers neuroprotective effects like the HPC used here), does appear to induce the differentiation of NeuN positive neurons in the cerebellum, apparently from Sox2+ and Nestin+ cells that reside in the Purkinje cell and internal granule layers of the cerebellum, which start off lacking any neuronal and glial differentiation markers (Ahlfeld et al., 2017). Also, it has been suggested that NeuN expression levels can be indicative of the physiological status of a post mitotic neuron (Weyer and Schilling, 2003), so we would have been gratified if we could have demonstrated changes after HPC.

Regarding our observations on microglial cells in the cerebellum, it was interesting to find that Iba1+ cells in the SVZ looked differently than those in the molecular layer (e.g., appeared less “activated”), but were strikingly abundant in both areas (especially as compared to the density of Iba1+ cells in the Purkinje cell layer). Also relevant was our finding that microglial cells in the supra SVZ responded to HPC by increasing the size of their soma and the complexity of their

processes, putting them more into their “activated” state (Noh et al., 2014; Sandvig et al., 2018). Microglia are thought to play a major role in the neuroinflammatory response in neurological diseases, potentiating neuronal recovery and in some cases regeneration (Noh et al., 2014; Sandvig et al., 2018). However, activation of microglia after HPC has not been reported in other brain areas, despite the fact that HPC protects these areas also (Chen et al., 2015). On the other hand, our results would suggest that in the cerebellum, and particularly in areas associated with CSF, the response of microglia may be stronger than elsewhere in the brain, and may synergize with the changes we observed in BG cells and cells in the VMC, and thereby play an important role in protecting the cerebellum from insult.

Regarding the increases in nestin protein-levels we observed after HPC, our first thought is that it may reflect the onset of some sort of vascular remodeling, which could be expected to occur after hypoxic preconditioning (Calderone, 2018). We are currently evaluating this possibility by imaging blood vessels after Dil staining, and already have the impression that capillaries are indeed wider at their branches at 4 days

post-HPC; however, this will be documented in subsequent reports.

Regarding the increase in BrdU incorporation we observed on the floor of the 4th ventricle (when we’d hoped to find it on the roof), the cells we found to respond to HPC might correspond to the tanyocyte-like cells recently observed in this area, known as the E2 and E3 cells, which are currently thought to relay chemical information from the CSF to underlying neural circuits along the ventral midline (Mirzadeh et al., 2017).

This is the same sort of function that we proposed for the VMC (González-González et al., 2017), but not finding any cell proliferation in this area in response to HPC did not help our proposal very much. In contrast, stem and progenitor cells have been shown to proliferate in response to HPC in other species and in other ventricular zones, such as in the SVZ of the lateral ventricles (Ara & De Montpelier, 2013; Blaise et al., 2009). All we can say is that the lack of BrdU we observed in the ependymal glial cells of the roof of the fourth ventricle is in line with previous reports, including our own (Grimaldi and Rossi, 2006; Su et al., 2014; Ahlfeld et al., 2017; González-González et al., 2017).

In summary, we here describe a broad range of structural and biochemical responses to HPC among cells on the roof and floor of the fourth ventricle,

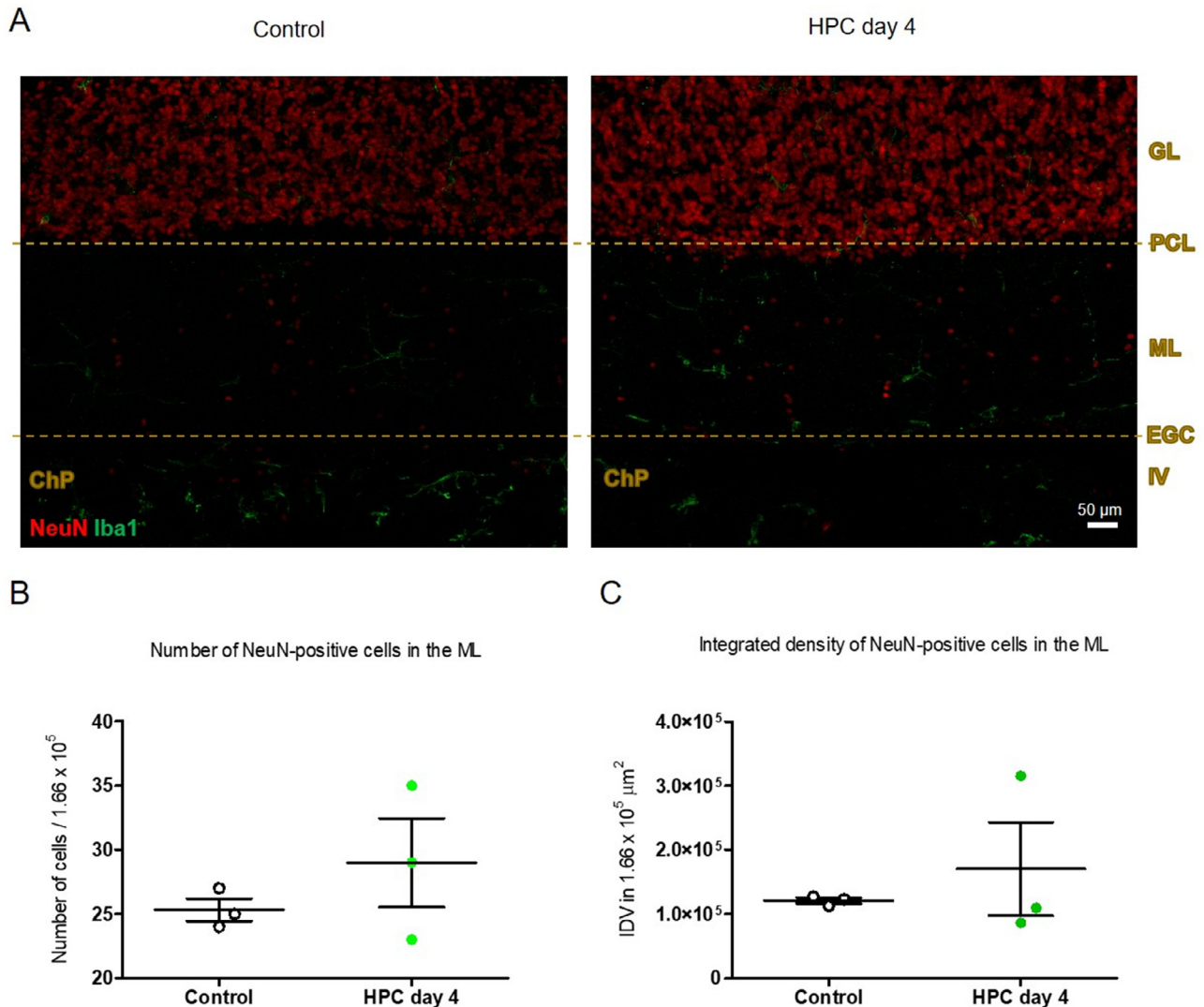


Fig. 9. Number of NeuN positive cells after the HPC. **(A):** Coronal slices from CD1 mice revealed no significant increase in the number of NeuN⁺ cells observed in the molecular layer as shown in **(B)**. **(C):** shows no significant differences in the integrated density of NeuN⁺ cells. Values are expressed as mean \pm SEM. HPC: Hypoxic preconditioning, GL: Granular layer, PCL: Purkinje cell layer, ML: Molecular layer, EGC: Ependymal glial cells. ChP: Choroid plexus, IDV: Integrated density values.

especially among the cells located in what we call the VMC, and especially involving the glial cells located therein. Broadly speaking, these observations support our original hypothesis that these cells are strategically placed to sense and respond to whatever changes may be induced in the CSF that bathes them. It will be fascinating to determine in future work, just what changes are occurring in the CSF, in response to stresses like HPC.

ACKNOWLEDGMENTS

Prof. H. Kettenmann (MDC-Berlin) and D. Reyes-Haro (INB-UNAM) for providing transgenic GFAP-EGFP mice; A.E. Espino and M. Ramírez, A. Castilla, M. García, D. Gasca, C. S. Flores and E. N. Hernández Ríos for technical assistance and Dr. R. Arellano's laboratory (INB-UNAM). Thanks to Prof. John Heuser for observations and editing the manuscript. This work was

supported by Grant A1-S-7659 from CONACyT to AMT. MBG and GBGG were supported by CONACyT (Fellowships 330119 and 277694), MBG is a doctoral student from the Programa de Doctorado en Ciencias Biomédicas, Universidad Nacional Autónoma de México (UNAM), MBG was supported by a PAEP travel grant. RVD was supported by a postdoctoral fellowship from UNAM-DGAPA. We thank to K. Engberg and K. Deisseroth from Stanford University. E.JG and PLA acknowledge financial support from the Spanish Ministry of Economy and Competitiveness (AEI/FEDER), through founded programs BIO2014-59614-JIN, RYC-2015-17935 and FIS2016-80455-R (AEI/FEDER), European Union grant EU-H2020 713140; the "Severo Ochoa" Programme for Centres of Excellence in R&D (SEV-2015-0522), Fundació Privada Cellex, Fundació Mig-Puig and the CERCA program and Laserlab-Europe (EU-H2020 654148). GBGG and AB acknowledge

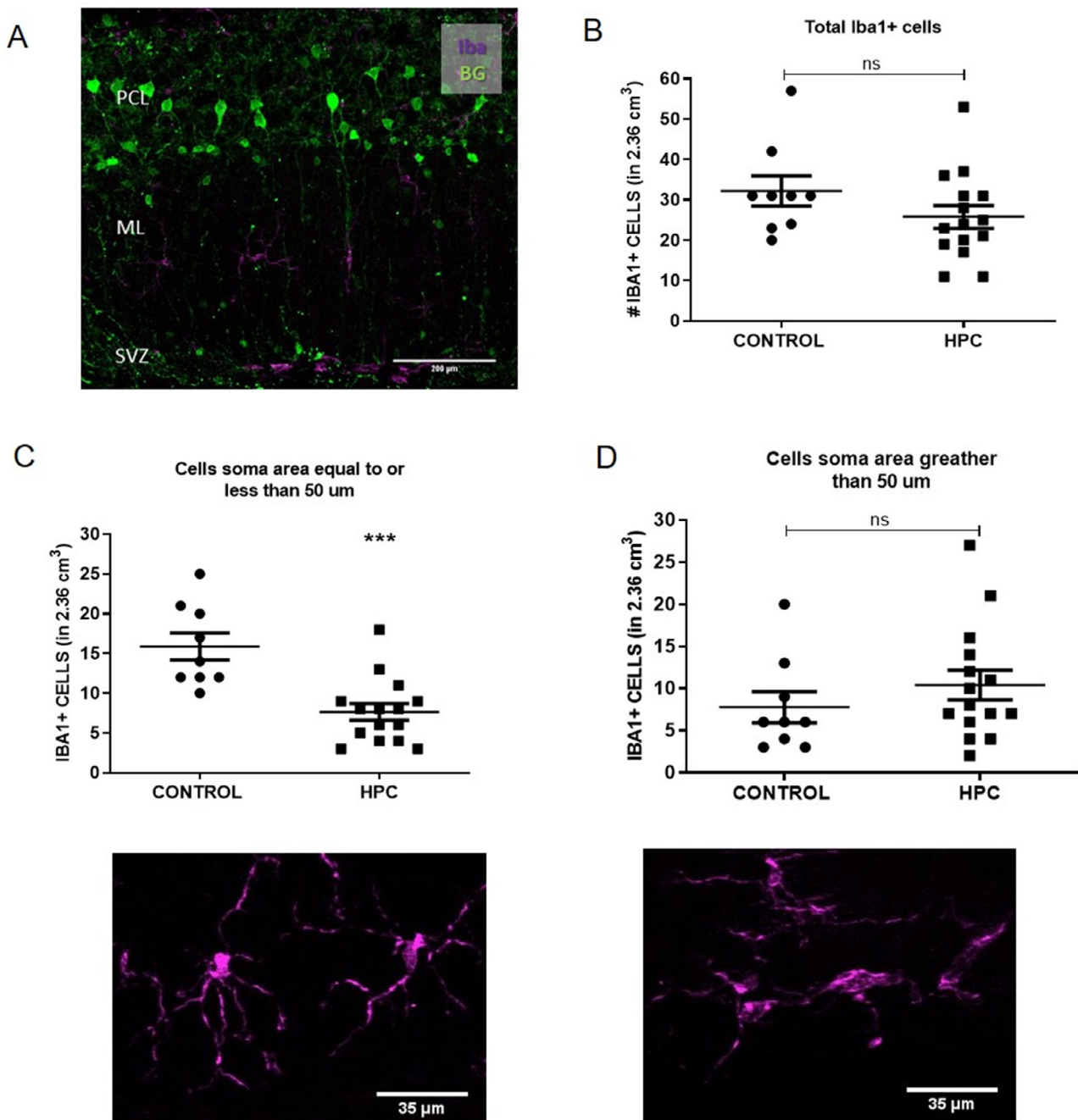


Fig. 10. Analysis of Iba1⁺ cells after HPC. Coronal slices from lobule I were analyzed by confocal microscopy after Iba1 immunodetection in GFAP-EGFP and Pax2-GFP mice. **(A):** Sample image that shows Iba1⁺ cell distribution across cerebellar layers of lobule I from control mice. Note the preferential presence of Iba1⁺ cells in the SVZ. **(B):** Total Iba1⁺ cells along lobule I did not change 4 days after HPC. **(C):** The number of Iba1⁺ cells with area of the soma equal to or less than 50 μm decreased in the supra SVZ 4 days after HPC; in contrast, **(D):** the number of cells with a soma larger than 50 μm remained unaltered after HPC. C and D show sample images of Iba1⁺ cells to contrast the size of the somata. BG: Bergmann glia, PCL: Purkinje cell layer, ML: molecular layer, SVZ: Subventricular zone, HPC: Hypoxic preconditioning. Bar: in A: 200 μm and in C, D: 35 μm.

financial support from the Italian Ministry of Higher Education and the University of Torino (Italy), under the auspices of I@UNITO – Visiting Scientists project, 2017

edition. J. G. Norris kindly edited the manuscript. AMT dedicated this paper to Prof. Ricardo Miledi (1927–2017), mentor and friend.

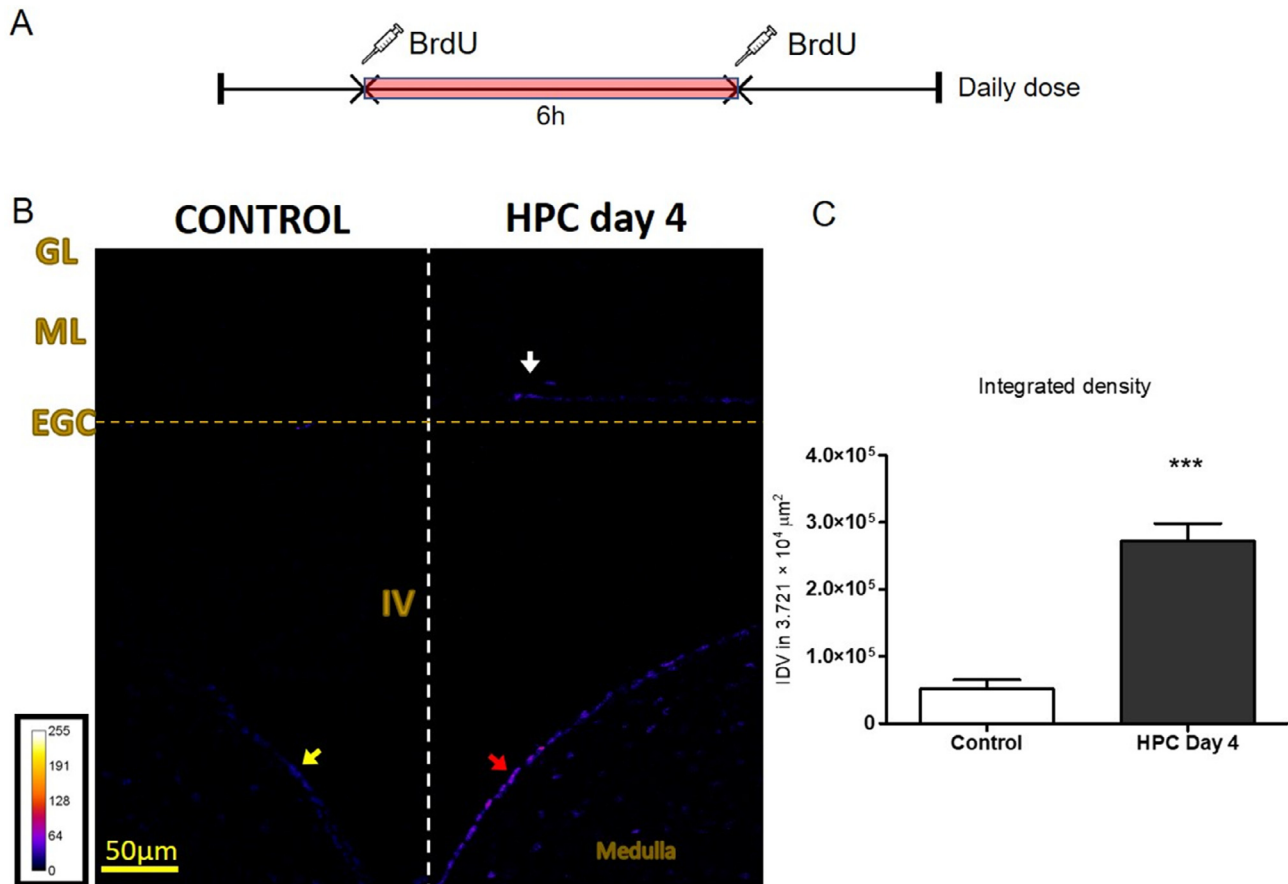


Fig. 11. Limited incorporation of BrdU was detected at the roof of the fourth ventricle after HPC. **(A):** Two BrdU injections (50 mg/kg) with a 6 h interval were intraperitoneally administered daily for 5 days after HPC and prior to euthanizing. **(B):** Control group showed some incorporation of BrdU in cells of the floor of the fourth ventricle corresponding to the medulla (yellow arrow), which became more evident 4 days after HPC (red arrow). This contrasted with the cerebellum, where BrdU was scarcely detected in controls but detected 4 days after HPC along the EGC (white arrow). **(C):** A statistical significant difference was observed in the integrated density values when comparing the BrdU incorporation in the roof of the fourth ventricle. HPC: Hypoxic preconditioning, GL: Granular layer, ML: Molecular layer, EGC: Ependymal glial cells, IV: Fourth ventricle, IDV: Integrated density values.

DECLARATIONS OF INTEREST

None.

REFERENCES

- Ahlfeld J, Filser S, Schmidt F, Wefers AK, Merk DJ, Glaß R, Herms J, Schüller U (2017) Neurogenesis from Sox2 expressing cells in the adult cerebellar cortex. *Sci Rep* 7:6137. Available at: <http://www.ncbi.nlm.nih.gov/pubmed/28733588> [Accessed January 13, 2019].
- Ara J, De montpellier S (2013) Hypoxic-preconditioning enhances the regenerative capacity of neural stem/progenitors in subventricular zone of newborn piglet brain. *Stem Cell Res* 11:669–686. Available at: <https://www.sciencedirect.com/science/article/pii/S1873506113000457?via%3Dihub> [Accessed June 4, 2018].
- Benitez SG, Castro AE, Patterson SI, Muñoz EM, Seltzer AM (2014) Hypoxic preconditioning differentially affects GABAergic and glutamatergic neuronal cells in the injured cerebellum of the neonatal rat. *PLoS One* 9.
- Blaise SA, Nédélec E, Alberto J-M, Schroeder H, Audonnet S, Bossenmeyer-Pouricé C, Guéant J-L, Daval J-L (2009) Short hypoxia could attenuate the adverse effects of hyperhomocysteinemia on the developing rat brain by inducing neurogenesis. *Exp Neurol* 216:231–238. Available at: <https://www.sciencedirect.com/science/article/pii/S0014488608004676> [Accessed June 4, 2018].
- Bonfanti L (2013) The (real) neurogenic/gliogenic potential of the postnatal and adult brain parenchyma. *ISRN Neurosci* 2013:354136. Available at: <http://dx.doi.org/10.1155/2013/354136> [Accessed March 6, 2018].
- Bradford MM (1976) A rapid and sensitive method for the quantitation of microgram quantities of protein utilizing the principle of protein-dye binding. *Anal Biochem* 72:248–254. Available at: <https://www.sciencedirect.com/science/article/pii/0003269776905273?via%3Dihub> [Accessed January 20, 2019].
- Brooks SP, Dunnett SB (2009) Tests to assess motor phenotype in mice: a user's guide. *Nat Rev Neurosci* 10:519–529.
- Calderone A (2018) The biological role of Nestin(+)-cells in physiological and pathological cardiovascular remodeling. *Front Cell Dev Biol* 6:15. Available at: <http://journal.frontiersin.org/article/10.3389/fcell.2018.00015/full> [Accessed April 23, 2019].
- Cerrato V, Mercurio S, Leto K, Fucà E, Hoxha E, Bottes S, Pagin M, Milanese M, Ngan CY, Concina G, Ottolenghi S, Wei CL, Bonanno G, Pavesi G, Tempia F, Buffo A, Nicolis SK (2018) Sox2 conditional mutation in mouse causes ataxic symptoms, cerebellar vermis hypoplasia, and postnatal defects of Bergmann glia. *Glia* 66:1929–1946.
- Chen C-Y, Sun W-Z, Kang K-H, Chou H-C, Tsao P-N, Hsieh W-S, Fu W-M (2015) Hypoxic preconditioning suppresses glial activation and neuroinflammation in neonatal brain insults. *Mediators*

- Inflamm 2015:632592. Available at: <http://www.ncbi.nlm.nih.gov/pubmed/26273140> [Accessed May 10, 2018].
- Cipolla MJ (2009) The cerebral circulation. *Morgan & Claypool Life Sciences*. Available at: <http://www.ncbi.nlm.nih.gov/pubmed/21452434> [Accessed June 4, 2018].
- Davis BM, Salinas-Navarro M, Cordeiro MF, Moons L, De Groef L (2017) Characterizing microglia activation: a spatial statistics approach to maximize information extraction. *Sci Rep*.
- De Zeeuw CI, Hoogland TM (2015) Reappraisal of Bergmann glial cells as modulators of cerebellar circuit function. *Front Cell Neurosci* 9:246. Available at: <http://journal.frontiersin.org/Article/10.3389/fncel.2015.00246/abstract> [Accessed April 11, 2018].
- Deacon RMJ (2013) Measuring motor coordination in mice. *J Vis Exp* Available. Available at: <http://www.jove.com/video/2609/measuring-motor-coordination-in-mice>.
- Del MR (1995) The ependyma: a protective barrier between brain and cerebrospinal fluid. *Glia* 14(1). Available at: <https://onlinelibrary.wiley.com/doi/pdf/10.1002/glia.440140102> [Accessed June 4, 2018].
- Diaz-Cintra S, Cintra L, Kemper T, Resnick O, Morgane PJ (1981) Nucleus raphe dorsalis: A morphometric golgi study in rats of three age groups. *Brain Res* 207:1–16. Available at: <https://linkinghub.elsevier.com/retrieve/pii/0006899381906752> [Accessed June 7, 2019].
- Emerson MR, Nelson SR, Samson FE, Pazdernik TL (1999) A global hypoxia preconditioning model: neuroprotection against seizure-induced specific gravity changes (edema) and brain damage in rats. *Brain Res Brain Res Protoc* 4:360–366. Available at: <http://www.ncbi.nlm.nih.gov/pubmed/10592346> [Accessed May 28, 2019].
- Eng LF (1985) Glial fibrillary acidic protein (GFAP): the major protein of glial intermediate filaments in differentiated astrocytes. *J Neuroimmunol*.
- Feliciano DM, Bordey A, Bonfanti L (2015) Noncanonical sites of adult neurogenesis in the mammalian brain. *Cold Spring Harb Perspect Biol* 7:a018846. Available at: <http://www.ncbi.nlm.nih.gov/pubmed/26384869> [Accessed April 20, 2018].
- Foerde K, Poldrack RA (2010) Procedural learning in humans. *Encyclopedia of neuroscience*, 2010.
- Gage GJ, Kipke DR, Shain W (2012) Whole animal perfusion fixation for rodents. *J Vis Exp*. Available at: <http://www.jove.com/video/3564/whole-animal-perfusion-fixation-for-rodents>.
- Gidday JM, Perez-Pinzon MA, Zhang JH (2013) Innate tolerance in the CNS: Translational neuroprotection by pre- and post-conditioning.
- González-González MA, Gómez-González GB, Becerra-González M, Martínez-Torres A (2017) Identification of novel cellular clusters define a specialized area in the cerebellar periventricular zone. *Sci Rep* 7.
- González-González MA, Ostos-Valverde A, Becerra-Hernández A, Sánchez-Castillo H, Martínez-Torres A (2015) The effect of carmustine on Bergmann cells of the cerebellum. *Neurosci Lett* 595:18–24. Available at: <https://www.sciencedirect.com/science/article/pii/S0304394015002700?via%3Dihub#!> [Accessed January 20, 2019].
- Grimaldi P, Rossi F (2006) Lack of neurogenesis in the adult rat cerebellum after Purkinje cell degeneration and growth factor infusion. *Eur J Neurosci* 23:2657–2668. Available at: <http://doi.wiley.com/10.1111/j.1460-9568.2006.04803.x> [Accessed January 14, 2019].
- Hanke S, Reichenbach A (1987) Quantitative-morphometric aspects of bergmann glial (Golgi epithelial) cell development in rats – a golgi study. *Anat Embryol (Berl)* 177:183–188.
- Hibi M, Matsuda K, Takeuchi M, Shimizu T, Murakami Y (2017) Evolutionary mechanisms that generate morphology and neural-circuit diversity of the cerebellum. *Dev Growth Differ* 59:228–243. Available at: <http://doi.wiley.com/10.1111/dgd.12349> [Accessed January 20, 2019].
- Hirayama Y, Ikeda-Matsuo Y, Notomi S, Enaida H, Kinouchi H, Koizumi S (2015) Astrocyte-mediated ischemic tolerance. *J Neurosci* 35:3794–3805. Available at: <http://www.ncbi.nlm.nih.gov/pubmed/25740510> [Accessed June 4, 2018].
- Hoogland TM, De Grujil JR, Witter L, Canto CB, De Zeeuw CI (2015) Role of synchronous activation of cerebellar Purkinje cell ensembles in multi-joint movement control. *Curr Biol* 25:1157–1165. Available at: <http://www.ncbi.nlm.nih.gov/pubmed/25843032> [Accessed January 20, 2019].
- Horie N, So K, Moriya T, Kitagawa N, Tsutsumi K, Nagata I, Shinohara K (2008) Effects of oxygen concentration on the proliferation and differentiation of mouse neural stem cells in vitro. *Cell Mol Neurobiol* 28:833–845.
- Kim H-Y (2015) Statistical notes for clinical researchers: post-hoc multiple comparisons. *Restor Dent Endod* 40:172–176. Available at: <http://www.ncbi.nlm.nih.gov/pubmed/25984481> [Accessed May 22, 2019].
- Kobayashi S, Chiu FC, Katayama M, Sacchi RS, Suzuki K, Suzuki K (1986) Expression of glial fibrillary acidic protein in the CNS and PNS of murine globoid cell leukodystrophy, the twitcher. *Am J Pathol* 125:227–243. Available at: <http://www.ncbi.nlm.nih.gov/pubmed/3538889> [Accessed January 20, 2019].
- Kriegstein A, Alvarez-Buylla A (2009) The glial nature of embryonic and adult neural stem cells. *Annu Rev Neurosci* 32:149–184. Available at: <http://www.annualreviews.org/doi/10.1146/annurev.neuro.051508.135600>.
- Lang H, Xing Y, Brown LN, Samuvel DJ, Panganiban CH, Havens LT, Balasubramanian S, Wegner M, Krug EL, Barth JL (2015) Neural stem/progenitor cell properties of glial cells in the adult mouse auditory nerve. *Sci Rep* 5. Available at: <https://www.nature.com/articles/srep13383>.
- Li S, Hafeez A, Noorulla F, Geng X, Shao G, Ren C, Lu G, Zhao H, Ding Y, Ji X (2017) Preconditioning in neuroprotection: from hypoxia to ischemia. *Prog Neurobiol*.
- Liu C, Peng Z, Zhang N, Yu L, Han S, Li D, Li J (2012) Identification of differentially expressed microRNAs and their PKC-isoform specific gene network prediction during hypoxic pre-conditioning and focal cerebral ischemia of mice. *J Neurochem* 120:830–841.
- Liu Y, Sun Z, Sun S, Duan Y, Shi J, Qi Z, Meng R, Sun Y, Zeng X, Chui D, Ji X (2015) Effects of hypoxic preconditioning on synaptic ultrastructure in mice. *Synapse*.
- López-Aguilera F, Plateo-Pignatari MG, Biaggio V, Ayala C, Seltzer AM (2012) Hypoxic preconditioning induces an AT2-R/VEGFR-2 (Flk-1) interaction in the neonatal brain microvasculature for neuroprotection. *Neuroscience* 216:1–9.
- Mandalos NP, Karampelas L, Saridakis M, McKay RDG, Cohen ML, Remboutsika E (2018) A role for Sox2 in the adult cerebellum. *J Stem Cell Res Ther* 8. Available at: <http://www.ncbi.nlm.nih.gov/pubmed/30568848> [Accessed January 13, 2019].
- Mann A, Chesselet MF (2014) Techniques for Motor Assessment in Rodents. *Movement disorders: genetics and models: second edition*, 2014.
- Mirzadeh Z, Kusne Y, Duran-Moreno M, Cabrales E, Gil-Perotin S, Ortiz C, Chen B, Garcia-Verdugo JM, Sanai N, Alvarez-Buylla A (2017) Bi- and unciliated ependymal cells define continuous floor-plate-derived tanyctytic territories. *Nat Commun* 8.
- National Research Council (U.S.), Committee for the Update of the Guide for the Care and Use of Laboratory Animals, Institute for Laboratory Animal Research (U.S.) (2011) *Guide for the care and use of laboratory animals*. National Academies Press.
- Noh H, Jeon J, Seo H (2014) Systemic injection of LPS induces region-specific neuroinflammation and mitochondrial dysfunction in normal mouse brain. *Neurochem Int* 69:35–40. Available at: <https://www.sciencedirect.com/science/article/pii/S0197018614000382?via%3Dihub> [Accessed June 4, 2018].
- Nolte C, Matyash M, Pivneva T, Schipke CG, Ohlemeyer C, Hanisch UK, Kirchhoff F, Kettenmann H (2001) GFAP promoter-controlled EGFP-expressing transgenic mice: a tool to visualize astrocytes and astrogliosis in living brain tissue. *Glia* 33:72–86.
- Olarte OE, Andilla J, Gualda EJ, Loza-Alvarez P (2018) Light-sheet microscopy: a tutorial. *Adv Opt Photonics* 10:111. Available at: <https://www.osapublishing.org/abstract.cfm?URI=aop-10-1-111> [Accessed June 14, 2018].

- Parmigiani E, Leto K, Rolando C, Figueres-Oñate M, López-Mascaraque L, Buffo A, Rossi F (2015) Heterogeneity and bipotency of astroglial-like cerebellar progenitors along the interneuron and glial lineages. *J Neurosci* 35:7388–7402. Available at: <http://www.ncbi.nlm.nih.gov/pubmed/25972168> [Accessed May 10, 2018].
- Ponti G, Peretto P, Bonfanti L (2008) Genesis of neuronal and glial progenitors in the cerebellar cortex of peripuberal and adult rabbits. *PLoS One* 3:e2366. Available at: <http://www.ncbi.nlm.nih.gov/pubmed/18523645> [Accessed April 20, 2018].
- Reyes-Haro D, González-González MA, Péttriz A, Rosas-Arellano A, Kettenmann H, Miledi R, Martínez-Torres A (2013) γ -Aminobutyric acid- ρ expression in ependymal glial cells of the mouse cerebellum. *J Neurosci Res* 91:527–534. Available at: <http://doi.wiley.com/10.1002/jnr.23183> [Accessed April 10, 2018].
- Rosas-Arellano A, Ochoa-de la Paz LD, Miledi R, Martínez-Torres A (2007) Brain distribution and molecular cloning of the bovine GABA ρ 1 receptor. *Neurosci Res* 57:347–353. Available at: http://www.ncbi.nlm.nih.gov/entrez/query.fcgi?cmd=Retrieve&db=PubMed&dopt=Citation&list_uids=17188384.
- Rybnikova E, Samoilov M (2015) Current insights into the molecular mechanisms of hypoxic pre- and postconditioning using hypobaric hypoxia. *Front Neurosci* 9.
- Saab AS, Neumeyer A, Jahn HM, Cupido A, Šimek AAM, Boele HJ, Scheller A, Le Meur K, Götz M, Monyer H, Sprengel R, Rubio ME, Deitmer JW, De Zeeuw CI, Kirchhoff F (2012) Bergmann glial AMPA receptors are required for fine motor coordination. *Science* (80-).
- Sandvig I, Augestad IL, Håberg AK, Sandvig A (2018) Neuroplasticity in stroke recovery. The role of microglia in engaging and modifying synapses and networks. *Eur J Neurosci*. Available at: <http://doi.wiley.com/10.1111/ejn.13959> [Accessed June 4, 2018].
- Santilli G, Lamorte G, Carlessi L, Ferrari D, Rota Nodari L, Binda E, Delia D, Vescovi AL, De Filippis L (2010) Mild hypoxia enhances proliferation and multipotency of human neural stem cells. *Najbauer J, ed.*. *PLoS One* 5:e8575. Available at: <http://dx.plos.org/10.1371/journal.pone.0008575>.
- Shiga T, Ichikawa M, Hirata Y (1983) A Golgi study of Bergmann glial cells in developing rat cerebellum. *Anat Embryol (Berl)* 167:191–201.
- Stefaniuk M, Gualda EJ, Pawlowska M, Legutko D, Matryba P, Koza P, Konopka W, Owczarek D, Wawrzyniak M, Loza-Alvarez P, Kaczmarek L (2016) Light-sheet microscopy imaging of a whole cleared rat brain with Thy1-GFP transgene. *Sci Rep* 6:28209. Available at: <http://www.nature.com/articles/srep28209> [Accessed January 20, 2019].
- Su X, Guan W, Yu Y-C, Fu Y (2014) Cerebellar stem cells do not produce neurons and astrocytes in adult mouse. *Biochem Biophys Res Commun* 450:378–383. Available at: <https://www.sciencedirect.com/science/article/pii/S0006291X14010201?via%3Dihub> [Accessed April 20, 2018].
- Sun D, Jakobs TC (2012) Structural remodeling of astrocytes in the injured CNS. *Neuroscientist* 18:567–588. Available at: <http://www.ncbi.nlm.nih.gov/pubmed/21982954> [Accessed January 20, 2019].
- Voogd J, Glickstein M (1998) The anatomy of the cerebellum. *Trends Neurosci* 21:370–375. Available at: <http://www.ncbi.nlm.nih.gov/pubmed/9735944> [Accessed April 9, 2018].
- Weyer A, Schilling K (2003) Developmental and cell type-specific expression of the neuronal marker NeuN in the murine cerebellum. *J Neurosci Res*.
- Witter L, De Zeeuw CI (2015) Regional functionality of the cerebellum. *Curr Opin Neurobiol* 33:150–155. Available at: <https://www.sciencedirect.com/science/article/pii/S0959438815000720?via%3Dihub> [Accessed January 20, 2019].
- Zhang N, Yin Y, Han S, Jiang J, Yang W, Bu X, Li J (2011) Hypoxic preconditioning induced neuroprotection against cerebral ischemic injuries and its cPKC γ -mediated molecular mechanism. *Neurochem Int* 58:684–692.
- Zhang Y-B, Guo Z-D, Li M-Y, Li S-J, Niu J-Z, Yang M-F, Ji X-M, Lv G-W (2015) Cerebrospinal fluid from rats given hypoxic preconditioning protects neurons from oxygen-glucose deprivation-induced injury. *Neural Regen Res* 10:1471–1476. Available at: <http://www.ncbi.nlm.nih.gov/pubmed/26604909> [Accessed January 20, 2019].
- Zhu LL, Wu LY, Yew DT, Fan M (2005) Effects of hypoxia on the proliferation and differentiation of NSCs. In: *Molecular neurobiology*. Humana Press. p. 231–242.

(Received 16 February 2019, Accepted 11 September 2019)
(Available online 2 November 2019)

SCIENTIFIC REPORTS



OPEN

Identification of novel cellular clusters define a specialized area in the cerebellar periventricular zone

María Alejandra González-González, Gabriela B. Gómez-González, Marymar Becerra-González & Ataúlfo Martínez-Torres

Received: 13 July 2016
Accepted: 05 December 2016
Published: 20 January 2017

The periventricular zone of cerebellum is a germinative niche during the embryonic development, nevertheless its structural organization and functional implications in adult have not been widely studied. Here we disclose the presence of two novel clusters of cells in that area. The first one was named the subventricular cellular cluster (SVCC) and is composed of cells that express glial and neuronal markers. The second was named the ventromedial cord (VMC) and appears as a streak of biciliated cells with microvillousities facing the ventricle, that includes GFAP⁺ and nestin⁺ cells organized along the periventricular vasculature. The dorsal limit of the SVCC is associated with myelinated axons of neurons of unknown origin. This paper describes the characteristics and organization of these groups of cells. They can be observed from late embryonic development in the transgenic mouse line GFAP-GFP. The SVCC and VMC expand during early postnatal development but are restricted to the central area of the ventricle in adulthood. We did not find evidence of cell proliferation, cell migration or the presence of fenestrated blood vessels. These findings provide new insights into the knowledge of the cellular composition and structural organization of the periventricular zone of cerebellum.

It has been shown previously that the subventricular zone of the cerebellum exhibits a diversity of cells that display different electrophysiological characteristics¹. Whole-cell patch-clamp revealed that electric responses obtained from the subventricular zone of the cerebellum, which corresponds to lobes I and X, include neurons, astrocytes, oligodendrocytes and stem-cell like cells¹. This evidence is consistent with other observations that demonstrated the presence of ependymal ciliated glial cells and fibers that seem to correspond to axons². Hitherto, as far as we know, structural evidence for the presence of oligodendrocytes or an active niche of stem cells on the roof of the fourth ventricle has not been shown. In our previous report¹, we provided evidence that cells forming the ependymal glial cell layer of the roof of the fourth ventricle respond to γ -aminobutyric acid (GABA), a neurotransmitter known for its modulatory role in neurogenesis and cell migration in the lateral ventricles^{3–6}.

Whereas the role of GABA neurotransmission in the periventricular area of the lateral ventricles has received much attention due to the presence of an active neurogenic niche^{7,8}, information concerning the cellular diversity and organization of the ependymal surface of the roof of the fourth ventricle is relatively scarce^{2,9}. We do not yet know the source of GABA that may evoke the electric responses generated by ependymal glial cells; however, the participation of the GABA-A receptors was established based on their electrophysiological and pharmacological characteristics: chloride currents blocked by bicuculline and 1,2,5,6-Tetrahydropyridin-4-yl methylphosphinic acid (TPMPA), as well as assessed by *in situ* hybridization and immunofluorescence¹. It is well known that GABA, acting through GABA-A receptors, triggers the differentiation of neuroblasts in postnatal subventricular zones. Thus, we considered worthwhile to explore the organization of the periventricular zone of the cerebellum in which we reported the presence and electrophysiological profile of GABA-A receptors.

A visual inspection of a 1-mm toluidine blue-stained coronal section of the roof of the fourth ventricle (lobes I and X) revealed that the area from which the electrophysiological GABA responses were obtained¹ forms an isolated cluster of cells with heterogeneous characteristics (Fig. 1A–C). This cluster is limited dorsally by the terminal feet of the Bergmann glia and ventrally by the ependymal glial cell layer (Fig. 1J, yellow and green arrowheads, respectively). We will refer to this structure as the subventricular cellular cluster (SVCC). A possible explanation for the presence of the SVCC is that this structure corresponds to remnants of proliferative zones that are active

Instituto de Neurobiología, Universidad Nacional Autónoma de México, Departamento de Neurobiología Celular y Molecular, Laboratorio de Neurobiología Molecular y Celular, Juriquilla, Querétaro, 76230, México. Correspondence and requests for materials should be addressed to A.M.-T. (email: ataulfo@unam.mx)

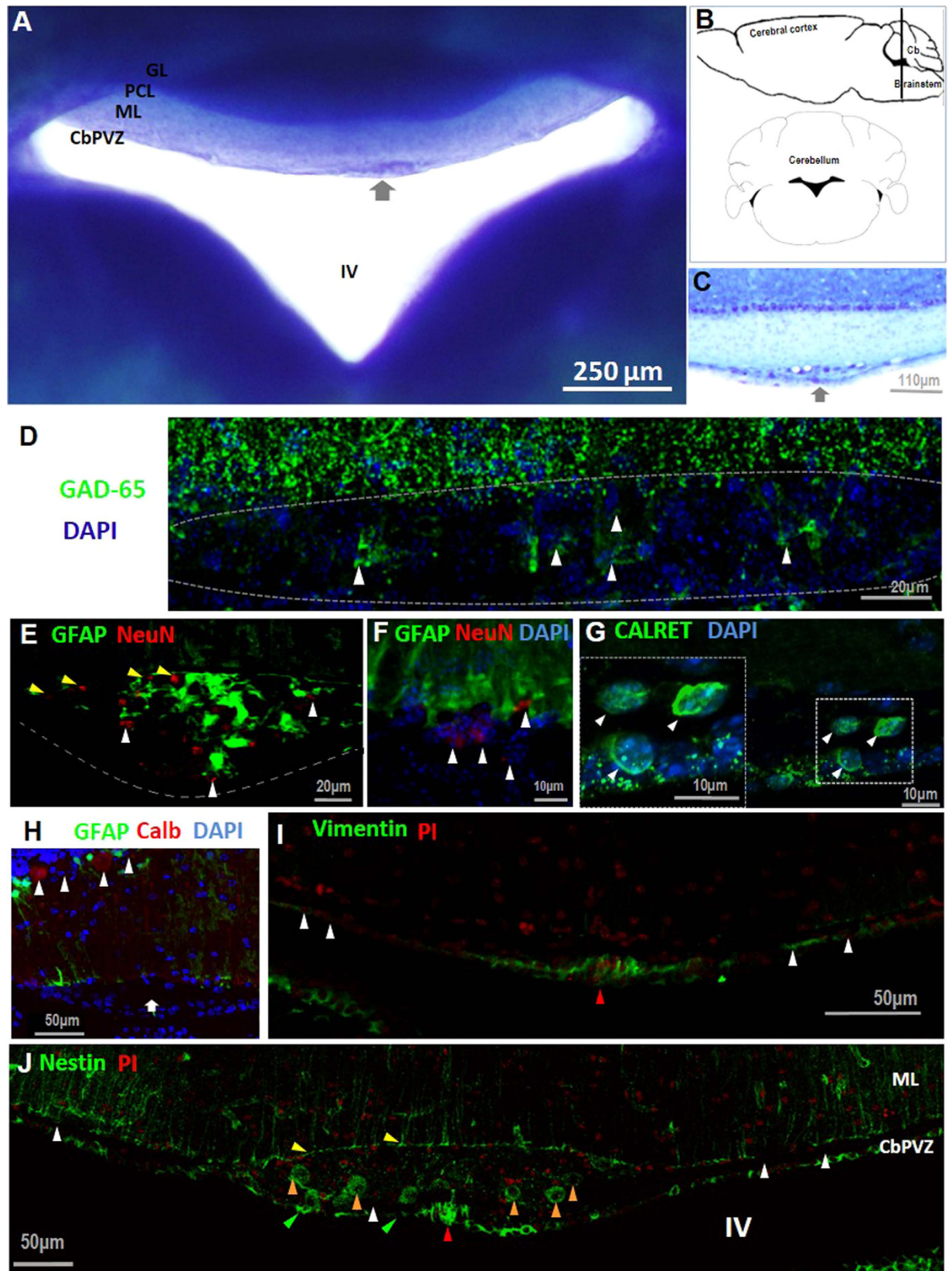


Figure 1. Position and organization of the subventricular cellular cluster. (A) and (C), toluidine blue stain of 1-mm and 40- μ m (respectively) coronal cerebellar slices; an arrow indicates the location of the SVCC in the CbPVZ. (B) a black line indicates the location of the SVCC in a sagittal plane, and below (C), it is shown in the coronal plane. (D). White arrowheads point to cells positive for GAD-65 in the SVCC. (E) Cells expressing the neuronal NeuN marker are distributed in the SVCC (white arrowheads); some of the cells are in vicinity with the terminal end feet of Bergmann glia (yellow arrowheads in E and white arrowheads in F). (G) Calretinin-

positive cells are distributed throughout the SVCC (white arrowheads); the insert shows an amplification. (H) The SVCC does not include calbindin-positive cells (arrow), in contrast to Purkinje neurons (arrowheads). (I) Vimentin label was found in a population of ependymal glial cells (red arrowhead) but absent in the SVCC. (J) SVCC includes cells positive for nestin (orange arrowheads), and is delimited dorsally by Bergmann glia (yellow arrowheads) and ventrally by ependymal cells (green arrowheads). Cb: cerebellum; GL: granular layer; PCL: Purkinje cellular layer; ML: molecular layer; CbPVZ: cerebellar periventricular zone; IV: fourth ventricle; PI: propidium iodide; CALRET: calretinin; GFAP: glial fibrillar acidic protein; Calb: calbindin; GAD-65: glutamate decarboxylase isoform 65.

during early development or that it is a specialized zone integrating signals among the parenchyma, cerebrospinal fluid and blood. To examine these possibilities and to explore potential roles for this cluster of cells we used a combination of techniques that include immunofluorescence, CLARITY, transmission and scanning electron microscopy as well as electrophysiology. Finally, we also tested the proliferation potential of the SVCC cells.

Materials and Methods

Ethics statement. All protocols and procedures were approved by the Bioethics Committee of the Instituto de Neurobiología, Universidad Nacional Autónoma de México (INB-UNAM license: INEU/SA/CB089) in accordance with the rules and regulations of the Society for Neuroscience: Policies on the Use of Animals and Humans in Neuroscience Research and on local and international bioethical guidelines including the NOM-062-ZOO which is in accordance with the recommendations of the National Institutes of Health publication: “Guide for the Care and Use of Laboratory Animals”.

Animals. CD1 and transgenic GFAP-GFP mice¹⁰ from embryonic (E) to postnatal day (P) 30 to P60 were obtained from the local vivarium.

Immunohistofluorescence. P30 male CD1 mice were deeply anesthetized with pentobarbital (30 mg/kg) and intracardially perfused with saline solution followed by PFA (4%) in phosphate-buffered saline (PBS), pH 7.2. For whole mount immunolabeling, PFA (4%) in PBS plus Triton (0.1%) was used¹¹. For slices, cerebella were processed as previously reported¹². The following antibodies were used in a 1:200 dilution: nestin (Santa Cruz, sc-21249), vimentin (Sigma, V4630), calbindin (Santa Cruz, sc7691), calretinin (Santa Cruz, sc11644), myelin basic protein (Abcam, ab40390), NG2 (Santa Cruz, sc30923) Ki67 (Abcam, ab15580), GAD65 (Santa Cruz, sc32270), NeuN (Millipore, MAB377), doublecortin (Sigma, D9693) and BrdU (Santa Cruz, 3H579). Secondary antibodies coupled to Alexa Fluor 488 or 594 (Invitrogen) were used (1:200 dilution). Propidium iodide (0.05 mg/mL) with RNase (0.01 µg/mL) or 4',6-diamidino-2-phenylindole (DAPI, 0.01 mg/mL) were used to stain cell nuclei. Preparations were processed for imaging in a confocal microscope (Zeiss, LSM-780), 15- to 20-µm z-stacks for coronal slices and 200- to 300-µm z-stacks for whole mount preparations were obtained with 10 X and/or 25 X objectives (n = 4 for each antibody tested).

The postnatal array of glial cells in the SVCC and the surface of the roof of the fourth ventricle were analyzed in transgenic GFAP-GFP male mice at postnatal ages: P0, P5, P10, P15, P20 and P30 (n = 3, each age). The brains were processed as described in the section on immunofluorescence; 40-µm slices that included lobules I and X were collected and cell nuclei stained with propidium iodide (0.05 mg/mL) including RNase (0.01 µg/mL), followed by dehydration in 96% and 100% ethanol and finally mounted in Vectashield (Vector Laboratories). Focal sections of 0.88 µm were obtained from 40-µm slices in a Zeiss LSM 510 confocal microscope.

Assays of cell proliferation. Two groups of P30 male CD1 mice were assessed; the first group was tested for rapid cell proliferation (four hours) and the second one for slow cell proliferation (five days). For the first group, either intraperitoneal BrdU (50 mg/kg) or PBS (n = 5) was administered, and four hours later the mice were anesthetized by intraperitoneal administration of pentobarbital (30 mg/kg) and intracardially perfused as indicated in the immunofluorescence section. To test for slow proliferation two doses of BrdU (50 mg/kg) were administered to the second group (n = 5) every six hours over four consecutive days, and on the fifth day mice were intracardially perfused with PFA (4%); brains were postfixed overnight at 4 °C and cryoprotected with three sucrose gradients (10–30%). Forty-µm slices were obtained and treated with HCl 2 N for 1 hour at 37 °C. An antibody against BrdU (Santa Cruz, 3H579) was used and detected with a secondary antibody coupled to Alexa 488 (Invitrogen, A-11006), and cell nuclei were stained with DAPI. Samples were observed in a Zeiss LSM 780 confocal microscope, and 1.0-µm optical slices were obtained from 40-µm stacks.

Test for fenestrated capillaries. To evaluate whether capillaries from the SVCC are fenestrated, Evans blue solution (4% in physiologic saline solution) was administered intraperitoneally (100 mg/kg) in 5 adult mice. When the skin of the mice turned blue (after 24 h), the mice were anesthetized and intracardially perfused with physiological saline solution. Brains were dissected immediately, and 50-µm slices were obtained using a vibratome (Leica, VT1000S). In addition, slices were labeled with the fluorescent marker for Nissl substance (Neuro Trace, Nissl stain, Molecular Probes, N-21480) and mounted. Samples were observed under a Zeiss LSM 780 confocal microscope, and 1.0-µm optical slices were obtained from 40-µm stacks.

mCherry adenoviral labeling and Dil labeling. We used a recombinant serotype 5 adenovirus (AdV) carrying mCherry under the control of the CMV promoter-enhancer (Vector BioLabs, Philadelphia, USA). The

virus was stereotaxically administered (3.3×10^7 viral particles/ μL at constant flow for 2 min) with a Hamilton Neuro syringe (Hamilton, 1710) into the parenchyma of the cerebellum (Bregma -6.36 mm, ventral -3.30 mm and lateral 0.0 mm, according to the Mouse Brain Atlas¹³) of anesthetized 2-month-old GFAP-GFP transgenic male mice ($10 \mu\text{L}/50$ g of ketamine/xylazine 7:3). After 72 h, mice were processed as described in the immunohistochemistry section ($n = 6$), cerebella were sliced into $45\text{-}\mu\text{m}$ thick coronal sections using a cryostat (Leica, CM3050s), the slices were collected and the nuclei were stained with DAPI (1 mg/mL). Samples were observed under a Zeiss LSM 510 confocal microscope, and 25- to $40\text{-}\mu\text{m}$ stacks of $1.0\text{-}\mu\text{m}$ optical slices were obtained.

For DiI ($1,1'$ -Dioctadecyl-3,3,3',3'-tetramethylindocarbocyanine perchlorate) staining, fixed brains were processed as described above ($n = 3$), a needle was impregnated with the tracer and applied $200\text{-}\mu\text{m}$ anterior to the SVCC in the whole cerebellum for 1 h and then the brains were incubated at 25°C for three months, $40\text{-}\mu\text{m}$ slices were obtained, stained with DAPI and mounted to be analyzed in a Zeiss LSM 780 confocal microscope.

CLARITY. For understanding the organization of astrocytes in the SVCC during development we performed CLARITY¹⁴ in whole brains of transgenic GFAP-GFP mice at embryonic ages (E10, E12, E15, E18, E19, $n = 4$) and postnatal ages (P0, P5, P10, P15, P20, P30, $n = 4$). Mice were intracardially perfused with PBS, followed with a cold Hydrogel Monomer Solution (HMS) containing: acrylamide (4.0%), bis-acrylamide (0.05%), A-044 initiator (0.25%, Wako VA044), PBS and PFA (4.0%); once the tissue was perfused it was immersed in HMS for 6–10 days at 4°C , the tissue was then placed into a 15-mL polypropylene centrifuge tube with fresh HMS; polymerization was induced at 37°C and allowed to proceed for 3 h. The HMS was removed, and brains were sectioned into 2.0-mm thick slices and immersed in a Clearing Solution (CS: 200 mM boric acid, 4% SDS, diluted with H_2O , pH 8.5). Passive CLARITY was performed at 37°C in a shaker incubator at 80 rpm. After brain clarification (approximately one month), the tissue was washed twice for 24 h in PBST (0.1% Triton in 1X PBS) at 37°C , 80 rpm. Cell nuclei were stained with propidium iodide in PBST for 24 h at 37°C , 80 rpm. Tissue was then mounted in glycerol (80%) and processed in a confocal microscope (Zeiss LSM 510); 2- to $5\text{-}\mu\text{m}$ optical slices were obtained from 380- to $600\text{-}\mu\text{m}$ stacks.

Scanning and transmission electron microscopy. The ultrastructure of the SVCC and surface of the roof of the fourth ventricle were analyzed by transmission and scanning electron microscopy (TEM and SEM, respectively). TEM was performed as previously reported¹²; 60- to 70-nm ultrathin slices were obtained in an ultramicrotome, mounted on copper grids and observed in a transmission electron microscope (JEOL JEM-1010 model, at 80 KV), $n = 3$. For SEM, the samples were dissected to expose the surface of the ventricle (see supplementary Fig. 1). Samples were dehydrated in a Tousimis dryer (Samdri-PVT-3D), covered in gold in a sputter coater (Denton Vacuum) and processed in a scanning electron microscopy (Zeiss, EVO 50), $n = 3$.

Whole-cell patch-clamp electrophysiology. Coronal slices of cerebellum ($250\text{-}\mu\text{m}$ thick) from 50- to 60-day-old C57 male mice that were anesthetized with isoflurane, were collected in an ice cold carbogen-bubbled sucrose-rich solution containing in mM: sucrose (212.7), KCl (5.0), NaH_2PO_4 (1.25), MgSO_4 (3.0), CaCl_2 (1.0), NaHCO_3 (26.0), and glucose (10.0), pH 7.4. Slices were incubated for 30 min at room temperature in this solution. Whole-cell patch clamp was performed at 37°C in artificial cerebrospinal fluid solution (ACSF) containing in mM: NaCl (125.0), KCl (2.5), NaH_2PO_4 (1.25), MgCl_2 (1.0), CaCl_2 (2.0), NaH_2PO_4 (1.25), NaHCO_3 (26.0) and glucose (10.0), pH 7.4. Electrical stimulation was performed using a 6–8 M Ω patch pipette containing in mM: K-gluconate (130), KCl (7), ATP-Mg (4.0), GTP-Na (0.3), phosphocreatine-di (Tris) (10), HEPES (10) and biocytin (0.4%), pH 7.2, 300 mOsm. Cells were visualized under a Nikon FN-S2N microscope. Whole-cell patch-clamp recordings were performed using a Multiclamp 700B amplifier (Molecular Devices). For characterizing the electrical profiles of the cells from the SVCC we applied three current protocols: (i) cells held at -80 mV, 160-msec voltage steps from -100 to $+20$ mV in 10-mV increments; (ii) cells held at -20 mV, 160-msec voltage steps from -40 to $+150$ mV in 10-mV increments; and (iii) cells held at -40 mV with 160-msec voltage steps from -60 to $+40$ mV in 10-mV increments. As the experiments progressed we established that these protocols disclosed diverse cell populations with different electrical responses.

To reveal the morphology of recorded cells, they were filled with biocytin, the slices were fixed in PFA (4%) for at least 12 h (4°C), endogenous peroxidase activity was blocked by incubating in hydrogen peroxide (3%) for 30 min, and avidin-biotin complexes were formed using the Vectastain ABC kit and detected with diaminobenzidine (Vector Laboratories). The $250\text{-}\mu\text{m}$ slices were cryoprotected and embedded in Tissue Tek O.C.T. (Sakura) to obtain $40\text{-}\mu\text{m}$ thick slices. Serial images from different focal depths were obtained in a light microscope (Olympus BX60). Image processing was performed with Helicon Focus software. Biocytin-labeled cells were hand drawn on paper using a *camera lucida*.

Results

Location and cellular composition of SVCC and VMC. Serial coronal sections of cerebellum were stained with toluidine blue as shown in Fig. 1A. A 1.0-mm slice evidenced the SVCC towards the central area of the roof of the ventricle (Fig. 1A, arrow), and consecutive $40\text{-}\mu\text{m}$ slices from 5 male mice indicated that the dimensions of the SVCC are $300 \pm 20\text{-}\mu\text{m}$ on the lateral extension and $160 \pm 20\text{-}\mu\text{m}$ along the anterior-posterior axis (arrow in Fig. 1C). The SVCC was composed on average of 314 ± 8 cells of diverse morphology.

Our previous report described electrophysiological responses that correspond to neurons and other cells that responded to GABA through activation of GABA-A receptors¹. Thus, to determine whether GABAergic cells were present in the SVCC, we used a selective antibody for GAD-65, the enzyme necessary to synthesize the GABA used in neurotransmission and associated with nerve terminals (white arrowheads in Fig. 1D). From three cerebella examined we found an average of 33 ± 1 GAD-65 positive cells. Further evidence of the presence of neurons in the SVCC was provided by immunolabeling with NeuN antibody, a selective marker of neurons,

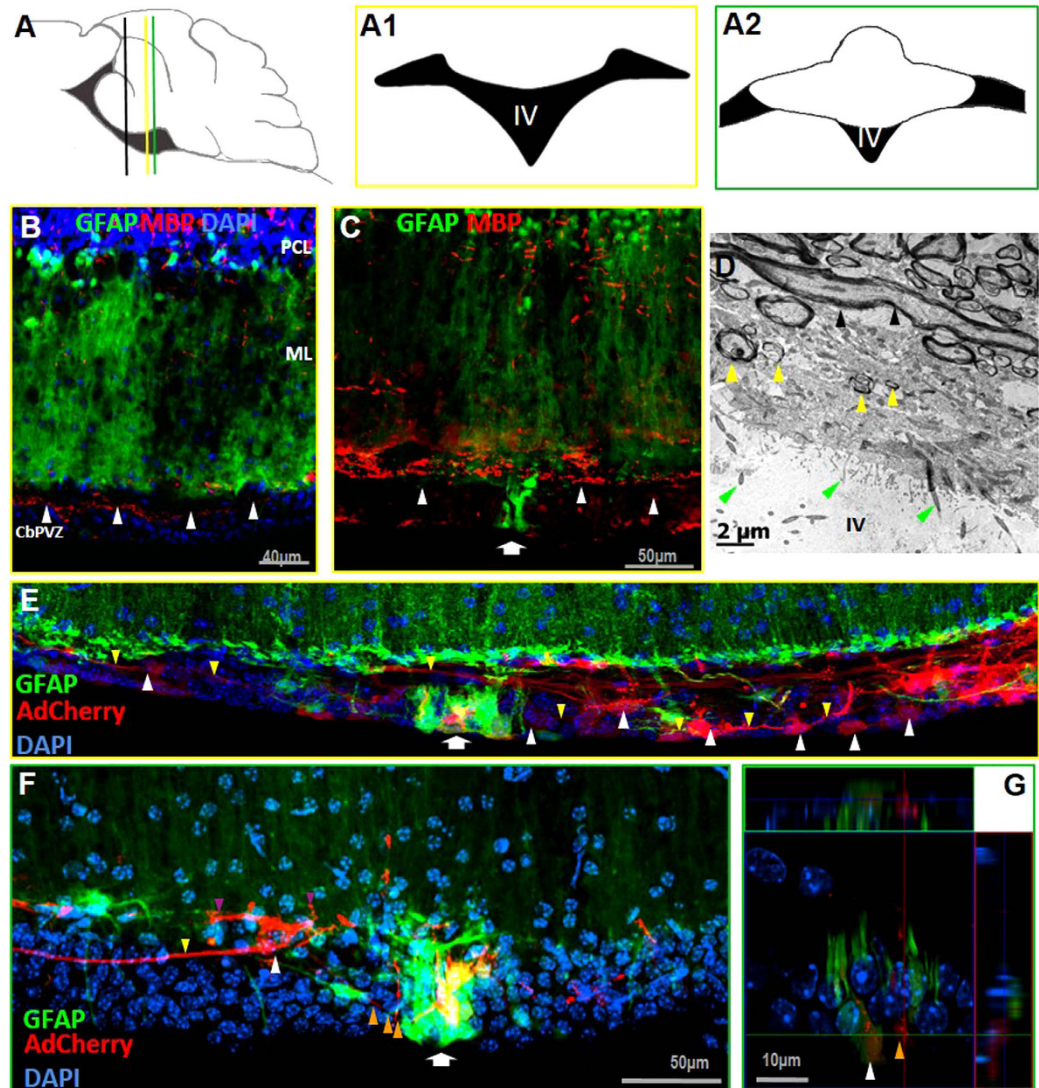


Figure 2. Evidence of neurons in and around the SVCC. (B) Cells labeled by MBP are distributed through the SVCC (white arrowheads), and the VMC is disclosed by the expression of GFP (arrow in C). (D) Transmission electron microscopy showed the presence of transversal and longitudinal axons (black and yellow arrowheads), the presence of multiciliated cells indicated the presence of ependymal cells (green arrowheads). A sagittal representation of the site of AdCherry administration (black line in panel A); yellow and green lines indicate the coronal planes represented in A1 and A2. (E) mCherry randomly labeled cells in the SVCC (white arrowheads); several cells present long processes (yellow arrowheads) that extend laterally. The VMC is indicated with an arrow (E,F), and it includes GFAP⁺ (in green) and GFAP⁻ cells, some cells labeled with mCherry (orange arrowhead in G) and several cells labeled with both fluorescent proteins. In (F) Individual cell labeling was obtained with mCherry (white arrowhead) and identified one cell extending a long projection laterally (yellow arrowhead); in addition, GFAP⁺ cells, morphologically similar to astrocytes, project several processes to the VMC (orange arrowheads) whereas others contact the terminal feet of Bergmann glia (purple arrowheads). In (G) an orthogonal plane of 2F is presented. GFAP: glial fibrillar acidic protein; AdCherry: adenoviral vector carrying the fluorescent protein Cherry gene; CbPVZ: cerebellar periventricular zone.

that indicated that on average 65 ± 4 neurons were present in the SVCC (arrowheads in Fig. 1E,F). In addition, an antibody selective for calretinin, a marker of interneurons in different areas of the brain, labeled the soma of several (10 ± 2) cells (arrowheads in Fig. 1G); an antibody selective for the calcium-binding protein calbindin did not label cells in the area, whereas Purkinje neurons were positive (arrow and arrowheads in Fig. 1H).

Since our electrophysiological recordings suggested the presence of precursor cells in this area¹ we tested for the expression of the intermediate filaments nestin and vimentin. No vimentin signal was observed in the SVCC, whereas scattered label was detected along the ependymal glial layer (arrows in Fig. 1I). A number of cells (39 ± 7) positive for nestin were labeled in the SVCC (orange arrowheads in 1J); these cells possess large soma and are embedded within the SVCC. A second cellular population of nestin⁺ and vimentin⁺ cells forms a compact cluster of cells detected medially in the ependymal layer (red arrowhead in Fig. 1I,J, respectively); however,

when consecutive serial slices from this area were examined, it was clear that these cells form a stream distributed ventromedially along the surface of the roof of the ventricle, in intimate contact with the cerebrospinal fluid (see below). We will refer to this array of cells as the ventromedial cord (VMC). Along with nestin⁺ cells from the VMC, we also found GFAP⁺ cells, some of which were positive for both markers (see below).

Electrophysiological evidence suggested the presence of neurons and oligodendrocytes in the SVCC; therefore, we used an antibody selective for myelin basic protein (MBP), which is the main component of the myelin membrane of oligodendrocytes. Distribution of MBP was sparse in cells facing the ventricle and more abundant in cells located towards the dorsal side of the SVCC, at the interface between the Bergmann glia end feet (arrowheads in Fig. 2B,C). The presence of myelinated axons was further confirmed by transmission electron microscopy (Fig. 2D), which showed many processes running along the transversal and longitudinal planes, isolating the cells of the SVCC from the end feet of Bergmann glia. We observed neither active synaptic zones in multiple images captured from this area nor contacts of Bergmann glia with those axons. The origin and destiny of these processes is still unknown.

Adenoviral labeling. To determine the morphology of individual cells of the SVCC and VMC we injected into the cerebellar parenchyma adenoviruses carrying mCherry, using a low concentration of viruses to achieve scattered, non-selective labeling of different cells. In the SVCC we observed 23 ± 2 cells ($n = 5$) with a large nucleus ($23 \pm 3 \mu\text{m}$ diameter; white arrowheads in Fig. 2E,F) that extended two main processes contralaterally (yellow arrowhead), and form an array of “beads on a string”, from these cells 9 ± 1 cells colocalize with the GFP. In this report we do not provide unequivocal evidence that these cells can be properly classified as neurons, and more studies are necessary to determine their electrical properties and role in this area of the cerebellum.

The mCherry adenovirus randomly labeled cells from the VMC, which defined the organization of this group of cells. The VMC is composed of GFAP⁻ and GFAP⁺ cells (yellow and white arrowheads, respectively, in Fig. 2G, Supplementary Fig. 4–5) that have the nucleus towards the ventricular surface and extend their processes toward the parenchyma; two or more astrocytes extend their processes to the VMC, which was closely associated with the microvasculature (orange arrowhead in Fig. 2F).

To gain some understanding of how the VMC contacts the ventricle, we processed cerebella from transgenic GFAP-GFP mice to expose the surface of the ventricle, then we labeled cells with an antibody against nestin. Towards the central area of the cerebellum a stream of GFAP⁺ cells was observed; these cells extend their processes rostrocaudally (arrow in Fig. 3A). This organization contrasts with GFAP⁺ cells from the rest of the roof of the ventricle, which show mostly multiciliated ependymal cells. This array was further observed by nestin labeling (arrow in Fig. 3B) that revealed the stream of cells towards the central region (arrowheads) and an array similar to a honeycomb in the rest of the roof of the ventricle. When the antibody that recognizes nestin was used on GFAP-GFP mice, we observed that many cells of the stream are positive to both markers, whereas others remain negative to nestin (yellow and white arrowheads in Fig. 3C). Therefore, in the VMC, GFAP⁺ cells intermingle with nestin⁺ cells and a large population is GFAP⁺/nestin⁺.

To document the organization of the VMC along the roof of the fourth ventricle and its association with blood vessels, we labeled the cell-cytoskeleton with phalloidin-rhodamine in GFAP-GFP mice (Fig. 3D–F). The stream of GFAP⁺/nestin⁺ cells was found along the rostro-caudal axis, in the central region of lobes I and X (arrow in 3D). GFAP⁺ cells of the VMC were in intimate contact with capillaries (diameter $18.8 \pm 1.5 \mu\text{m}$, mean \pm SD) that run in parallel to this structure along the anterior-posterior plane (yellow arrowheads in Fig. 3D). GFAP⁺ cells on the surface of the ventricle extend their processes to the microvasculature, contacting endothelial cells (Fig. 3E).

Dil labeling showed that cells of the VMC incorporate into the cerebellar parenchyma between lobes I and X (supplementary Fig. 3), but the destiny of these cells was not determined. Analysis of the ventricle surface labeled with phalloidin-rhodamine (Fig. 3D and F, red arrowheads) revealed scattered cell arrays similar to the pinwheel array associated with neurogenic niches in the lateral ventricles¹⁵.

Analysis of this area by SEM revealed a thickening in the central area of the roof of the fourth ventricle that corresponds to the VMC (arrow in Fig. 4A). The ventricular surface of these cells possesses two cilia and multiple microvilli (yellow and red arrowheads respectively in Fig. 4B and D); blood vessels were surrounded and contacted by cell processes, most probably from astrocytes (white and yellow arrowheads in Fig. 4E). In contrast, cells distributed laterally to the VMC present multiple cilia, a common feature of ependymal glial cells of the ventricles (Fig. 4C).

Assays of cell proliferation and fenestrated capillaries. The presence of GFAP⁺/nestin⁺ cells surrounding blood vessels on the ventricular surface led us to test their potential to integrate BrdU and for immunolabeling with Ki67. The ability to incorporate BrdU was compared with the cells from lateral ventricles, where high rates of cell proliferation are well known¹⁶. Two protocols were used (see methods); the rapid proliferation test did not show evidence of cells that incorporated BrdU. On the other hand, BrdU was integrated in a small, but consistent number of cells of the SVCC in the slow incorporation protocol (6 ± 2 BrdU⁺, $n = 5$); the BrdU⁺ cells were found to be associated with blood vessels (Fig. 5A, white arrowheads). This incorporation contrasted with the high number of BrdU⁺ cells in the lateral ventricles (Fig. 5B). Ki67 was not detected in the SVCC (5D), whereas the lateral ventricle exhibited strong labeling (white arrowheads in Fig. 5E). This finding is consistent with the well-known limited rate of neurogenesis in the cerebellum. We then determined whether this area is associated with blood irrigation by using the glycoprotein isolectin IB4 to label endothelial cells of blood vessels. As illustrated in Fig. 5F, capillaries ($18.8 \pm 1.5 \mu\text{m}$ diameter) were observed in all extensions of the SVCC (yellow arrowheads), which contrasted with the discrete labeling of IB4 in the capillaries of the lateral areas of the roof of the ventricle ($10.2 \pm 1.60 \mu\text{m}$ diameter). We then tested whether these blood capillaries are fenestrated, as are capillaries of circumventricular organs (CVOs), by administering the albumin-binding dye Evans blue. In

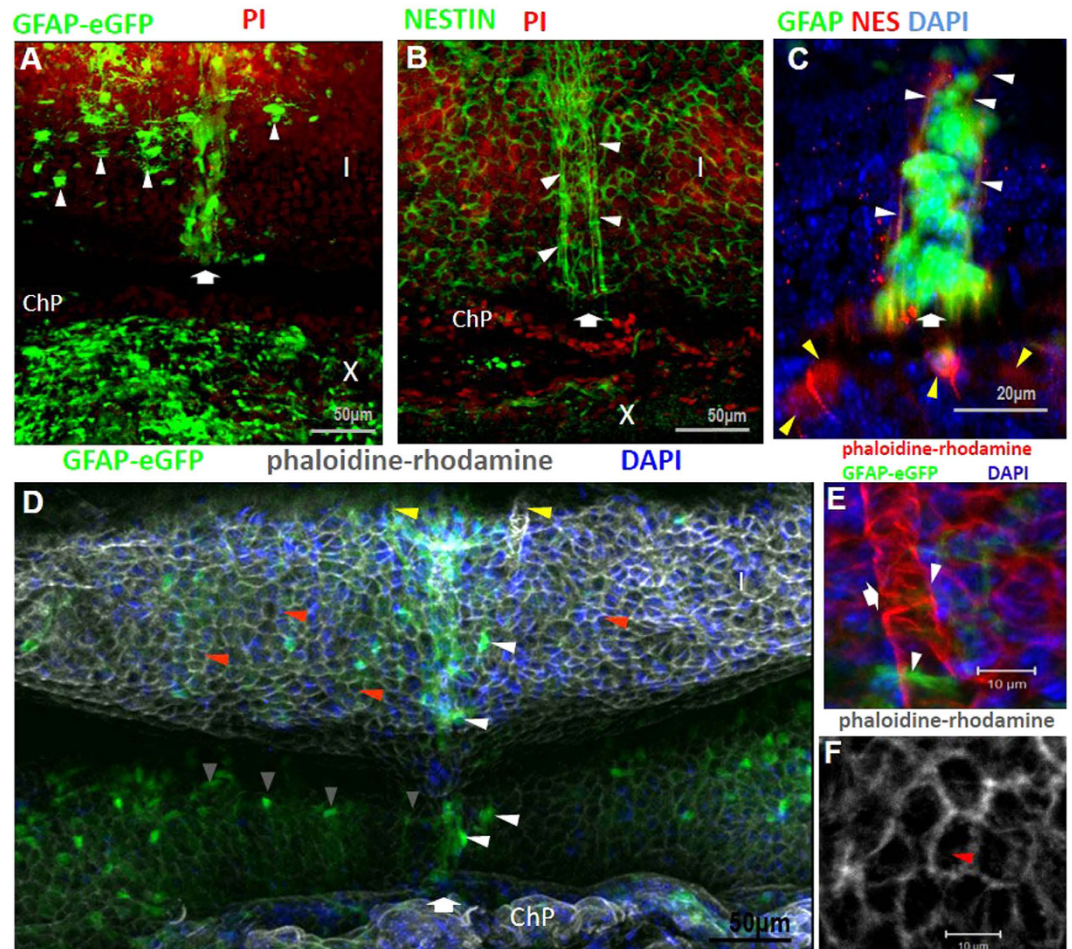


Figure 3. Distribution of ventromedial cord on the roof of the fourth ventricle. The distribution of the VMC on lobe I (I) is indicated with an arrow in (A,B,C and D). In A GFAP⁺ cells are aligned ventromedially; additionally, several individual glial cells with large somas were found lateral to the VMC (white arrowheads). (B) Cells positive for nestin are distributed in the VMC (white arrowheads), and in (C) white arrowheads point to some nestin⁺ cells in the VMC (labeled in red), and yellow arrowheads indicate nestin⁺ cells lateral to the VMC. (D) Phalloidine-rhodamine showed the surface of the roof of the fourth ventricle in the GFAP-GFP transgenic mouse. The VMC is indicated by white arrowheads; two capillaries run along this structure (yellow arrowheads in D and white arrow in E), and they are contacted by long glial processes extending from the VMC (arrowheads in E). Some glial cells with radial morphology extend longitudinally along the interface between the choroid plexus (ChP) and lobe I (gray arrowheads in D). (F) Pinwheel-like structures are present on the surface of the ventricle (red arrowheads in D and F). PI: propidium iodide; NES: nestin; GFAP: glial fibrillar acidic protein; I: lobe I; ChP: choroid plexus.

seven independent assays we found no evidence of dye incorporation in the SVCC (square in Fig. 5G), whereas the choroid plexus, a CVO with fenestrated capillaries, readily incorporated the dye (ChP in Fig. 5G,H).

Electrophysiological characteristics of cells in the SVCC. We performed whole-cell patch-clamp recordings in acute slices from cerebellum; cells with different morphology were analyzed. We noticed that these cells presented low input resistance and were divided in two populations: 1) cells with resistance of 40–50 MΩ (Fig. 6A–D) and 2) cells with resistance of 18–20 MΩ (Fig. 6E,F). Three different current profiles were observed; the linear current-voltage relations are plotted in Fig. 6A,C and E. The electrophysiological characteristics correlate with the morphology and position of the cells: 1) a cell population located in the lateral portion of the SVCC, with larger soma (20–25 μm), short projections and one long process that projects laterally (Fig. 6B); 2) cells with smaller soma (5–8 μm) and two long lateral processes (Fig. 6D); 3) cells with small soma (8–10 μm) and multiple projections extending transversally into the medial portion of the SVCC (Fig. 6F); these cells also present different current profiles (Fig. 6E), similar to neuroblasts from the subventricular zone of the lateral ventricles⁷, and in contrast with the profiles of the cells in 6B and D that correspond to glial cells.

Development of SVCC and VMC. We analyzed the glial organization of the SVCC and VMC during pre- and postnatal development. We obtained consecutive coronal sections of cerebella from transgenic GFAP-GFP

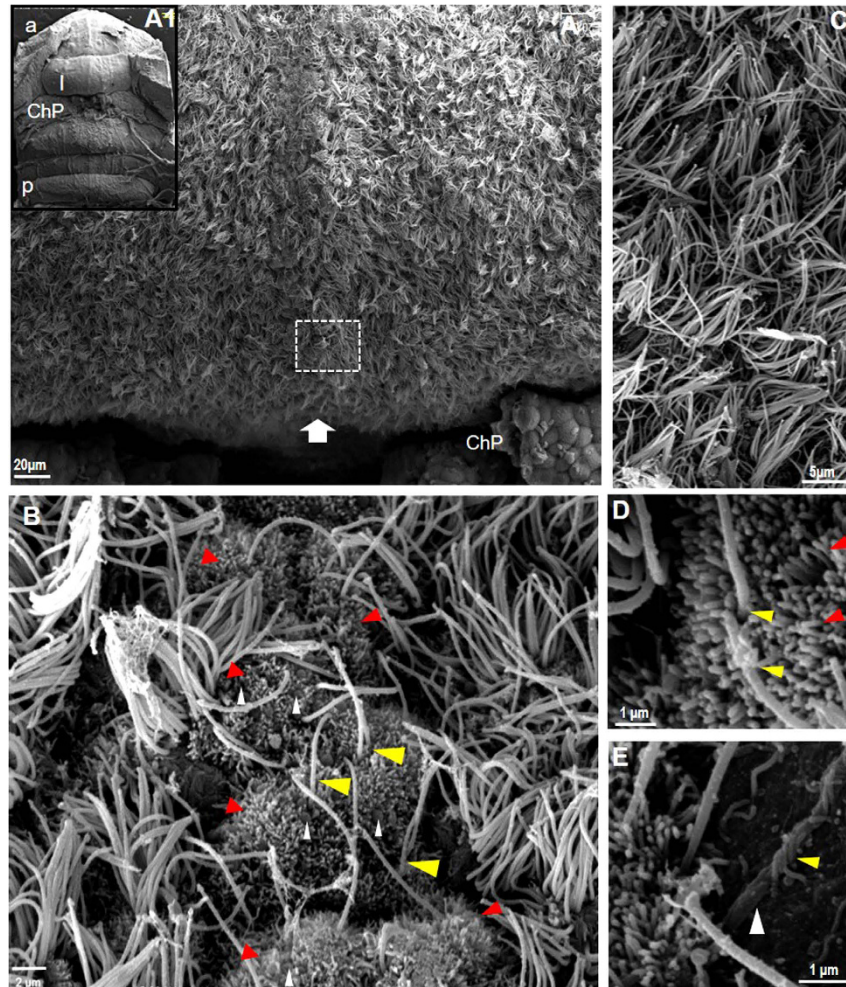


Figure 4. Surface of the roof of the fourth ventricle. SEM image in A1 shows a panoramic view of the ventricle, with lobule I (I) anterior to the choroid plexus (a, anterior, p, posterior). Magnification of the area shows the cilia that characterize the ependymal cells and a thickening that corresponds to the VMC (white arrow); this structure includes cells with only two cilia (yellow arrowheads in B,D) and with multiple small cilia (red arrowheads in B,D). These cells also contain several spheroid structures (white arrowheads in B), and blood vessels were observed near this area (white arrowhead in E). The VMC is different from the uniform cellular organization found laterally that consists of multiple ciliated cells shown in (C) I: lobule I; ChP: choroid plexus; a: anterior; p: posterior.

mice processed for CLARITY (Fig. 7). From 13 slices of lobule I at P0 we observed that the SVCC is formed by GFP⁺ cells apparently in migration towards the white matter (Fig. 7B–G, blue and yellow arrowheads). This organization suggests that this section may be a niche of glial cells actively proliferating during early postnatal development, since after P5 the number of GFP⁺ cells decreased, and the label was limited to the central section of the SVCC and the ependymal glial cell layer (blue arrowhead in Fig. 7C,C'), whereas in the adult (P30), the GFP⁺ cells remained only in the VMC (blue arrowhead in Fig. 7G,G').

Analysis of cerebella processed by CLARITY showed that in the SVCC numerous GFP-expressing cells are present from E15 and probably correspond to sites of gliogenic activity (orange arrowheads in Fig. 7A and supplementary Fig. 4). In the P0 cerebellum the cells that express GFP form the VMC and are densely concentrated in the central area of the SVCC (Fig. 7B'); consistent with observations in slices of cerebellum, the cells that express GFP were confined to the central region of the SVCC and form the VMC along the roof of the ventricle (blue arrowhead in Fig. 7B'–G').

All these observations indicate that the SVCC expands during early development and in the adult, it remains as a niche that contains a variety of cells including astrocytes, oligodendrocytes and neurons.

Discussion

Some of the results considered in this report are based on previous observations that disclosed the presence of diverse electrophysiological profiles of cells distributed along the periventricular zone of cerebellum¹. In brief, ependymal glial cells, astrocytes, oligodendrocytes and neurons were detected in lobules I and X that form the roof of the fourth ventricle. Figure 8 summarizes the findings reported in this paper. This zone of the cerebellum

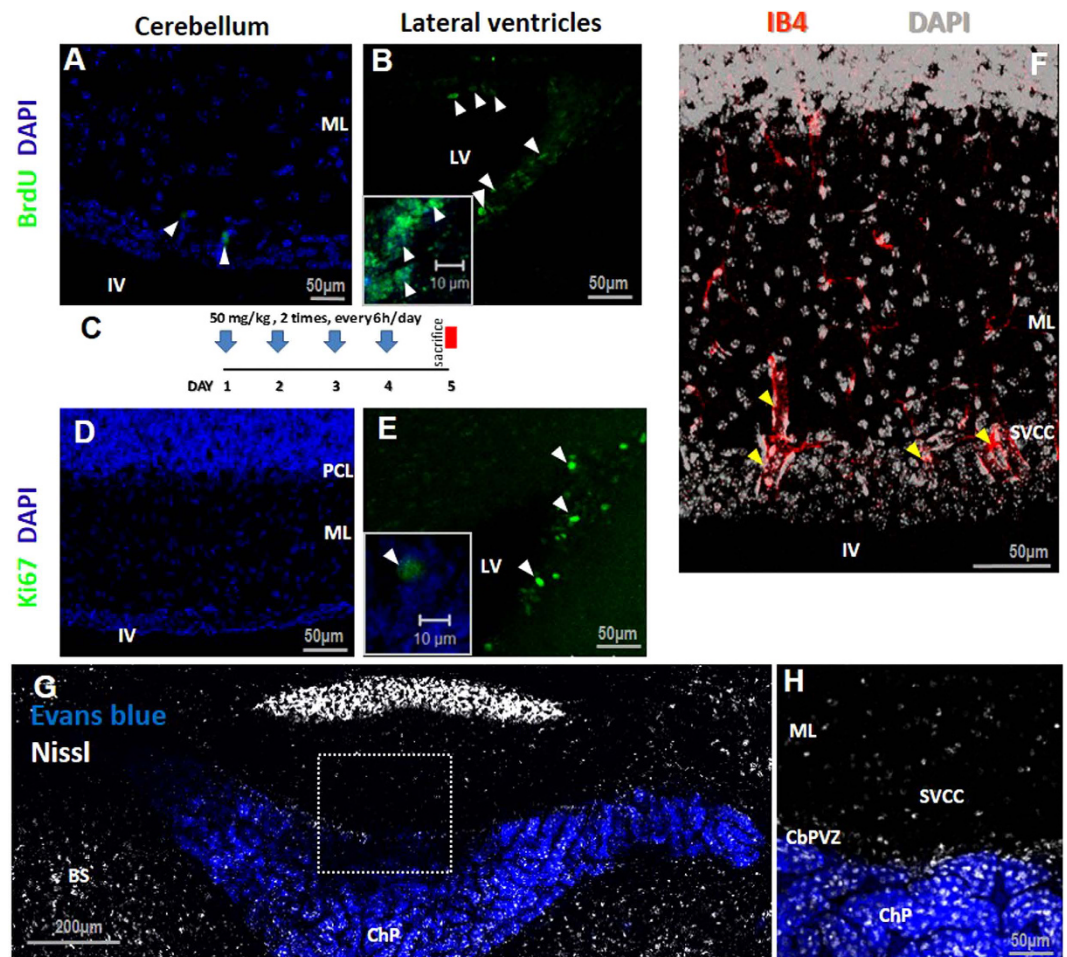


Figure 5. Proliferation assay and blood vessels of the SVCC. (A) BrdU labeling assay (administration protocol in C). Several cells were identified in the SVCC associated with blood vessels (arrowheads in A); no signal for Ki-67 or incorporation of BrdU was detected (A,D), whereas cells in the lateral ventricle were positive. (F) Blood vessels were observed in the SVCC by IB4 (yellow arrowheads). (G,H) Evans blue did not label the SVCC, whereas the choroid plexus (ChP) readily incorporated the stain. LV: lateral ventricles; IV: fourth ventricle; ML: molecular layer; SVCC: subventricular cellular cluster; CbPVZ: cerebellum periventricular zone; ChP: choroid plexus; IB4: isolectin IB4.

has not been widely studied, but the organization of ependymal cells and their responses to GABA have been documented^{1,2,9,17}. In contrast, substantial evidence for a diversity of cellular phenotypes in periventricular zones comes from studies of the lateral ventricles^{18,19} and the central canal^{20,21}; these cells are associated with neurogenic niches or homeostatic control.

In adult cerebellum the presence of niches with active proliferating cells have been documented in white matter and in the Purkinje cellular layer, giving rise to GABAergic interneurons and astrocytes, respectively^{22,23} but this level of specialization has not been observed in the periventricular zone of cerebellum. Thus our unexpected anatomical observations presented in Fig. 1 and the electrophysiological responses previously reported¹ prompted us to determine the properties of this cluster of cells.

Lobules I and X of the cerebellum face the ventricle, and their organization is clearly specialized to communicate intimately with the CSF. Bergman glial cells of lobules II to IX send their processes radially, and their foot-plates contact the basal lamina and form the glia limitans; there is little or no interaction with astrocytes in this zone, which contrasts with the mainly astrocytic composition of the glia limitans in the forebrain and spinal cord²⁴. Towards the central region of the ventricular face of the cerebellum, the end-feet of the Bergmann cells project to the dorsal side of the SVCC, where they contact blood vessels and surround neurons that project transversally. The SVCC includes diverse cellular components that we found to be positive for the following identity markers: a) nestin, b) GFAP, c) vimentin, d) MBP, e) NeuN, f) GAD65, and g) calretinin. All these markers confirm the presence of astrocytes, oligodendrocytes and neurons that were identified previously by electrophysiology¹. The SVCC was not labeled by antibodies against NG2. The myelinated axons running transversally and longitudinally along the dorsal border of the SVCC and ependymal glia are of unknown origin (Fig. 2D), and it is yet to be determined whether these neurons form a local circuit within the cerebellum or come from other regions of the brain. On the other hand, the electrophysiological responses from glial cells shown in Fig. 6

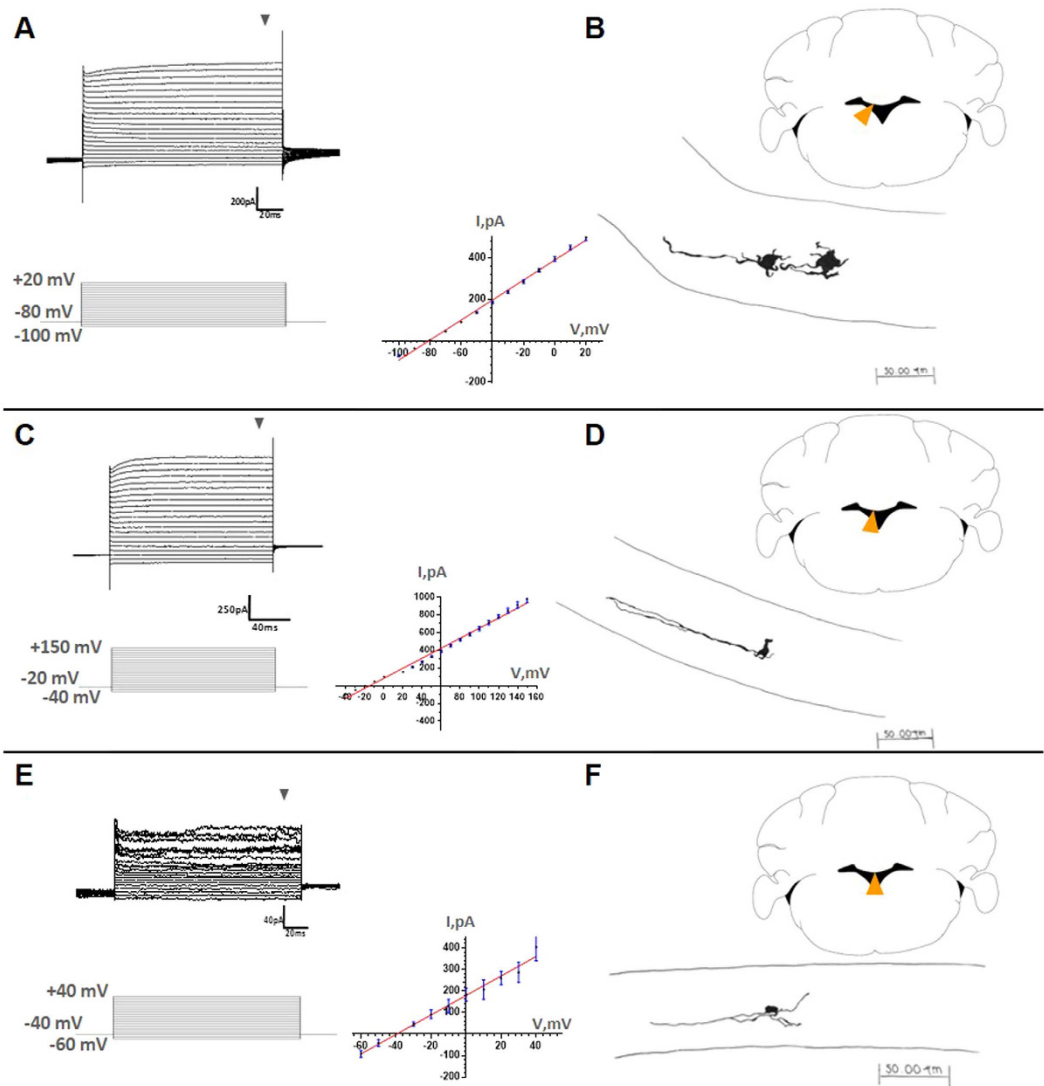


Figure 6. Electrophysiological characteristics of cells of the SVCC. Whole-cell patch-clamp sample recordings from cells at different locations in the SVCC (orange arrowheads in coronal cerebellar slices). Different current profiles were dissected after application of the protocols indicated (A–C and E). Recordings in (A–C) correspond to glial cells, while E is similar to those of neuroblasts of the lateral ventricles. Notice the linear current–voltage relation (I–V plots); these were calculated at the end of the current steps (gray arrowheads). During the recordings, the cells were filled with biocytin. The current profiles correlate with diverse cell morphologies unveiled by drawing on paper the biocytin labeled cells, using a *camera lucida* (B, D–F). Cells in B were located in the lateral portion of the SVCC and possess large soma (20–25 μm), short projections and one long processes that projects laterally. In D, cells with smaller soma (5–8 μm) and two long lateral processes; in F, cells were distributed medially, with small soma (8–10 μm) and multiple projections extended transversally in the medial portion of the SVCC.

correspond to astrocytes, although the morphological characteristics of these cells (small soma and long main processes running laterally accompanied of shorter processes), are not the typical characteristics of astrocytes from cerebellum^{22,25}. This may suggest novel morphologies of the cell type in the SVCC with potential different functional characteristics.

The presence of fenestrated capillaries in the SVCC was disproven by the null penetration of Evans blue into the area, although extensive vasculature was found. Extravasation of Evans blue was observed in the choroid plexus and other circumventricular organs, indicating that the labeling was effective. The absence of fenestrated capillaries makes it improbable that the SVCC forms a structure with functions like those of CVOs^{26–28}, since intimate communication of cells, either glia or neurosecretory neurons, with blood would be blocked by tight junctions preventing a functional neuroendocrine system. In addition, the limited labeling of BrdU and Ki67 in the SVCC suggest that, despite the presence of nestin⁺/GFAP⁺ cells, extended blood irrigation and contact with the CSF, this area is not a neurogenic niche, such as that found in the lateral ventricles¹⁶, this was supported by the absence of cells expressing the immature neuronal marker DCX (not shown). Cells of the floor of the

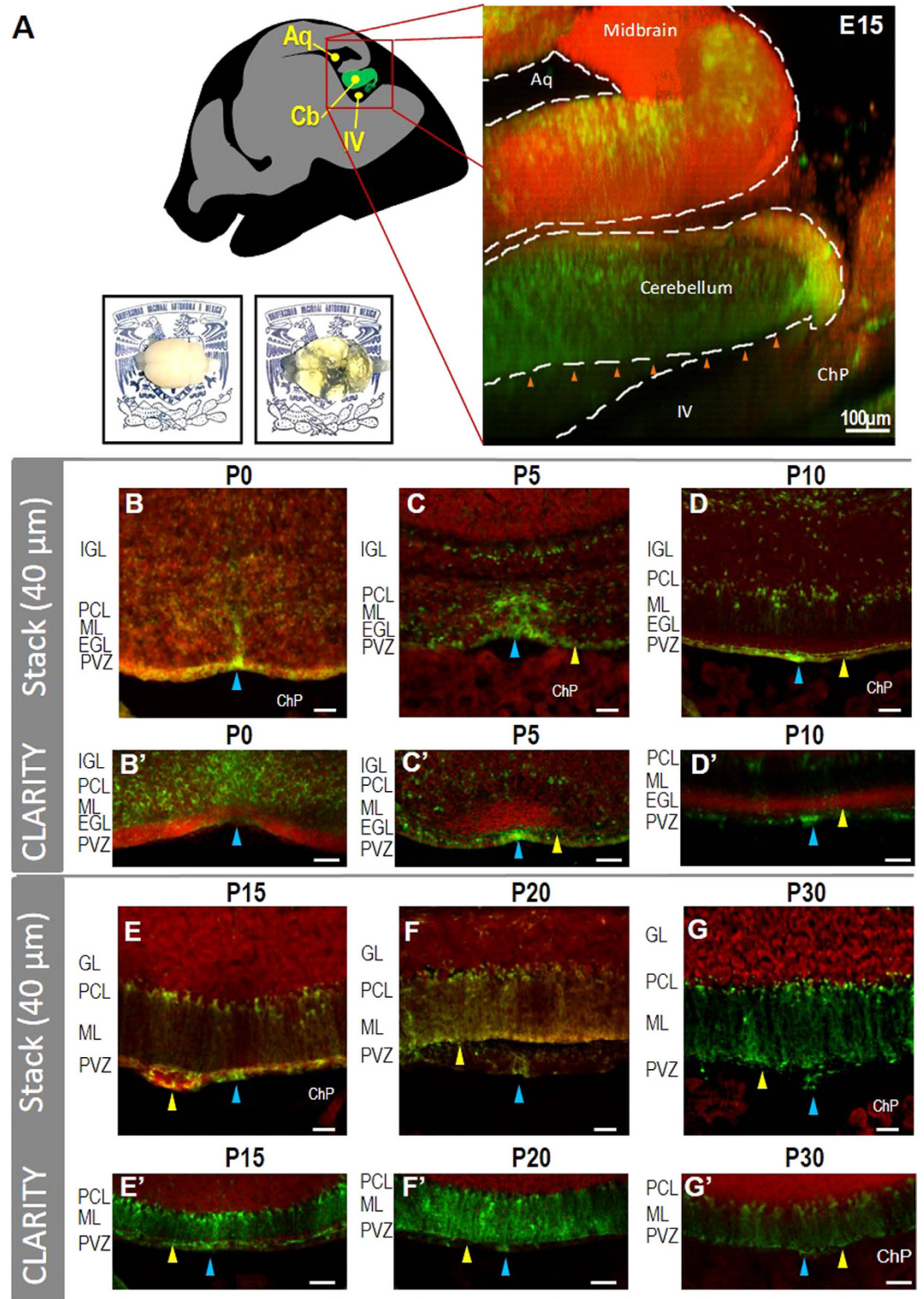


Figure 7. Development of the SVCC and VMC. The VMC is observed from embryonic (E) day 15 (orange arrowheads in A) in a 2-mm sagittal section of a clarified GFAP-GFP cerebellum (see also supplementary videos). From P0 to P5 the SVCC and VMC expand, whereas from P10 the VMC is ventromedially limited to the ependymal glial cell layer (blue arrowheads in B-G stacks of 40 μ m and optical slices from CLARITY B'-G'). From P5 to P30 the SVCC was found to be delimited by the end feet of the Bergmann glia (yellow arrowheads in 40- μ m stacks [C-G] and optical slices from CLARITY [C'-G']) of transgenic GFAP-GFP mice (red nuclei labeled with propidium iodide). An example of clarified adult brain is presented in the bottom in A. IGL: Internal granular layer; PCL: Purkinje cellular layer, ML: Molecular layer, EGL: external granular layer, GL: granular layer; PVZ: Periventricular zone, ChP: Choroid plexus, P: postnatal stage. Barr: 50 μ m.

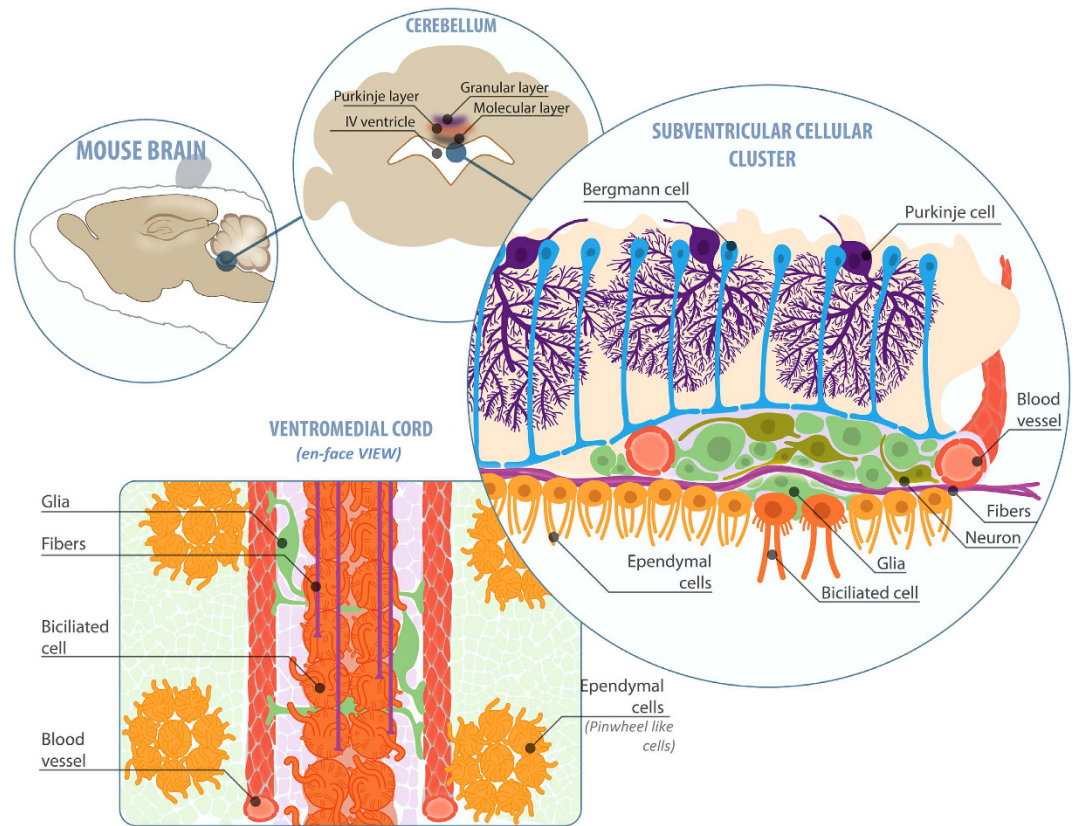


Figure 8. Organization of the SVCC and VMC. The drawing summarizes the organization of the peri- and subventricular zones in cerebellum. Top right, the SVCC is dorsally limited by the terminal feet of Bergmann glial cells (blue) and ventrally by multiciliated (yellow) and biciliated (orange) ependymal cells. Two capillaries are lateral to this structure (red). The glial cells (soft green) contact the blood vessels, as well as neurons (dark green) and myelinated axons (purple). Lower left, the VMC on the roof of the fourth ventricle is composed of two rows of biciliated cells (orange); fibers (purple) and glial cells (soft green) extend their processes towards two capillaries (red). The presence of pinwheel-like structures was also evidenced (yellow). Illustration by F. Serrano.

fourth ventricle can be induced to proliferate and differentiate into astrocytes and oligodendrocytes when mice are perfused with a mix of FGF2, EGF and heparin²⁹ and it had been reported that in adult New Zealand white rabbit, neurogenesis take place in some restricted niches located in the subpial zone³⁰. It is well documented that different cellular populations in the cerebellum, including inferior olivary neurons and Purkinje cells have more plasticity than previously thought^{31–33}. We have not yet explored whether the cells from the SVCC have these abilities, but it is a possibility worth studying.

The ventricular position of the SVCC and VMC, their cellular organization and the considerable number of GFAP⁺ cells that compose them during ontogenic development suggest that they may be an active niche of proliferative cells that is spatially restricted after cerebellar development is completed (Fig. 7). CLARITY and coronal slices of transgenic GFAP-GFP mice revealed that the SVCC and VMC occupy a larger proportion of the area during early development than in adulthood. A stream of GFAP⁺ cells in apparent migration towards the parenchyma is observed in newborn mice; this organization is transformed in such a way that, after the second week of age, GFAP⁺ cells from the VMC, are reduced to only a few cells in coronal slices, and are more apparent in the *en-face* preparation. The VMC forms an array that is structurally similar to the rostral migratory stream of the lateral ventricles; indeed, several disperse, pinwheel-like structures were detected (Fig. 3D and F), similar structures are associated with adult active neurogenic niches in the lateral ventricles^{15,34,35}; however, as previously shown, no evidence of active cell proliferation was detected. Further studies will be necessary to determine the role of these organizational features in this area of the cerebellum.

On the surface of the central region of the roof of the fourth ventricle we found a cellular complex that forms a cord running along the medial line and is composed of nestin⁺ and GFAP⁺ cells. We have named this structure the Ventromedial Cord or VMC that, due to the morphology of GFAP⁺ cells, appears to be composed of cells in migration (Fig. 3); however, despite applying several experimental strategies (not shown), we did not observe active movement of these cells. The VMC accompanies a series of blood vessels associated with GFAP⁺ cells that contact the CSF (most probably astrocytes and/or pericytes); these cells are in a strategic position that permits sensing the conditions of the circulatory system and CSF. These cells possess microvillousities and two cilia unlike the ependymal glial cells that possess multiple cilia, are widely distributed on the roof of the ventricle and have the morphology previously observed of ependymal glial cells².

The results shown here do not unequivocally demonstrate a functional role for the cluster of cells described; we do not know whether the cells from the VMC and SVCC transform into glia or neurons, or if they are migrating along the surface of the ventricle. High proliferative and differentiation potentials of the cells within these niches would present considerable discrepancies with the general view of limited neurogenic and gliogenic activity in the adult cerebellum. It is interesting, however, to speculate that they may form a novel specialized structure with an unknown function, and their association with novel myelinated axons makes the SVCC even more intriguing. It will be a fascinating challenge to develop a strategy to resolve this puzzle. For now, it is worth mentioning that the SVCC has been observed in three different species of rodents, in rat: *Ratus norvegicus*, in *Neotomodon alstoni* and in the North American prairie vole: *Microtus ochrogaster* (not shown) which suggests that it is evolutionarily preserved.

References

1. Reyes-Haro, D. *et al.* γ -Aminobutyric acid- ρ expression in ependymal glial cells of the mouse cerebellum. *J Neurosci Res.* **91**(4), 527–534 (2013).
2. Alvarez-Morujó, A. J. *et al.* The ependymal surface of the fourth ventricle of the rat: a combined scanning and transmission electron microscopic study. *Histol. Histopathol.* **7**, 259–266 (1992).
3. Hsieh, Y. C. & Puche, A. C. GABA modulation of SVZ-derived progenitor ventral cell migration. *Dev. Neurobiol.* **75**, 791–804 (2015).
4. Liu, X., Wang, Q., Haydar, T. F. & Bordey, A. Nonsynaptic GABA signaling in postnatal subventricular zone controls proliferation of GFAP-expressing progenitors. *Nat Neurosci.* **8**, 1179–1187 (2005).
5. Pallotto, M. & Deprez, F. Regulation of adult neurogenesis by GABAergic transmission: signaling beyond GABA_A-receptors. *Front. Cell Neurosci.* **8**, 166 (2014).
6. Pathania, M. & Bordey, A. A symphony of signals conducts early and late stages of adult neurogenesis. *Neuropharmacology.* **58**, 865–876 (2010).
7. Young, S. Z., Platel, J. C., Nielsen, J. V., Jensen, N. A. & Bordey, A. GABA(A) increases calcium in subventricular zone astrocyte-like cells through l- and t-type voltage-gated calcium channels. *Front. Cell Neurosci.* **4**, 8 (2010).
8. Young, S. Z., Taylor, M. M. & Bordey, A. Neurotransmitters couple brain activity to subventricular zone neurogenesis. *Eur. J. Neurosci.* **33**, 1123–1132 (2011).
9. Oda, Y. & Nakanishi, I. Ultrastructure of the caudal portion of the fourth ventricular roof in the mouse. *J. Comp. Neurol.* **256**, 299–307 (1987).
10. Nolte, C. *et al.* GFAP promoter-controlled EGFP-expressing transgenic mice: a tool to visualize astrocytes and astrogliosis in living brain tissue. *Glia* **33**, 72–86 (2001).
11. Mirzadeh, Z., Doetsch, F., Sawamoto, K., Wichterle, H. & Alvarez-Buylla, A. The subventricular zone en-face: wholemount staining and ependymal flow. *J. Vis. Exp.* **39**, 1938 (2010).
12. Rosas-Arellano, A., Machuca-Parra, A. L., Reyes-Haro, D., Miledi, R. & Martínez-Torres, A. Expression of GABA ρ receptors in the neostriatum: localization in aspiny, medium spiny neurons and GFAP-positive cells. *J. Neurochem.* **122**, 900–910 (2012).
13. Paxinos, G. & Franklin, K. B. J. *The Mouse Brain In Stereotaxic Coordinates 2nd edn.* (Academic Press, 2001).
14. Chung, K. & Deisseroth, K. CLARITY for mapping the nervous system. *Nat. Methods* **10**, 508–513 (2013).
15. Mirzadeh, Z., Merkle, F. T., Soriano-Navarro, M., Garcia-Verdugo, J. M. & Alvarez-Buylla, A. Neural stem cells confer unique pinwheel architecture to the ventricular surface in neurogenic regions of the adult brain. *Cell Stem Cell* **3**, 265–278 (2008).
16. Ihrie, R. A. & Álvarez-Buylla, A. Lake-front property: a unique germinal niche by the lateral ventricles of the adult brain. *Neuron* **70**, 674–686 (2011).
17. Hermann, A. *et al.* Rostro-caudal gradual loss of cellular diversity within the periventricular regions of the ventricular system. *Stem Cells* **27**, 928–941 (2009).
18. Alvarez-Buylla, A. & Garcia-Verdugo, J. M. Neurogenesis in adult subventricular zone. *J. Neurosci.* **22**, 629–634 (2002).
19. Zhao, C., Deng, W. & Gage, F. H. Mechanisms and functional implications of adult neurogenesis. *Cell* **132**, 645–660 (2008).
20. Alfaro-Cervello, C., Soriano-Navarro, M., Mirzadeh, Z., Alvarez-Buylla, A. & Garcia-Verdugo, J. M. Biciliated ependymal cell proliferation contributes to spinal cord growth. *J. Comp. Neurol.* **520**, 3528–3552 (2012).
21. Hamilton, L. K., Truong, M. K., Bednarczyk, M. R., Aumont, A. & Fernandes, K. J. Cellular organization of the central canal ependymal zone, a niche of latent neural stem cells in the adult mammalian spinal cord. *Neuroscience* **164**, 1044–1056 (2009).
22. Altman, J. & Bayer S. A. *Development of the cerebellar system in relation to its evolution, structures and functions.* New York: CRC Press (1997).
23. Parmigiani, E. *et al.* Heterogeneity and bipotency of astroglial-like cerebellar progenitors along the interneuron and glial lineages. *J. Neurosci.* **35**, 7388–7402 (2015).
24. Liu, X., Zhang, Z., Guo, W., Burnstock, G., He, C. & Xiang, Z. The superficial glia limitans of mouse and monkey brain and spinal cord. *Anatomical record (Hoboken)* **296**, 995–1007 (2013).
25. Buffo, A. & Rossi, F. Origin, lineage and function of cerebellar glia. *Prog. Neurobiol.* **109**, 42–63 (2013).
26. Joly, J. S. *et al.* Windows of the brain: towards a developmental biology of circumventricular and other neurohemal organs. *Semin Cell Dev Biol.* **18**(4), 512–524 (2007).
27. Bennett, L., Yang, M., Enikolopov, G. & Iacovitti, L. Circumventricular organs: a novel site of neural stem cells in the adult brain. *Mol. Cell Neurosci.* **41**, 337–47 (2009).
28. Langlet, F., Mullier, A., Bouret, S. G., Prevot, V. & Dehouck, B. Tanycyte-like cells form a blood-cerebrospinal fluid barrier in the circumventricular organs of the mouse brain. *J. Comp. Neurol.* **521**, 3389–3405 (2013).
29. Martens, D. J., Seaberg, R. M. & van der Kooy, D. *In vivo* infusions of exogenous growth factors into the fourth ventricle of the adult mouse brain increase the proliferation of neural progenitors around the fourth ventricle and the central canal of the spinal cord. *Eur. J. Neurosci.* **16**, 1045–1057 (2002).
30. Bonfanti, L. & Ponti, G. Adult mammalian neurogenesis and New Zealand white rabbit. *Vet J.* **175**(3), 310–331 (2008).
31. Carulli, D., Buffo, A. & Strata, P. Reparative mechanisms in the cerebellar cortex. *Prog Neurobiol.* **72**(6), 373–398 (2004).
32. Carulli, D., Foscarin, S., Faralli, A., Pajaj, E. & Rossi, F. Modulation of semaphoring3A in perineuronal nets during structural plasticity in the adult cerebellum. *Mol Cell Neurosci.* **57**, 10–22 (2013).
33. Doetsch, F., Caillé, I., Lim, D. A., García-Verdugo, J. M. & Alvarez-Buylla, A. Subventricular zone astrocytes are neural stem cells in the adult mammalian brain. *Cell* **97**, 703–716 (1999).
34. Capilla-Gonzalez, V., Lavell, E., Quiñones-Hinojosa, A. & Guerrero-Cazares, H. Regulation of subventricular zone-derived cells migration in the adult brain. *Adv. Exp. Med. Biol.* **853**, 1–21 (2015).
35. Rossi, F., Borsello, T., Vaudano, E. & Strata, P. Regressive modifications of climbing fibres following Purkinje cell degeneration in the cerebellar cortex of the adult rat. *Neuroscience.* **53**(3), 759–778 (1993).

Acknowledgements

We thank the Universidad Nacional Autónoma de México. This work was supported by grants from CONACYT (220224) and PAPIIT-DGAPA (206616) to AMT. MAGG, GBGG and MBG are doctoral students in the Programa de Doctorado en Ciencias Biomédicas, Universidad Nacional Autónoma de México, and are supported by CONACYT fellowships: 339430, 277694 and 330119, respectively. We thank Prof. N. Inestrosa and Dr. W. Cerpa (Pontificia Universidad Católica, Santiago, Chile) for providing necessary support for electrophysiological recordings and Prof. H. Kettenmann (MDC-Berlin) and Dr. D. Reyes for the GFAP-GFP transgenic mice. We thank the following people for their valuable technical support: from INB-UNAM: A.E. Espino-Saldaña, E.N. Hernandez-Rios, M.L. Palma-Tirado, T.E. Garay-Rojas J.M. García-Servin, A.R. Aguilar-Vázquez and L. Casanova-Rico; from U.A.Q: A.L. Tovar-Álvarez and from Stanford University: K. Engberg and K. Deisseroth. We thank C.A. Rodríguez-Arzate for drawing the biocytin stained cells in Fig. 6 and F. Serrano-González for preparing the illustration for this publication in Figure 8. We are also indebted to Dr. A. Álvarez-Buylla (University of California, San Francisco, USA) and Dr. A. Cárabez-Trejo (INB-UNAM) for their helpful suggestions to this project. Dr. D.D. Pless kindly edited the manuscript. Prof. Ricardo Miledi supported this project throughout all its stages.

Author Contributions

A.M.-T., M.A.G.-G. G.B.G.-G. and M.B.-G. designed the research; M.A.G.-G., G.B.G.-G. and M.B.-G. performed the experiments. All authors analyzed the results and reviewed the manuscript. M.A.G.-G. and A.M.-T. wrote the paper.

Additional Information

Supplementary information accompanies this paper at <http://www.nature.com/srep>

Competing financial interests: The authors declare no competing financial interests.

How to cite this article: González-González M. A. *et al.* Identification of novel cellular clusters define a specialized area in the cerebellar periventricular zone. *Sci. Rep.* 7, 40768; doi: 10.1038/srep40768 (2017).

Publisher's note: Springer Nature remains neutral with regard to jurisdictional claims in published maps and institutional affiliations.



This work is licensed under a Creative Commons Attribution 4.0 International License. The images or other third party material in this article are included in the article's Creative Commons license, unless indicated otherwise in the credit line; if the material is not included under the Creative Commons license, users will need to obtain permission from the license holder to reproduce the material. To view a copy of this license, visit <http://creativecommons.org/licenses/by/4.0/>

© The Author(s) 2017

Development of Collagen/Poly(vinyl alcohol)/Chondroitin Sulfate and Collagen/Poly(vinyl alcohol)/HA Electrospun Scaffolds for Tissue Engineering

Luis Humberto Delgado-Rangel¹, Julia Hernández-Vargas², Marymar Becerra-González³,
Ataúlfo Martínez-Torres³, Evgen Prokhorov², and J. Betzabe González Campos^{1*}

¹*Institute of Chemical and Biological Research, Michoacan University of Saint Nicholas of Hidalgo, Morelia 58030, Mexico*

²*Center for Research and Advanced Studies of the National Polytechnic Institute, Queretaro 76230, Mexico*

³*Laboratorio de Neurobiología Molecular y Celular, Instituto de Neurobiología, Universidad Nacional Autónoma de México, Querétaro 76230, México*

(Received April 4, 2019; Revised June 18, 2019; Accepted June 26, 2019)

Abstract: The combination of collagen (CG), chondroitin sulfate (CS), and hyaluronic acid (HA) with poly(vinyl alcohol) (PVA) was explored to produce 3D tri-component scaffolds with enhanced mechanical properties and potential use in tissue engineering. The CG/PVA/CS and CG/PVA/HA electrospun scaffolds were crosslinked with citric acid, a cytocompatible crosslinker, which induced improved mechanical properties in both dry and wet state, especially with large elongation at break in the wet state. Ultimate tensile stress under the dry and wet state are significantly higher than those previously reported about collagen based nanofibers. IR, DSC and dielectric analysis demonstrated homogenous blending without phase separation and strong interactions between components. All scaffolds had swelling pH-sensitive behavior, making them promising materials for drug delivery systems. The nanofiber mats permitted adhesion and proliferation of human embryonic kidney cells; this cell line formed clusters that adapted well to the mats' surface, through which the cells extended their processes.

Keywords: Collagen-based scaffolds, HEK293 cells, Tri-component scaffolds, PVA, Electrospinning

Introduction

Polymer electrospun nanofibers have demonstrated unique characteristics attractive for tissue engineering [1]. Electrospinning is a highly attractive methodology for fabricating polymer nanofibers due to its versatility, relatively high production rate and simplicity of the setup [2, 3]. In particular, through the electrospinning of natural polymers, their biocompatibility and natural biophysical and biochemical cues might be exploited [4].

The extracellular matrix (ECM) consists of a crosslinked network of collagen and elastin fibrils interspersed with glycosaminoglycans. Collagen (CG) is the most abundant ECM protein; therefore, CG-based electrospun fibers are of particular interest in tissue engineering because their high porosity and large surface area closely mimic the architecture of native tissues, simulating the native milieu and thereby eliciting responses similar to those of native cells [5]. CG is completely biocompatible and degraded by animal collagenases, and its fibrillar network imparts mechanical strength to a gel or tissue. Cell adhesion epitopes exist naturally within the matrix and have the potential to guide cells within a network similar to the topography of natural ECM [6]. Chondroitin sulfate (CS), another important component of the ECM, has recently received focused attention as a proliferation and cell adhesion enhancer in biomaterials [7]. CS is able to interact with various positively charged bioactive molecules, particularly basic

fibroblast, insulin-like, vascular endothelial and platelet-derived growth factors [8]. CS is involved with other important cellular processes, such as receptor binding and migration [9], and introduces bioactive and biosignaling sites, causing chondrocytes to secrete a large amount of collagen [10]. Hyaluronic acid (HA) is another important component of ECM, expressed through the body in many different tissues; HA is highly hygroscopic, plays an important role in tissue hydration and osmotic balance and is involved in a variety of different biological processes, including cellular motility, proliferation and inflammation [11].

These three biopolymers, CG, CS and HA, have been blended to obtain bicomponent electrospun scaffolds. The CG/CS combination is a good example of a biomimetic material able to recapitulate the cartilage environment while reducing inflammation at the site of the implant [12], and studies have reported that the addition of CS to CG could enhance the tensile strength of nanofiber mats [13,14]; nonetheless, the reported mechanical properties are still low. The CG/HA nanofibers demonstrated no toxicity to L929 cells [15], while the toxicity of the CS/HA blend has not been reported yet.

These biopolymers are poorly spinnable, and the weak mechanical properties of the produced nanofibers have led to seek alternatives to overcome these drawbacks without compromising biological compatibility; crosslinking and blending CG and CS with synthetic polymers are common alternatives for this purpose [5,13,16]. In this regard, polyvinyl alcohol (PVA) has gained great attention as a key

*Corresponding author: jbgonzalez@umich.mx

component of polymer blends to generate electrospun scaffolds for tissue engineering. PVA is readily electrospinnable, offers great control over the structure of electrospun nanofibers, has high mechanical properties in the form of nanofiber mats and is nontoxic and biocompatible [17].

CG and CS have been blended with PVA to produce bicomponent electrospun nanofiber scaffolds with excellent results in the biomedical field. PVA/CG electrospun crosslinked nanofiber mats were investigated for cell-nanofiber interactions with the A549 lung epithelial cell line [17]. PVA/CG electrospun scaffolds might sustain the differentiation of mesenchymal stem cells to enhance cartilage repair [16]. The addition of CS to PVA-based fibers enhances cartilage-specific type II CG synthesis *in vitro* and *in vivo* [18] and helps to enhance the cytocompatibility of PVA nanofibers [19].

The production of multicomponent nanofiber mats mainly constituted by natural components is a great challenge; nonetheless, tri-component scaffolds have demonstrated potential for tissue engineering applications [20,21]. PVA/gelatin/chondroitin sulfate nanofibrous scaffolds show no cell toxicity, and L929 mouse fibroblast cells attach and proliferate well on the scaffold surface [20]. However, compared to gelatin, electrospun collagen provides many favorable surfaces for cell adhesion [22]. To the best of our knowledge, there have been few reports related to tri-component nanofiber scaffolds mainly based on natural components [20,21].

Moreover, different crosslinkers have been used to improve the mechanical properties and aqueous stability of biopolymer-based scaffolds, and glutaraldehyde is predominantly used [20,23]. Nonetheless, some of the crosslinking agents used are cytotoxic or provide limited improvement in properties [23]. In this sense, citric acid is a biocompatible crosslinker that improves the mechanical properties and stability of materials without compromising cytocompatibility [23-25].

In light of producing tri-component biomaterials based on natural biopolymers, we explored the combination of CG, CS and HA with PVA, seeking to produce hybrid biocompatible and biodegradable 3D scaffolds with enhanced mechanical properties and potential use in tissue engineering by crosslinking with citric acid, a cytocompatible crosslinker. We note that CG/PVA/CS and CG/PVA/HA electrospun scaffolds have not been previously studied for tissue engineering. For this purpose, we selected the HEK293 human cell line because it is an immortalized cell line derived from human embryonic kidneys and is widely used in cell biology experiments for studying protein biochemistry and cell signaling [26,27] and for testing the viability of polymer electrospun scaffolds [28-30].

On the other hand, the mechanical properties testing of nanofiber scaffolds under the wet state are more representative of physiological conditions; however, there are a few reports related to collagen based nanofiber mechanical properties

under wet condition [31-34]. In this work, the fabrication of CG/PVA/CS and CG/PVA/HA 3D scaffolds with enhanced mechanical properties under the dry and wet conditions and pH-sensitive swelling is reported. These 3D materials sustain the growth of HEK293 cells, suggesting their potential for tissue engineering. This is the first report on the use of these scaffolds in tissue engineering analysis.

Experimental

Type I CG Type I CG from bovine Achilles tendon, poly(vinyl alcohol) (PVA, Mw 89,000-98,000, +99 % hydrolyzed), chondroitin sulfate (CS, bovine trachea), hyaluronic acid sodium salt (HA, Mw 90,000-110,000, sodium salt from *Streptococcus equi*) and 1,1,1,3,3,3-hexafluoro-2-propanol (HFIP) were purchased from Sigma-Aldrich. Four solutions were prepared for the subsequent preparation of CG-based blends. 1) CG was dissolved into HFIP to obtain a 3.2 wt% solution, 2) PVA was dissolved into distilled water to obtain an 8 wt% solution, 3) CS was dissolved into distilled water to obtain a 2.5 wt% solution and 4) HA was dissolved into distilled water to obtain a 0.5 wt% solution.

These four solutions were blended at different ratios to obtain CG/PVA/CS and CG/PVA/HA tri-component combinations.

Based Solutions and Blend Preparation

The CG/PVA/CS combination was tested using three different volume ratios: a) CG/PVA/CS (1:1.5:1.5), b) CG/PVA/CS (1:2:1) and c) CG/PVA/CS (1:1:2). To prepare 100 ml of the CG/PVA/CS (1:1.5:1.5) solution, 25 ml of the CG-based solution, 37.5 ml of the PVA-based solution and 37.5 ml of the CS solutions were mixed. The CG/PVA/HA combination was blended using the CG/PVA/HA (1:1.5:1.5) and CG/PVA/HA (1:2:1) ratios.

The solutions were labeled as follows: CGPVACS, CG2PVACS, CGPVA2CS, CGPVAHA and CG2PVAHA for the CG/PVA/CS (1:1.5:1.5), CG/PVACS (1:2:1), CG/PVA/CS (1:1:2), CG/PVA/HA (1:1.5:1.5) and CG/PVA/HA (1:2:1) blends, respectively.

Electrospinning

The described solutions were electrospun using a NaBond electrospinning unit (NaBondTechnologies Co.). The electrospinning parameters analyzed were voltage, distance between the needle and collector, flow rate, temperature and type of collector. FESEM images were obtained with a JEOL JSM-7600F field emission scanning electron microscope. The average diameter of the nanofibers was determined from the FESEM images, and at least 200 fibers were analyzed from different regions of the image using ImageJ software.

The electrospun scaffolds were crosslinked using a cytocompatible citric acid crosslinker. Ten milliliters of citric acid were diluted in 50 v/v % ethanol aqueous solution

at pH 1-2 adjusted by 0.4 M hydrochloric acid. The volume of citric acid was calculated considering 10 wt% of the dry weight of scaffolds [24]. The crosslinking was performed by immersing the scaffolds in the citric acid solution for 24 h at room temperature. Afterwards, the scaffolds were soaked in ethanol for 1 h, immersed in methanol two times for 1 h each and finally oven dried at 60 °C for 24 h.

Infrared Spectroscopy

The molecular interactions between components were analyzed by Fourier transform infrared spectroscopy on a Perkin-Elmer spectrophotometer using the ATR accessory in the range 4000-650 cm^{-1} ; the resolution was set to 4 cm^{-1} , and the spectra shown are an average of 32 scans.

Thermal Analysis

DSC measurements were performed using a TA Instruments differential scanning calorimeter (DSC 2500). The TGA curves were obtained using a Mettler Toledo apparatus (model TGA/SDTA 851e) with a sample mass of approximately 3 mg and an aluminum sample holder under an argon atmosphere with a flow rate of 75 ml/min. The heating rate was set to 5 °C/min. Two scans were performed: the first one was from room temperature to 120 °C to account for and eliminate moisture, followed by cooling to 40 °C; the second scan was carried out from 40 °C until 400 °C.

Dielectric Spectroscopy

Dielectric spectroscopy characterization was carried out using a Solartron 1260 impedance analyzer with a dielectric interface (1296), which allows the measurement of samples in the 100 Ohm to TOhm impedance range. The measurements were carried out on as-prepare samples in the frequency range of 0.5 Hz to 100 kHz with the amplitude of the measuring signal at 500 mV. The temperature dependence measurements were performed in a closed chamber from 20 to 165 °C. First, the samples were annealed at 165 °C (with the aim to evaporate moisture), and then the measurements were carried out upon quenching and reheating.

Mechanical Testing

A Universal Testing Machine (Zwick/Roell model Z005), equipped with a 500 N load cell, was used to determine the mechanical properties of the nanofiber scaffolds. The samples were prepared with a dog-bone geometry for tensile testing according to the ASTM D638 standard method. The tensile experiments were run in triplicate at dry and wet state by immersion in phosphate-buffered saline (PBS) during 15 min previous testing, at a crosshead speed of 30 mm/min under ambient conditions. The average specimen thickness and dimension were measured using a Mitutoyo digital micrometer. The machine-recorded data were used to plot the tensile stress-strain curves of each specimen. The measurements of Young's modulus, ultimate tensile strength, tensile stress at break and elongation at break were obtained from the stress-strain curves.

Swelling Ratio

The swelling ratio (SR) was determined at different pH

levels and room temperature as follows [35]:

$$SR = \frac{W_0 - W_d}{W_d} \times 100$$

where W_d and W_0 are the weights of the dried and immersed samples, respectively.

The dried sample (W_d) was soaked in distilled water and acidic (HCl buffer pH 1.0) and basic (NaOH buffer pH 8.0) solutions at different times to determine the swelling kinetics. The excess surface water was blotted with tissue paper before weighing the sample (W_0).

Cell Culture of HEK293

The human embryonic kidney 293 (HEK293) cells were grown in a T25 flask at 37 °C in a humidified chamber containing 5 % CO_2 , and the following supplemented media was used: DMEM (Gibco®, cat. # 11995-040), fetal bovine serum 10 % (FBS Gibco®, cat. # 10437-028) and penicillin-streptomycin 1 % (10,000 U/ml, Gibco®, cat. # 15140). The media was replaced every two days. When the monolayer reached 90 % confluence, the cells were passaged with trypsin and replated. Scaffolds with a thickness of approximately 80 μm (measured by FESEM) were cut into 0.5 mm^2 squares and sterilized by UV light for 10 min on each side; UV light sterilization was used because it does not influence fiber morphology [36]. The scaffolds were glued on the surface of a 35 mm Petri dish. The HEK293 cells were transferred from a T25 flask, and growth was monitored under a light microscope every 24 h. Forty-eight hours after seeding on the scaffolds, the cell medium was replaced, and 2.5 μl of 3.3×10^7 VP/ml of adenovirus Ad-eGFP was included. Cells attached to the surface of the Petri dish were taken as controls for each scaffold ($n=6$ for each scaffold). Detailed analysis of cell morphology was focused on the soma area, number and length of the processes. The following were used for comparing cell clusters: number of clusters per area, number of cells per cluster and area of cluster. The images were taken under an LSM510 Zeiss confocal microscope, using a 20X Zeiss Plan-APOCHROMAT, NA=0.8, WD=0.55 mm (Cat. No. 440641-9911) objective. The cellular and cluster characteristics were determined using ImageJ. One-way ANOVA followed by Tukey's post hoc test was performed using GraphPad Prism version 5.00 for Windows (GraphPad Software, La Jolla California USA, www.graphpad.com).

EdU Cell Proliferation Assay

This assay was performed for the CGPVACS, CG2PVACS, CGPVA2CS and CG2PVAHA scaffolds using the HEK293 cell line; in all cases, four replicates were assayed. The cell proliferation rate was determined by cell counting over time (24 h, 48 h and 72 h). EdU labeling allows visualization of cells that are actively synthesizing nuclear DNA. Then, the label index (LI) was estimated as the percentage of nuclei that exhibit the EdU label over the total number of nuclei stained with DAPI.

The scaffolds were glued on round glass coverslips (12 mm - Electron Microscopy Cat. # 72196-12), and the HEK293 cells were seeded on each scaffold and on glass coverslips. Four-well plates with a surface area of 2 cm² (ASi Alkali Scientific Inc., Cat. TP9004) were used to hold the scaffold. The cell-seeding density was 0.05×10⁶ cells per well as determined with a Neubauer chamber. The EdU cell proliferation assay was performed as follows: a stock solution of EdU [10 μM] was dissolved in DMSO. Ten microliters of a 10 mM stock solution was further dissolved in 5 ml of prewarmed culture medium to make a 20 μM EdU labeling solution. Half of the growth medium from the HEK293 culture was replaced with an equal volume of EdU labeling solution (final concentration of 10 μM). The cells were incubated in a CO₂ chamber for 2 h. Each coverslip was transferred into a new well, and 1 ml of 3.7 % formaldehyde in PBS was added to each well and incubated at RT for 15 min. Then, the formaldehyde was removed, and the cells were washed twice with 1 ml of 3 % BSA in 1X PBS. The wash solution was removed, and 1 ml of 0.5 % Triton[®] X-100 in 1X PBS was added to each well and incubated for 20 min at room temperature. The permeabilization buffer was removed from the cells, which were then washed twice with 1 ml of 3 % BSA in 1X PBS. The wash solution was removed, and a reaction cocktail was added to each well for 30 min, protected from light. The reaction cocktail was removed, and each well was washed once with 1 ml of 3 % BSA in 1X PBS. The labeled cells were mounted with VECTASHIELD[®], and the nuclei were labeled with DAPI. The images were obtained by an epifluorescence microscope with a 10X objective for cell counting from digital images.

Statistics

The data were normalized by calculating the LI of each replicate. To determine the effect of the four different scaffolds in three time-lapses over the EdU+ cells (i.e., the LI), a two-way ANOVA with Bonferroni post testing was performed using GraphPad Prism version 5.00 for Windows.

Results and Discussion

Electrospinning

The voltage, flow rate, needle-collector distance and collector were varied to obtain nanofiber mats with the best quality. The electrospinning parameters with the best results

for producing electrospun tri-component mats were determined after several assays and are shown in Table 1. Figure 1 shows the SEM images of the CGPVACS, CG2PVACS and CGPVA2CS samples (see Table 1). A random three-dimensional arrangement and high nanofiber content are produced by raising the electrospinning temperature to 40 °C.

The increase in PVA volume proportion considerably reduces the bead production (sample CG2PVACS, Figure 1(B)). In general, nanofiber diameters between 20 and 150 nm were observed. The increase in the CS volume ratio is not favorable for producing nanofiber mats from the CGPVACS (1:1:2) solution (sample CGPVA2CS). At this concentration of polymer solution, the charged jet destabilizes and breaks down into small spherical droplets, which solidify between the emitter tip and are deposited on the collector, turning the process from electrospinning to electrospraying and producing spherical micro- and nanoparticles (see Figure 1(C)). Nonetheless, this architecture is also highly attractive for biomedical applications because it has a high surface-to-volume ratio and high CS content, which could improve cellular adhesion [7].

The injection flow rate of the polymer solution was varied from 0.3 to 1.5 ml/h. As the flow rate increased, the amount of polymer solution ejected at a specific given time increased, resulting in a simultaneous increase in the diameters of the nanofibers. In the CG/PVA/CS blends, at low flow rates, the polymer jet was cut several times because an insufficient amount of polymer solution was injected and stretched by the electric field. Thus, an injection flow rate of 1 ml/h was chosen as the optimum flow rate for electrospinning the CG, PVA and CS blends. When the voltage was varied while other parameters were kept constant, there was no observable effect on the diameter of the nanofibers. However, at voltages lower than 20 kV, the number of beads increased in the CG/PVA/CS blends; the voltage was crucial for producing the Taylor cone. The increase in temperature from 25 to 40 °C favored the production of nanofibers and reduced the nanofiber diameters. The increase in the needle-collector distance represented a weak electric field favoring the formation of thin fibers; nonetheless, at shorter distances, the production of beads was considerably reduced.

In addition, the CGPVAHA tri-component blends were tested in the electrospinning process to analyze the effect of switching from CS to HA. The injection flow rate of the

Table 1. Electrospinning parameters for producing tri-component nanofiber mats

Label	Blend	Volume ratio	Voltage (kV)	Flow rate (ml/h)	Needle-collector distance (cm)	Temperature (°C)	Collector
CGPVACS	CG/PVA/CS	1:1.5:1.5	20	1	12	40	Static
CG2PVACS	CG/PVA/CS	1:2:1	20	1	12	40	Static
CGPVAHA	CG/PVA/HA	1:1.5:1.5	20	1.5	12	20	Static
CG2PVAHA	CG/PVA/HA	1:2:1	14.5	0.6	12	40	Rotating drum

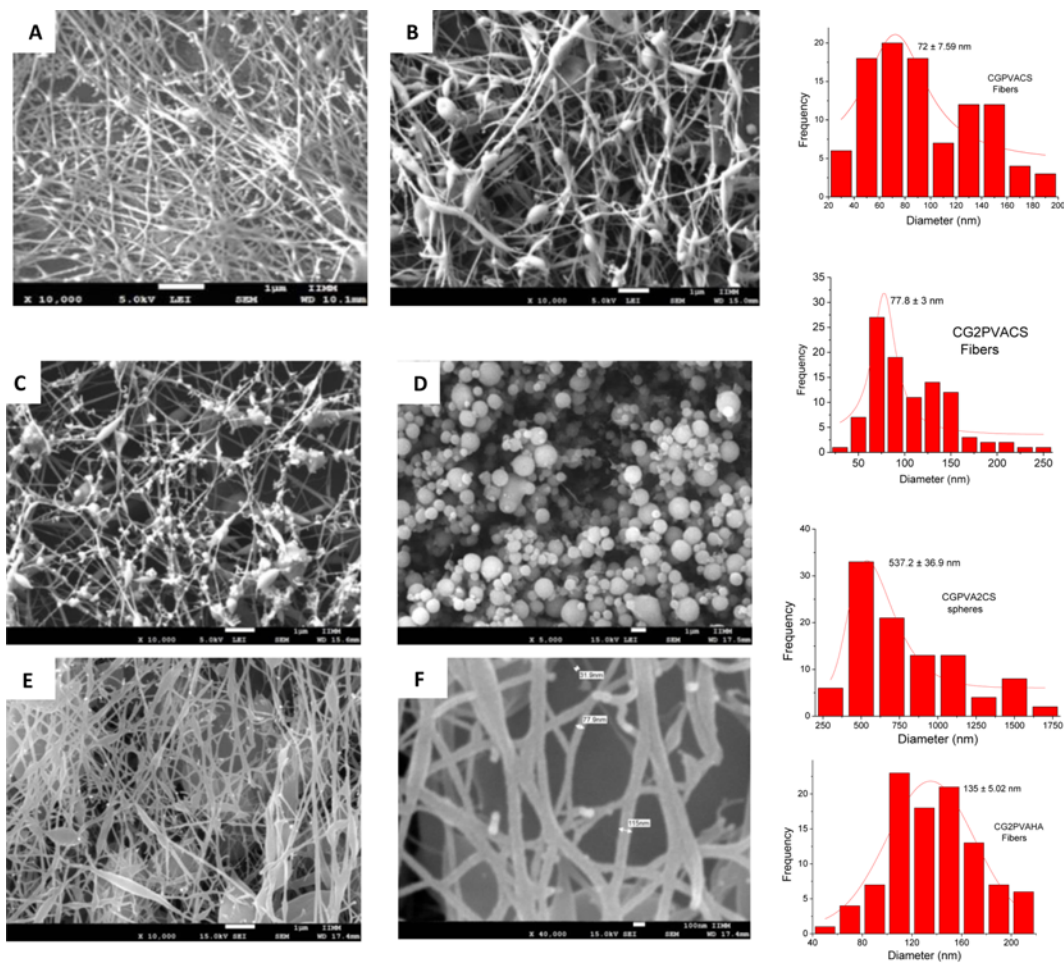


Figure 1. SEM images of electrospun samples of CG/PVA/CS blends; (A) CGPVACS25, (B) CGPVACS40, (C) CG2PVACS40, (D) CGPVA2CS40, (E) CG2PVAHA, and (F) CG2PVAHA nanofiber diameter. Size distribution is shown in the right.

polymer solution was reduced to 0.6 ml/h at 40 °C. In general, the quality of the CGPVAHA nanofibers improved by increasing the PVA content and temperature and by using a rotating drum; however, the presence of beads could not be eliminated (see Figure 1(D)).

As shown by the SEM images, the nanofiber production is high but not as perfect as that previously reported for collagen-based electrospun blends [21]. Despite several attempts, the production of nanofiber beads could not be eliminated; nonetheless, we decided to investigate the effect of the tri-component combination on cell growth since the 3D architecture could be highly favorable. The CG2PVACS (1:2:1), CGPVACS (1:1.5:1.5) (1:1:2), and CG2PVAHA (1:2:1) electrospun scaffolds with minimal defects and the CGPVA2CS samples in the form of micro- and nanospheres were selected for further characterization and for the *in vitro* cell growth tests.

Infrared Spectroscopy

Figure 2 shows the IR spectra of CGPVACS composites

compared with the spectra of pure PVA, CG and CS. The FTIR spectrum of the composite shows characteristic bands of CG, PVA and CS together. The two bands assigned to the stretching and bending vibrations of several hydroxyl groups (between 3800 and 3650 cm^{-1} and at 917 cm^{-1} , respectively) of pure PVA decreased in intensity and redshifted. In the composite nanofiber spectra, the OH stretching vibration is overlapped by N-H stretching vibrations characteristic of the amide I groups of CS and CG [37,38]. In contrast, the characteristic amide bands of CG and CS located at 1670 and 1645 cm^{-1} [37,38], respectively, in the CGPVACS composites shifted to 1660 cm^{-1} and were considerably reduced in intensity. This observation is an indication of variations in the backbone conformation or hydrogen-bonding pattern because of chemical interactions between the OH and NH_2 groups of the three components.

The vibration band of pure PVA at 1750 cm^{-1} , which is associated with C=O stretching vibrations (acetate group, crystalline), is hardly observed in the spectrum of the composite. The band at 1089 cm^{-1} , which is associated with

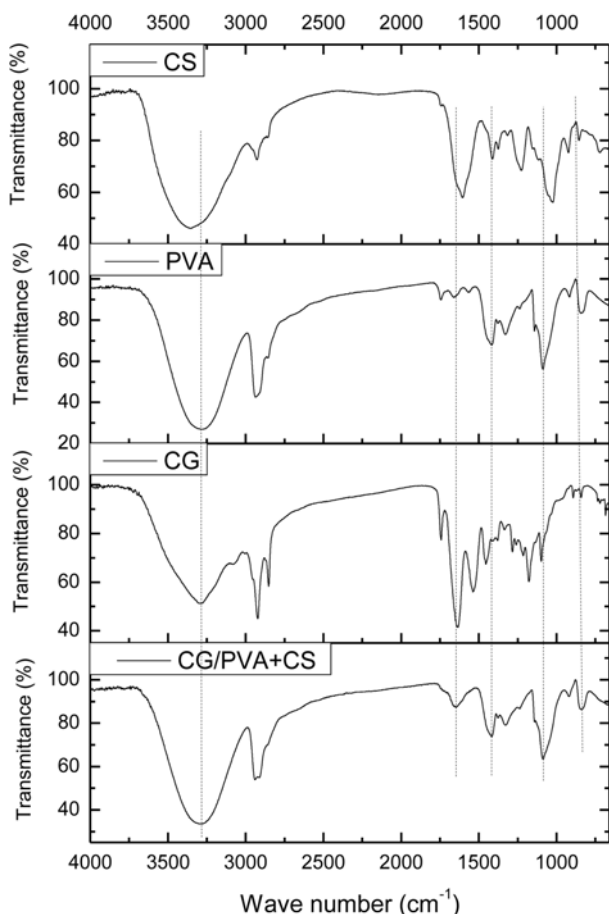


Figure 2. IR spectra of pure components and CG2PVACS nanofiber mat.

vibrations of the remaining C-O acetyl groups present on the partially hydrolyzed PVA backbone, shifts from 1089 cm^{-1} to 1060 cm^{-1} in the spectrum of the composite. This finding suggests that C=O groups are available for making hydrogen bonds with -OH groups.

The crystalline-related vibrations at 1417 and 1329 cm^{-1} in pure PVA [39] decrease in intensity and shift to lower wavenumbers as the CS content increases. Importantly, the IR spectra of the CG/PVA/HA combination also show clear evidence of a strong interaction between the components (not shown). These IR changes are an indication of intermolecular interactions between the polymers at the molecular level through hydrogen bonding, which affects the crystalline fraction of PVA.

Thermal Analysis

Figure 3A shows the DSC thermograms from the second scans of pure PVA, CS and CG. A first scan from room temperature to $120\text{ }^{\circ}\text{C}$ was performed for water elimination. Upon quenching and reheating, the DSC curve of PVA shows the three characteristic thermal events: the β_c relaxation at $135\text{ }^{\circ}\text{C}$ caused by changes in the crystalline volume fraction [40], the sharp endothermic peak at $228\text{ }^{\circ}\text{C}$ associated with the melting of the crystalline domains, and the endothermic peak at $288\text{ }^{\circ}\text{C}$ related to thermal degradation [41]. The DSC curve of pure CS shows two exothermic peaks located at $242\text{ }^{\circ}\text{C}$ and $299\text{ }^{\circ}\text{C}$; these peaks are related to the beginning of decomposition and the thermal degradation of CS, respectively [38,42,43]. The DSC thermogram of pure CG shows a thermal event at $225\text{ }^{\circ}\text{C}$, which is called the first-order transition of denaturation of dehydrated collagen, associated with the conformational changes of the collagen molecules from a triple helix structure to a random coil [44, 45]. Additionally, the peaks at $283\text{ }^{\circ}\text{C}$ and $340\text{ }^{\circ}\text{C}$ are related to the two-stage degradation of collagen [45,46].

The DSC curves of the CG2PVACS, CGPVACS and CGPVAHA nanofiber mats show five thermal events between $25\text{ }^{\circ}\text{C}$ and $400\text{ }^{\circ}\text{C}$ (notably, the CGPVA2CS nanofiber mat showed a similar DSC behavior as that of the CGPVAHA sample; see Figure 3(B)); the thermal transitions of pure PVA were superposed for comparison. The endothermal peak at approximately $225\pm 1\text{ }^{\circ}\text{C}$ is observed in all samples. These peaks are small, broad and slightly

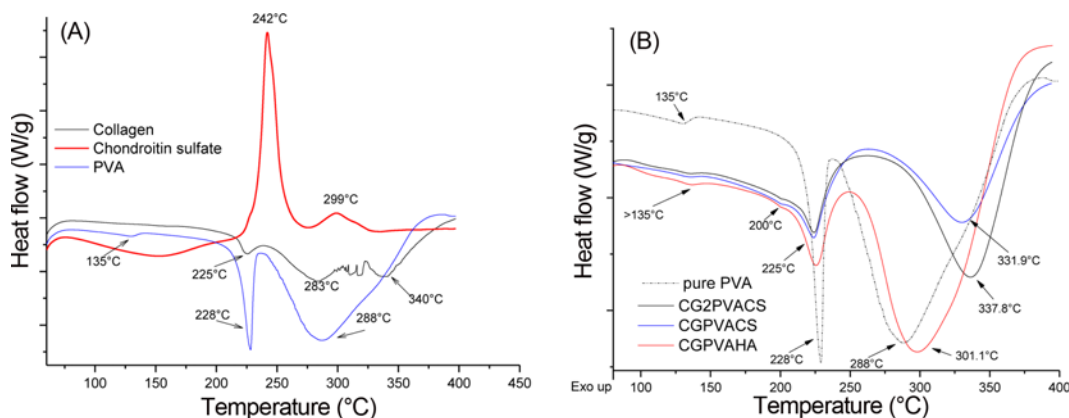


Figure 3. DSC curves; (A) pure PVA, CG and CS and (B) CG2PVACS, CGPVACS and CGPVAHA nanofiber mats.

moved to low temperatures compared to the pure PVA peak; a melting temperature depression is a characteristic feature of miscible polymer materials with intermolecular interactions between the components [47,48]. In addition, the decrease in the melting temperature suggests that the crystallinity and perfection of the crystal structure are reduced [49]; this observation is an indication of decreased ordered association of the PVA molecules because of crosslinking with CG and CS, meaning that the PVA molecules were highly constrained by these polymers.

The decrease of the crystalline domains of PVA due to its interaction with CG and CS affects the β_c relaxation (observed at 135 °C in the DSC curve of PVA); this thermal event is related to changes in the crystalline volume fraction of PVA (see Figure 3(C)) [40]. In the CGPVACS, CG2PVACS and CGPVA2CS samples, this thermal event shifts from 135 °C to 140 °C compared to that in pure PVA (see Figure 3(B)) and is similar to the characteristic step-like change in heat capacity, which is related to the glass transition of the polymer amorphous fraction, rather than the characteristic peak of the β_c relaxation. This phenomenon is further discussed below in light of dielectric spectroscopy.

The last endothermic peak above 300 °C observed in all blends is associated with polymer chain thermal degradation. A single thermal degradation located at 288 °C is observed in pure PVA, while pure CS and CG exhibit two-stage thermal degradation, as shown above. The single degradation temperature of the nanofiber mats decreases as the CS content increases (CGPVA2CS < CGPVACS < CG2PVACS) and increases as the PVA content increases. This result suggests high strength in the systems with high PVA content due to crosslink formation. The differences in the thermal profiles of CGPVACS, CG2PVACS, CGPVA2CS and CGPVAHA samples compared to those of pure components indicate that the CG/PVA/CS and CG/PVA/HA combinations blended homogeneously without phase separation and formed strong interactions, as demonstrated by IR analysis.

Dielectric Spectroscopy

The DSC curves of the CGPVA, CG2PVACS, CGPVA2CS and CGPVAHA composites show that the thermal event at approximately 140 °C (which in pure PVA is related to the β_c relaxation) looks like the characteristic step-like change in heat capacity related to the glass transition of the polymer amorphous fraction (see Figure 3(B)). To confirm this DSC observation, impedance measurements were carried out on the CG2PVACS nanofibers and film composite. Dielectric spectroscopy is an effective tool to measure the molecular mobility around the glass transition [40,50,51], since this technique can be used to observe the glass transition even in polysaccharides with controversial glass transition temperatures (T_g) such as chitin and chitosan [50,51].

The rapid increase in molecular mobility around the glass transition in heating of a material can be observed by dielectric measurements in the appearance of α -relaxation and the rapidly increasing permittivity [52-54]; the dielectric constant of materials typically exhibits a pronounced peak denoting T_g [52-54]. If a varying electric field is applied, polar groups will align with the field. Below T_g , the rotation of the bonds is not possible; consequently, the dielectric constant will be low. With increasing temperature, the dielectric constant will drastically increase around T_g , and above T_g , the increased thermal vibrations cause the dielectric constant to drop again. Therefore, T_g can be identified as a pronounced peak in the temperature dependence of the dielectric constant [52-54].

Figure 4 shows the temperature dependence of the dielectric constant at the limit of zero frequency measured in the CG2PVACS nanofiber mat and film. In both cases, the dielectric constant exhibits a peak (or a glass transition temperature) at approximately 130 °C and 145 °C for the nanofiber mats and films, respectively. Therefore, the dielectric measurements confirm the DSC observations: in CG2PVACS composites, the thermal event detected by DSC at approximately 140 °C is related to the T_g .

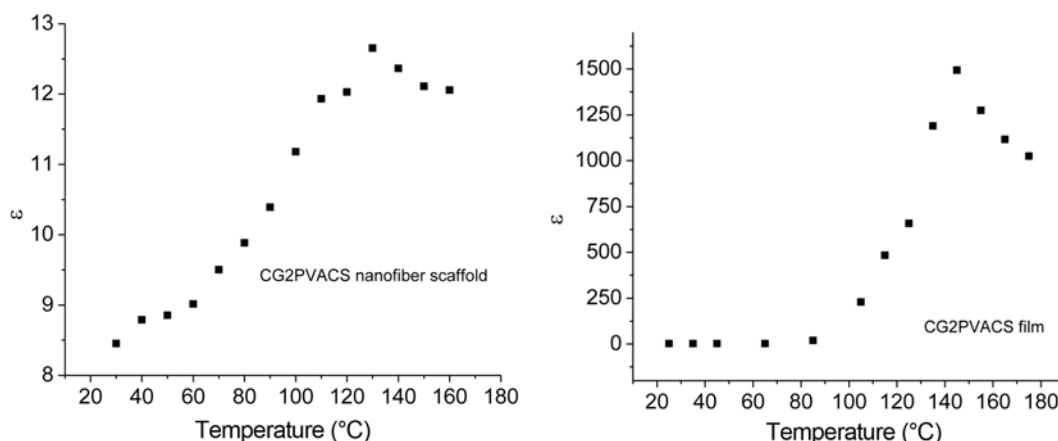


Figure 4. Dependence of static dielectric constant on the temperature measured in CG2PVACS nanofiber mats and films.

From dielectric measurements, a value of $T_g=82.4$ °C has been previously observed for pure PVA [40]; consequently, the interaction of PVA with CG and CS raises T_g to 135 °C. In the glassy state, structural relaxation requires molecular mobility and available free volume. However, in these systems, crosslinking restricts motion and decreases the free volume, leading to an increase in T_g [55]. Importantly, full miscibility is characterized by a single glass transition temperature of blends [56], as in this case.

Mechanical Testing

Figure 5 shows the stress-strain dependence of the uncrosslinked and crosslinked (dry and wet conditions) CGPVACS, CG2PVACS and CG2PVAHA scaffolds. Mechanical testing for the CGPVA2CS sample was not possible because the final architecture of this composite, which was composed of micro- and nanospheres (see Figure 1(D)), is not favorable for the production of proper samples for this test. The Young's modulus (MPa), ultimate tensile strength (MPa), tensile stress at break (MPa) and elongation at break (%) of the tested samples are given in Table 2. The stress-strain curves of the CGPVACS and CG2PVACS scaffolds (Figure 5(A)) exhibit the same behavior displayed

by other collagen- and PVA-based nanofibrous materials previously reported [31,57,58]. These curves show a linear range in which the stress increases in proportion to the strain; the slope of this region gives the Young's modulus and characterizes the stiffness of the material. As shown in Table 2, the Young's modulus, ultimate tensile strength and elongation at break increase with increasing PVA content.

The stiffness of the CGPVACS, CG2PVACS and CG2PVAHA scaffolds is considerably higher than those previously reported for collagen/PVA-based nanofiber materials with uniform structures [31,57-62]. Nanofibers have inferior mechanical properties when beads are present. Nanofibers with beads have low Young's modulus, tensile strength, and elongation at break because the beads induce stress concentration as the nanofibers are stretched. However, in some cases, the production of uniform nanofibers requires a certain polymer concentration that will result in a reduction in modulus and strength [63], which could be because fibers produced at low polymer concentrations have small diameters; hence, the nanofiber diameter could play an important role. As shown in Table 2, the PVA concentration and crosslinking are key parameters for improving mechanical properties rather than beads content; a higher

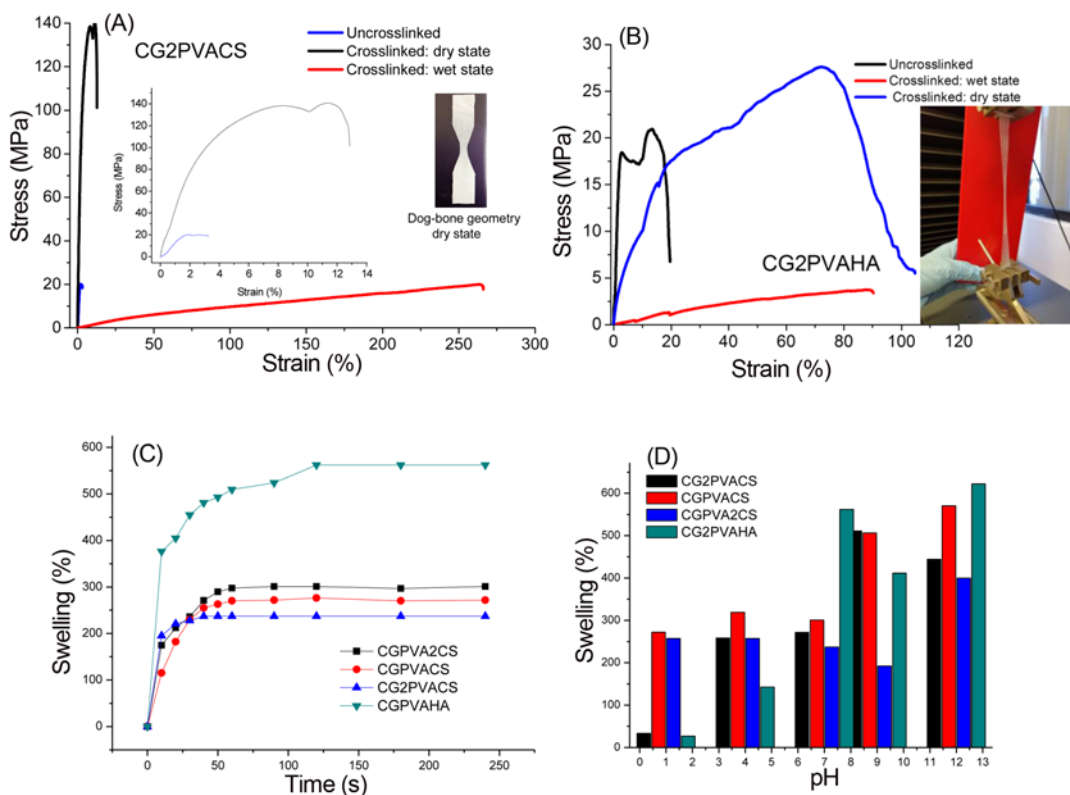


Figure 5. (A) Stress-strain dependence of CG2PVACS scaffold (uncrosslinked and crosslinked dry and wet states). The dog-bone geometry of the samples according to the ASTM D638 standard method for mechanical testing is shown in the insert. Zoomed-in view of the stress-strain dependence data of the uncrosslinked and crosslinked CG2PVACS scaffolds, (B) stress-strain dependence of CG2PVAHA scaffold (uncrosslinked and crosslinked dry and wet states). The high elasticity of scaffolds is shown in window insert, (C) swelling kinetics of nanofiber scaffolds, and (D) swelling behavior at different pH levels.

Table 2. Mechanical properties of electrospun scaffolds

Sample	Young's modulus (MPa)	Ultimate tensile strength (MPa)	Tensile stress at break (MPa)	Elongation at break (%)
CGPVACS				
Uncrosslinked	958.9	11	10.98	2.19
CG2PVACS				
Uncrosslinked: dry state	1134.9	13.2	11.98	2.86
Crosslinked: dry state	5449.99	92.6	140.59	12.87
Crosslinked: wet state	10.82	7.94	19.96	266.42
CG2PVAHA				
Uncrosslinked: dry state	1416.6	29.9	20.7	29.4
Crosslinked: dry state	324.18	4.35	27.62	104.79
Croslinking: wet state	30.26	0.6	4.09	48.81

PVA content and acetic acid crosslinking induce higher Young's modulus, ultimate tensile strength, tensile stress and elongation at break. A higher PVA content is related to lower bead production. This phenomenon means that after crosslinking, uniform CG2PVACS nanofibers would have enhanced mechanical performance. We attribute the increase in mechanical properties to the high bonding strength in the systems due to the crosslink formation. The primary crosslinking effect appears not to affect the chain extensibility.

The mechanical properties under wet state are more representative of physiological conditions [31]; therefore, the crosslinked scaffolds were tested under wet condition. As shown in Figure 5(A), the Young's modulus, ultimate tensile strength and tensile stress at break of CG2PVACS scaffold obviously decreased, while the elongation at break increased by almost 20 times compared to the dry condition. The decreased mechanical properties in the wet state suggested that the hydrogen and the electrostatic bonds or other chemical bonding that hold polymeric fibrils together were break down by water molecules [31].

CG2PVAHA crosslinked scaffold also shows higher mechanical properties compare with the uncrosslinked state (see Figure 5(B) and Table 2). Crosslinking favors the non-linear elasticity, increasing the elongation at break almost by two times in the wet state. In general, the elastic modulus of our collagen-based scaffolds is significantly higher than the reported value for human cartilage (6.0 MPa) [64].

Ultimate tensile stress of electrospun collagen and collagen blends is usually reported in the dry state where values range from 0.02 to 30 MPa [31], while there are a few studies under the wet state where tensile strength range from 0.05 to 0.75 MPa [31-34]; both values are considerable lower than the reported herein for the dry and wet state.

Based on these results, we can highlight that although the production of beads could not be eliminated, the mechanical properties of the scaffolds were not affected. Therefore, we believe that all scaffolds prepared in this work are suitable for tissue engineering and might be suitable for systems

requiring high mechanical resistance.

Swelling Ratio

Swelling capacity is very important in biomedical and pharmaceutical applications because the equilibrium degree of swelling influences the surface properties, surface mobility, mechanical properties and solute diffusion coefficient through the hydrogel [65]. The SR of the CGPVACS, CG2PVACS, CGPVA2CS and CG2PVAHA scaffolds at different times and pH levels are shown in Figures 5(C) and 5(D), respectively. All scaffolds reached maximum swelling within seconds; these values are almost two (for CG/PVA/CS-based scaffolds) and three (for CG/PVA/HA-based scaffolds) times higher than those previously reported for CG/PVA and CG/chitosan/PVA electrospun matrices [66]. The swelling ratio of pure electrospun CG nanofibers is approximately 100 % [65], which indicates that with the addition of PVA, CS and HA, water uptake is more than two times higher than that of pure CG.

Swelling in PVA is affected by the degree of crystallinity; the water uptake of PVA decreases as the crystallinity degree increases [67]. In this case, the swelling ratio increases as the CS content increases (Figure 5(C)). This observation is ascribed to changes in the crystalline fraction of PVA induced by the CS content. As determined by IR and DSC analysis, the crystalline fraction of PVA is reduced as the CS content increases; therefore, scaffolds with high CS contents show high swelling ratios. The degree of crystallinity can be estimated by comparison of the experimental DSC melting enthalpy with literature values relative to 100 % crystalline PVA (138.6 J/g) [68]. The nominal degree of crystallinity obtained from the DSC curve of pure PVA and CG2PVACS, CGPVACS and CGPVA2CS samples are 53.13 %, 15.5 %, 24.4 % and 27.6 %, respectively, in agreement with swelling behavior.

Figure 5(D) shows that the swelling behavior of all the scaffolds is pH-responsive, showing high swelling at basic pH; at this pH, the hydrogen bonding is disrupted, the

carboxylic acid moieties are ionized, and the electrostatic repulsion between the COO^- groups enhances the swelling capacity [69]. At acidic pH, most of the carboxylate groups are protonated, so the decreased repulsion of anionic groups leads to a decreased swelling ratio, and the materials aggregate [69,70]. pH-sensitive biomaterials are of great interest as promising smart drug delivery systems, filters and membranes for selective diffusion and sensors [70,71].

Cell Culture

The ability of the CGPVACS, CG2PVACS and CGPVA2CS and CG2PVAHA scaffolds to grow mammalian cells was tested by growing HEK293 cells (Figure 6). The HEK293 cell line is commonly used to assess the cytocompatibility of biomaterials [71]. Hence, pseudopodia formation and the number and area of cells are important morphological features of normal cellular growth [27,28,72-74]. All the attached cells on the tested nanofibers developed a polygonal morphology with a dominant pseudopodium, suggesting the

presence of adhesion molecules and the balance of hydrophilicity and hydrophobicity within the microenvironment [75]. The pseudopodium is indicative of cellular polarization, which leads to cellular migration [76]. Although no significant differences were observed in the process length (Figure 7(a)), long pseudopodia were consistently developed on the CGPVACS nanofiber mat (Figure 6, lower panel – CGPVACS, Figures 8(A) and 8(B), yellow arrowhead). On the other hand, short pseudopodia were observed on the CG2PVACS nanofiber mat (Figure 1(C)), which is consistent with a previous report [4]. The cells grown on the CG2PVAHA nanofiber mat developed the second longest processes compared with those on the other two CG/PVA/CS samples. This result makes sense because the hydrophilic nature of hyaluronic acid has a strong influence on rapid cellular adhesion [77].

The topography and composition of electrospun materials have diverse effects on cellular behavior [78], influencing the number of cells per cluster and the area covered by the clusters. These differences may arise from structural features of the nanofiber mats that alter nutrient transfer [28]. High cell densities indirectly suggest increased basal activity that leads to cellular growth [79]. Thus, as nuclear size is proportional to the size of the cell, differences in cell body area may be interpreted as possible alterations in the size and shape of the nucleus, which in turn have a strong influence on cell proliferation. In summary, the larger the cell cluster area is, the more extensive the cell spreading, suggesting strong cytoskeleton tension and nuclear elongation [80].

The HEK293 cells attached well to the surface of all four scaffolds. After three days *in vitro*, the cells expressing GFP were imaged by confocal and epifluorescence microscopy; for epifluorescence, the nuclei were stained with DAPI (Figure 6). No significant differences were found in the size of cell bodies and the number of processes, but a statistically significant difference ($P < 0.05$) was observed in the average process length in cells growing on the CG2PVACS scaffolds (Figure 7(a)). The cells formed clusters with a similar number of cells on the surface of the scaffolds, and there was no significant difference in the number of clusters within the area of the scaffold, suggesting similar cellular growth rates in all of the scaffolds (Figure 7(b)).

Confocal fluorescence microscopy provides high resolution for determining how cells interact with each other and with the surface of the scaffolds. Figure 8 shows sample 3D projections of HEK293 cells induced to express GFP. The cells' bodies were round when they contacted each other, but the processes extended toward free spaces. The lengths of the processes were similar among the scaffolds except for CG2PVACS. An animated reconstruction of the cells grown on the CGPVA2CS scaffold is shown in the Supplementary Information section (see Video 1, supplementary information).

Figure 9 shows HEK293 cells labeled with EdU and DAPI. In all cases, the tested scaffolds showed a reduced

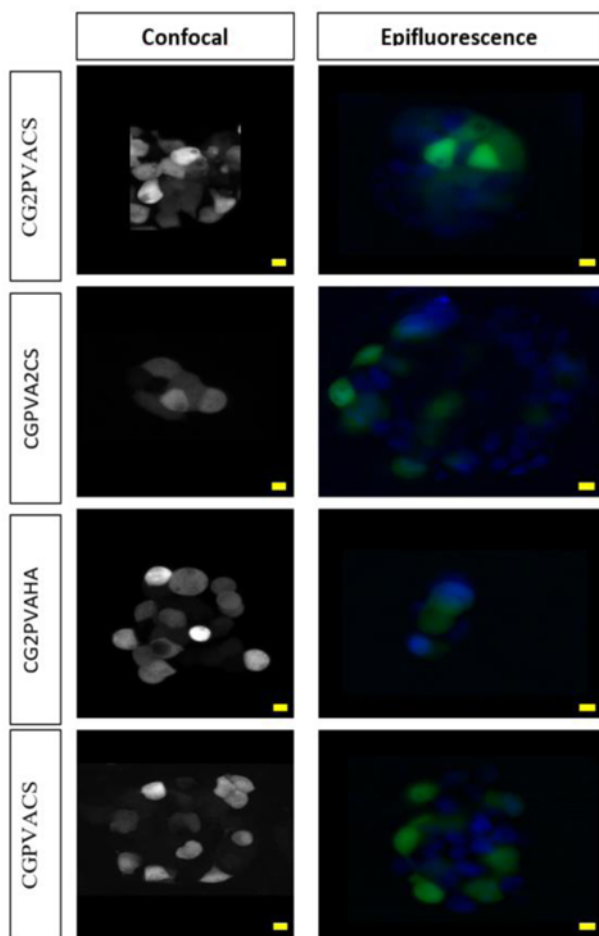


Figure 6. HEK293 cells grow on scaffolds forming clusters. The images show the array of cell clusters formed on each scaffold. The cells were infected with the adenovirus CMV-GFP (bar=10 μm), and the nuclei were stained with DAPI (bar=20 μm).

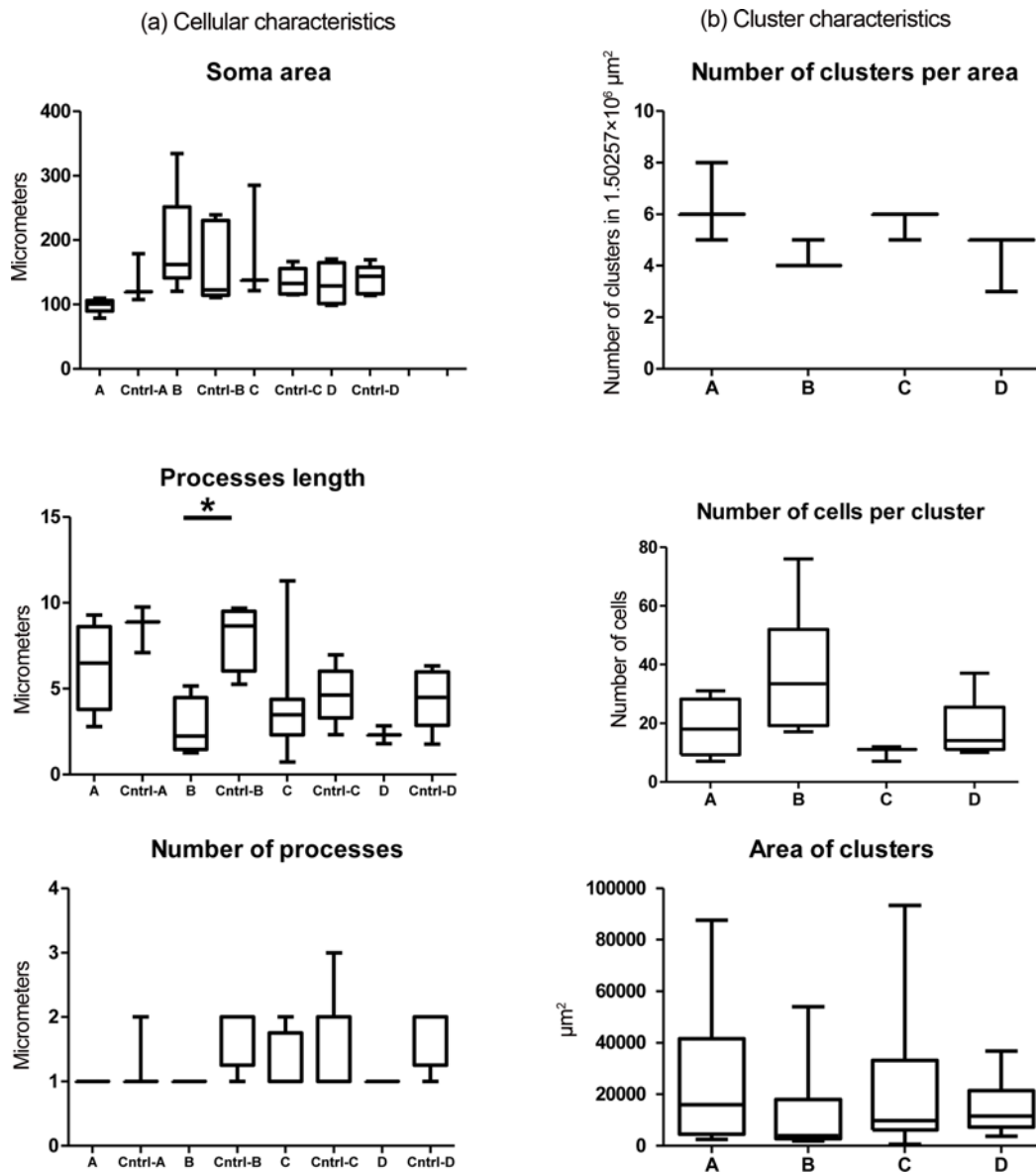


Figure 7. HEK293 cells preserve the typical morphology when growing on the scaffolds labeled as CGPVACS (Cntrl-A), CG2PVACS (Cntrl-B), CGPVA2CS (Cntrl-C) and CGPVAHA (Cntrl-D). (a) The cells showed no significant differences in soma size or number of processes. Slight differences in the length of the processes were detected and (b) the cells grew on scaffolds forming clusters of regular areas and conformed to a similar number of cells.

number of cells that incorporated EdU over time; even in the CGPVACS (4) scaffold at 72 h, the number of cells attached to the scaffold decreased. The rest of the scaffolds showed an increase in the number of nuclei stained with DAPI after 72 h (except CGPVA2CS), and little or no EdU labeling was detected (Figure 9(A)).

Quantitative analyses suggested that EdU incorporation depended on the scaffold in which the cells were grown and was time-independent; that is to say, the interaction of the variables (time vs scaffold) was not significant: $F_{(8,59)}=1.55$, P value=0.1607. Even LI decreased over time in all scaffolds

(P value < 0.0001); each scaffold had a different effect on LI, as observed in the tested time-lapses: $F_{(4,59)}=4.22$, P value=0.0045 (Figure 6(B)).

The tissue-like architecture of nanofiber mats is suitable for mammalian cell growth, providing a favorable environment for the diffusion of nutrients. Due to their porous surface, scaffolds may provide a substrate for vascularization. Another property of these new materials is that they do not show autofluorescence, as do some of scaffolds derived from poly(3-hydroxybutyrate-g-vinyl alcohol) [81]. This property results in better imaging under epifluorescence and confocal

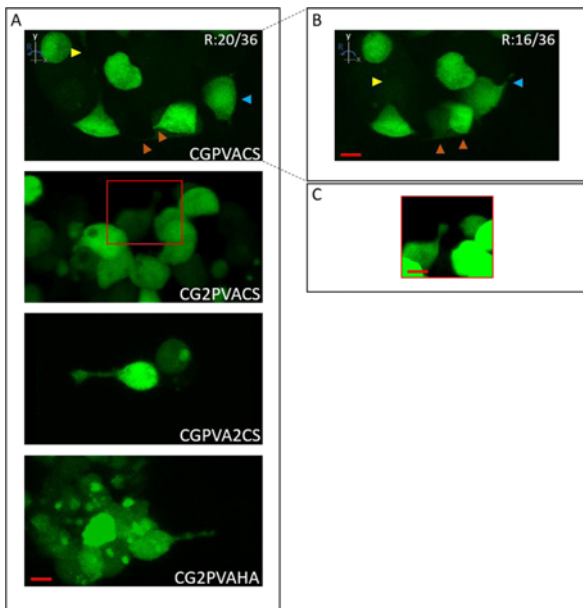


Figure 8. 3D projections of cell clusters growing on scaffolds. (A) The yellow arrowhead points to a large process extending from the cell body and still visible in the rotation shown in B. The orange arrowheads point to shorter processes, and the blue arrowhead points to a cell whose processes are not visible in A but are clearly observed after rotation (B). The second image in panel A shows an example of tiny cell processes (C). The two bottom images in A show examples of long processes extending from the cell bodies toward the free space of the scaffold.

microscopy.

All the tested scaffolds were biocompatible mats capable of inducing cell adhesion and proliferation in 3 days, forming homogeneous numbers of clusters, which covered almost the same area and contained a similar number of cells. We think this cellular self-organization resembles a tissue-like structure where the topological arrangement produces isolated environments, which is convenient for some assays. Compared with the 2D culture (consisting of cells attached to a surface), these electrospun mats produced a 3D architecture where material biocompatibility led cells to form functional clusters [37]. Furthermore, cellular morphology appeared to develop properly. We suggest further testing for specific tissue engineering applications and drug delivery systems, particularly the *in vivo* evaluation of cartilage-like tissue for repairing applications.

Conclusion

We have developed novel tri-component electrospun scaffolds based on natural polymers with enhanced mechanical properties in the dry and wet states and pH-sensitive swelling behavior. The presence of CS affects the chemical interaction between the components, the spinnability of the blends and the mechanical properties of the electrospun materials. The use of a biocompatible crosslinker produced high bonding strength providing high thermal stability and enhanced mechanical properties in the dry and

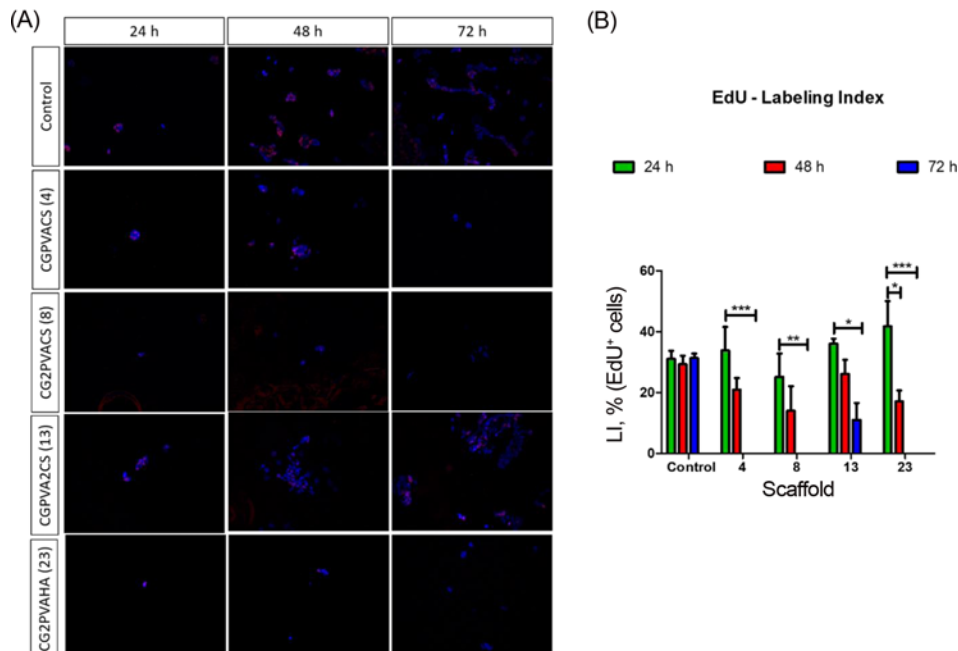


Figure 9. Labeling index is reduced over time. (A) Tested scaffolds at 24 h, 48 h and 72 h. Epifluorescence imaging shows HEK293 cells with the EdU reaction and DAPI staining and (B) Quantitative analysis shows a consistent reduction in LI over time. In all cases with the exception of the CGPVA2CS scaffold, by 72 h, none of the cells underwent proliferation, as suggested by the lack of EdU labeling. Note the consistency in LI under control conditions compared to each scaffold.

wet states. The crosslinking increased the Young's modulus of CG2PVACS scaffold by almost 4.8 times, and in the wet state the elongation at break increased by almost 20 times compared to the dry state. The swelling behavior of all scaffolds is pH-sensitive, which makes these materials attractive for smart applications, including biomedical devices, drug delivery carriers, and filters and membranes for selective diffusion and sensors. In general, the ultimate tensile stress of CG/PVA/CS and CG/PVA/HA scaffolds are considerable higher than those previously reported for electrospun collagen and collagen blends in the dry and wet states.

The architecture of the nanofiber mats is appropriate to allow HEK293 cell attachment and is a favorable environment for the ingrowth and proliferation of cells. The topography and composition of the electrospun scaffolds have a specific effect on cellular behavior, and differences in cellular density suggest effects on nutrient transfer. The tested scaffolds are promising candidates for tissue engineering and drug delivery systems.

Acknowledgments

The authors thank CIC-UMSNH and CONACyT for financial support (A1-S-21845 to JBGC and A1-S-7659 to AMT: Projects supported by the Sectoral Fund for Education) and M.I. Gerardo A. Fonseca Hernández (CFATA-UNAM) for technical assistance in mechanical testing.

Electronic Supplementary Material (ESM) The online version of this article (doi: 10.1007/s12221-019-9341-x) contains supplementary material, which is available to authorized users.

References

1. S. Bhowmick, D. Scharnweber, and V. Koul, *Biomaterials*, **88**, 83 (2016).
2. Kenry and C. T. Lim, *Progr. Polym. Sci.*, **70**, 1 (2017).
3. V. Rajesh and S. K. Dhirendra, *Int. J. Nanomed.*, **1**, 15 (2006).
4. R. J. Wade and J. A. Burdick, *Nanotoday*, **9**, 722 (2014).
5. J. X. Law, L. L. Liau, A. Saim, Y. Yang, and R. Idrus, *J. Tissue Eng. Regen. Med.*, **14**, 699 (2017).
6. C. J. Lowe, I. M. Reucroft, M. C. Grota, and D. I. Shreiber, *ACS Biomater. Sci. Eng.*, **2**, 643 (2016).
7. F. Saporito, G. Sandri, M. C. Bonferoni, S. Rossi, L. Malavasi, C. Del Fante, B. Vigani, L. Black, and F. Ferrari, *Polymers*, **10**, 208 (2018).
8. G. Sandri, M. C. Bonferoni, S. Rossi, F. Ferrari, M. Mori, M. Cervio, F. Riva, I. Liakos, A. Athanassiou, F. Saporito, L. Marini, and C. Caramella, *Expert Opin. Drug. Deliv.*, **12**, 525 (2015).
9. S. Avram, S. A. Shaposhnikov, C. Buiu, and M. Mernea, *Biomed. Res. Int.*, **2014**, 1 (2014).
10. K. Y. Chang, L. H. Hung, I. M. Chu, C. S. Ko, and Y. D. Lee, *J. Biomed. Mater. Res. Part A*, **92**, 712 (2010).
11. P. T. Bot, I. E. Hoefler, J. J. Piek, and G. Pasterkamp, *Curr. Med. Chem.*, **15**, 786 (2008).
12. B. Corradetti, F. Taraballi, S. Minardi, J. Van Eps, F. Cabrera, L. W. Francis, S. A. Gazze, M. Ferrari, B. K. Weiner, and E. Tasciotti, *Stem. Cells. Transl. Med.*, **5**, 670 (2016).
13. S. Akhshabi, E. Biazar, V. Singh, S. H. Keshel, and G. Nagaraja, *Mat. Technol. Adv. Perform. Mat.*, **33**, 253 (2018).
14. S. Akhshabi, E. Biazar, V. Singh, S. H. Keshel, and N. Geetha, *Int. J. Nanomed.*, **13**, 4405 (2018).
15. R. L. Fischer, M. G. McCoy, and S. A. Grant, *J. Mater. Sci. Mater. Med.*, **23**, 1645 (2012).
16. G. Abedi, A. Sotoudeh, M. Soleymani, A. Shafiee, P. Mortazavi, and M. R. Aflatoonian, *J. Biomater. Sci. Polym. Ed.*, **22**, 2445 (2011).
17. X. Li, S. Yan, J. Dai, Y. Lu, Y. Wang, M. Sun, J. Gong, and Y. Yao, *Colloids Surf. B Biointerfaces*, **162**, 390 (2018).
18. J. M. Coburn, M. Gibson, S. Monagle, Z. Patterson, and J. H. Elisseeff, *PNAS*, **109**, 10012 (2012).
19. J. Gou, H. Zhou, M. Y. Akram, X. Mu, J. Nie, and G. Ma, *Carbohydr. Polym.*, **143**, 239 (2016).
20. A. Sadeghi, M. Pezeshki-Modaress, and M. Zandi, *Int. J. Biol. Macromol.*, **114**, 1248 (2018).
21. J. Yan, L. Liu, X. Li, F. Wang, T. Zhu, P. Yuan, and Q. Zhang, *Chinese J. Rep. Reconstr. Surg.*, **2**, 130 (2006).
22. X. Qiao, S. J. Russell, X. Yanq, G. Tronci, and D. J. Wood, *J. Funct Biomater.*, **6**, 667 (2015).
23. N. Reddy, R. Reddy, and Q. Jiang, *Trends Biotechnol.*, **33**, 362 (2015).
24. Q. Jiang, N. Reddy, S. Zhang, N. Roscioli, and Y. Yang, *J. Biomed. Mater. Res. Part A*, **101**, 1237 (2013).
25. J. Ding, M. Chen, W. Chen, M. He, X. Zhou, and G. Yin, *Polymers*, **10**, 747 (2018).
26. Y. C. Lin, M. Boone, L. Meuris, I. Lemmens, N. Van Roy, A. Soete, J. Reumers, M. Moisse, S. Plaisance, R. Drmanac, J. Chen, F. Speleman, D. Lambrechts, Y. Van de Peer, J. Tavernier, and N. Callewaert, *Nat. Commun.*, **5**, 4767 (2014).
27. L. Ouyang, R. Yao, X. Chen, J. Na, and W. Sun, *Biofabrication*, **7**, 015010 (2015).
28. A. Romo-Urbe, A. Meneses-Acosta, and M. Domínguez-Díaz, *Mat. Sci. Eng. C*, **81**, 236 (2017).
29. G. Zhou, G. Zhang, Z. Wu, Y. Hou, M. Yan, H. Liu, X. Niu, A. Ruhan, and Y. Fan, *J. Nanomater.*, **2013**, 764239 (2013).
30. A. Romo-Urbe in "Materials for Biomedical Engineering: Hydrogels and Polymer-based Scaffolds", 1st ed. (A. M. Holban and A. Grumezescu Eds.), Chap.7, pp.221-234, Elsevier, MA United States, 2019.
31. X. Luo, Z. Guo, P. He, T. Chen, L. Li, S. Ding, and H. Li, *Int. J. Biol. Macromol.*, **113**, 476 (2018).
32. L. Meng, O. Arnoult, M. Smith, and G. E. Wnek, *J. Mater. Chem.*, **22**, 19412 (2012).

33. G. P. Huang, S. Shanmugasundaram, P. Masih, D. Pandya, S. Amara, G. Collins, and T. L. Arinzeh, *J. Biomed. Mater. Res. A*, **103**, 762 (2015).
34. C. P. Barnes, C. W. Pemble, D. D. Brand, D. G. Simpson, and G. L. Bowlin, *Tissue Eng.*, **13**, 1593 (2007).
35. N. A. Peppas and R. W. Kormsmeier in "Hydrogels in Medicine and Pharmacy", 1st ed. (N. A. Peppas Ed.), Vol. 3, pp.109-135, CrC Press, Boca Ratón FL, 1987.
36. T. A. M. Valente, D. M. Silva, P. S. Gomes, M. H. Fernandes, J. D. Santos, and V. Sencadas, *ACS Appl. Mater. Interfaces*, **8**, 3241 (2016).
37. X. Zhang, K. Tang, and X. Zheng, *J. Wuhan Univ. Technol. Mater. Sci. Ed.*, **30**, 840 (2015).
38. A. R. Fajardo, M. B. Silva, L. C. Lopes, J. F. Piai, A. F. Rubira, and E. C. Muniz, *RSC Adv.*, **2**, 11095 (2012).
39. A. Asran, K. Razghandi, N. Aggarwal, G. H. Michler, and T. Groth, *Biomacromolecules*, **11**, 3413 (2010).
40. J. B. González-Campos, Z. Y. García-Carvajal, E. Prokhorov, J. G. Luna-Bárceñas, M. E. Mendoza-Duarte, J. Lara-Romero, R. E. del Rio, and I. C. Sanchez, *J. Appl. Polym. Sci.*, **125**, 4082 (2012).
41. E. Fathi, N. Atyabi, M. Imani, and Z. Alinejad, *Carbohydr. Polym.*, **84**, 145 (2011).
42. S. C. da Costa Sanches, F. de Vasconcelos, C. E. Ferreira da Costa, P. S. Barbosa Marinho, M. R. Guilherme, E. J. Madureira Tavares, J. A. Picanço Diniz Jr, J. O. Carréira Silva Jr, and R. M. Ribeiro-Costa, *J. Therm. Anal. Calorim.*, **120**, 991 (2015).
43. I. Khalid, M. Ahmad, M. U. Minhas, and K. Barkat, *Carbohydr. Polym.*, **181**, 1169 (2018).
44. V. Samouillan, F. Delaunay, J. Dandurand, N. Merbahi, J. P. Gardou, M. Yousfi, A. Gandaglia, M. Spina, and C. Lacabanne, *J. Funct. Biomater.*, **2**, 230 (2011).
45. V. Samouillan, N. Merbahi, M. Yousfi, J. P. Gardou, F. Delaunay, J. Dandurand, and C. Lacabanne, *IEEE Trans. Plasma Sci.*, **40**, 1688 (2012).
46. L. Bozec and M. Odlyha, *Biophys. J.*, **101**, 228 (2011).
47. S. W. Kou and F. C. Chang, *Macromolecules*, **34**, 4089 (2001).
48. J. S. Park, J. W. Park, and E. Ruckenstein, *J. Appl. Polym. Sci.*, **82**, 1816 (2001).
49. G. M. Kim in "Fabrication of Bio-nanocomposite Nanofibers Mimicking the Mineralized Hard Tissues via Electrospinning Process" in Book: "Nanofibers", (A. Kumar Ed.), pp.69-88, INTECH, Croacia, 2010.
50. J. B. González-Campos, E. Prokhorov, G. Luna-Bárceñas, A. Mendoza-Galván, I. C. Sanchez, S. M. Nuño-Donlucas, B. García-Gaytan, and Y. Kovalenko, *J. Polym. Sci. Part B Polym. Phys.*, **47**, 932 (2009).
51. J. B. González-Campos, E. Prokhorov, G. Luna-Bárceñas, A. Fonseca-García, and I. C. Sanchez, *Polym. Sci. Part B Polym. Phys.*, **47**, 2259 (2009).
52. J. Bicerano, "Prediction of Polymer Properties" 3rd ed. CRC Press, New York, 2002.
53. H. Fröhlich, "Theory of Dielectrics", Oxford University Press, UK, 1956.
54. S. Kumar-Krishnan, E. Prokhorov, M. Ramirez, M. A. Hernandez-Landaverde, D. G. Zarate-Triviño, Y. Kovalenko, I. C. Sanchez, J. Mendez-Nonell, and G. Luna-Barceñas, *Soft Matter*, **10**, 8673 (2014).
55. C. L. Lewis, K. Stewart, and M. Anthamatten, *Macromolecules*, **47**, 729 (2014).
56. J. Qiu, C. Xing, X. Cao, H. Wang, L. Wang, L. Zhao, and Y. Li, *Macromolecules*, **46**, 5806 (2013).
57. F. Zou, R. Li, J. Jiang, X. Mo, G. Gu, Z. Guo, and Z. Chen, *J. Biomater. Sci. Polym. Ed.*, **28**, 2255 (2017).
58. H. Lee, K. Yamaguchi, T. Nagaishi, M. Murai, M. Kim, K. Wei, K. Q. Zhang, and I. S. Kim, *RSC Adv.*, **7**, 43994 (2017).
59. S. H. Chen, C. H. Chen, K. T. Shalumon, and J. P. Chen, *Int. J. Nanomed.*, **9**, 4079 (2014).
60. G. H. Kim, S. Ahan, Y. Y. Kim, Y. Cho, and W. Chun, *J. Mater. Chem.*, **21**, 6165 (2011).
61. F. H. Zulkifli, F. S. J. Hussain, M. S. B. A. Rasad, and M. M. Yusoff, *Polym. Degrad. Stabil.*, **110**, 473 (2014).
62. A. S. Asran, S. Henning, and G. H. Michler, *Polymer*, **51**, 868 (2010).
63. E. P. S. Tan and C. T. Lim in "Nanotechnology and Tissue Engineering: The Scaffold", 1st ed. (C. T. Laurencin and L. S. Nair Eds.), pp.221-242, CRC Press Boca Raton FL, 2008.
64. G. S. Beaupré, S. S. Stevens, and D. R. Carter, *J. Rehab. Res. Develop.*, **37**, 145 (2000).
65. L. Kaur, J. Singh, and Q. Liu in "Nanomaterials and Nanosystems for Biomedical Applications" (M. R. Mozafari Ed.), pp.83-98, Springer, Dordrecht, 2007.
66. H. Y. Lin, Y. J. Kuo, S. H. Chang, and T. S. Ni, *Biomed. Mater.*, **8**, 025009 (2013).
67. A. A. M. Basma, K. H. Hussain, and A. K. A. S. Nagam, *Iraqi J. Chem. Pet. Eng.*, **13**, 29 (2012).
68. N. A. Peppas and E. W. Merrill, *J. Appl. Polym. Sci.*, **20**, 1457 (1976).
69. M. Sadeghi and H. Hosseinzadeh, *Brazilian J. Chem. Eng.*, **30**, 379 (2013).
70. L. K. Tomar, C. Tyagi, Y. E. Choonara, P. Kumar, and V. Pillay, *APCBEE Procedia*, **9**, 192 (2014).
71. J. T. Kim, D. Y. Lee, Y. H. Kim, I. K. Lee, and Y. S. Song, *J. Sens. Sci. Technol.*, **21**, 256 (2012).
72. M. R. Ramezani, H. Naderi-Manesh, and H. A. Rafieepour, *Biocell.*, **38**, 11 (2014).
73. T. Pospíšil, L. Ferhatović Hamzić, L. Brkić Ahmed, M. Lovrić, S. Gajović, and L. Frkanec, *Biomater. Sci.*, **4**, 1412 (2016).
74. D. Cui, F. Tian, C. S. Ozkan, M. Wang, and H. Gao, *Toxicol. Lett.*, **155**, 73 (2005).
75. H. W. Yang, S. R. Collins, and T. Meyer, *Nat. Cell Biol.*, **18**, 191 (2016).
76. S. Y. Cho and R. L. Klemke, *J. Cell Biol.*, **156**, 725 (2002).
77. T. Lu, Y. Li, and T. Chen, *Int. J. Nanomed.*, **8**, 337 (2013).

78. G. Criscenti, A. Vasilevich, A. Longoni, C. De Maria, C. A. van Blitterswijk, R. Truckenmuller, G. Vozzi, J. De Boer, and L. Moroni, *Acta Biomater.*, **55**, 310 (2017).
79. M. Morita, A. Nakane, Y. Fujii, S. Maekawa, and Y. Kudo, *PLoS One*, **10**, e0137610 (2015).
80. B. Chen, C. Co, and C. C. Ho, *Biomaterials*, **67**, 129 (2015).
81. A. Péttriz Reyes, A. Martínez Torres, M. P. Carreón Castro, J. R. Rodríguez Talavera, S. Vargas Muñoz, V. M. Velázquez Aguilar, and M. González Torres, *Sci. Rep.*, **6**, 31140 (2016).



CLARITY with neuronal tracing and immunofluorescence to study the somatosensory system in rats

Guadalupe Martínez-Lorenzana, Mohammed Gamal-Eltrabily, Irma Alejandra Tello-García, Araulfo Martínez-Torres, Marymar Becerra-González, Abimael González-Hernández, Miguel Condés-Lara *

Departamento de Neurobiología del Desarrollo y Neurofisiología, Instituto de Neurobiología, Universidad Nacional Autónoma de México, Campus Juriquilla, Boulevard Juriquilla, No. 3001, C.P. 76230, Querétaro, Mexico

ARTICLE INFO

Keywords:

Neuronal tracers
Immunofluorescence
CLARITY

ABSTRACT

Background: The CLARITY technique enables researchers to visualize different neuronal connections along the nervous system including the somatosensory system.

New method: The present work describes the antero-lateral and dorsal column pathways until the thalamic and cortical stations, as well as descending oxytocinergic and vasopressinergic innervations by means of combined CLARITY, neuronal tracing, and immunofluorescence techniques. We used male Sprague-Dawley rats of 13, 30, and 60 days.

Results: The main results are as follows: A) CLARITY is a reliable technique that can be combined with fluorescent neuronal tracers and immunofluorescence techniques without major procedure modifications; B) at spinal level, some primary afferent fibers were labeled by CGRP, as well as the presence of neuronal populations that simultaneously project to the gracile and ventral posterolateral thalamic nuclei; C) corticothalamic connections were visible when retrograde tracers were injected at thalamic level; D) oxytocin receptors were expressed in the spinal dorsal horn by GABAergic-positive neurons, reinforcing previous outcomes about the possible mechanism for oxytocin blocking the primary afferent sensory input.

Comparison with existing methods and Conclusions: The CLARITY technique lets us observe in a transparent way the entire processed tissue compared with classical histological methods. CLARITY is a potentially useful tool to describe neuroanatomical structures and their neurochemical status.

1. Introduction

Many studies have aimed at describing the fine structure of the central nervous system (CNS) and its relationship with specific motor, sensory or affective functions, among others. The beginning of this field was highlighted by the emergence of staining techniques, neuronal tracers (Mesulam, 1982) and immunohistochemical procedures to describe the biochemical nature of the CNS. In this context, techniques that make the brain transparent (e.g., CLARITY and CUBIC) have been to applied to understand the organization of the CNS or even whole organisms (for reviews, see Aswendt et al., 2017; Richardson and Lichtman, 2015; Silvestri et al., 2016).

Recently, Wang et al. (2020) described that both FG and FR, unlike viral tracers, were compatible with some other tissue clearing

techniques e.g. FRUIT and 3DISCO which were implicated to successfully visualize primary motor cortex descending projections to the spinal cord. They could visualize the entire cortico spinal pathway using a two-photon microscope.

Specifically, CLARITY has been successfully applied in mouse brain immunostained against tyrosine hydroxylase, choline acetyltransferase parvalbumin glial fibrillary acidic protein, and DAPI (Chung and Deisseroth, 2013a,b; Chung et al., 2013a,b). The CLARITY technique has also been used in immunofluorescence procedures in rat brains for neuropeptide Y, and anti-pro-oxyphysin (Zheng and Rinaman, 2016). The combination between fluorescent dyes and tissue clearing technique may result challenging, since the latter can induce some tissue changes that diminish fluorescent proteins affinity, as well as, issues related to autofluorescence (Lai et al., 2017). However, Chung et al. (2013a,b)

* Corresponding author.

E-mail address: condes@unam.mx (M. Condés-Lara).

<https://doi.org/10.1016/j.jneumeth.2020.109048>

Received 7 September 2020; Received in revised form 15 December 2020; Accepted 18 December 2020

Available online 24 December 2020

0165-0270/© 2020 Elsevier B.V. All rights reserved.

discussed the efficiency of CLARITY technique use in obtaining 3D fluorescence images of adult mouse brain.

From our perspective, CLARITY procedure can be important in visualizing numerous elements in CNS including the ascending and descending nociception-related structures involving the neurochemical factors related.

In this sense, the somatosensory system includes two independent systems that transmit the incoming sensory information from specific peripheral receptors to the supraspinal structures. The two systems are: 1) the anterior lateral (AL) and 2) the dorsal column–medial lemniscus (DC). Recent evidence suggests that some spinal neuronal populations project simultaneously within both systems (Condés-Lara et al., 2018), adding more complexity to their organization. Calcitonin gene-related peptide (CGRP) is another important peptide related to the somatosensory process at the level of primary afferent fibers (Cameron et al., 1988; Hökfelt et al., 1992). Moreover, descending oxytocinergic projections at spinal have been related to nociception modulation through local GABAergic mechanisms (Rojas-Piloni et al., 2007; Breton et al., 2008).

These observations demand further analysis to reinforce the structural organization of the CNS and provide the basis for functional approaches (i.e., electrophysiology); thus, a reliable, clear microscopic view of the nervous system, maintaining the integrity of the tissue and its neuronal connections instead of reconstructing the nervous system from sections, is required.

Afterward, the structure, organization, and function of brain cells has been a big challenge for neuroscientists and CLARITY could become a solution to the problem.

Indeed, combining neuroimaging techniques with ex vivo brain cleaning and light-sheet imaging, described as incompatible by Aswendt et al. (2017), at present, they could provide a new entry for studying the CNS organization, as well as function-structure relations by their possible combination with electrophysiological approaches.

In this study, we describe the performance of CLARITY in rats within different age groups and its successful combination with fluorescent neuronal tracers and immunofluorescence techniques to study elements of the somatosensory system, including the ascending AL and DC systems, the participation of CGRP in primary afferent fibers, and the descending oxytocinergic innervations and their local relation to local spinal GABAergic neurons.

2. Materials and methods

The experiments were carried out in accordance with the animal procedures and protocols approved by the Institutional Ethics Committee and following the ethical guidelines of the IASP (Zimmermann, 1983) and the Guide for the Care and Use of Laboratory Animals established by the NIH (2011). Also, ARRIVE guidelines was taken into account. *Male Sprague-Dawley rats divided into 3 groups: 1) group 1 (n = 2) of 13 days of birth; 2) group 2 (n = 2) of 30 days of birth and group 3 (n = 3) of adult rats of 60 days of age (with an average weight of 280–310 g) (see Table 1).*

The rats were individually housed in a temperature-controlled environment ($23 \pm 3^\circ\text{C}$) and under a 12 h/12 h light/dark cycle with

Table 1

Experimental conditions and tracer or immunofluorescent type used in each experimental group.

Groups	Experimental conditions
Group 1: animals of 13 days of birth (n = 2)	Neuronal tracer TB, NB, TMR
Group 2: rats of 30 days of birth (n = 1)	Neuronal tracer TMR Immunofluorescent CGRP staining (n = 1)
Group 3: adult rats of 60 days of age (n = 1)	Neuronal tracer FG, TMR Immunofluorescent GABA/OTR, OT/AVP staining (n = 2)

food and water *ad libitum*.

2.1. Injection of neural tracers

The animals were anesthetized by intraperitoneal injection of a mixture of ketamine and xylazine (70/6 mg/kg) and mounted in a stereotaxic apparatus. Then, 100 nl tetramethylrhodamine-labeled dextran (TMR, 3000 MW, lysine fixable from Invitrogen™) were injected in the left ventral posterolateral nucleus (VPL) of the thalamus, whereas 100 nl Fluoro-Gold™ (FG, Fluorochrome LLC, USA) or Neurobiotin® 488 (NB, Vector, laboratories) were injected into the right VPL with a Hamilton syringe coupled to a vernier. *In the case of animals with >30 days of age the following interaural stereotaxic coordinates were used: AP 5.4; L 3.2; H 3.5 mm (Paxinos and Watson, 1998). In the case of rats with 13 days-old rats we used external coordinates, from lambda (4.2 ± 0.2 mm anterior; from the medial line 2.8 ± 0.3 mm; and from the skull 4 ± 0.2 mm in deep).*

Furthermore, two granules of True Blue (TB, Sigma) were administered to the left side of the gracile nucleus (GRA). The rats were left for 4 or 13 days of survival depending on their age. Subsequently, the animals were deeply anesthetized with sodium pentobarbital (45 mg/kg; i.p.), and the extracted tissue was processed through CLARITY, a passive tissue clearing technique described by Zheng and Rinaman (2016).

2.2. CLARITY technique

Transcardiac perfusion was performed using 20 mL of cold 1X phosphate-buffered saline (PBS, pH 7.4) (Invitrogen, GIBCO 10,010) for rats of 13 days of birth and 40 mL for animals of 30 or 60 days of age, followed by hydrogel solution (150 mL for rats of 13 days of birth and 200 mL for animals 30 or 60 days of age) which contains 4% paraformaldehyde (Electron Microscopy Sciences, 15,710-S), 4% acrylamide (Bio-Rad, 161–0140) and 0.25% VA-044 initiator (Wako, 27776–21-2) in 50 mL a conical falcon tube with hydrogel solution for post-fixation and stored overnight in the same solution at 4°C . The next procedure followed was to fill the Falcon tube with hydrogel solution and carefully seal it with parafilm, to avoid the eventual hydrogel immersed brain hybrids to oxygen in the air. We did not use of mineral oil nor nitrogen degassing described in other studies as a necessity for subsequent polymerization of acrylamide monomers (Chung et al., 2013a,b; Yang et al., 2014; Zheng and Rinaman, 2016). On the next day, polymerization was carried out for 3 h in a 37°C water bath without shaking. The brain and spinal cord were placed in 40 mL of tissue clearing solution (0.2 M boric acid, pH 8.5 (Sigma-Aldrich, 339,067) containing 4.0% sodium dodecyl sulphate (SDS) (Promega, H5114) in 50-ml falcon tubes. Later, the samples were placed in a rotating shaker incubator at 100 rotations/ minutes at 37°C . The tissue clearing solution was replaced daily during the first week and then every 3 days. The samples were cleared for 14 days in case of animals of 13 and 30 days and for 30 days in case of adult animals.

Some tissues were analyzed only for neuronal tracers and others underwent an immunofluorescence procedure (see Table 1).

3. Immunofluorescence

For immunofluorescence procedures, the cleared tissue was transferred to 15 mL Falcon tubes to be washed in a 0.5 M boric acid (pH 8.5) solution containing 0.1% Triton X-100 (rinsing buffer) to remove SDS residues. The following primary antibodies were used: anti-neurophysin (PS60, mouse, monoclonal, diluted 1: 250; a gift from Dr. H. Gainer from the National Institute of Neurological Disorders and Stroke, NIH, Bethesda MD); anti-AVP (polyclonal, rabbit, diluted 1: 500; Cat.no. AB1565, Millipore, Chemicon International, Temecula CA), anti-GABA (polyclonal, rabbit, diluted 1: 1500; Cat. No. A2052, SIGMA, USA), anti-CGRP (polyclonal, rabbit, diluted 1: 2000; Cat. No. AB15360 Chemicon International, Temecula CA), anti-OTR (polyclonal, goat, diluted 1: 400, Cat.no. sc-8103; Santa Cruz Biotechnology Inc, Santa

Cruz, CA, USA). A cocktail of two primary antibodies (2.5 mL) raised from different species were used in a 15 mL falcon tube and placed in a rotating shaker incubator for 72 h at 37 °C. Then, a 24 h wash was performed with a rinsing buffer, and the following secondary antibodies were added, diluted 1:300, depending on the characteristics of the primary antibody: donkey anti-goat IgG (Alexa Fluor 647 conjugate, Cat. no. A-21,447 or Alexa Fluor 488 conjugate, Cat.no. A11055); donkey anti-Rabbit IgG (Alexa Fluor 647 conjugate, Cat.no.A-31573, Alexa Fluor 555 conjugate, Cat.no A31572); donkey anti-mouse IgG (Alexa Fluor 488 conjugate, Cat.no. A21202). All secondary antibodies were obtained from Invitrogen, USA. Samples were incubated for 48 h at 37 °C in a rotating shaker in a 2.5 mL volume in a 15 mL falcon tube. Finally, the unbound antibodies were removed by washing in the rinsing solution.

Before imaging, the tissue was equilibrated in 1X PBS overnight at room temperature, then placed in 2,2-thiodiethanol (TDE, Sigma-Aldrich, 166,782) at serial concentrations of 20 %, 40 % and 60 % consecutively for 4–12 hours in each of them at room temperature without shaking. The tissue was kept in 60 % TDE for observation. Image acquisition was performed using a Zeiss 780 DUO confocal microscope with an Argon Multiline laser (emission 458–488–514 nm), DPSS laser emission at 561 nm and HeNe laser emission at 633 nm; as well as a multiphotonic system, the range of wavelength used to detect the different tracer and fluorophore are plotted in Table 2, with objectives of EC Plan-Neofluar 10x / 0.30 M27 lens with working distance of 5.2 mm – cover glass 0.17 mm and LD LCI Plan-Apochromat 25X / 0.8 lmm Korr DIC M27 (multi-immersion) with working distance of 0.57 mm – cover glass 0.17 mm, motorized stage and Zen by Zeiss software.

Depending on the thickness of the sample, 23.5–1025 Z-plane optical sections were obtained in steps of 0.5 or 5.00 µm. Images were rendered from the lumbar and thoracic segments of the spinal cord, as well as from complete brain tissue. Depending on the size of the sample, optical sections were acquired at a resolution of 1024 × 1024 or 512 × 512 pixels and scanned 4 times to reduce noise. In all cases, the images were enhanced (brightness and gamma) and analyzed with the ZEN 2 Blue Edition software (Carl Zeiss Microscopy GmbH, Göttingen, Germany). A two-dimensional projection, a single optical section or a 3D projection of the image (see supplementary video) was performed as applicable; the images were imported in file format (TIFF).

4. Results

Cleared CNS tissue was analyzed under a multiphotonic microscope to simultaneously detect neuronal fluorescent tracers and selective fluorescent antibodies. This tissue preparation allowed optimal observation of the tissue under light, fluorescence or confocal microscopes, thus providing a range of potential applications. Here we show the utility of the CLARITY and histological techniques in different areas of the CNS related to the somatosensory system.

Our first approach was to study the primary afferent fibers arriving at the spinal cord. The lumbar segment of the spinal cord of a 30-day-old animal was cut cross-sectionally into 4-mm blocks and processed for anti-CGRP immunofluorescence, and a confocal image projection was

obtained from this region. In Fig. 1, the CGRP-labeled fibers noticeably arrive at the dorsal horn layers of the L4 segment of the spinal cord.

Furthermore, we continued with the histological analysis of cleared lumbar segments with different fluorescent neuronal tracers (see Fig. 2A) under confocal microscopy. This tissue presented labeled neurons on both sides of the dorsal horn of the spinal cord in 13-day-old animals. In the 13-day-old group, animals were injected with TB in the left GRA, TMR in the left VPL and NB in the right VPL. Fig. 2B shows a Z-stack projection of confocal mosaic images of this area. Upon analyzing ventrodorsally the spinal dorsal horn of the lumbar segment, and taking the midline as a reference, the TB-labeled neuronal groups were observed at the depth between 25–95 µm and 145–235 µm on both sides of the lumbar segment, in the middle and lateral parts of the Y axis. An example of TB-labeled cells is shown in Fig. 2D. TMR-labeled neurons were found at a depth between 80–125 µm and 165–340 µm on both sides and well distributed in both the middle and lateral parts of the horn (Fig. 2C). Regarding the NB tracer, the highest portion of labeled neurons was found at a depth of 200–235 µm, also distributed from the middle to lateral part of the spinal horn with respect to the midline and Y axis; an example of these cells is shown in Fig. 2E. Furthermore, we observed double- and triple-labeled neurons along the spinal horn; examples of these cells are shown in Fig. 2 F1–5.

The neural tracers are retained in cells after CLARITY technique, as well as their rostro-caudal distribution along the entire X axis of the lumbar segment of the spinal cord. In addition, it is worth mentioning that after CLARITY procedures, the TMR was preserved in magnificent conditions. Independently of animal age, TMR was successfully detected, without apparent alterations, in 30-day-old animals. In these animals, the TMR was injected unilaterally into the right VPL and many neurons were observed throughout the lumbar segment of the spinal cord from the rostral to the caudal part (Fig. 3A). These neurons are widely distributed on both sides of the horn, from the mid-region to its lateral part; an example of a group of TMR-labeled neurons is shown in Fig. 3B.

Further analysis was done regarding the distribution of neuronal tracer labeling in the spinal cord at L5 level. In this condition, the tissue portion in Fig. 2B was transversally analyzed. TMR injected into the left VPL (Fig. 4A), NB into the right VPL (Fig. 4B), and TB into the left GRA (Fig. 4C) labeled neurons bilaterally at L5 level. Fig. 4D shows a merged image of the same region in the different channels, and white spots depict triple-labeled cells. In Fig. 4E, a superimposition of this image with a scheme of the spinal cord at L5 presents the bilateral and deep distribution of spinal cord cells projecting to supraspinal levels.

Furthermore, we analyzed the corticothalamic projections of the somatosensory system. The ipsilateral VPL projections towards the cerebral cortex (Cx) were analyzed in two animals, one with TMR injected into the right VPL and the other with FG injected into the left VPL. The brain of the first animal was cleared, and a coronal block from interaural 6.88 mm to 1.20 mm, examined under the confocal microscope in a single field rostro-caudal extension, was obtained (see Fig. 5A). In this field, at S1HL level, a characteristic and stratified neuronal group was detected along layer VI of the Cx (Fig. 5A). The brain of the second animal was cleared, and a sagittal block from the lateral 1.90 mm–3.90

Table 2

Characteristics used in confocal microscopy for the use and detection of different neuronal tracers and fluorophores. The parameters used as Laser type, intensity, excitation and emission wavelengths, and the range of wavelength used for True blue (TB), Neurobiotin® 488 (NB), tetramethylrhodamine-labeled dextran (TMR), Fluoro-Gold™ (FG) and Alexa Fluor-488, -555, -647 detection are plotted. Excitation and Emission fluorescence values are approximate.

Tracer or Fluorophores	Lasers nm	Laser power %	Excitation Wavelength nm.	Emission Wavelength nm.	Range of wavelength used nm.
TB	750 multiphotonic system	8.0	365	425	371–451
NB	488	2.6	493	517	492–540
TMR	561	2.6	555	580	560–581
FG	730 multiphotonic system	6.5	373	565	498–594
Alexa Fluor-488	488	3.5	495	519	495–519
Alexa Fluor-555	561	1.2	555	565	556–579
Alexa Fluor-647	633	5.0	650	668	638–671

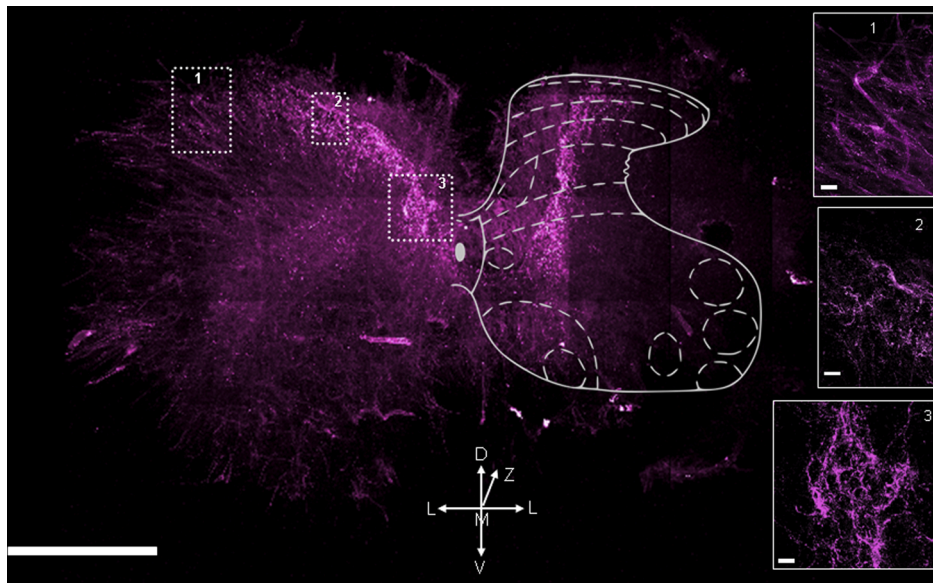


Fig. 1. Image from a cleared block of the lumbar segment (L4) of a 30-day-old animal's spinal cord. Transverse section from a block of 4 mm thick showing peripheral CGRP-labeled fibers coming into the dorsal horn. Image obtained with an objective LD LCI Plan-Apochromat 25x/0.8 Imm Korr DIC M27, stack size; X=2720.62 μ m, Y=2040.46 μ m and Z=115 μ m at a step size of 1.00 μ m, scale bar=500 μ m. The scale bar in 1, 2, and 3 are 20 μ m.

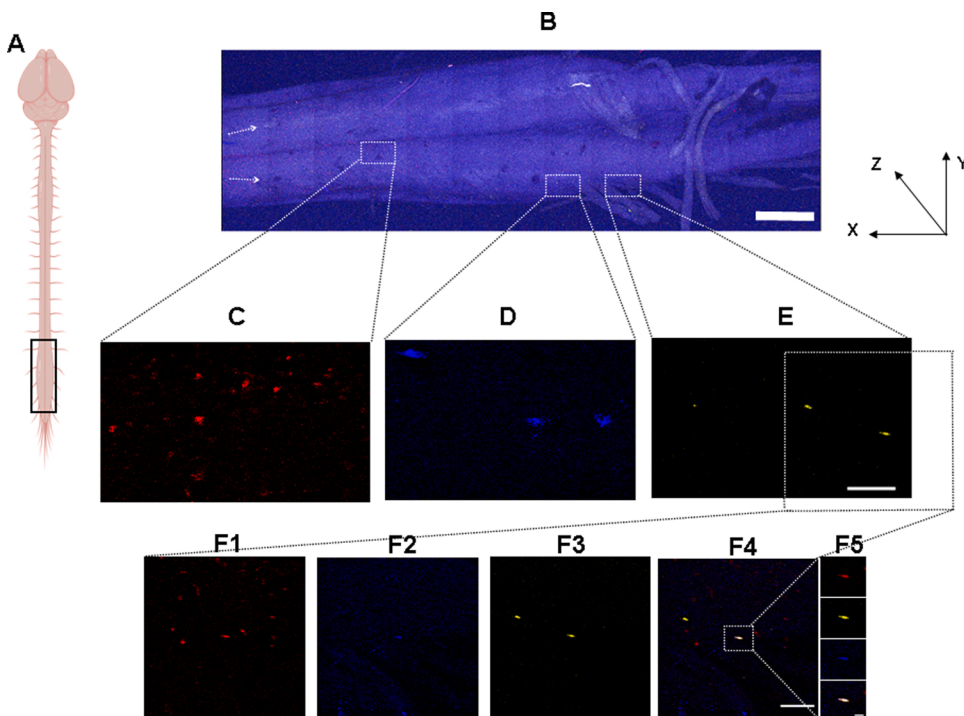


Fig. 2. Retrograde tracer preserved after CLARITY in the 13-day-old rat spinal cord. (A) A diagram of the spinal L1-S1 segment chosen for the analysis. (B) A projection of confocal images of the lumbar segment with neural tracers; the midline is clearly visible X = anteroposterior plane; Y = mediolateral plane; Z = dorsoventral plane (stack size; X=11052.50 μ m, Y=3400.77 μ m and Z=1100.00 μ m). Notice that the clearest portion of the dorsal horn shows the stained cells (by transparency; see the arrow). For the mosaic, we used a step size of 5.00 μ m (scale bar = 1 mm). (C) TMR-labeled neurons, injected in the left VPL, (D) TB-labeled neurons, injected in the left GRA, and (E) NB-labeled neurons, injected in the right VPL, scale bar=100 μ m. (F) Multiple labeling in a neuronal group: (F1) TMR-labeled cells, (F2) TB-labeled cells, (F3) NB-labeled cells, (F4) the merge (F1+F2+F3) depicting a triple-labeled neuron (scale bar=100 μ m), and (F5) a crop of the triple-labeled neuron obtained with all the neuronal tracers, scale bar=20 μ m. Images obtained with a Zeiss 780 confocal microscope with an EC Plan Neofluar 10x/0.30 M27 lens. Image in B is illustrated in 3-D in SUPPLEMENTARY MATERIAL Fig. 1.

mm was analyzed under the confocal microscope in a medio-lateral extension, and a group of FG-labeled neurons was found in the same S1HL region (Fig. 5B).

In these same animals, the lumbar segment of the spinal cord was cleared and processed for anti-GABA or anti-OTR immunofluorescence in a 4 mm block from L5 to S2 segments to observe descending pathways. A Z-series of images revealed a large population of GABA- and OTR-labeled cells, which resulted in double-labeled neurons (Fig. 6 B1-B3). Fig. 6C1-C3 depicts GABAergic interneurons expressing OTR with 3.0x confocal zoom magnification.

Finally, the thoracic spinal segment obtained from adult animals was

also cleared and observed under a confocal microscope. Dorsoventral images were acquired at the level of T8 segment, where OT and AVP-labeled fibers were observed on both sides of the spinal cord along its rostro-caudal extension. This suggests that these fibers pass through the lateral intermediate nucleus (IML) of the spinal cord since they are observed approximately 300 μ m lateral to the midline (Fig. 7B). In addition, single optical sections from this area showed the presence of double-labeled fibers (OT/AVP) (Fig. 7B1 and B2).

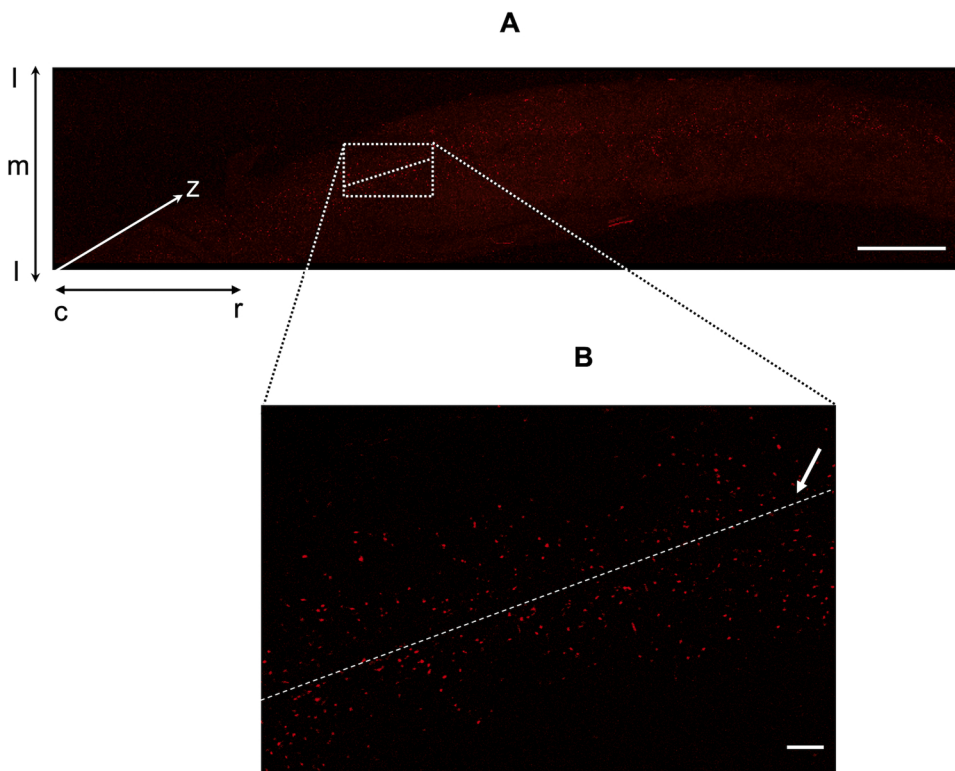


Fig. 3. CLARITY technique with TMR neuronal tracer applied in the spinal cord lumbar segment of a 30-day-old animal. (A) Confocal imaging of the lumbar enlargement (10x objective, stack size; X caudal (c) to rostral (r)= 11902.69 μm ; Y medium (m) - lateral (l)= 2550.58 μm and Z=1025.00 μm at step size of 5.00 μm , scale bar = 1 mm). (B) A single optical section of TMR-labeled neurons on both sides of the dorsal horn; the arrow indicates the dotted line that demarcates the midline, scale bar=100 μm . Z: Dorso-Ventral Y: Medio-Lateral X: Caudal-Rostral.

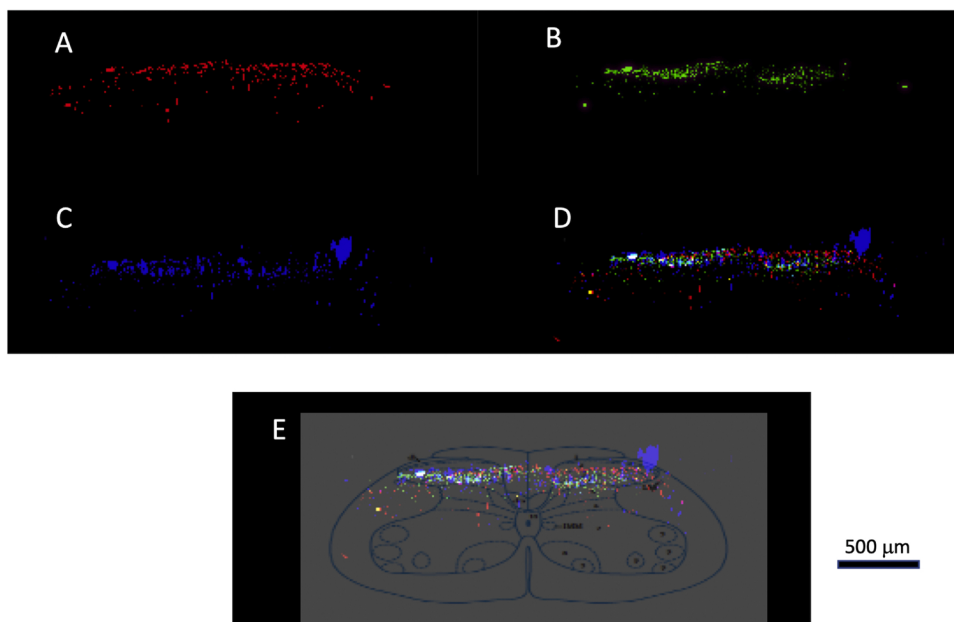


Fig. 4. Supraspinal retrograde transport to the spinal dorsal horn in CLARITY tissue. Using the confocal projection from Fig. 1, we observed L5 segment in a transversal section. (A) TMR-labeled neurons after injection into the left VPL. (B) NB-labeled neurons after injection into the right VPL. (C) right TB-labeled neurons after injected into the GRA. (D) A merged image is depicting triple-labeled neurons in white. (E) Merged image is superimposed to an L5 spinal cord diagram to illustrate the neuronal distribution. Notice that positive cells are present on both sides of the spinal dorsal horn, nevertheless the injected side.

5. Discussion

Here, we demonstrate that the CLARITY technique could be successfully performed in young animals (13 and 30 days of age) and adult animals (60 days of age). Besides, our results show that neuronal tracing or immunofluorescence techniques can be combined with the CLARITY technique and adequately conserved after tissue clearing.

The CLARITY technique has been performed in young animals of up to 24 days of age (Zheng and Rinaman, 2016). Many concerns were postulated about the possibility of applying this procedure in nervous tissue obtained from adult animals. Our results show that the CLARITY

technique can be successfully performed in 60-day-old animals, suggesting that it could be a valuable tool for studying morphological aspects of the nervous system in both young and adult animals.

As a first approach, we studied the first afferent coming from the skin receptors with the CLARITY technique combined with an immunofluorescent procedure to notice the CGRP (see Fig. 1). The CGRP neuropeptide was selected for its involvement in somatosensory and nociception processing and has been reported mainly in the dorsal root ganglion neuron somas (Cameron et al., 1988; Hökfelt et al., 1992; McNeill et al., 1988). Additionally, CGRP was detected in unmyelinated C and finely myelinated A fibers within laminae I, II outer (I_o) and V of

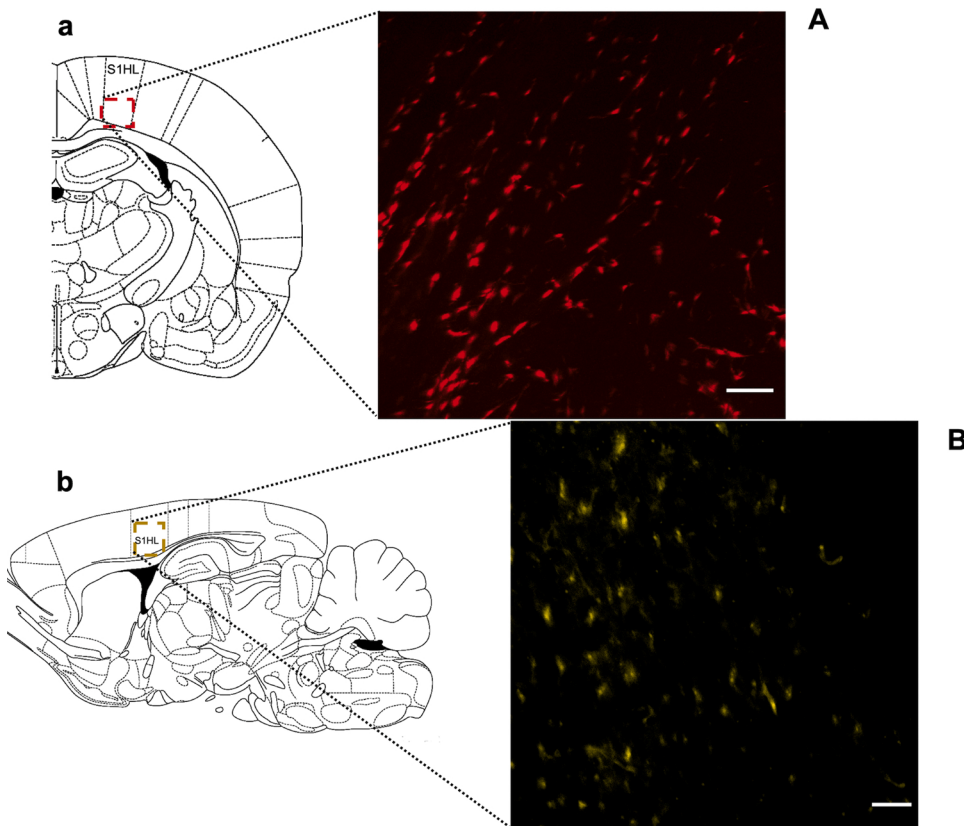


Fig. 5. TMR labeling cerebral cortex cells after neuronal tracers injected into the VPL of an adult animal. **(A)** Confocal image (10x objective, stack size; X=850.19 μ m, Y=850.19 μ m and Z=712.00 μ m at a step size of 1.00 μ m, scale bar=100 μ m) of TMR-labeled neurons in cortex obtained from coronal block at AP 6.88 mm interaural **(a)**. **(B)** Confocal image of FG-labeled cortical neurons (25x objective; stack size X=340.08 μ m, Y=340.08 μ m and Z=25.00 μ m at step size of 1.00 μ m, scale bar=100 μ m) of a sagittal block at L: 1.90 mm (Paxinos and Watson, 1998) **(b)**.

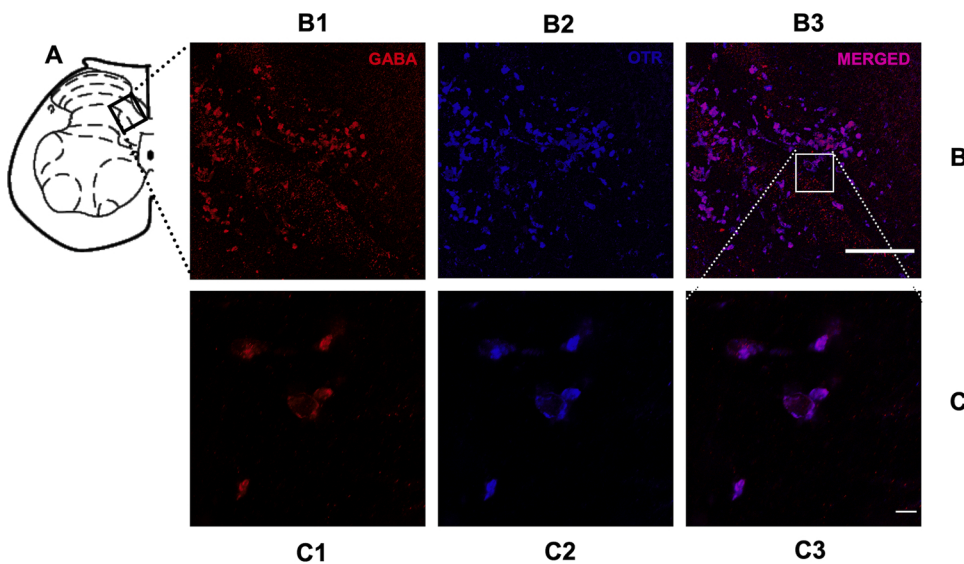


Fig. 6. GABA and OTR immunofluorescence in CLARITY tissue at L5 to S2 region of an adult rat. **(A)** A L5 segment with a box in the spinal cord's dorsal horn obtained from (Paxinos and Watson, 1998). **(B)** The images show the colocalization of GABAergic interneurons (RED) with OTR (BLUE) (25x objective, stack size; X=340.08 μ m, Y=340.08 μ m and Z=133.00 μ m at step size of 0.50 μ m, scale bar=100 μ m). **(B1)** GABA-labeled neurons **(B2)** OTR-labeled cells and **(B3)** double-labeled cells coming from the merge of (B1) and (B2). **(C)** The image shows a crop from (B) obtained in all the channels (25x objective, 3.0x confocal zoom, stack size; X=112.34 μ m, Y=112.34 μ m and Z=23.50 μ m at step size of 0.50 μ m, scale bar=10 μ m). **(C1)** GABA-labeled neurons **(C2)** OTR-labeled cells and **(C3)** the merge of (C1) and (C2) showing double-labeled cells.

the spinal dorsal horn and, to a lesser extent, in sympathetic and motor neurons in the intermediolateral and ventral horns (Gibson et al., 1984; Hökfelt et al., 1992; Ishida-Yamamoto and Tohyama, 1989; Marti et al., 1987; Senba and Tohyama, 1988; Willis and Coggeshall, 2004; Woolf and Wiesenfeld-Hallin, 1986). Interestingly, spinal cord injury (a chronic pain model) increased CGRP labeling, identified by means of immunocytochemistry techniques, in laminae III and IV bilaterally at the level of the hemisection, as well as in the two rostral and caudal segments close to the lesion site (Christensen and Hulsebosch, 1997; Sliwinski et al., 2018). In this study, we observed the presence of CGRP-labeled fibers (see Fig. 1 (O)) in laminae I–V and the contour of the

ventral horn on both sides of the spinal cord at L4 level detected by combined CLARITY and immunofluorescence techniques without any peripheral or spinal cord lesions. We believe that the CLARITY technique, when combined with immunofluorescence tools, can be useful for the detection of peptides or receptor expression in the spinal cord of adult rats.

In this context, neuronal tracers of the carbocyanine family (lipophilic neuronal tracers like DiI) were cleared using the CLARITY technique (Jensen and Berg, 2016). However, modifications in the compound's molecular structure were required to avoid neuronal tracer clearance from the tissue during the rinsing process (Jensen and Berg,

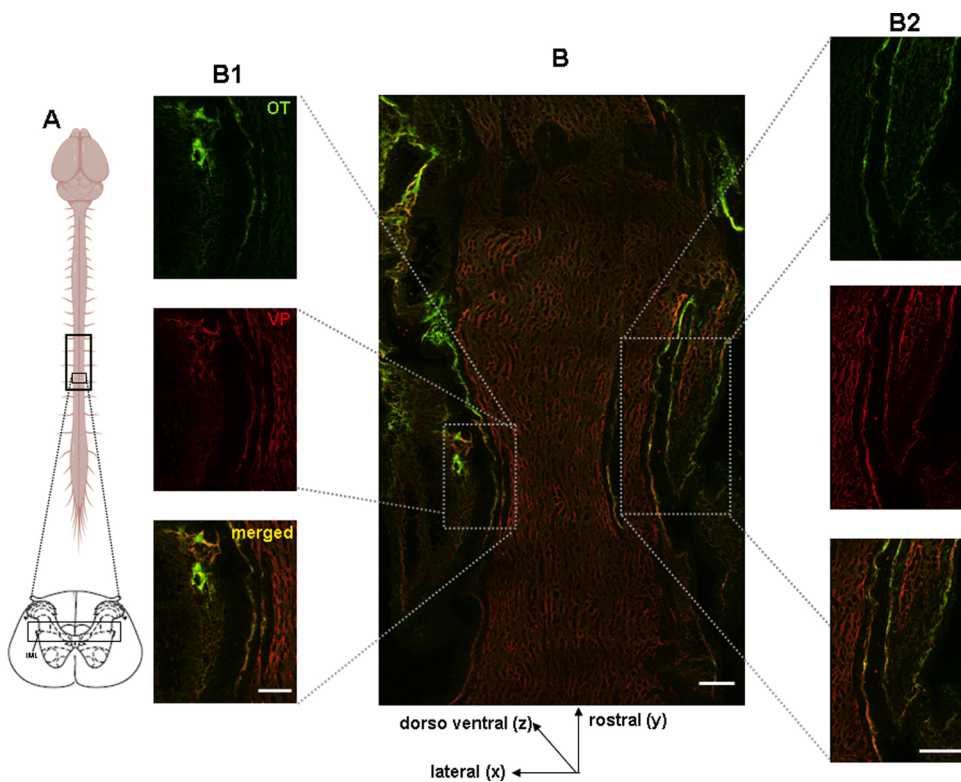


Fig. 7. Combined CLARITY and immunofluorescence (anti-OT and anti-VP) techniques in the spinal thoracic segment of an adult animal. (A) A diagram of the spinal cord showing the area analyzed in CLARITY. (B) Dorsomedial projection of confocal images obtained from the thoracic region at T8 level, where oxytocinergic fibers are labeled in green and vasopressinergic fibers labeled in red present at both lateral ends of the spinal cord running along the rostro-caudal axis (25x objective, stack size; X=1020.23 μm , Y=1700.38 μm and Z=295.00 μm at step size of 1.00 μm , scale bar=100 μm). (B1) An example of double-labeled fibers (OT/AVP fibers) obtained from a single optical section on the left side and (B2) on the right side of the spinal segment. In (B1) and (B2), OT-labeled fibers are in green, VP-labeled fibers in red and the double-labeled fibers are in yellow, scale bar=100 μm .

2016). We show that fluorescent dextran tracers with fixable lysin sidechains (i.e. TMR), biotin-based tracers (i.e. neurobiotin), and other small tracers i.e. FG and TB (Köbbert et al., 2000; Vercelli et al., 2000), were successfully conserved during the passive CLARITY process.

An important thing to consider when using the FG is the range of wavelength as well as with all other tracers, but in the case, it is an easy tracer but with a broad wavelength. See Table 2. Moreover, FG is a retrograde tracer, and it is not so good as a pathway's tracer at least in our case, we use FG to stain cellular corps of projecting neurons. Moreover, As FG is an inherently fluorescing compound, the only procedure necessary to study transport is sectioning and fluorescence microscopy. No histology other than fixation is required. Even in fresh tissue, fluorescence is intense. The addition of an anti-fading agent to the mounting medium is not necessary since FG has a remarkable photobleaching-resistance capacity.

Our results show the presence of spinal neurons that project towards the ipsilateral GRA (TB-labeled) and bilaterally to the VPL (NB-labeled and TMR-labeled) (Fig. 2C-D-E). These projections have been previously described as part of the AL and DC systems involved in transmitting somatosensory and pain information, respectively (Condés-Lara et al., 2018). The presence of triple-labeled neurons (TMR-TB-NB positive) (Fig. 2F) suggests the existence of certain neuronal populations in the spinal cord dorsal horn that participate in both pathways. A previous study in our laboratory described the presence of bifurcated spinal neurons in 60-day-old rats (Condés-Lara et al., 2018). Here, using a combined neuronal tracer and CLARITY technique, we show this neuronal population (Fig. 4) in both 13-day-old and 30-day-old animals.

Regarding the corticothalamic pathways, reciprocal interconnections between somatosensory cortices (SI and SII) and the thalamic VPL have been documented (Jones, 1985). Cappe et al. (2007) described a dual pattern of the cortical projections towards the VPL in rodents; numerous innervations arising from cortical layer VI end in small terminations within the VPL and, unlikely, fewer projections from layer V that form giant terminations in this thalamic nucleus. Monconduit et al. (2006) studied the SI-VPL interconnections in the somatosensory process and demonstrated, by means of neuronal tracer

and histochemical techniques, the presence of retrogradely labeled neurons with apical dendrites in layer VI of the SI, being denser between bregma -1.3 and 0.8 mm (Paxinos and Watson, 2007) and progressively decreasing in both caudal and rostral directions. These studies support our results regarding the characteristic and stratified neuronal group detected along layer VI of the SI (TMR- and FG-labeled neurons) (Fig. 5) upon injection of these tracers in the VPL followed by brain tissue clearance.

In rats, immunofluorescence techniques were used alone for OT detection in the hypothalamic paraventricular nucleus (PVN) (Gamal-Eltrabily et al., 2018) or combined with the CLARITY technique (Zheng and Rinaman, 2016). Oxytocinergic innervations from the PVN towards the spinal cord have been previously described using neuronal tracing and immunohistochemistry (Condés-Lara et al., 2007; Saper et al., 1976; Sawchenko and Swanson, 1982; Swanson, 1977; Swanson and McKellar, 1979). In this context, PVN projections destinate the IML (Hosoya, 1980) and send collaterals to the dorsal horn at cervical and lumbar levels (Condés-Lara et al., 2003). Here, through combined CLARITY and immunofluorescence techniques, we describe the presence of oxytocinergic and vasopressinergic fibers throughout the thoracic segment of the spinal cord in adult rats. These fibers are clearly identified at the dorsal and ventral depth of the T8 segment and bilaterally reaching the IML. Interestingly, some fibers were double-labeled (OT-AVP positive), which is consistent with previous findings on the peptidergic nature of PVN projections to the spinal dorsal horn at lumbar level (Gamal-Eltrabily et al., 2018). These results potentiate the described role of PVN descending modulatory role in pain, as well as autonomic system modulation (Christensen and Hulsebosch, 1997; Sliwinski et al., 2018)

Our group has reported that PVN stimulation decreases the activity of spinal wide dynamic range neurons upon peripheral noxious stimulation. This effect is mediated by a descending oxytocinergic mechanism and could involve local GABAergic interneuron activity (Rojas-Piloni et al., 2007). The distribution of OT binding sites coincides with the innervations of OT, suggesting a modulating role for this peptide in sensory and autonomic functions (Reiter et al., 1994). Furthermore, immunocytochemical and immunofluorescence studies have shown that

GABA is predominantly found in interneurons in laminae I-III in the lumbar segment of the spinal dorsal horn (Moreno-López et al., 2013; Todd and McKenzie, 1989). A similar distribution of GABA has been described in the cervical, thoracic, lumbar and sacrum segments of the spinal cord, mainly laminae I-III; as well as immunoreactive fibers and small neurons in lamina X (Magoul et al., 1987). However, GABAergic neurons have also been described between layers I-V of the spinal cord at lumbosacral level (Zou et al., 2002). In this work, using CLARITY and immunofluorescence techniques, we identified GABA-labeled neurons within laminae IV and V at L5 level. Also, we analyzed OTR expression in the same region where we observed the presence of GABAergic neurons that express OTR (Fig. 6 B3 and C3). These findings support the possible involvement of GABAergic neurons in the OT-induced suppression of afferent activity (Condés-Lara et al., 2003; Miranda-Cárdenas et al., 2006; Rojas-Piloni et al., 2007) at this level. However, contrasting results regarding OTR expression in the spinal cord have been described. In rats, OTR-expressing neurons were identified in laminae I-III in the spinal dorsal horn, but no OTR expression by GABAergic neurons was documented (Moreno-López et al., 2013). In mouse, OTR was mainly expressed in laminae I-II of the spinal dorsal horn and lamina X (Wrobel et al., 2011). This suggests that the detection of OTR and/or its colocalization with GABA could vary depending on the depth of the spinal cord laminae. In this context, the CLARITY technique amplifies OTR and GABA labeling detection (see Fig. 6), which makes it better than immunofluorescence alone, as also observed with CGRP labeling. Finally, considering the size of GABA-OTR labeled neurons, we believe they are interneurons that express OTR; however, further studies using electron microscopy techniques are required to demonstrate the nature of these cells. In fact, the expression of OTR by GABAergic neurons could prove that OT inhibitory action is mediated by GABA interneurons. Nevertheless, the OT inhibitory action mechanism could be direct at the presynaptic level of primary sensory afferents.

In conclusion, our results show that the CLARITY technique can be performed in nervous tissue obtained from young (13- and 30-day-old) and adult (60-day-old) rats. Fixable fluorescent neuronal tracers can be combined with CLARITY, but the degree of dye loss has not been estimated. The quantity of tracers lost by the CLARITY procedure was not estimated and we only could give a qualitative result regarding the positive cells and fibers. CLARITY was used to identify central pathways of both AL and DL systems, which are involved in somatosensory and nociception processes. Additionally, combined CLARITY and immunofluorescence techniques were successful, and we identified descending oxytocinergic and vasopressinergic fibers in the spinal thoracic system, as well as OTR expression and GABAergic interneuron distribution at lumbar level, which could be the core mechanism for OT descending inhibition. Finally, CGRP labeling detection was notably improved when CLARITY was used in the absence of nervous lesions. Together, these data point out the potential use of CLARITY to study neuro-morphological data in physiological and pathological conditions at different ages.

CRedit authorship contribution statement

Guadalupe Martínez-Lorenzana: Investigation, Software, Formal analysis, Methodology, Writing - review & editing, Data curation, Project administration. **Mohammed Gamal-Eltrabily:** Investigation, Software, Formal analysis, Methodology, Writing - review & editing, Data curation, Project administration. **Irma Alejandra Tello-García:** Investigation, Software, Formal analysis, Methodology. **Ataulfo Martínez-Torres:** Conceptualization, Resources, Supervision. **Marymar Becerra-González:** Investigation, Software, Formal analysis, Methodology. **Abimael González-Hernández:** Conceptualization, Resources, Supervision. **Miguel Condés-Lara:** Conceptualization, Resources, Supervision, Formal analysis, Writing - review & editing, Data curation, Project administration.

Declaration of Competing Interest

The authors declare that the research was conducted in the absence of any commercial or financial relationships that could be construed as a potential conflict of interest.

Acknowledgements

We acknowledge Elsa Nydia Hernández Ríos for her technical assistance with the confocal microscope and Jessica González Norris for proofreading the manuscript. This research was financially supported by the Programa de Apoyo a Proyectos de Investigación e Innovación Tecnológica (PAPIIT-UNAM Mexico) under Grant agreement no. IN200415 to MCL and Grant no. IA203119 to AGH.

Appendix A. Supplementary data

Supplementary data associated with this article can be found, in the online version, at <https://doi.org/10.1016/j.jneumeth.2020.109048>.

References

- Aswendt, M., Schwarz, M., Abdelmoula, W.M., Dijkstra, J., Dedeurwaerdere, S., 2017. Whole-brain microscopy meets in vivo neuroimaging: techniques, benefits, and limitations. *Mol. Imaging Biol.* 19, 1–9.
- Breton, J.D., Veinante, P., Uhl-Bronner, S., Vergnano, A.M., Freund-Mercier, M.J., Schlichter, R., Poisbeau, P., 2008. Oxytocin-induced antinociception in the spinal cord is mediated by a subpopulation of glutamatergic neurons in lamina I-II which amplify GABAergic inhibition. *Mol. Pain* 29, 4–19.
- Cameron, A.A., Leah, J.D., Snow, P.J., 1988. The coexistence of neuropeptides in feline sensory neurons. *Neuroscience* 27, 969–979.
- Cappe, C., Morel, A., Rouiller, E.M., 2007. Thalamocortical and the dual pattern of corticothalamic projections of the posterior parietal cortex in macaque monkeys. *Neuroscience* 146, 1371–1387.
- Christensen, M.D., Hulsebosch, C.E., 1997. Spinal cord injury and anti-NGF treatment results in changes in CGRP density and distribution in the dorsal horn in the rat. *Exp. Neurol.* 147, 463–475.
- Chung, K., Deisseroth, K., 2013a. CLARITY for mapping the nervous system. *Nat. Methods* 10, 508–513.
- Chung, K., Deisseroth, K., 2013b. CLARITY for mapping the nervous system. *Nat. Methods* 10, 508–513.
- Chung, K., Wallace, J., Kim, S.Y., Kalyanasundaram, S., Andalman, A.S., Davidson, T.J., Deisseroth, K., et al., 2013a. Structural and molecular interrogation of intact biological systems. *Nature* 497 (7449), 332–337.
- Chung, K., Wallace, J., Kim, S.-Y., Kalyanasundaram, S., Andalman, A.S., Davidson, T.J., Deisseroth, K., et al., 2013b. Structural and molecular interrogation of intact biological systems. *Nature* 497, 332–337.
- Condés-Lara, M., González, N.M., Martínez-Lorenzana, G., Delgado, O.L., Freund-Mercier, M.J., 2003. Actions of oxytocin and interactions with glutamate on spontaneous and evoked dorsal spinal cord neuronal activities. *Brain Res.* 976, 75–81.
- Condés-Lara, M., Martínez-Lorenzana, G., Rojas-Piloni, G., Rodríguez-Jiménez, J., 2007. Branched oxytocinergic innervations from the paraventricular hypothalamic nuclei to superficial layers in the spinal cord. *Brain Res.* 1160, 20–29.
- Condés-Lara, M., Martínez-Lorenzana, G., Rojas-Piloni, G., Tello-García, I.A., Manzano-García, A., Rubio-Beltrán, E., González-Hernández, A., 2018. Axons of individual dorsal horn neurons bifurcated to project in both the anterolateral and the postsynaptic dorsal column systems. *Neuroscience* 371, 178–190.
- Gamal-Eltrabily, M., Márquez-Morales, C., Martínez-Lorenzana, G., González-Hernández, A., Condés-Lara, M., 2018. Peptidergic nature of nociception-related projections from the hypothalamic paraventricular nucleus to the dorsal horn of the spinal cord. *Neurosci. Lett.* 685, 124–130.
- Gibson, S.J., Polak, J.M., Bloom, S.R., Sabate, I.M., Mulderry, P.M., Ghatei, M.A., McGregor, G.P., Morrison, J.F., Kelly, J.S., Evans, R.M., 1984. Calcitonin gene-related peptide immunoreactivity in the spinal cord of man and of eight other species. *J. Neurosci.* 4, 3101–3111.
- Höfkelt, T., Arvidsson, U., Ceccatelli, S., Cortes, R., Cullheim, S., Dagerlind, A., Johnson, H., Orazzo, C., Piehl, F., Pieribone, V., Schalling, M., Terenius, L., Ulfhake, B., Verge, V.M., Villar, M.Z., Wiesenfeld-Hallin, Z., Xu, X.J., Xu, Z., 1992. Calcitonin gene-related peptide in the brain, spinal cord, and some peripheral systems. *Ann. N. Y. Acad. Sci.* 657, 119–134.
- Hosoya, Y., 1980. The distribution of spinal projection neurons in the hypothalamus of the rat, studied with the HRP method. *Exp. Brain Res.* 40, 79–87.
- Ishida-Yamamoto, A., Tohyama, M., 1989. Calcitonin gene-related peptide in the nervous tissue. *Prog. Neurobiol.* 33, 335–386.
- Jensen, K.H.R., Berg, R.W., 2016. CLARITY-compatible lipophilic dyes for electrode marking and neuronal tracing. *Sci. Rep.* 6.
- Jones, E.G., 1985. *The Thalamus*. Springer US, New York.

- Köbbert, C., Apps, R., Bechmann, I., Lanciego, J.L., Mey, J., Thanos, S., 2000. Current concepts in neuroanatomical tracing. *Prog. Neurobiol.* 62, 327–351.
- Lai, H.M., Ng, W.L., Gentleman, S.M., Wu, W., 2017. Chemical probes for visualizing intact animal and human brain tissue. *Cell Chem. Biol.* 24 (6), 659–672.
- Magoul, R., Onteniente, B., Geffard, M., Calas, A., 1987. Anatomical distribution and ultrastructural organization of the gabaergic system in the rat spinal cord. An immunocytochemical study using anti-GABA antibodies. *Neuroscience* 20, 1001–1009.
- Marti, E., Gibson, S.J., Polak, J.M., Facer, P., Springall, D.R., van Aswegen, G., Aitchison, M., Koltzenburg, M., 1987. Ontogeny of peptide- and amine-containing neurones in motor, sensory, and autonomic regions of rat and human spinal cord, dorsal root ganglia, and rat skin. *J. Comp. Neurol.* 266, 332–359.
- McNeill, D.L., Chung, K., Carlton, S.M., Coggeshall, R.E., 1988. Calcitonin gene-related peptide immunostained axons provide evidence for fine primary afferent fibers in the dorsal and dorsolateral funiculi of the rat spinal cord. *J. Comp. Neurol.* 272, 303–308.
- Mesulam, M., 1982. *Tracing Neuronal Connections with Horseradish Peroxidase*. Wiley, New York, p. 251.
- Miranda-Cárdenas, Y., Rojas-Piloni, G., Martínez-Lorenzana, M., Rodríguez-Jiménez, J., López-Hidalgo, M., Freund-Mercier, M.J., Condés-Lara, M., 2006. Oxytocin and electrical stimulation of the paraventricular hypothalamic nucleus produce antinociceptive effects that are reversed by an oxytocin antagonist. *Pain* 122, 182–189.
- Monconduit, L., Lopez-Avila, A., Molat, J.L., Chalus, M., Villanueva, L., 2006. Corticofugal output from the primary somatosensory cortex selectively modulates innocuous and noxious inputs in the rat spinothalamic system. *J. Neurosci.* 26, 8441–8450.
- Moreno-López, Y., Martínez-Lorenzana, G., Condés-Lara, M., Rojas-Piloni, G., 2013. Identification of oxytocin receptor in the dorsal horn and nociceptive dorsal root ganglion neurons. *Neuropeptides* 47, 117–123.
- Paxinos, G., Watson, C., 2007. *The Rat Brain in Stereotaxic Coordinates*. Academic Press.
- Reiter, M.K., Kremarik, P., Freund-Mercier, M.J., Stoeckel, M.E., Desaulles, E., Feltz, P., 1994. Localization of oxytocin binding sites in the thoracic and upper lumbar spinal cord of the adult and postnatal rat: a histoautoradiographic study. *Eur. J. Neurosci.* 6, 98–104.
- Richardson, D.S., Lichtman, J.W., 2015. Clarifying tissue clearing. *Cell* 162, 246–257.
- Rojas-Piloni, G., López-Hidalgo, M., Martínez-Lorenzana, G., Rodríguez-Jiménez, J., Condés-Lara, M., 2007. GABA-mediated oxytocinergic inhibition in dorsal horn neurons by hypothalamic paraventricular nucleus stimulation. *Brain Res.* 1137, 69–77.
- Saper, C.B., Loewy, A.D., Swanson, L.W., Cowan, W.M., 1976. Direct hypothalamo-autonomic connections. *Brain Res.* 117, 305–312.
- Sawchenko, P.E., Swanson, L.W., 1982. Immunohistochemical identification of neurons in the paraventricular nucleus of the hypothalamus that project to the medulla or to the spinal cord in the rat. *J. Comp. Neurol.* 205, 260–272.
- Senba, E., Tohyama, M., 1988. Calcitonin gene-related peptide containing autonomic efferent pathways to the pelvic ganglia of the rat. *Brain Res.* 449, 386–390.
- Silvestri, L., Costantini, L., Sacconi, L., Pavone, F.S., 2016. Clearing of fixed tissue: a review from a microscopist's perspective. *J. Biomed. Opt.* 21, 081205.
- Sliwinski, C., Nees, T.A., Puttagunta, R., Weidner, N., Blesch, A., 2018. Sensorimotor activity partially ameliorates pain and reduces nociceptive fiber density in the chronically injured spinal cord. *J. Neurotrauma* 35, 2222–2238.
- Swanson, L.W., 1977. Immunohistochemical evidence for a neurophysin-containing autonomic pathway arising in the paraventricular nucleus of the hypothalamus. *Brain Res.* 128, 346–353.
- Swanson, L.W., McKellar, S., 1979. The distribution of oxytocin- and neurophysin-stained fibers in the spinal cord of the rat and monkey. *J. Comp. Neurol.* 188, 87–106.
- Todd, A.J., McKenzie, J., 1989. GABA-immunoreactive neurons in the dorsal horn of the rat spinal cord. *Neuroscience* 31, 799–806.
- Vercelli, A., Repici, M., Garbossa, D., Grimaldi, A., 2000. Recent techniques for tracing pathways in the central nervous system of developing and adult mammals. *Brain Res. Bull.* 51, 11–28.
- Wang, P., Zhang, D., Bai, S., Tao, B., Li, S., Wang, T., Shang, A., 2020. Feasibility of commonly used fluorescent dyes and viral tracers in aqueous and solvent-based tissue clearing. *Neurosci. Lett.* 737, 135301.
- Willis, W.D., Coggeshall, R.E., 2004. *Sensory Mechanisms of the Spinal Cord*. Springer US, New York.
- Woolf, C., Wiesenfeld-Hallin, Z., 1986. Substance P and calcitonin gene-related peptide synergistically modulate the gain of the nociceptive flexor withdrawal reflex in the rat. *Neurosci. Lett.* 66, 226–230.
- Wrobel, L., Schorscher-Petcu, A., Dupré, A., Yoshida, M., Nishimori, K., Tribollet, E., 2011. Distribution and identity of neurons expressing the oxytocin receptor in the mouse spinal cord. *Neurosci. Lett.* 495, 49–54.
- Yang, B., Treweek, J.B., Kulkarni, R.P., Deverman, B.E., Chen, C.K., Lubeck, E., Shah, S., Cai, L., Gradinaru, V., 2014. Single-cell phenotyping within transparent intact tissue through whole-body clearing. *Cell* 158 (4), 945–958.
- Zheng, H., Rinaman, L., 2016. Simplified CLARITY for visualizing immunofluorescence labeling in the developing rat brain. *Brain Struct. Funct.* 221, 2375–2383.
- Zimmermann, M., 1983. Ethical guidelines for investigations of experimental pain in conscious animals. *Pain* 16, 109–110.
- Zou, X., Lin, Q., Willis, W.D., 2002. The effects of sympathectomy on capsaicin-evoked fos expression of spinal dorsal horn GABAergic neurons. *Brain Res.* 958, 322–329.